SCUOLA DI DOTTORATO
UNIVERSITÀ DEGLI STUDI DI MILANO-BICOCCA

Dipartimento di / Department of

FISICA

Dottorato di Ricerca in / PhD program FISICA E ASTRONOMIA Ciclo / Cycle XXXVI

Curriculum in ASTROFISICA

The Influence of the Environment on the Dark Matter and Gas Content of Galaxies in a High-Resolution Cosmological Simulation

Cognome / Surname Herzog Nome / Name Georg

Matricola / Registration number 872999

Tutore / Tutor: Prof. Monica Colpi

Supervisor: Prof. Michele Fumagalli

Coordinatore / Coordinator: Stefano Ragazzi

ANNO ACCADEMICO / ACADEMIC YEAR 2022/2023

The Influence of the Environment on the Dark Matter and Gas Content of Galaxies in a High-Resolution Cosmological Simulation

Georg Herzog

UNIVERSITA' DEGLI STUDI DI MILANO
BICOCCA

Milano 2024

The Influence of the Environment on the Dark Matter and Gas Content of Galaxies in a High-Resolution Cosmological Simulation

Georg Herzog

PhD Thesis in Astrophysics
Dipartimento di Fisica "Giuseppe Occhialini"
Università degli studi di Milano-Bicocca
Milano

XXXVI Cycle
Georg Herzog
di Graz, Austria

Milano, January 31st, 2024

Supervisor: Michele Fumagalli
Co-Supervisor: Alejandro Benítez-Llambay
Tutor: Monica Colpi

Contents

1 Introduction 1

1.1 The Universe Now and Then 1

1.2 Cosmological background 3

1.2.1 The Cosmological Principle and its Consequences 4

1.2.2 Relativistic Cosmology 6

1.2.3 The flat universe 8

1.3 Initial Conditions for Structure Formation 9

1.3.1 The Big Bang and Inflation 10

1.3.2 Nucleosynthesis 11

1.3.3 Cosmic Microwave Background 12

1.4 Compostion of the Universe 15

1.4.1 Matter 15

1.4.2 Dark Energy 16

1.4.3 Radiation and Curvature 17

1.5 Structure Formation 17

1.5.1 Growth of density perturbations 18

1.5.2 Gravitational Collapse of DM haloes 21

1.5.3 Collapse of Baryons in DM halos 24

1.5.4 Transfer Functions 26

1.5.5 The final state of large scale structure formation: The Cosmic Web 27

1.6 Environmental Interactions 30

1.7 Research Question 31

2 Cosmological Simulations 33

2.1 Gravity with N-body simulations 34

2.2 Hydrodynamics in Lagrangian Formulation 36

2.3 SPH - Smoothed Particle Hydrodynamics 37

2.4 A high-resolution cosmological simulation 39

2.4.1 Gravitational interactions and the TreePM algorithm 39

2.4.2 Entropy formulation of SPH 41

2.4.3 Resolution of simulation 43

2.4.4 Initial Conditions 43

2.4.5 Subgrid Physics: The `EAGLE` model of galaxy formation 44

2.5 Halo Finders and Merger trees 49
2.5.1 Finding substructure and linking it through time 50
2.5.2 Mass accretion histories 50
2.6 Virial Quantities 56
2.7 Visualization, Movies, and Calculation of Column Densities 57

3 Galaxies and their Interactions with the Environment 59
3.1 The need for a cosmological representative sample 59
3.2 The present-day gas content of simulated field dwarf galaxies 60
3.2.1 Introduction 61
3.2.2 Methods 63
3.2.3 Results 66
3.2.4 Discussion 76
3.2.5 Summary and Conclusions 84

4 Dark-Matter-Deficient Galaxies 87
4.1 Introduction 87
4.2 Results 88
4.3 Discussion and Summary 94

5 The influence of large-scale structure on galaxy properties 97
5.1 The circumgalactic medium and the galaxy environment 97
5.2 The Influence of the Environment on the CGM of galaxies 99
5.2.1 Introduction 99
5.2.2 Methods 102
5.2.3 Simulation 102
5.2.4 Results 109
5.2.5 Discussion 120
5.2.6 Conclusions 128
5.3 Post-processing of ionization states and comparison with observations . . . 129

6 Conclusions and Future Research 137

Ringraziamenti - Danksagung 163

List of Figures

1.1 View of the Perseus Cluster by `Euclid`. Credit: ESA/Euclid/Euclid Consortium/NASA, image processing by J.-C. Cuillandre (CEA Paris-Saclay), G. Anselmi, CC BY-SA 3.0 IGO. 2

1.2 Fluctuations of the cosmic microwave background as observed by Planck. Figure 9 from Planck Collaboration et al. (2016). 3

1.3 Temperature power spectrum of the CMB as observed by `Planck`. Figure 11 from Planck Collaboration et al. (2016). 14

1.4 Gas distribution in a high-resolution cosmological simulation at four different redshifts. The simulation is the one we used for this thesis and is explained in detail in Sec. 2.4. In the top left panel, we show the gas distribution at $z = 10$ in the full simulation box. The cosmic web did not yet form, but instead one can see overdensities and under densities in the gas distribution. In the top right panel at $z = 3$, we can see already the filaments of the cosmic web and some galaxies as bright dots. In the two lower panels at $z = 1$ and $z = 0$ the cosmic web is fully assembled and galaxies can be found in groups and in isolation along filaments. 28

2.1 Mass accretion history of a galaxy. The solid black line shows the dark matter mass, the dashed line is the gas mass and the dotted line is the stellar mass. The blue line is the critical mass that needs to be exceeded for star formation to happen. The red line is the baryon fraction. The galaxy is born at around ~ 0.5 Gyrs and reaches a halo mass of $\sim 5 \times 10^9$ $\mathrm{M}_\odot$ after about 2 Gyrs. From there the galaxy slowly continues to grow and at the present day it has a halo mass of $\sim 10^{10}$ $\mathrm{M}_\odot$ and a stellar mass of $M_* \sim 10^7$ $\mathrm{M}_\odot$. Since the halo mass is always above the critical mass for star formation, this galaxy continues to form stars until the present day. 51

2.2 Mass accretion history of a galaxy where the wrong galaxy was selected as the main progenitor. The black solid line is the dark matter mass, the dashed line is the gas mass, and the dotted line is the stellar mass. The blue line shows the critical mass necessary for star formation and the red line is the baryon fraction. At a time of around 8 Gyrs, there is a sharp jump in all the tracked masses. This is because here the tracking went wrong and a low-mass halo was chosen as the main progenitor. We show a visualization of this jump from the starless dark matter halo to the galaxy in Fig. 2.3. The grey-shaded area corresponds to the timespan shown in the visualization. 52

2.3 Visualization of the jump from the star less dark matter halo to the galaxy. The first three panels show the star less dark matter halo that has been wrongly identified as the main progenitor as it approaches a more massive galaxy. In panel four and five the halo finder identified the right galaxy as the main galaxy. These wrong identifications of the main progenitor happen for about 10% of the field galaxies and need to be corrected if one is interested in the evolution of the galaxy sample. 53

2.4 Mass accretion history of a galaxy where gas particles are wrongly associated with the halo. The lines show the same as before. At around 6 Gyrs the galaxy undergoes an environmental interaction that removes some of its dark matter and all of its gas. Shortly after 6 Gyrs, we can see a spike in the gas mass and after 10 Gyrs it seems like the galaxy is accreting some gas again. However, this is only due to a failure of the unbinding procedure in `HBT+` that wrongly associates gas particles with this dark matter halo, while traveling through ambient gas. We show a visualization of this galaxy before stripping and in the timespan marked by the grey-shaded area in Fig. 2.5. 54

2.5 Visualization of the galaxy that wrongly has gas particles associated with it by `HBT+`. In the first panel, we see the galaxy before the stripping event with the gas concentrated in the center. In the next four panels, we see the galaxy after the stripping event, where the second and the third panels show the galaxy at snapshots where `HBT+` did not associate gas particles with them, while the fourth and the fifth panels show the galaxy at snapshots with gas associated with them by `HBT+`. Since there is no gas concentrated at the center of the galaxy, and one can rather only see the ambient gas, one has to correct the gas mass by hand and set it to zero. 54

2.6 Mass accretion history of a galaxy where a freely floating star particle is wrongly associated with the dark matter halo. We see that the stellar mass seems to oscillate, i.e. it seems like the galaxy forms stars and loses stars several times. However, since the gas mass is zero, even before the first star is acquired, this star particle cannot come from the transformation of a gas particle into a star particle. Instead, it captures a freely floating star particle that has been formed somewhere else, whenever the stellar mass is non-zero. 55

2.7 Visualization of a “galaxy” that has captured a freely floating star particle. In each panel, we mark the virial radius of the “galaxy” by a white circle, and the star particles close to the galaxy with white stars. In the first panel, there are four star particles, and although one is at the edge of the virial radius of the galaxy, it is not counted as a bound particle by `HBT+`. In the second and fourth panels, the star particle is counted as bound, while in the third and fifth panels, it is again not bound to the galaxy. 56

3.1 Present-day stellar mass, $M_\star$, as a function of virial mass, M_{200}, for the isolated galaxies identified in the simulation. Galaxies are coloured according to their virial gas mass fraction, $M_{\rm gas}/M_{200}$, relative to the universal baryon fraction, $\bar{f}_{\rm b} = \Omega_b/\Omega_m$. The various lines display different abundance matching expectations, as labelled. Yellow stars show the galaxies inhabiting the 20 most massive haloes of the simulation. 64

3.2 The left panel shows the present-day gas mass as a function of halo mass for our galaxy sample. We display galaxies with $M_{\rm gas} = 0$ with an arbitrarily low value (horizontal arrow). Galaxies are coloured as in Fig. 3.1, i.e., according to their gas mass fraction relative to the universal baryon fraction. The solid black line indicates the running median of the distribution for galaxies with $M_{\rm gas} > 0$, and the dot-dashed lines indicate the 16-84th percentiles, as measured in bins equally spaced logarithmically in mass (black symbols). The grey line and shaded region show the gas mass that results from applying the BL20 model. The vertical dot-dashed line indicates the critical virial mass above which gas cannot remain in hydrostatic equilibrium according to this model. The oblique lines display the universal baryon fraction, $\bar{f}_{\rm b} = \Omega_b/\Omega_m$, 10 per cent, and 1 per cent of this value. The green diamonds indicate four example galaxies (G1, G2, G3, and G4) that inhabit halos of the same mass today but contain very different gas masses. The right panel shows the star formation rate (SFR), in units of the past average, as a function of present-day halo mass. The red histogram shows the fraction of systems for which SFR>0 (scale on the right). We display galaxies with SFR $= 0$ with an arbitrarily low value (horizontal arrow). Galaxies less massive than the BL20 critical mass are quiescent, as expected. In both panels, the yellow stars indicate the 20 most massive systems in the simulation. 65

3.3 Spatial distribution of simulated galaxies spanning the narrow range in virial mass, $10^9 < M_{200}/M_\odot < 3 \times 10^9$, in cubic regions of 10 Mpc side length equally spaced to cover the entire simulated volume. Panels A, B, C, and D may be combined to form a slice spanning the coordinates range, $(x, y, z) = (0-20, 0-20, 0-10)$ Mpc, whereas panels E, F, G, and H may be combined to cover the remaining half of the box, i.e., $(x, y, z) = (0-20, 0-20, 10-20)$ Mpc. As in Fig. 3.2, we colour galaxies according to their present-day gas fraction relative to the universal baryon fraction. Yellow stars indicate the location of the 20 most massive galaxies in the simulation. The colour map in the background displays the projected gas density. Gas-deficient galaxies (blue triangles with white edges) cluster either along the filaments of the cosmic web or close to massive systems, in sharp contrast with the other galaxies in the same halo mass range. The strongly clustered distribution of gas-deficient galaxies thus points to the role of the environment in shaping their present-day gas content. 67

3.4 Time evolution of 4 individual simulated dwarf galaxies. Different rows show the projected gas density around each dwarf at various times. The white circle indicates the virial radius of the galaxy. The first row shows the evolution of G1, which loses its gas by cosmic web stripping. The second row displays G2, which, although an isolated system today, approached a massive system in the past and lost gas and dark matter via tidal and ram pressure forces. The third row shows the evolution of G3, a galaxy embedded in a dense but otherwise isolated environment, in contrast to G4 (fourth row), which evolves in a less dense but isolated environment. 69

3.5 Mass assembly histories of the four individual dwarfs shown in Fig. 3.4. The black-solid, dashed, and dot-dashed lines show the dark matter (DM), gas, and stellar mass, respectively. The blue line corresponds to the critical mass for the onset of star formation, as predicted by the BL20 model. The red line shows the baryon fraction, $M_{\rm gas}/M_{200}$, in units of the universal baryon fraction (scale on the right). The grey shaded area spans the time interval shown for each dwarf in Fig. 3.4. 72

3.6 The top panel, analogous to Fig. 3.1, shows the present-day stellar mass versus halo mass for our galaxy sample. The cyan circles indicate flyby galaxies, as defined in Sec. 3.2.3. Interestingly, flybys scatter off the stellar mass versus halo mass relation followed by non-flybys. The lower panel, analogous to Fig. 3.2, shows the current gas mass as a function of halo mass. As in Fig. 3.2, we show gas-free galaxies with an arbitrary gas mass value, $M_{\rm gas} = 2 \times 10^4$ M$_\odot$. The majority of flybys (cyan circles) are essentially devoid of gas. 75

3.7 Analogous to Fig. 3.3, but we now display the spatial distribution of flyby galaxies (cyan symbols), as defined in Sec. 3.2.3. Flyby galaxies exhibit a characteristic clustering pattern towards the more massive systems of the simulation (yellow stars). 76

3.8 The top panel, analogous to Fig. 3.1, but in which we removed flyby galaxies, shows the present-day stellar mass as a function of halo mass for our galaxy sample. The red circles indicate COSWEB galaxies, as defined in Sec. 3.2.3. The lower panel, analogous to Fig. 3.2, shows the gas mass as a function of halo mass for all galaxies but flybys. As in the top panel, we show COSWEBs with red circles. Gas-free galaxies are indicated with a lower gas mass, $M_{\rm gas} = 2 \times 10^4$ $\rm M_\odot$. 77

3.9 Analogous to Fig. 3.3, but we now display the spatial distribution of COSWEB galaxies only (red symbols), as defined in Sec. 3.2.3. COSWEBs exhibit much less clustering towards massive systems (yellow stars) than flybys (see Fig. 3.7), and they depict the location of the filaments of the cosmic web well. We have verified that those COSWEB galaxies close to a massive system today are approaching the host for the first time. These galaxies have been stripped of their gas several virial radii away from the massive systems, so their gas removal is not directly related to ram-pressure exerted by the host's hot gaseous halo. 78

3.10 Fraction of gas-deficient (black line), flyby (blue line), and COSWEB (red area) galaxies, as a function of halo mass. We define gas-deficient galaxies as those whose virial gas mass fraction is under 1% of the universal baryon fraction, $\bar{f}_{\rm b} = \Omega_{\rm b}/\Omega_m$. For consistency, we only considered those flyby galaxies that are also gas-deficient. We, therefore, excluded only 17 flybys that do not fulfil this requirement. Below a halo mass, $M_{200} \sim 5 \times 10^8$ $\rm M_\odot$, all galaxies become gas deficient (see text for a discussion on this). Below a halo mass, $M_{200} \sim 3 \times 10^8$ $\rm M_\odot$, all gas-deficient galaxies become flybys. . . 81

3.11 The left panel shows the gas mass as a function of halo mass for our galaxy sample, excluding gas-deficient galaxies. Galaxies are coloured according to their "ambient" density, i.e., the mean gas density within a shell between 2 to 3 times the virial radius of the systems, in units of the mean density of the Universe. The coloured lines show the median and the 16-84th percentiles of the distribution. The oblique lines show the expected gas mass for haloes that have retained the universal baryon fraction (solid line), 10% of this value (dashed line), and 1% (dotted line). The vertical line shows the BL20 critical mass. The right panel shows the median "ambient" density relative to the mean baryon density of the Universe, as a function of halo mass, for galaxies whose gas mass is above the 84th percentile (green line), and for galaxies whose gas mass is under the 16th percentile (blue line). The difference in "ambient" density between gas-rich and gas-poor galaxies indicates that the gas mass of these halos is affected, to some extent, by the amount of gas located beyond the virial radius of the systems. 82

4.1 Time evolution of a galaxy that is undergoing n-body interactions in an assembling group and is subsequently slingshotted out. Each panel shows the projected gas density around the galaxy in a cube of 1 cMpc side length. The virial radius of the galaxy that is stripped is marked with a black circle. In the first and second panel, the galaxy is inside an assembling group and is losing dark matter due to tidal interactions. In the third panel, the galaxy received a kick due to n-body interactions and is leaving the gravitational field of its host. In the fourth and fifth panel, the galaxy is then travelling again through the simulation volume. 89

4.2 Mass accretion history of a galaxy undergoing n-body interactions and which subsequently is slingshotted out. The black solid line shows the dark matter mass, the dashed line is the gas mass, and the dashed-dotted line is the stellar mass. We marked by a grey shaded area the timespan shown in Fig. 4.1. During the n-body process, which starts around $z = 4$ and ends around $z = 1.5$ the galaxy loses more than an order of magnitude of its dark matter mass. The tidal interactions are so strong, that even part of the stellar mass is lost due to the stripping. 89

4.3 Path of the galaxy in the simulation volume after it experiences n-body interactions. We show the gas distribution at $z = 0$ and mark the virial radius of the host that was responsible for the stripping with a black circle. Additionally, we mark the path of the galaxy that gets slingshotted out by black crosses. The $z = 0$ position of the galaxy that got slingshotted out is at the center of the picture. We can see that the galaxy after receiving the kick quickly leaves the gravitational field of the host. Towards $z = 0$ it makes another turn-around, which is due to the collision with another galaxy. At $z = 0$ the distance between the host and the galaxy that got slingshotted out is about 1.6 Mpc. 90

4.4 Dark matter map (left panel) and gas map (right panel) of a region where we preliminarily identified a collection of more than 20 freely floating star particles. The dark matter and gas map is overplotted with all the star particles in the region marked yellow stars in the left panel and blue stars in the right panel. We can see two collections of star particles that seem to be gravitationally bound, a big one towards the lower left corner and a small one towards the upper right corner. When calculating the mass profiles around these clusters of star particles they were dark matter dominated. Apart from the two clusters of star particles, many star particles seem to be scattered around the volume without being gravitationally bound. We had to introduce the threshold of $n = 20$ star particles because otherwise, we picked up too often random collections of such freely floating particles that were not gravitationally bound. 93

5.1 Stellar mass plotted against the halo mass for all galaxies in our sample, where for the halo mass we took the total bound mass for each galaxy. In the left panel, we mark galaxies that are classified as group galaxies as blue stars while galaxies that are classified as isolated galaxies are marked as red stars. Satellite galaxies are marked as grey dots. In the right panel, we show again the stellar mass-halo mass relation for all the galaxies in our sample with isolated centrals being marked as red stars, satellite galaxies as green dots, and the hosts of the satellites within Bin1 and Bin2 as black stars. All other group galaxies are marked as grey stars. We chose two bins in stellar mass and halo mass marked by the rectangles spanning the area of $\log_{10}\mathrm{M}_* = [8, 8.5]$ $\mathrm{M}_\odot$ and $\log_{10}M_{200} = [10.6, 11.1]$ $\mathrm{M}_\odot$ in the stellar mass-halo mass plane for Bin1 and $\log_{10}\mathrm{M}_* = [8.5, 9]$ $\mathrm{M}_\odot$ and $\log_{10}\mathrm{M}_{200} = [10.8, 11.3]$ $\mathrm{M}_\odot$ in the stellar mass-halo mass plane for Bin2. At low halo and stellar masses, we find both isolated and group galaxies, while at intermediate halo and stellar masses, isolated galaxies dominate. At very high halo masses we find only group galaxies. Therefore, we cannot analyze a bin at intermediate or high halo and stellar masses, since there is no area in the stellar mass-halo mass plane with sufficient group as well as isolated galaxies to do a proper comparison. 106

5.2 Spatial distribution of simulated galaxies with $\mathrm{M}_* > 10^8$ $\mathrm{M}_\odot$ in the simulation volume. In panels A, B, C and D the gas within a slice $0 < z < 10000$ kpc is projected onto the xy-plane, while in panels E, F, G and H it is the gas within $10000 < z < 20000$ kpc, i.e. panels A, B, C and D can be moved directly above panels E, F, G and H to span the full cube. Blue stars mark central galaxies that are in a group environment, red stars are central galaxies that are in isolation and green dots are satellite galaxies as identified by `HBT+`. We split the sample of central galaxies into group and isolated galaxies by means of a distance criterion (see text). Group galaxies reside in denser environments marked by the darker color of the underlying gas structure in the simulation Although some isolated galaxies seem to cluster in groups or seem to be group galaxies like for example in the lower part of panel F, these galaxies fulfill the isolation condition and the apparent clustering is just a projection effect. 110

5.3 Radial profiles of density and temperature for Bin1 (left column) and Bin2 (right column). *Upper panels:* Radial profiles of the average gas density for group galaxies (blue) and isolated galaxies (red). The solid line is the median, while the shaded areas are the percentiles. Isolated galaxies and group galaxies do not show a difference in the density profile up to about $4 \times R_{half}$. After that a small difference is visible with group galaxies having a slightly higher gas density. *Lower panels:* Radial profile of average gas temperature for group galaxies (blue) and isolated galaxies (red). The solid line shows the median and the shaded area the 16/84 percentiles. The temperature profiles for isolated galaxies and group galaxies are the same up to about 4 half mass radii. Only at radii R> 4×R_{half} the temperature of galaxies in groups is slightly higher compared to isolated galaxies. . . . 112

5.4 Covering fraction of hot (upper row), warm (middle row) and cold gas (lower row) for group galaxies (blue) and isolated galaxies (red). The left column is for Bin1 and the right column for Bin2. We can clearly see that if the gas around galaxies is selected in real space and the galaxies in the sample are exactly matched in stellar mass, halo mass and them being the central galaxies of their dark matter halo there is no difference in the covering fraction of different gas phases. 114

5.5 *Upper row:* Radial profile of the average gas density for all the gas in satellites (green), the bound gas of the satellites (cyan) and all the gas in isolated central galaxies (black) in Bin1 (left panel) and Bin2 (right panel). The solid lines are the medians, while the shaded areas are the percentiles. Satellites have a higher gas density than isolated centrals at each radius. Up to about 1 half mass radius the density profile for satellites is dominated by bound gas, while after 1 half mass radius it is dominated by unbound gas. Furthermore, at around 1 half mass radius also the difference in the densities between the gas around satellites and the gas around isolated central galaxies starts to increase which is due to the presence of gas belonging to the host in the case of satellites. *Lower row:* Radial profile of average gas temperature for all gas in satellite galaxies (green), only the bound gas in satellites (cyan) as well as all the gas in isolated central galaxies (black) for Bin1 (left panel) and Bin2 (right panel). The solid line shows the median and the shaded area the 16/84 percentiles. The temperature profiles for satellites and isolated centrals of the same stellar mass and halo mass bin differ significantly. At radii $R > 1 \times R_{half}$ the temperature profiles start to diverge with satellites reaching much higher temperatures than isolated centrals of the same mass bin. This is especially driven by unbound gas, i.e. gas that does not belong to the galaxy itself but to its more massive host galaxy. 116

5.6 Covering fractions of all the gas (upper row), bound gas (middle row) and unbound gas (lower row) for satellite galaxies and isolated central galaxies in the stellar mass-halo mass Bin1. We show the median (solid line) and 16/84 percentiles (shaded area) for satellites (blue) and isolated centrals (red). In the upper row we also show the covering fraction of the hosts of the satellites (black). When looking at all the gas we see that satellites show a higher covering fraction compared to isolated centrals, especially for the warm and hot phase. Furthermore, the covering fraction of satellites for the warm and hot phase is comparable to the covering fraction of their hosts. The covering fraction for bound gas is similar for both satellites and isolated centrals while for unbound gas the covering fraction is much higher for satellite galaxies. This means that what we saw in the radial profiles is also true for the covering fraction, namely that the difference between satellites and isolated centrals is mostly driven by unbound gas in the satellites that belongs to their more massive hosts. 121

5.7 Same as in Fig. 5.6 but for Bin2. Again, satellites show a much higher covering fraction than isolated centrals and this difference is again mostly driven by the additional unbound gas in satellites, i.e. the gas that belongs to their hosts. 122

5.8 Covering fractions for hot, warm and cold gas when the gas is selected in a window of ±500 km/s in velocity space around the galaxy. We show the median (solid lines) and 16/84 percentiles (shaded area) of group galaxies (blue) and isolated galaxies (red) in the same stellar mass-halo mass bins as in Fig. 5.4. For better comparison we also show the medians of group galaxies (solid black line) and isolated galaxies (dashed black line) from Fig. 5.4 where the gas was selected in a sphere around the galaxies. Selecting the gas in velocity space has almost no effect on cold gas. The situation is different for the warm and hot phases where a difference between group and isolated galaxies emerges. This shows that associating gas to galaxies in a window of ±500 km/s in velocity space can artificially introduce a difference for the warm and hot phases. 123

5.9 Covering fraction for hot (left panel), warm (middle panel) and cold gas (right panel) for group galaxies (blue) and isolated galaxies (red) when matching the sample in stellar mass with an allowed difference of 0.3 dex. Solid lines show the medians while shaded areas show the 16/84 percentiles. There is no difference between group and isolated galaxies for hot and cold gas with the medians and the percentiles almost perfectly overlapping. For warm gas the median in groups is slightly higher than the median for isolated galaxies. However, the median for groups lies within the 16/84 percentiles of isolated galaxies and the percentiles of both samples also almost perfectly overlap. 124

5.10 Covering fraction for hot (left panel), warm (middle panel) and cold gas (right panel) for group galaxies (blue) and isolated galaxies (red) as defined by the observational group finder and when matching the sample in stellar mass with an allowed difference of 0.3 dex. Solid lines show the medians while shaded areas show the 16/84 percentiles. While the medians of group galaxies are slightly higher than the medians of isolated galaxies, the percentiles overlap. Therefore, using the observational group finder that uses a window of ±500 km/s in velocity space to link in the z-direction is merely a complicated way of relabeling galaxies and does not significantly influence the observed covering fractions. 124

5.11 Covering fraction of Mg II in our simulation (blue lines) overplotted with the cumulative covering fractions of Mg II (solid lines) using an equivalent with of $EW = 0.1$ Å (red lines) and $EW = 0.03$ Å (purple lines) together with their 1σ errors (dashed lines) for all galaxies with $M_* < 10^{10}$ $\mathrm{M}_\odot$ from Dutta et al. (2021). At radii $R < 200$ kpc our covering fractions are much too high compared to observations, while at radii $R > 200$ kpc the median seems to match observations. We used a column density of 10^{12} cm^{-2} per pixel as a threshold for detection in the simulation. 131

5.12 Covering fraction of C IV in our simulation (blue lines) overplotted with the cumulative covering fractions of C IV using an equivalent with of $EW = 0.1$ Å (red solid lines) and $EW = 0.03$ Å (purple solid lines) together with their 1σ errors (dashed lines) for all galaxies with $M_* < 10^{10}$ $\mathrm{M}_\odot$ from Dutta et al. (2021). At radii $R < 100$ kpc our covering fraction sees a sharp upturn which is not seen in observations, while at radii $R > 150$ kpc our covering fractions are too low. We used a column density of 10^{13} cm^{-2} per pixel as a threshold for detection in the simulation. 132

5.13 Mg II absorbers per unit redshift at different redshifts. We show the values from the simulation at $z = 0$, $z = 1$ and $z = 3$ for a detection limit of 10^{12} cm^{-2} and 10^{13} cm^{-2}. We compare it to the parametrization for dN/dz from Mathes et al. (2017) which we obtained by transforming their parametrization for dN/dX from their eq. (7) and their Table 1. We show the results for an equivalent width of $EW = 0.01$ Å which corresponds to a column density detection limit of 2.3×10^{11} cm^{-2} and $EW = 0.3$ Å which corresponds to a column density detection limit of 7×10^{12} cm^{-2}. Ideally, our results for a detection limit of 10^{12} cm^{-2} should lie between the two curves for $EW = 0.01$ Å and $EW = 0.3$ Å. However, apart from $z = 0$ which is on the line of $EW = 0.3$ Å all the other measurements are below that line and therefore too low. This means we do not have enough Mg II absorbers in our simulation volume. 133

5.14 C IV absorbers per unit redshift for different redshifts. We show the values from the simulation at $z = 0$, $z = 1$ and $z = 3$ for a detection limit of 10^{13} cm^{-2} and compare them with the values from Hasan et al. (2020) and Burchett et al. (2015) for an equivalent width $EW = 0.05$ Å which corresponds to 1.24×10^{13} cm^{-2}. Since the values we get in the simulation are far below the values from observations, there are not enough C IV absorbers in our simulation. 134

5.15 Column density of all the gas in the simulation (left panel), Mg II (middle panel) and C IV (right panel) where the ions have been obtained by using `TRIDENT` during post-processing. We can see that in the left panel, the column density of the total gas distribution is smooth. However, in the middle and right panel where the column density for the two ions is shown the column density seems to be very pixelated instead of smooth as we would expect. This let us suspect that something during the post-processing of the ionization states by `TRIDENT` went wrong. 135

List of Tables

5.1 Values of $l(z)$ for Mg II and C IV at different redshifts for three different detection limits. We calculated $l(z)$ with eq. (5.2). 131

Abstract

We analyze a high-resolution hydrodynamical cosmological simulation based on the EAGLE model of galaxy formation. We used this simulation to investigate the influence of the environment on galaxy properties such as the gas content, dark matter content and the circumgalactic medium (CGM) of simulated galaxies.

We found that two distinct processes can influence the evolution and final properties of field dwarf galaxies. The first one termed "cosmic web stripping", removes gas from galaxies by hydrodynamical interactions when plowing through cosmic web filaments. This process can shut down star formation in galaxies and makes them gas-deficient at $z = 0$. About 10% of the total sample is undergoing this process, while it is more important for dwarf galaxies.

The second process we termed "flyby" process. It removes from galaxies gas due to hydrodynamic interactions and dark matter due to tidal interactions when close to a more massive host. After this interaction, they leave the host and are again found in isolation at z=0. Almost all galaxies undergoing the flyby process are devoid of gas after the interaction. Furthermore, these galaxies are scattered off the stellar mass-halo mass relation due to the loss of dark matter. This allows the creation of galaxies with a halo mass below the minimum mass for star formation. About 15% of the total sample are flyby galaxies, with the majority of them being dwarf galaxies. Furthermore, below a halo mass of about 3×10^8 $M_\odot$ all galaxies are flyby galaxies implying that any isolated galaxy with a halo mass below that limit must have undergone the flyby process. Since in theory the flyby process can produce dark matter deficient galaxies in isolation, we checked for such galaxies in our simulation, but did not find any.

In a first attempt to model systematically the influence of the environment on the CGM of galaxies in a cosmological context, we found that galaxies in groups have slightly more gas in their CGM compared to galaxies in isolation. This effect is strongly enhanced if one includes satellite galaxies in the sample. Furthermore, also the use of a velocity window to assign gas to galaxies can increase the measured gas mass around a galaxy. Additionally, we checked whether ionization states from post-processing can be used to make a direct comparison with observations. However, since we were not able to reproduce several observable, we concluded that this is not possible with our simulation.

Sommario

Analizziamo una simulazione cosmologica idrodinamica ad alta risoluzione basata sul modello EAGLE di formazione delle galassie. Abbiamo utilizzato questa simulazione per studiare l'influenza dell'ambiente sulle proprietà delle galassie, come il contenuto di gas, il contenuto di materia oscura e il mezzo circumgalattico delle galassie (CGM) simulate.

Abbiamo scoperto che due processi distinti possono influenzare l'evoluzione e le proprietà finali delle galassie nane di campo. La prima, denominata "cosmic web stripping", rimuove il gas dalle galassie per mezzo di interazioni idrodinamiche quando attraversa i filamenti della rete cosmica. Questo processo può bloccare la formazione di stelle nelle galassie e renderle carenti di gas a $z = 0$. Circa il 10% del campione totale subisce questo processo, mentre è più importante per le galassie nane.

Il secondo processo viene definito “flyby”. Esso rimuove dalle galassie il gas a causa delle interazioni idrodinamiche e la materia oscura a causa delle interazioni mareali quando sono vicine a un ospite più massiccio. Dopo questa interazione, lasciano l’ospite e si ritrovano nuovamente isolate a $z = 0$. Quasi tutte le galassie che subiscono il processo di flyby sono prive di gas dopo l’interazione. Inoltre, queste galassie sono disperse dalla relazione massa stellare-massa dell’alone a causa della perdita di materia oscura. Ciò consente la costituzione di galassie con una massa dell’alone inferiore alla massa minima per la formazione stellare.

Circa il 15% del campione totale è costituito da galassie flyby, la maggior parte delle quali sono galassie nane. Inoltre, al di sotto di una massa dell’alone di circa 3×10^8 $\mathrm{M}_\odot$, tutte le galassie sono galassie flyby. Questo implica che qualsiasi galassia isolata con una massa dell’alone inferiore a questo limite deve aver subito il processo flyby. Poiché in teoria il processo di flyby può produrre galassie isolate carenti di materia oscura, abbiamo verificato la presenza di tali galassie nella nostra simulazione, ma non ne abbiamo trovate.

Nel primo tentativo di modellare sistematicamente l’influenza dell’ambiente sulla CGM delle galassie in un contesto cosmologico, abbiamo scoperto che le galassie in gruppo hanno una quantità di gas leggermente maggiore nella loro CGM rispetto alle galassie isolate. Questo effetto è fortemente amplificato se si includono nel campione le galassie satellite. Inoltre, anche l’uso di una finestra di velocità per assegnare il gas alle galassie può aumentare la massa di gas misurata intorno a una galassia. Inoltre, abbiamo verificato se gli stati di ionizzazione ottenuti in post-processing possono essere utilizzati per fare un confronto diretto con le osservazioni. Tuttavia, poiché non siamo riusciti a riprodurre diverse osservabili, abbiamo concluso che questo non è possibile con la nostra simulazione.

Die Folter endet nie.
The torture never ends.
La tortura non ha fine.

Tocotronic

Chapter 1

Introduction

1.1 The Universe Now and Then

When observing the universe at the current time we see a plethora of structures. We not only see single stars and galaxies but the galaxies are assembled in groups and clusters. An example of such a large-scale structure can be seen in Fig. 1.1 where we show an image of the Perseus Cluster taken by `Euclid` ESA (2023). However, if we go back in time the picture completely changes. In the earliest observation of the universe we currently have, which is the Cosmic Microwave Background (CMB) shown in Fig. 1.2, no large-scale structure exists. Instead of rich structure all one sees is a uniform background radiation of ~ 2.7 K with only small fluctuations on the scale of μK. During the evolution from this uniform background to the large-scale structure, we see today, galaxies form and are undergoing interactions with their environment. How the environment and the interactions with it influence the evolution of galaxies and their gaseous content is the topic of this thesis.

The thesis is structured as follows: in the first part we will discuss the theoretical background of large-scale structure formation starting by introducing the mathematical framework of modern physical cosmology in Sec. 1.2. We will then present the Big Bang, Inflation, Nucleosynthesis as well as the Cosmic Microwave Background in Sec. 1.3 which set the initial conditions for large-scale structure formation. In Sec. 1.4 we will present the different components of the universe in the standard ΛCDM model, before discussing the principles of large-scale structure formation in Sec. 1.5. We will present possible environmental interactions galaxies can undergo during their evolution in Sec. 1.6, which then allows us to formulate our research question in Sec. 1.7.

In the second chapter, we will discuss the main methods used for the research for this thesis, i.e. cosmological simulations. This includes the simulation of gravity in Sec. 2.1, hydrodynamics in the lagrangian formulation in Sec. 2.2 and smoothed-particle hydrodynamics in Sec. 2.3. We then present the simulation used in this thesis in Sec. 2.4 and the halo finding thechniques in Sec. 2.5. Additionally, we discuss also how virial quantities are defined in Sec. 2.6 and how to visualize the simulation output in Sec. 2.7.

Equipt with all the methods, we will present the thesis results in Chs. 3, 4 and 5. First,

Figure 1.1: View of the Perseus Cluster by `Euclid`. Credit: ESA/Euclid/Euclid Consortium/NASA, image processing by J.-C. Cuillandre (CEA Paris-Saclay), G. Anselmi, CC BY-SA 3.0 IGO.

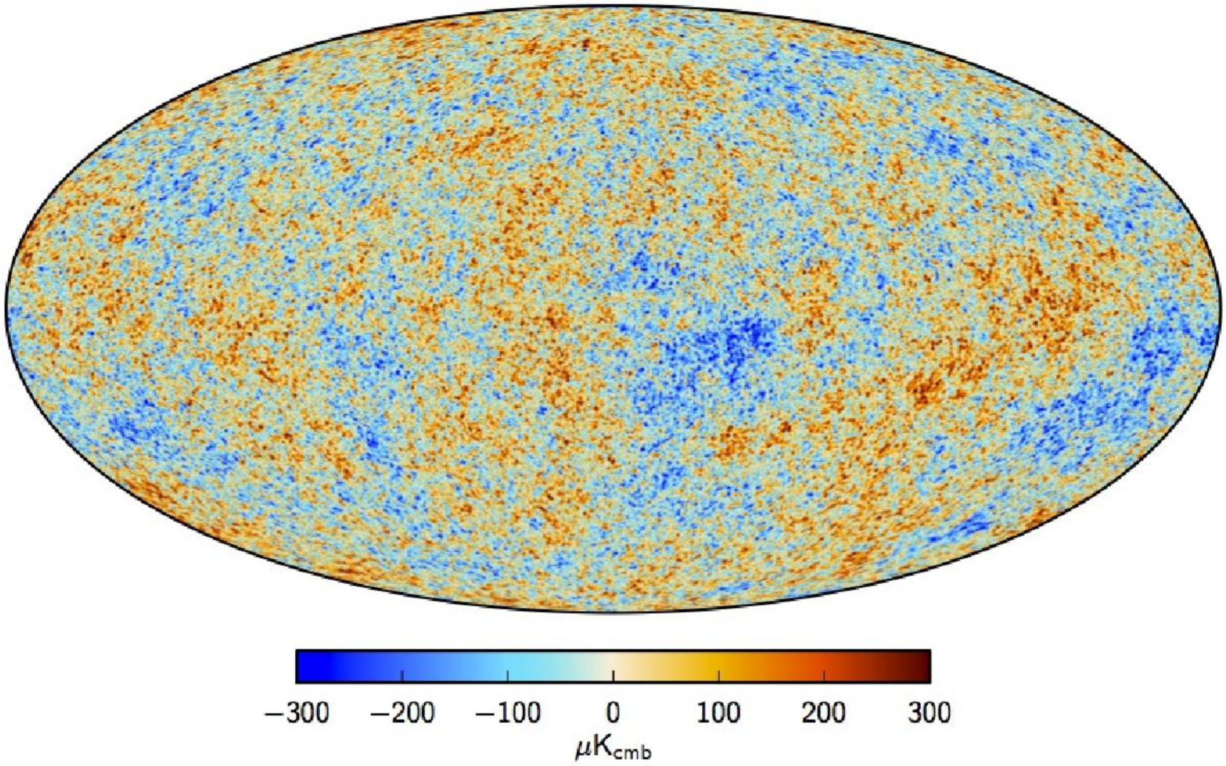

Figure 1.2: Fluctuations of the cosmic microwave background as observed by Planck. Figure 9 from Planck Collaboration et al. (2016).

in Ch. 3 we discuss how ram pressure stripping and tidal stripping influence the gas and dark matter content of field dwarf galaxies. Next, we will discuss our search for dark matter deficient galaxies in our simulation volume in Ch. 4. Finally, we discuss in Ch. 5 how the CGM of a galaxy is influenced by the large-scale structure the galaxy is embedded in. This chapter also includes in Sec. 5.3 a discussion on why the post-processing of ionization states in the simulation cannot be used for our analysis. We conclude the thesis with our conclusions and future research directions in Ch. 6.

1.2 Cosmological background

The theory of General Relativity not only describes how gravity in our universe works but can also be used to describe the evolution of spacetime, that is the universe itself. Implementing the *Cosmological Principle* which means assuming *isotropy* and *homogeneity* one arrives at the equations governing the evolution of the universe. In this subsection, we summarize all the equations necessary to understand the cosmological background of structure formation in an expanding universe. We will follow the notation of Mo et al. (2010) for all mathematical descriptions in this thesis, but also heavily draw from Ta-Pei (2010), Hobson et al. (2006) and Kenyon (2023) for this summary of the mathematics governing cosmology.

1.2.1 The Cosmological Principle and its Consequences

When observing the local universe we see that matter is distributed unequally with the majority of matter clustering in galaxies, which are assembled in groups and galaxy clusters, while other parts of the universe are almost empty. However, when going to large enough scales like the CMB the picture changes, and matter is basically distributed isotropically. Therefore, the cosmological principle states (Mo et al., 2010, p. 102):

> *On sufficiently large scales, the Universe can be considered spatially homogenous and isotropic.*

Here, spatial homogeneity means that all points in space are the same, while isotropy means that the universe is the same under all orientations. This can also be rephrased as the universe being invariant under spatial translations and rotations, i.e. there is no preferred position or direction in the universe when going to large enough scales (Mo et al., 2010; Hobson et al., 2006).

The cosmological principle can also be reformulated in a way such that it states that at each point in space, a fundamental observer exists for whom the universe is isotropic. This fundamental observer defines a *cosmological rest frame* in which the only allowed motion is expansion or contraction of space itself (Mo et al., 2010), i.e. they have fixed spatial coordinates which are called *comoving coordinates* (Hobson et al., 2006). For all the fundamental observers at the different locations in space, one can find a three-dimensional hypersurface on which properties like temperature, density, and expansion rate are uniform. Furthermore, there exists a universally agreed cosmic time that evolves these properties (Mo et al., 2010; Hobson et al., 2006). The hypersurfaces defined in this way by the fundamental observers constitute maximally symmetric hypersurfaces.

Using spherical coordinates we can write the metric of such maximally symmetric hypersurface as (Mo et al., 2010):

$$dl^2 = a^2(t)\left[\frac{dr^2}{1-Kr^2} + r^2(d\vartheta^2 + sin^2\vartheta d\varphi^2)\right] \tag{1.1}$$

where $a(t)$ is the time-dependent scale factor, K is a constant that defines the curvature of spacetime and can take the values $1, 0$ or -1. If $K = 1$ the universe has a positive spatial curvature, $K = 0$ constitutes a flat universe without any curvature, and $K = -1$ is a universe with negative spatial curvature.

Since the line element in Eq. 1.1 is only for a spatial hypersurface in 3 dimensions for which time is constant we need to add the time dimension to arrive at the line element for the 4-dimensional spacetime that describes the universe (Mo et al., 2010):

$$ds^2 = c^2dt^2 - dl^2 = c^2dt^2 - a^2(t)\left[\frac{dr^2}{1-Kr^2} + r^2(d\vartheta^2 + sin^2\vartheta d\varphi^2)\right], \tag{1.2}$$

where c is the speed of light. This metric is called the *Friedmann-Robertson-Walker* (FRW) metric (Friedmann, 1922, 1924; Lemaître, 1931a,c; Robertson, 1935, 1936a,b; Walker, 1937).

The scale factor $a(t)$ relates the distance between fundamental observers when switching from comoving coordinates to physical coordinates. In the comoving frame, the distance between fundamental observers stays the same as long as there is no peculiar velocity. However, the universe expands and one has to account for the expansion by relating the comoving coordinates to the physical coordinates with the scale factor. Accounting for the scale factor one gets a *physical distance* l between two fundamental observers which depends on the curvature K of the universe (Mo et al., 2010).

The physical distance can be written as (Mo et al., 2010):

$$l = a(t) \int_0^{r_1} \frac{dr}{\sqrt{1 - Kr^2}} = a(t)\chi(r_1) \tag{1.3}$$

with the curvature dependend comoving distance $\chi(r)$ being:

$$\chi(r) = \begin{cases} sin^{-1}r & \text{if } K = 1, \\ sinh^{-1}r & \text{if } K = -1, \\ r & \text{if } K = 0. \end{cases} \tag{1.4}$$

With the physical distance between two fundamental observers we are now able to define the expansion rate of the universe. The expansion rate of the universe at a certain time t is characterized by the *Hubble parameter* $H(t)$ and defined as the change in the physical distance l between two fundamental observers in units of l, i.e. $dl/dt \equiv H(t)l$. We can write the Hubble parameter also in terms of the scale factor $a(t)$ and the derivative of the scale factor with respect to t as (Mo et al., 2010):

$$H(t) = \frac{\dot{a}(t)}{a(t)}. \tag{1.5}$$

The expansion rate at the present time H_0 is called the *Hubble constant* (Hubble, 1929). The Hubble constant H_0 is obtained by observations and varies depending on the method used (Blakeslee et al., 2021; Planck Collaboration et al., 2020a; Birrer et al., 2020). This dependence of the Hubble constant on the chosen observational method is one of the big unresolved questions in current cosmology but beyond the scope of this thesis.

Instead of using H_0 one often uses a quantity called *"little"* h, which is defined as (Mo et al., 2010):

$$h \equiv \frac{H_0}{100 \text{ km s}^{-1}\text{Mpc}^{-1}}. \tag{1.6}$$

Due to the expansion of the universe signals that get emitted, like light from galaxies or supernovae, are becoming redshifted while traveling through space. The redshift is defined as the ratio between the scale factor at present time $a(t_0)$ and the scale factor at the time of emission $a(t_e)$ as (see eg Mo et al. (2010) for a detailed derivation):

$$1 + z \equiv \frac{a(t_0)}{a(t_e)}. \tag{1.7}$$

The redshift serves as both a time measurement and a distance measurement since it tells us not only how far back in time the signal was emitted, but also how far a signal had to travel to arrive at the observer.

1.2.2 Relativistic Cosmology

If one applies General Relativity to the matter distribution of a homogeneous and isotropic universe as dictated by the cosmological principle, one arrives at the equations that govern the evolution of the universe. Starting from the Einstein field equation (Einstein, 1915, 1916):

$$R_{\mu\nu} - \frac{1}{2} g_{\mu\nu} R - g_{\mu\nu}\Lambda = \frac{8\pi G}{c^4} T_{\mu\nu} \ , \tag{1.8}$$

one can rewrite them using $R + 4\Lambda = -\frac{8\pi G}{c^4} T$ as (see eg Hobson et al. (2006) or Mo et al. (2010) for more details)

$$R_{\mu\nu} + g_{\mu\nu}\Lambda = \frac{8\pi G}{c^4} \left(T_{\mu\nu} - \frac{1}{2} g_{\mu\nu} T \right) . \tag{1.9}$$

with $R_{\mu\nu}$ being the Ricci tensor and $g_{\mu\nu}$ the metric. Furthermore, $R = R_{\mu\nu} g^{\mu\nu}$ is the Ricci scalar, Λ is the cosmological constant and $T_{\mu\nu}$ is the energy-momentum tensor of the universe with $T = T^{\mu}_{\mu}$.

Assuming a uniform ideal fluid, $T_{\mu\nu}$ is given by

$$T^{\mu\nu} = (\rho + P/c^2) U^{\mu} U^{\nu} - g^{\mu\nu} P \tag{1.10}$$

where ρc^2 is the energy density, P the pressure and U^{μ} the four velocity of the fluid. In a homogeneous and isotropic universe $U^{\mu} = (c, 0, 0, 0)$, because no peculiar motion is allowed (Mo et al., 2010) and so T is given by

$$T = T^{\mu}_{\nu} = \mathrm{diag}(\rho c^2, -P, -P, -P) = \rho c^2 - 3P \ . \tag{1.11}$$

As we showed in Sec. 1.2.1, a homogeneous and isotropic universe is described by the FRW-metric as given by Eq. (1.2). Using the FRW-metric one can express the Ricci tensor $R_{\mu\nu}$ in terms of the scale factor $a(t)$ and the curvature K, which in turn allows us to rewrite Eq. (1.9) as

$$\left(\frac{\dot{a}}{a} \right)^2 = \frac{8\pi G}{3} \rho - \frac{K c^2}{a^2} + \frac{\Lambda c^2}{3} \ . \tag{1.12}$$

This equation is called the *Friedmann equation* and describes how the expansion of the universe is connected to its curvature and energy density. In its essence it is an equation for energy conservation (Kenyon, 2023).

The expansion rate of the universe is not necessarily constant but can change. A change in the expansion rate of the universe is governed by the so-called acceleration equation (Mo et al., 2010):

$$\frac{\ddot{a}}{a} = -\frac{4\pi G}{3}\left(\rho + 3\frac{P}{c^2}\right) + \frac{\Lambda c^2}{3} \ . \tag{1.13}$$

It relates the acceleration of the expansion to the pressure P, density ρ, and the cosmological constant Λ. While the matter content ρ and P slow down the expansion, the cosmological constant Λ is speeding it up since it acts as a negative pressure with $P_\Lambda = -\rho_\Lambda c^2$ (Mo et al., 2010; Kenyon, 2023). In fact, it has been observed using supernovae Ia that the expansion of the universe accelerates (Riess et al., 1998). The force driving this acceleration of the expansion is called *dark energy*. The exact nature of dark energy is an open question in current cosmology, which is beyond the scope of this thesis.

Finally, we also need an equation that tells us how the density ρ and pressure P change with the expansion of the universe. This is done by the equation (Mo et al., 2010):

$$\frac{d\rho}{da} + 3\left(\frac{\rho + P/c^2}{a}\right) = 0, \tag{1.14}$$

that tells us the change of ρ and P with a changing expansion factor $a(t)$. To fully determine a, P, and ρ at each point in time we now need to specify the exact equation of state $P(\rho)$ that relates the density to the pressure.

The equation of state will allow us to determine how P and ρ as well as the temperature T scale with the expansion factor. Introducing an equation of state parameter w we can write (Mo et al., 2010):

$$P = w\rho c^2 \ . \tag{1.15}$$

This together with eq. 1.14 leads to (Mo et al., 2010):

$$\rho \propto a^{-3(1+w)} \ . \tag{1.16}$$

The pressure P as well as the temperature T scale differently and are related differently depending on whether the universe is radiation-dominated, matter-dominated or dominated by dark energy. An exact derivation can be found for example in Mo et al. (2010). Here we just give the relations:

1. For $w = 0$ we get a *matter dominated* universe with the following relations:

$$\rho \propto a^{-3}, \quad P \propto a^{-5}, \quad T \propto a^{-2} \ . \tag{1.17}$$

2. For $w = 1/3$ we get a *radiation dominated* universe with:

$$\rho \propto a^{-4}, \quad P \propto a^{-4}, \quad T \propto a^{-1} \ . \tag{1.18}$$

3. Finally, $w = -1$ gives us a *dark energy dominated* universe with the following relations:

$$\rho \propto a^{0}, \quad P \propto a^{0} \ . \tag{1.19}$$

With eqs. 1.12 and 1.14 together with the equation of state for each epoch and the initial conditions from the Big Bang we have all the ingredients to describe the scale factor a, the pressure P and the density ρ at each point in time during the evolution of the universe.

1.2.3 The flat universe

The curvature K of the universe is given by its matter content ρ. If the total energy density of the universe is equal to the *critical density* ρ_{crit}, the universe is flat (Kenyon, 2023). The critical density is given by (Mo et al., 2010):

$$\rho_{crit}(t) \equiv \frac{3H(t)^2}{8\pi G} \tag{1.20}$$

The critical density can also be written in terms of the contributions from different sources as (Kenyon, 2023):

$$\rho_{crit} = \rho_r + \rho_m + \rho_\Lambda \ , \tag{1.21}$$

where ρ_r is the contribution from radiation, ρ_m the contribution from baryonic and *dark matter* and ρ_Λ is the contribution from the cosmological constant. We can also express all the contributions in terms of fractions of the critical density ρ_{crit} as $\Omega_i = \rho_i/\rho_{crit}$. In this case we have (Kenyon, 2023):

$$\Omega \equiv \Omega_r + \Omega_m + \Omega_\Lambda = 1 \tag{1.22}$$

The deviation from a flat universe is characterized by the curvature contribution Ω_K defined as (Mo et al., 2010):

$$\Omega_K \equiv -\frac{Kc^2}{H^2a^2} = 1 - \Omega \ . \tag{1.23}$$

Since current observations of the *Planck* collaboration show that our universe is basically flat with $\Omega_K = 0.001 \pm 0.002$ (Planck Collaboration et al., 2020a), we will continue to discuss only the case of a flat universe from now on.

The density parameter Ω develops over time. The time dependence of Ω is given by

$$\Omega(t) \equiv \frac{\rho(t)}{\rho_{crit}(t)}. \tag{1.24}$$

Since we have seen in eqs. 1.17, 1.18 and 1.19 that the evolution of ρ with the scale factor depends on the component one is looking at, also the evolution of the density parameter is different for each component. We can write the time evolution of the different components in terms of the redshift z as (Mo et al., 2010):

$$\Omega_\Lambda(z) = \frac{\Omega_{\Lambda,0}}{E^2(z)}, \quad \Omega_m(z) = \frac{\Omega_{m,0}(1+z)^3}{E^2(z)}, \quad \Omega_r(z) = \frac{\Omega_{r,0}(1+z)^4}{E^2(z)} \tag{1.25}$$

where $E(z)$ is given by (Mo et al., 2010):

$$E(z) = [\Omega_{\Lambda,0+} + (1-\Omega_0)(1+z)^2 + \Omega_{m,0}(1+z)^3 + \Omega_{r,0}(1+z)^4]^{1/2} \tag{1.26}$$

Finally, the evolution of the total density parameter is given by (Mo et al., 2010):

$$\Omega(z) - 1 = (\Omega_0 - 1)\frac{(1+z)^2}{E^2(z)} \tag{1.27}$$

Furthermore, the evolution of the scale factor $a(t)$ with time t depends on the epoch one is in. For the three cases radiation dominated, matter-dominated, and dark energy-dominated $a(t)$ develops as (Mo et al., 2010):

$$a(t) = \begin{cases} \left(\frac{32\pi G\rho_{r,0}}{3}\right)^{1/4} t^{1/2} & \text{if radiation dominated,} \\ \left(\frac{3H_0 t}{2}\right)^{2/3} & \text{if matter dominated,} \\ e^{H_0(t-t_0)} & \text{if dark energy dominated.} \end{cases} \tag{1.28}$$

From this, it follows that due to eq. 1.5 also the Hubble parameter $H(t)$ develops differently depending on the epoch.

Finally, knowing that our universe is a flat universe we can calculate the age of the universe at each redshift z from the components Ω_m and Ω_Λ at the present time denoted as $\Omega_{m,0}$ and $\Omega_{\Lambda,0}$. The age of the universe at redshift z is given by (Mo et al., 2010):

$$t(z) = \frac{1}{H_0}\frac{2}{3\sqrt{\Omega_{\Lambda,0}}}\ln\left[\frac{\sqrt{\Omega_{\Lambda,0}(1+z)^{-3}} + \sqrt{\Omega_{\Lambda,0}(1+z)^{-3} + \Omega_{m,0}}}{\Omega_{m,0}}\right] . \tag{1.29}$$

This gives us all the mathematical tools to describe structure formation in an expanding universe.

1.3 Initial Conditions for Structure Formation

In Sec. 1.2 we discussed how General Relativity together with the Cosmological Principle allows us to derive equations that describe the evolution of the universe. The mathematics derived in that section allows us not only to describe our own universe, but many different cosmological models, like models with zero spatial curvature, but also models with positive or negative spatial curvature. However, using this mathematical framework only tells us how certain equations evolve in different scenarios like the scale factor in a radiation-dominated, matter-dominated, or dark energy-dominated universe in eq. 1.28, but it tells us nothing about the actual values of cosmological observables that go into these equations like the Hubble constant H_0 or the contributions of different components to the overall energy density of the universe, like Ω_m or Ω_Λ. Furthermore, it also does not tell us how the large-scale structure of the cosmic web we observe today with galaxies, groups, and clusters formed. In this section, we will therefore give a more detailed overview of the evolution of our universe up to the cosmic microwave background which sets the initial conditions for large-scale structure formation. We will include all the necessary parts to understand how the initial conditions of large-scale structure formation in our universe came about.

1.3.1 The Big Bang and Inflation

One of the observations leading to the current standard model of cosmology was that all galaxies outside the local group galaxies are receding from us (Hubble, 1929; Kirshner, 2004; Mo et al., 2010). Extrapolating back in time one arrives at the conclusion that at some point in the past, the whole universe was concentrated in one point (Lemaître, 1931b; Ta-Pei, 2010). This is taken as the beginning of the universe and was termed *Big Bang* from when on the universe expanded until the present.

Directly after the Big Bang, it is assumed that the universe grew by about 30 orders of magnitude during a period called inflation (Ta-Pei, 2010). The motivation for this assumption comes from two observations of the universe today that are challenging to explain without such an inflationary period. First, in the present day, the curvature of the universe has a value $\Omega_K = 0.001 \pm 0.002$ (Planck Collaboration et al., 2020a). This is statistically consistent with zero and therefore we can consider the universe spatially flat. Since the curvature of the universe is given by eq. 1.23, which means that $\Omega_K \propto \frac{1}{\dot{a}(t)^2}$, the curvature must increase in time if $K \neq 0$, since the denominator is always decreasing (Ta-Pei, 2010). Therefore, if the current value of the curvature is $\Omega_K = 0.001 \pm 0.002$, it must have been even closer to zero at previous times with a value of $\Omega_K(t_{bbn}) = \mathcal{O}(10^{-15})$ at the time of big bang nucleosynthesis (Ta-Pei, 2010).

Second, observations of the Cosmic Microwave Background show that the universe is homogeneous and isotropic over very large scales with only small fluctuations. However, only very small patches of the CMB could have been in causal contact in the past, if the universe only underwent the expansion during the radiation and matter-dominated eras. Therefore, the question is how we could arrive at a universe that is so isotropic and homogeneous, where it seems that parts of the universe have been in causal contact in the past to average out any inhomogeneities that might have existed to produce the highly isotropic CMB we observe today (Ta-Pei, 2010). Both these observations can be naturally explained if there was a period of inflation after the Big Bang during which the universe underwent a period of exponential growth, since such a period would both, blow up the area that has been in causal contact and smooth out existing curvature (Kenyon, 2023).

Several mechanisms have been proposed to get an inflationary period (Brout et al., 1978; Starobinsky, 1980; Kazanas, 1980; Sato, 1981; Guth, 1981; Linde, 1982; Albrecht and Steinhardt, 1982; Mo et al., 2010) and they can be tested with observations from the cosmic microwave background (Vazquez et al., 2018; Planck Collaboration et al., 2020b). However, no matter what the exact mechanism behind inflation is, the advantage of such a period and why it is included in standard cosmology is not only that it solves the above-mentioned flatness and horizon problems, but that it gives a natural explanation for the origin of small perturbations that grow into the large scale structure we see today. Small quantum fluctuations grow during the period of inflation to fluctuations of the scale bigger than the horizon. These initial fluctuations were Gaussian and scale-invariant and then became seeds for galaxy formation (Hobson et al., 2006; Ta-Pei, 2010).

1.3.2 Nucleosynthesis

In the universe we see today almost all the baryonic matter is found in atoms. However, at earlier times the universe was much hotter and quarks, leptons, and photons existed in an unbound state, before being confined into hadrons, which subsequently annihilated and decayed. At some point, only protons, i.e ionized hydrogen, and neutrons were left behind which then were synthesized into helium and some heavier elements during the period of nucleosynthesis. Since the ratio of hydrogen to helium as well as metals are the initial conditions from which star and galaxy formation starts to proceed, we will now describe the period of nucleosyntesis in more detail.

Nucleosynthesis starts from an initial abundance of neutrons and protons in the early universe. At temperatures of $T \gg 10^{10}$ K there are as many protons as neutrons, but when the temperature drops to about 1 MeV the number density of neutrons also starts to drop due to the higher mass of neutrons compared to protons (Mo et al., 2010). The neutrinos start to decouple also at around a temperature of 1 MeV which means that the weak interactions that kept neutrons and protons in thermal equilibrium are not fast enough anymore to maintain this equilibrium and the ratio of protons to neutrons freezes out at a value of $\frac{n_n}{n_p} \approx 0.2$. Since neutrons are unstable they continue to decrease exponentially according to $X_n \propto e^{-\frac{t}{\tau_n}}$, where $X_n \equiv \frac{n_n}{n_n+n_p}$ and $\tau_n = (879.4 \pm 0.6)$ s is the mean lifetime of neutrons (Workman and Others, 2022; Mo et al., 2010). Only when nucleosynthesis starts and neutrons are bound in elements like deuterium or helium they become stable (Mo et al., 2010).

The synthesis of deuterium and helium starts when the universe has cooled down to a temperature of $T \approx 10^9$ K. At these low temperatures, helium cannot be produced directly by many-body interactions such as $2\,\mathrm{n} + 2\,p \rightarrow {}^4\mathrm{He}$ due to the low number densities of protons and neutrons (Mo et al., 2010). Therefore, the reactions to produce helium has to go through the intermediate step of producing deuterium. Deuterium is produced by the reaction (Kenyon, 2023):

$$\mathrm{p} + n \rightarrow {}^2\mathrm{H} + \gamma \tag{1.30}$$

From deuterium the subsequent synthesis of helium proceeds. The detailed chain of two-body reactions is given for example in (Mo et al., 2010). We only give the most important ones (Kenyon, 2023):

$${}^2\mathrm{H} + {}^2\mathrm{H} \rightarrow {}^3\mathrm{H} + \mathrm{p}, \quad {}^2\mathrm{H} + {}^2\mathrm{H} \rightarrow {}^3\mathrm{He} + \mathrm{n}, \tag{1.31}$$

$$\mathrm{p} + {}^2\mathrm{H} \rightarrow {}^3\mathrm{He} + \gamma, \quad \mathrm{n} + {}^2\mathrm{H} \rightarrow {}^3\mathrm{H} + \gamma, \tag{1.32}$$

$${}^3\mathrm{H} + p \rightarrow {}^4\mathrm{He} + \gamma, \quad {}^3\mathrm{He} + n \rightarrow {}^4\mathrm{He} + \gamma. \tag{1.33}$$

Finally, there is also a small amount of lithium-7 produced during primordial nucleosynthesis, for example by the reaction (Mo et al., 2010):

$${}^4\mathrm{He} + {}^3\mathrm{H} \rightarrow {}^7\mathrm{Li} + \gamma \tag{1.34}$$

or by an intermediate step via beryllium. Although beryllium is produced in intermediate steps in the reaction network, no element heavier than ^{7}Li is produced by primordial nucleosynthesis (Mo et al., 2010).

The primordial abundances of hydrogen, helium, and lithium can be obtained by observations. The primordial abundance of helium-4 is $\frac{^4\mathrm{He}}{\mathrm{H}} = 0.24 \pm 0.01$. The ratio of deuterium to hydrogen is $\frac{\mathrm{D}}{\mathrm{H}} = 2.82 \pm 0.53 \times 10^{-5}$. The abundance of helium-3 is $\frac{^3\mathrm{He}}{\mathrm{H}} \approx 10^{-5}$ and the abundance of primordial lithium is $\frac{^7\mathrm{Li}}{\mathrm{H}} \approx 5 \times 10^{-10}$ (Mo et al., 2010). These results, especially the one from the ratio of deuterium to helium, can be used to constrain the number density of baryons in the universe via the present-day baryon-to-photon ratio η given by (Mo et al., 2010):

$$\eta \equiv \frac{n_b}{n_\gamma} \approx 2.72 \times 10^{-8} \Omega_{b,0} h^2. \tag{1.35}$$

The part important for galaxy evolution and especially simulations of large-scale structure formation is the ratio:

$$\frac{^4\mathrm{He}}{\mathrm{H}} = 0.24 \pm 0.01, \tag{1.36}$$

since it gives the starting conditions for baryonic matter in simulations.

1.3.3 Cosmic Microwave Background

The Cosmic Microwave Background (CMB) is an almost perfectly isotropic radiation with a temperature of about $T = 2.7$ K that is observed all around the sky. What we observe as the CMB today are the photons from the hot plasma of the early universe that started to travel freely when protons and electrons recombined into neutral hydrogen. Due to recombination Thomson scattering off free electrons and Coulomb scattering of free protons was not possible anymore and so the universe became transparent to photons (Kenyon, 2023). This happened when the universe was about 2×10^5 yrs old and had a temperature of about $T \approx 4000$ K (Mo et al., 2010). Due to the expansion of the universe, the radiation cooled down and is now observed at a temperature of $T = 2.7255$ K showing an almost perfect black body spectrum. However, there are small anisotropies in the CMB temperature on the scale of a few μK as shown in Fig. 1.2. These anisotropies were created by quantum fluctuations during inflation described in Sec. 1.3.1 and are the seeds for large-scale structure formation (Kenyon, 2023).

The temperature fluctuations seen in Fig. 1.2 can be described mathematically by (Mo et al., 2010):

$$\frac{\Delta T}{T}(\hat{\mathbf{n}}) \equiv \frac{T(\hat{\mathbf{n}}) - \overline{T}}{\overline{T}} \tag{1.37}$$

where $T(\hat{\mathbf{n}})$ is the temperature at a certain point $\hat{\mathbf{n}} = (\vartheta, \varphi)$ in the sky and $\overline{T}$ is the average temperature. This gives us the deviation from the mean temperature at each point in the sky in spherical coordinates. Expanding the temperature fluctuations in spherical harmonics we get (Mo et al., 2010):

$$\frac{\Delta T}{T}(\hat{\mathbf{n}}) = \sum_{l,m} a_{l,m} Y_{l,m}(\vartheta, \varphi). \tag{1.38}$$

The correlation of fluctuations between two points in the sky separated by an angle ϑ is defined as (Mo et al., 2010):

$$C(\vartheta) = \left\langle \frac{\Delta T}{T}(\hat{\mathbf{n}}_1) \frac{\Delta T}{T}(\hat{\mathbf{n}}_2) \right\rangle, \tag{1.39}$$

while the power spectrum of the temperature fluctuations is given by (Mo et al., 2010):

$$C_l = \left\langle |a_{lm}|^2 \right\rangle. \tag{1.40}$$

The correlation of fluctuations is related to the power spectrum C_l by Mo et al. (2010):

$$C(\vartheta) = \frac{1}{4\pi} \sum_{l} (2l+1) C_l P_l(cos\vartheta) \tag{1.41}$$

where $cos\vartheta = \hat{\mathbf{n}}_1 \cdot \hat{\mathbf{n}}_2$ and P_l are the Legendre Polynomials. A first observable of interest for cosmology is the angular power spectrum of temperature fluctuations D_l^{TT} given by Kenyon (2023):

$$D_l^{TT} = \frac{l(l+1)}{2\pi} C_l \langle T \rangle^2. \tag{1.42}$$

We show D_l^{TT} plotted against the multipole moment l from the 2015 `Planck` results Planck Collaboration et al. (2016) in 1.3.

In Fig. 1.3 we see that the peaks of the angular power spectrum have different heights and different locations along the x-axis. From the heights and locations of the different peaks, we can extract information on the composition of the universe. The relative height of the even peaks with respect to the odd peaks determines the baryon-to-dark matter ratio. The location of the peaks on the other hand can be used to determine the curvature of the universe since a universe with positive curvature would lead to smaller perceived angular sizes moving peaks to the right, while negative curvature would lead to bigger angular sizes moving peaks to the left. From the location of the peaks one determines $\Omega_{m,0} + \Omega_{\Lambda,0}$. If the universe is flat, this is equal to one (Kenyon, 2023). Combining this with measurements of baryon acoustic oscillations and the acceleration of the universe from SNe (Riess et al., 1998) one can obtain even more stringent values for $\Omega_{m,0}$ and $\Omega_{\Lambda,0}$ (Kenyon, 2023).

Finally, the temperature fluctuations of the CMB also serve as seeds for large-scale structure formation. To compare the fluctuations of the CMB with the current large-scale matter distribution, one has to give them in terms of a Fourier transform of the spatial distribution of fluctuations and evolve them in time (Kenyon, 2023). The Fourier transform of the spectrum in terms of the coordinate $\mathbf{r}$ is the perturbation power spectrum in $\mathbf{k}$. It

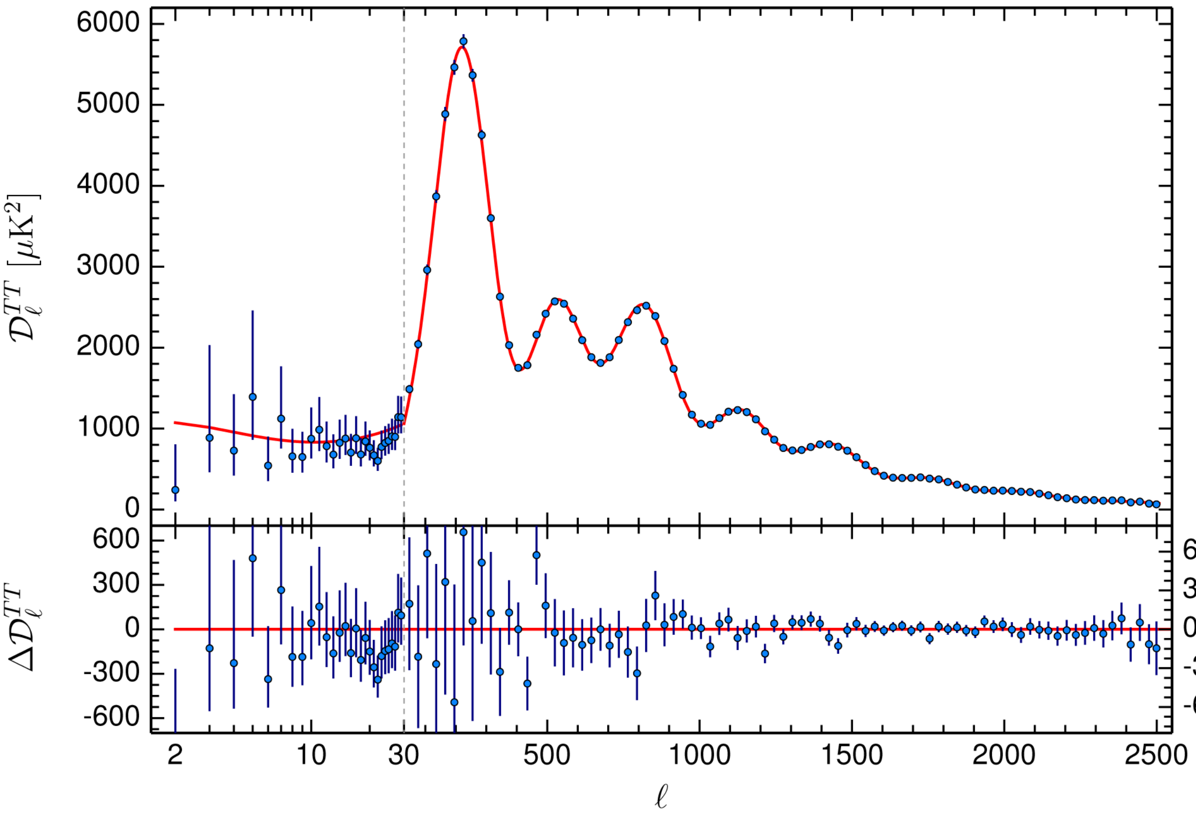

Figure 1.3: Temperature power spectrum of the CMB as observed by `Planck`. Figure 11 from Planck Collaboration et al. (2016).

is parameterized by the following power law (Kenyon, 2023; Planck Collaboration et al., 2020b):

$$P(k)dk = 2\pi^2 A_s k^{-3} \left[\frac{k}{k_p}\right]^{n_s-1} dk, \tag{1.43}$$

where k_p was chosen by the Planck Collaboration to be 0.05 Mpc^{-1} and A_s is:

$$A_s = \frac{k_p^3}{2\pi^2} P(k_p). \tag{1.44}$$

By fitting to data one gets the amplitude $A_s \approx 10^{-9}$, which makes the fluctuations $\sqrt{A_s}$ of order 10^{-5} Kenyon (2023).

Therefore, there are two main takeaways from the cosmic microwave background for large-scale structure formation. First, the small density fluctuations seen in the CMB are the seeds for large-scale structure formation. This process can be split into a linear regime where it is still possible to follow the growth of structure analytically and a non-linear regime where we need simulations. Second, from the CMB we we can infer the exact composition of the universe which allows us to settle on one specific cosmological model. This has the advantage that we only need to run this one model when simulating large-scale structure formation numerically, compared to early times when the exact composition was not yet known and one had to run several different cosmological models (see eg. Davis et al. (1985), Katz et al. (1996)).

1.4 Compostion of the Universe

When discussing the mathematical structure to describe cosmology in Sec. 1.2 we were only able to give quite general relations for the different components of the universe. For example eq. 1.22 gave us the total composition of the universe in terms of radiation, matter, and the cosmological constant without specifying the exact amount, while eq. 1.23 gives the curvature of the universe. With the data from CMB observations it is now possible to give estimates for Ω_r, Ω_m, Ω_Λ and Ω_K in our universe, as already hinted at in Sec. 1.2.3. We will now present the different main components of the universe as found by the `Planck` collaboration in their most recent release (Planck Collaboration et al., 2020a). However, since many simulations like the one we are analyzing still use earlier Planck results as the initial conditions for the simulations, we will also give the 2013 results of the Planck collaboration (Planck Collaboration et al., 2014) which are the initial conditions of our simulation.

1.4.1 Matter

The total matter content of the universe does not only contain the baryonic matter that we can observe in the electromagnetic spectrum but there have been several independent observations hinting at the existence of some kind of *dark matter* that only interacts gravitationally. The most prominent one is definitely the observation of flat rotation curves of galaxies that can only be explained, if a galaxy is embedded in some kind of dark matter halo (Rubin et al., 1980; Bosma, 1981; Faber and Gallagher, 1979; Schneider, 2015). However, there is also other evidence for the existence of dark matter, for example from gravitational lensing (Massey et al., 2010), from galaxy clusters (Arbey and Mahmoudi, 2021) or from the CMB itself (Planck Collaboration et al., 2020a). The total matter content of the universe is given by the `Planck` collaboration. Their most recent results give a value for the matter density parameter as $\Omega_m = 0.315 \pm 0.007$ (Planck Collaboration et al., 2020a). The results from 2013 had a value of $\Omega_m = 0.29 \pm 0.02$ (Planck Collaboration et al., 2014). Since the total matter density of the universe Ω_m can be further split into two parts, dark matter, and baryonic matter, we will now give the results for these two constituents of the total matter density.

Dark Matter

There are several models for dark matter currently explored in research. Among them are cold dark matter, warm dark matter, hot dark matter, or self-interacting dark matter. Although there is a myriad of proposed candidates to explain dark matter as a particle, like Axions or WIMPs (Boveia et al., 2022; Mo et al., 2010; Schneider, 2015), no dark matter particle has so far been detected and it is still unknown what dark matter exactly is. However, in ΛCDM the current standard model for cosmology, dark matter is assumed to be non-interacting and cold. By non-interacting it is meant that when modeling dark matter, the only force that it is acting on it is gravity, which is the same as saying that dark matter is collisionless. That dark matter is "cold" means that whatever constitutes dark matter, be it yet undetected particles or something else, is non-relativistic (Kenyon, 2023) and has a velocity dispersion that is negligible compared to those velocities relevant in astrophysics like the virial velocity of low mass halos (Schneider, 2015). The fraction of matter that is in the form of cold dark matter is given by the `Planck` collaboration as $\Omega_c h^2 = 0.120 \pm 0.001$ (Planck Collaboration et al., 2020a) which is about $\Omega_{CDM} \approx 0.26$. The measurement from 2013 gave $\Omega_c h^2 = 0.1186 \pm 0.0031$ (Planck Collaboration et al., 2014) which is as well $\Omega_{CDM} \approx 0.26$.

Baryonic Matter

Baryonic matter is the ordinary matter we see everywhere around us. The fraction of baryonic matter is given by the `Planck` collaboration as $\Omega_b h^2 = 0.0224 \pm 0.0001$ (Planck Collaboration et al., 2020a) which is approximately $\Omega_b \approx 0.05$. The results from 2013 were $\Omega_b h^2 = 0.02217 \pm 0.00033$ (Planck Collaboration et al., 2014) which also amounts to $\Omega_b \approx 0.05$.

1.4.2 Dark Energy

One of the biggest changes to the standard model of cosmology was the observation that the expansion of the universe is accelerating (Riess et al., 1998). The force responsible for the acceleration of the expansion was termed *dark energy.* It is still unclear what the exact nature of *dark energy* is, but it is very well described by a cosmological constant Λ (Schneider, 2015). Therefore, the observation of the accelerated expansion ruled out all cosmological models without a cosmological constant Λ which do not have to be considered anymore when simulating large-scale structure formation. The most recent results of Ω_Λ as presented by the `Planck` collaboration give $\Omega_\Lambda = 0.6847 \pm 0.0073$ (Planck Collaboration et al., 2020a), while the results from 2013 had $\Omega_\Lambda = 0.67^{+0.027}_{-0.023}$ (Planck Collaboration et al., 2014).

1.4.3 Radiation and Curvature

In eq. 1.22, which is giving all contributions to the total energy density of the universe, we find apart from the contribution of matter and a cosmological constant also the contribution from radiation Ω_r. However, since all the components are determined with their value today (marked with a subscript zero) and since the contribution of radiation to the total energy budget today is negligible we can consider $\Omega_{r,0} = 0$. Then, knowing Ω_m and Ω_Λ we know the curvature of the universe due to eq. 1.23. The value of Ω_K given by the Planck 2018 results is $\Omega_K = 0.001 \pm 0.002$ (Planck Collaboration et al., 2020a). The old value of Ω_K from the 2013 results is $\Omega_K = -0.0096^{+0.010}_{-0.0082}$ (Planck Collaboration et al., 2014). Both values are consistent with zero given the errors so that we can consider the universe spatially flat.

1.5 Structure Formation

In the current model of structure formation, the large-scale structure we see today formed hierarchically from smaller structures. That means that in a first step, dark matter collapsed to form halos. In these dark matter halos, baryons collapsed and formed stars which became the first galaxies. These first galaxies grew by accretion of dark matter and baryons and by merging with other galaxies to form the large-scale structure of filaments, galaxies, groups, and clusters we see today (c.f. Blumenthal et al., 1984; Dekel and Silk, 1986; Quinn et al., 1986; Frenk et al., 1985; Peebles, 1983).

In this section, we will therefore describe in detail how this hierarchical process of structure formation happened and how the large-scale structure we see today formed from the initial density perturbations that are seen in the CMB as temperature anisotropies. First, we start by describing the formation of dark matter halos from gravitational collapse. We will then go on to describe the collapse of baryons in dark matter halos, including the processes necessary to cool down gas and form stars. We will then briefly describe how with the first galaxies the reionization of the universe started and what effect that had on galaxy formation. Finally, we will describe how the current universe is built by mergers of galaxies.

1.5.1 Growth of density perturbations

As we saw in Sec. 1.3.3 small inhomogeneities existed in the CMB, which are the temperature fluctuations described by eq. 1.37. These fluctuations were produced by small density perturbations which were of the order of 10^{-5}. However, the density difference we see today is many orders of magnitude bigger with a density contrast between a virialized halo and the average density of the universe being about 200 (Schneider, 2015). Therefore, the small inhomogeneities we see in the CMB had to grow over time to form the structure we see today.

We can get a qualitative understanding of this growth by looking at the evolution of a density contrast in a cosmological context. First, we can define the relative density contrast similar to eq. 1.37 as (Schneider, 2015):

$$\delta(\mathbf{r},t) := \frac{\Delta\rho(\mathbf{r},t)}{\bar{\rho}(t)} = \frac{\rho(\mathbf{r},t) - \bar{\rho}(t)}{\bar{\rho}(t)}, \tag{1.45}$$

with $\bar{\rho}(t)$ being the mean cosmic density at time t. In general, the evolution of the universe is governed by the mean density $\bar{\rho}(t)$. However, each density perturbation $\Delta\rho(\mathbf{r},t)$ creates an additional gravitational field with respect to the gravitational field created by $\bar{\rho}(t)$. If there is a region that has a higher density than the average density, then $\Delta\rho > 0$ and therefore also $\delta > 0$. This creates a stronger gravitational field compared to the mean gravitational field, which leads to a slower expansion of the overdense region compared to the general expansion due to the additional self-gravity. Due to the slower expansion, the density in the overdense region decreases more slowly compared to the general mean, which leads to an increase in the density contrast and an even stronger gravitational field compared to the cosmic mean. For underdense regions, it works the other way around. Underdense regions have a lower self-gravity compared to the cosmic mean, therefore they expand faster and the density will decrease faster compared to the cosmic mean again increasing the density contrast. Both these processes are runaway processes making overdense regions become more overdense and underdense regions more underdense over time. Thus the density contrast increases (Schneider, 2015).

The growth of density perturbations can be described in a more formal way using Newtonian theory of small perturbations when the perturbations are much smaller than the horizon. Since the perturbations which are much smaller than the horizon are the ones that collapse into galaxies, we will restrict ourselves to these perturbations. Furthermore, we can use an ideal fluid approximation, if we want to describe a baryonic gas in thermal equilibrium or a pressureless dust, i.e. collisionless or cold dark matter. Doing so we can describe the time evolution of the density ρ and the velocity $\mathbf{u}$ under the influence of a gravitational field with potential Φ by three equations (Mo et al., 2010). First, the continuity equation (Mo et al., 2010):

$$\frac{\mathrm{D}\rho}{\mathrm{D}t} + \rho\nabla_{\mathbf{r}} \cdot \mathbf{u} = 0 \tag{1.46}$$

describes the conservation of mass. The Euler equations (Mo et al., 2010):

$$\frac{\mathrm{D}\mathbf{u}}{\mathrm{D}t} = -\frac{\nabla_{\mathbf{r}} P}{\rho} - \nabla_{\mathbf{r}}\phi \tag{1.47}$$

are the equations of motion. And finally, the Poisson equation (Mo et al., 2010):

$$\nabla^2_{\mathbf{r}}\phi = 4\pi G\rho \tag{1.48}$$

describes the gravitational field. In all these equations $\mathbf{r}$ is the physical coordinate. With $\partial/\partial t$ being the partial derivative for fixed $\mathbf{r}$ we can write $\frac{\mathrm{D}}{\mathrm{D}t}$ as:

$$\frac{\mathrm{D}}{\mathrm{D}t} \equiv \frac{\partial}{\partial t} + \mathbf{u}\cdot\nabla_{\mathbf{r}} \tag{1.49}$$

which is the convective time derivative describing the time derivative of a quantity that moves with the fluid (Mo et al., 2010). Since eqs. 1.46 to 1.48 give 5 equations for the 6 unknowns ρ, u_x, u_y, u_z, P and Φ we also need an equation of state.

To solve these equations in an expanding universe it is best to change to comoving coordinates $\mathbf{x}$ with $\mathbf{r} = a(t)\mathbf{x}$. The physical velocity $\mathbf{u} = \dot{\mathbf{r}}$ can be written as $\mathbf{u} = \dot{a}(t)\mathbf{x} + \mathbf{v}$ with $\mathbf{v} \equiv a\dot{\mathbf{x}}$. Writing the density ρ as a perturbation to the background as:

$$\rho(\mathbf{x}, t) = \bar{\rho}(t)[1 + \delta(\mathbf{x}, t)] \tag{1.50}$$

and using the fact that in a matter-dominated universe $\rho \approx a^{-3}$ (c.f. eq. 1.17) one can write the set of equations (1.46)-(1.48) as (Mo et al., 2010):

$$\frac{\partial\delta}{\partial t} + \frac{1}{a}\nabla\cdot[(1+\delta)\mathbf{v}] = 0 \tag{1.51}$$

$$\frac{\partial\mathbf{v}}{\partial t} + \frac{\dot{a}}{a}\mathbf{v} + \frac{1}{a}(\mathbf{v}\cdot\nabla)\mathbf{v} = -\frac{\nabla\Phi}{a} - \frac{\nabla P}{a\bar{\rho}(1+\delta)} \tag{1.52}$$

$$\nabla^2\Phi = 4\pi G\bar{\rho}a^2\delta, \quad \Phi \equiv \phi + a\ddot{a}x^2/2 \tag{1.53}$$

This is the most general form of the equations for small perturbations in the Newtonian regime. Specifying the cosmology to specify the evolution of $a(t)$ as well as the equation of state these equations are solvable (Mo et al., 2010).

If the pressure of the fluid only depends on the density the equation of state has the form $P = P(\rho)$. However, in the more general case where the pressure of the fluid also depends on the entropy S the pressure is a function of both the density and the entropy as $P = P(\rho, S)$. In this general case when assuming an ideal non-relativistic monatomic gas one can obtain the following equation for the evolution of small perturbations δ (see Mo et al. (2010) for a detailed derivation):

$$\frac{\partial^2\delta}{\partial t^2} + 2\frac{\dot{a}}{a}\frac{\partial\delta}{\partial t} = 4\pi G\bar{\rho}\delta + \frac{c_s^2}{a^2}\nabla^2\delta + \frac{2}{3}\frac{\overline{T}}{a^2}\nabla^2 S \tag{1.54}$$

where $c_s = \left(\frac{\partial P}{\partial \rho}\right)_S^{1/2}$ is the adiabatic sound speed and $\overline{T}$ is the temperature of the background. The second term on the left-hand side suppresses the growth of perturbations due to the expansion of the universe, while the first term on the right-hand side makes perturbations grow due to gravitational instability. The second and third terms on the right-hand side are pressure terms due to spatial variations in density and specific entropy (Mo et al., 2010).

Jeans Length: Taking the Fourier transform of eq. (1.54) we get (Mo et al., 2010):

$$\frac{\mathrm{d}^2\delta_{\mathbf{k}}}{\mathrm{d}t^2} + 2\frac{\dot{a}}{a}\frac{\mathrm{d}\delta_{\mathbf{k}}}{\mathrm{d}t} = \left[4\pi G\bar{\rho} - \frac{k^2 c_s^2}{a^2}\right]\delta_{\mathbf{k}} + \frac{2}{3}\frac{\overline{T}}{a^2}k^2 S_k. \tag{1.55}$$

Assuming the special case where initial perturbations were only in the density and the evolution is adiabatic, then $k^2 S_{\mathbf{k}} = 0$. Furthermore, when neglecting the expansion of the universe eq. (1.55) becomes (Mo et al., 2010):

$$\frac{\mathrm{d}^2\delta_{\mathbf{k}}}{\mathrm{d}t^2} = -\omega^2\delta_{\mathbf{k}} \quad \text{where} \quad \omega^2 = \frac{k^2 c_s^2}{a^2} - 4\pi G\bar{\rho}. \tag{1.56}$$

With this equation, it is possible that $\omega^2 < 0$ for certain values of k which means that ω becomes imaginary if $\omega^2 < 0$, i.e. $\omega \propto i\alpha$ with α being some real value. In these cases the solution of eq. (1.56), which is given by $\delta_{\mathbf{k}}(t) = \exp(\pm i\omega t)$ becomes $\delta_{\mathbf{k}}(t) \propto \exp(\pm\alpha t)$ which corresponds to exponential growth or decay, i.e. the perturbation is unstable (Mo et al., 2010). Therefore, the wavenumber k_J for which $\omega = 0$ lets us define the *Jeans length* as (Mo et al., 2010):

$$\lambda_J \equiv \frac{2\pi a}{k_J} = c_s\sqrt{\frac{\pi}{G\bar{\rho}}}. \tag{1.57}$$

This is the characteristic length a sound wave can travel in one gravitational free-fall time $t_{ff} \propto \sqrt{1/G\rho}$. All perturbations which have $\lambda > \lambda_J$ have $k < k_j$ collapse under gravity. Taking the expansion of the universe into account this solution is slightly modified in the way that the growth of unstable modes is slowed down (Mo et al., 2010).

Growth of perturbations in a pressureless fluid: We now want to consider the special case of the growth of density perturbations in a pressureless fluid. In this case eq. (1.55) becomes (Mo et al., 2010):

$$\frac{\mathrm{d}^2\delta_{\mathbf{k}}}{\mathrm{d}t^2} + 2\frac{\dot{a}}{a}\frac{\mathrm{d}\delta_{\mathbf{k}}}{\mathrm{d}t} = 4\pi G\overline{\rho}_m\delta_{\mathbf{k}}, \tag{1.58}$$

with $\overline{\rho}_m$ being the mean density of the fluid. This differential equation has two solutions, a growing mode δ_+ and a decaying mode δ_- (Mo et al., 2010). The decaying mode δ_- is proportional to the Hubble parameter, i.e. $\delta_- \propto H(t)$, while the growing mode δ_+ can be written as (Mo et al., 2010):

$$\delta_+ \propto H(t)\int_0^t \frac{dt'}{a^2(t')H^2(t')}. \tag{1.59}$$

Writing this in terms of the scale factor a we get (Schneider, 2015):

$$\delta_+ \propto D_+(a) \propto \frac{H(a)}{H_0} \int_0^a \frac{da'}{[\Omega_m/a' + \Omega_\Lambda a'^2 - (\Omega_m + \Omega_\Lambda - 1)]^{3/2}}, \tag{1.60}$$

which holds for arbitrary values of matter and vacuum energy density (Schneider, 2015). In general, we can write the solution of the differential equation eq. (1.58) as (Schneider, 2015):

$$\delta(\mathbf{x}, t) = D_+(t)\delta_0(\mathbf{x}), \tag{1.61}$$

where $D_+(t)$ is the growth fractor. From this follows an important conclusion: During linear growth, the shape of the density perturbations in comoving coordinates is fixed. The only thing that changes is the density contrast (Schneider, 2015).

1.5.2 Gravitational Collapse of DM haloes

In Sec. 1.5.1 we saw how the initial density perturbations grow when the density contrast is small, i.e. in the case of $\delta \ll 1$. In this case, the growth of density perturbations is well described by linear theory. However, due to the constant growth of the density contrast, at some point, the density perturbations reach the limit of Jeans instability and start to collapse under their own gravity. This process when $\delta \gg 1$ is in general non-linear and one has to use numerical simulations to study it in detail (Mo et al., 2010; Kenyon, 2023; Schneider, 2015). However, some idealized analytical solutions exist which we will discuss now.

When the first overdensities started to collapse, the influence of the cosmological constant Λ was still negligible. Therefore, we can treat the collapse of overdensities in the early universe by setting $\Lambda = 0$. In this case, the radius of a spherical density perturbation or mass shell evolves according to (Mo et al., 2010):

$$\frac{\mathrm{d}^2 r}{\mathrm{d}t^2} = -\frac{GM}{r^2}. \tag{1.62}$$

Integrating this once one arrives at the equation (Mo et al., 2010):

$$\frac{1}{2}\left(\frac{\mathrm{d}r}{\mathrm{d}t}\right)^2 - \frac{GM}{r} = \epsilon \tag{1.63}$$

with ϵ being the specific energy contained within the radius r. This equation has two solutions for $\epsilon \neq 0$. For $\epsilon > 0$ it will expand infinitely. However, for $\epsilon < 0$ it will expand to a maximum radius before it recollapses onto itself (Mo et al., 2010). In this case, we can parameterize the evolution of the perturbation as (Mo et al., 2010):

$$r = A(1 - \cos\theta); \quad t = B(\theta - \sin\theta). \tag{1.64}$$

In this equation A and B are constants that can be determined from the underlying cosmology (Mo et al., 2010). After some mathematics (Mo et al., 2010) one finds that A and

B can be written as (Mo et al., 2010):

$$A = \frac{1}{2} \frac{r_i}{[5\delta_i/3 + 1 - \Omega_i^{-1}]}; \quad B = \frac{3}{4} \frac{t_i}{[5\delta_i/3 + 1 - \Omega_i^{-1}]^{3/2}}. \tag{1.65}$$

Here r_i is the radius of the mass shell that collapses, $\Omega_i = \overline{\rho}(t_i)/\rho_{crit}(t_i)$ is the density parameter at time t_i and δ_i the average overdensity within the mass shell. This overdensity within the mass shell is related to the enclosed mass M and the radius r_i by (Mo et al., 2010):

$$(1 + \delta_i)\overline{\rho}(t_i)\frac{4\pi r_i^3}{3} = M. \tag{1.66}$$

At $\theta = \pi$ the mass shell reaches its maximum expansion and one can write $t_{max} = \pi B$ and $r_{max} = 2A$. At the maximum expansion, the mass shell will do a turn-around and start to collapse again. Theoretically, it will be concentrated in one point at $t_{col} = 2t_{max}$ (Schneider, 2015). However, at small r the above approximation is not true anymore and particles within the mass shells cross each other multiple times before $2t_{max}$ forming a *virialized halo* in this way (Mo et al., 2010). Nevertheless, $t_{col} \equiv 2t_{max}$ is still a useful timescale to describe the collapse of overdensities, since it gives the timescale needed for virialization.

For the special case of $\Omega_m = 1$ and $\Omega_\Lambda = 0$ one can find a critical overdensity δ_c for which the time for the collapse is smaller than the age of the universe, i.e. $t_{col} < t_0$. Overdensities with an initial density contrast $\delta_0 > \delta_c$ manage to fully collapse until the present day. This critical overdensity for $\Omega_m = 1$ and $\Omega_\Lambda = 0$ is approximately $\delta_c \approx 1.69$ (Schneider, 2015). The modifications to δ_c when using other combinations of the density parameters are rather small, which makes $\delta_c \approx 1.69$ a good approximation. Finally, for a collapse to occur before a certain redshift z the density contrast needs to be: (Schneider, 2015)

$$\delta_0 \geq \delta_c(1 + z). \tag{1.67}$$

Collisionless Dynamics In the current standard model for structure formation dark matter overdensities collapse first to form virialized halos. The dark matter component of the universe is assumed to be cold (see. Sec. 1.4) and can be described by collisionless dynamics. However, due to the low probability of direct encounters between stars, also the stellar component of a galaxy is best described by collisionless dynamics. We will now introduce some of the most important time scales in collisionless dynamics before introducing the equations governing the dynamics.

There are four important time scales for collisionless dynamics: first, the time scale for direct collisions between two particles in the system t_{direct}; second, t_{cross} which is the average time for a particle to cross the system; third, the time scale for close encounters t_{close}; and fourth, t_{relax} which is the time scale on which the system relaxes. The time scale for direct collisions is given by (Mo et al., 2010):

$$t_{direct} = \frac{\lambda}{v} \simeq \left(\frac{r}{r_p}\right)^2 \frac{t_{cross}}{N}, \tag{1.68}$$

where λ is the mean free path of a particle, v the velocity of the particle, r is the size of the whole system, r_p is the radius of a single particle in the system and N the number of particles in the system (Mo et al., 2010). The crossing time is simply given as (Mo et al., 2010):

$$t_{cross} = \frac{r}{v}. \tag{1.69}$$

With these two timescales, one can estimate the time it takes that two solar-like stars collide in a typical Milky-Way like galaxy. One finds that $t_{direct} \simeq 10^{21}$ yrs, which is more than 10 orders of magnitude more than the Hubble time $t_H \sim 10^{10}$ yrs. Therefore, collisions between stars can be neglected in a galaxy and the stellar component can be treated as collisionless (Mo et al., 2010).

If two particles have an encounter but are far from each other, the change in velocity induced by the encounter is negligible. Only when the impact parameter b is of the order of $b_1 \equiv \frac{Gm}{v_0^2} \equiv \frac{r}{N}$ the change in velocity δv becomes similar to the approaching velocity v_0. Therefore, for an encounter to count as a close encounter the impact parameter b has to be $b \lesssim b_1$. In this case, the time scale for close encounters is given by (Mo et al., 2010):

$$t_{close} = \left(\frac{r}{b_1}\right)^2 \frac{t_{cross}}{N} \simeq N t_{cross} \tag{1.70}$$

The relaxation time is the time it takes for a collisionless system to reach equilibrium by two-body interactions. One can define the relaxation time as the time it takes a particle to change its velocity vector by 90° by close encounters (Schneider, 2015), or in other words $\Delta v_\perp^2 \approx v^2$ (Mo et al., 2010). Defining the relaxation time in this way t_{relax} is given by (Mo et al., 2010):

$$t_{relax} = \frac{N}{10 \mathrm{ln} N} t_{cross}, \tag{1.71}$$

For galaxies and dark matter halos, where the dark matter does not have any self-interactions the following relation holds (Mo et al., 2010):

$$t_{direct} \gg t_{close} \gg t_{relax} \gg t_H \gg t_{cross}. \tag{1.72}$$

The dynamics of a collisionless system is given by its distribution function $f(\mathbf{x}, \mathbf{v}, t)$ in phase space. If the particle number is conserved, the flow in phase space is described by the collisionless Boltzmann equation (Mo et al., 2010):

$$\frac{\mathrm{d}f}{\mathrm{d}t} = \frac{\partial f}{\partial t} + \sum_i v_i \frac{\partial f}{\partial x_i} - \sum_i \frac{\partial \Phi}{\partial x_i} \frac{\partial f}{\partial v_i} = 0 \tag{1.73}$$

The gravitational potential Φ in the collisionless Boltzmann equation is given by (Mo et al., 2010);

$$\nabla^2 \Phi(\mathbf{x}) = 4\pi G \rho(\mathbf{x}). \tag{1.74}$$

When studying structure formation with simulations one has to treat the collisionless Boltzmann equation numerically. We will discuss in detail how this is done in Ch. 2.

Relaxation Mechanisms: As we have seen in eq. (1.72) the time for a collisionless system to reach equilibrium by two-body interactions is longer than the age of the universe. However, in our current universe, we see many virialized systems, which means that other mechanisms need to exist that let a collisionless system reach equilibrium. The main mechanisms are i) *phase mixing* and *chaotic mixing* where particles that originally are close in phases space separate and shear out which leads to a smoothing of the distribution function $f(\mathbf{x}, \mathbf{v}, t)$. ii) *violent relaxation* where a change in the gravitational potential Φ due to the gravitational collapse of the system induces a change in the energies of the particles, letting them both lose and gain energy, with some even becoming unbound; and iii) *Landau damping* which converts the energy of a wave into random motion (Mo et al., 2010).

Virial Theorem: As soon as a collisionless system reaches equilibrium the *virial theorem* applies. The virial theorem relates the mean kinetic energy $\langle E_{kin} \rangle$ of particles to their mean potential energy $\langle E_{pot} \rangle$ when in equilibrium by Kenyon (2023):

$$\langle E_{pot} \rangle = -2 \langle E_{kin} \rangle . \tag{1.75}$$

In a universe with $\Omega_m = 1$ and $\Omega_\Lambda = 0$ a collapsed and virialized overdensity has a mean density that is about 178 times the average density of the universe Somerville and Davé (2015). As we will see in Ch. 2, what is usually used to define a virialized region is a density contrast of 200 between a sphere and the background.

1.5.3 Collapse of Baryons in DM halos

The structure we observe today is not only consisting of collapsed dark matter, but mostly of galaxies consisting of billions of stars. Therefore, the formation of galaxies requires that the baryons that existed in the early universe after nucleosynthesis as a gas of hydrogen and helium fall into the dark matter halos, that they cool down, and collapse to form stars (c.f. Blumenthal et al., 1984; Dekel and Silk, 1986). We will now continue to explain in detail how these processes work in order for galaxies to form in collapsed dark matter halos.

Equations for Gas Dynamics: In many applications in structure formation, we can use the ideal fluid approximation for the gas. That lets us write the continuity, Euler, and energy equations in physical coordinates $\mathbf{r}$ as (Mo et al., 2010):

$$\frac{\partial \rho}{\partial t} + \nabla \cdot (\rho \mathbf{v}) = 0, \tag{1.76}$$

$$\frac{\partial \mathbf{v}}{\partial t} + (\mathbf{v} \cdot \nabla)\mathbf{v} = -\left(\nabla \Phi + \frac{\nabla P}{\rho} \right) \tag{1.77}$$

$$\frac{\partial}{\partial t}\left[\rho\left(\frac{v^2}{2} + \epsilon\right)\right] + \nabla \cdot \left[\rho\left(\frac{v^2}{2} + \frac{P}{\rho} + \epsilon\right)\mathbf{v}\right] - \rho \mathbf{v} \cdot \nabla \Phi = \mathcal{H} - \mathcal{C}. \tag{1.78}$$

In these equations, ρ is the density, $\mathbf{v}$ the velocity, P the pressure, and ϵ the specific internal energy, while $\mathcal{H}$ and $\mathcal{C}$ are the heating and cooling rates. The gravitational potential again fulfills the Poisson equation $\nabla^2\Phi = 4\pi G\rho$ where ρ contains both baryonic and dark matter. As the equation of state for an ideal gas, one has $P = \rho(\gamma - 1)\epsilon$ with γ being the adiabatic index (Mo et al., 2010). Note that eqs. (1.76) and (1.77) are the same as eqs (1.46) and (1.47). However, we added the energy equation (1.78) which tells us that when dealing with the collapse of gas we also have to consider processes contributing to the cooling and heating of the gas.

When dark matter halos collapse, the baryons within them collapse as well. However, their behavior during collapse is very different, since dark matter is collisionless, while baryons interact with each other leading to a transformation of potential energy into thermal energy, i.e. the heating of the gas (Schneider, 2015). The relation of potential energy to kinetic energy for a system in equilibrium is described by the virial theorem in eq. (1.75) equating the kinetic energy to half the potential energy. The temperatures that gas can therefore reach in a collapsed and virialized dark matter halo can be calculated by equating thermal energy per unit volume to half the potential energy per unit volume (Schneider, 2015). In this way we get (Schneider, 2015):

$$\frac{3}{2} n k_B T = \frac{3}{2}\frac{\rho k_B T}{\mu m_p} = \frac{v}{2}\rho\frac{GM}{r}, \tag{1.79}$$

where we expressed the number density of particles as $n = \frac{\rho}{\mu m_p}$ with μm_p being the mean mass per particle in the gas. Since $v \sim 1$ and by ignoring prefactors of order unity we get the virial temperature as (Schneider, 2015):

$$T_{vir} := \frac{\mu m_p}{2k_B} V_c^2 \approx 3.6 \times 10^5 K \left(\frac{V_c}{100\text{km/s}}\right)^2 \tag{1.80}$$

where we exploited the relation for the circular velocity $V_c^2 = \frac{GM}{r}$.

To radiate away thermal energy and cool down the gas, cooling mechanisms need to exist. There are several of them with the first one being Compton cooling where photons get scattered off from electrons. If the energy of the electrons is higher than the energy of the photons, i.e. $T_\gamma \ll T_e$, the photons are carrying away energy of the electrons in this way cooling the gas. However, the important mechanism for structure formation is radiative cooling. At high temperatures in ionized gas, i.e. above $T > 10^6$ K, energy is radiated away due to bremsstrahlung. At lower temperatures ($T \lesssim 10^{5.5}$ K), one has collisional ionization, recombination, and collisional excitation as cooling mechanisms (Mo et al., 2010). When the gas due to cooling sinks to the center of the dark matter halo, it can become self-gravitating and then collapse under its own gravity to form stars.

For star formation to happen the gas has to collapse so that it can get compressed and nuclear fusion starts. The condition to be fulfilled for a gas cloud to collapse is similar to the case in collisionless dynamics. Also for a gas cloud, one can define a Jeans mass which is given by (Mo et al., 2010):

$$M_J = \left(\frac{3}{4\pi\rho_{gas}}\right)^{1/2} \left(\frac{5 f_{gas} k_B T}{\mu m_p G}\right)^{3/2}, \tag{1.81}$$

with $f_{gas} \equiv \frac{M_{gas}}{M}$ the gas fraction. If $M_{gas} > M_J$ the system collapses.

The rate at which a galaxy is able to form stars is described by the star formation rate $\dot{\Sigma}_* = \frac{\dot{M}_*}{\mathrm{area}}$ which is the change in stellar mass per area in a certain time. An empirical law relating the star formation rate to the surface density of gas is the Kennitcutt-Schmidt law given by (Mo et al., 2010; Kennicutt, 1998):

$$\dot{\Sigma}_* = (2.5 \pm 0.7) \times 10^{-4} \left(\frac{\Sigma_{\mathrm{gas}}}{\mathrm{M}_{\odot}\mathrm{pc}^{-2}}\right)^{1.4 \pm 0.15} \mathrm{M}_{\odot}\mathrm{yr}^{-1}\mathrm{kpc}^{-2}. \tag{1.82}$$

The formation of stars in galaxies leads to two consequences. First, the stars act as a source of reionization for the intergalactic medium. This happens by photoionization which increases the temperature of the intergalactic medium. When simulating large-scale structure formation, one also has to take this behavior into account, since it increases the minimum halo mass necessary for star formation to happen. In simulations this is usually implemented with the so-called UV-background, which we will discuss in detail in Sec. 2.4.5.

Second, stars undergo an evolution and if their mass is high enough will explode in supernovae at the end of their lifetime. These explosions are reinjecting energy into the intergalactic gas and heating it up. Furthermore, during stellar evolution and supernova explosions heavier elements than lithium are created which are then deposited into the gas, influencing the cooling. Also, this behavior has to be accounted for during simulations and its implementations will be discussed in Sec. 2.4.5.

1.5.4 Transfer Functions

After seeing how individual density perturbations grow and then collapse to first form dark matter halos and then galaxies we are now interested in the question of how the initial density perturbations as a whole develop in a cosmological context. To be more precise, the question we are after is, how do the initial density perturbations created during inflation evolve during the different epochs of the expanding universe until after recombination? The answer to this question is especially important for numerical simulations of structure formation, since one cannot start a simulation straight after inflation ends, but rather at a redshift z after recombination and the creation of the CMB. Therefore, one has to know how the density fluctuations develop until the point where one can start the simulation. This evolution of the initial density fluctuations is described by the so-called *transfer function* (c.f. Hahn and Abel, 2011; Eisenstein and Hu, 1998, 1999; Peacock, 1997; Seljak and Zaldarriaga, 1996).

The most formal way to define a transfer function $T(k,t)$ is by (Mo et al., 2010):

$$\Phi(k,t) = K\beta(k)T(k,t_m)\frac{D(t)}{a(t)}\frac{a(t_m)}{D(t_m)}, \tag{1.83}$$

where $\Phi(k,t)$ are the amplitudes of the density perturbations, K is a normalization factor, $\beta(k)$ specifies the initial conditions, $T(k,t_m)$ is the transfer function, $D(t)$ is the linear growth factor after recombination and t_m is a time after recombination when the universe is already matter dominated but curvature and cosmological constant can still be neglected (Mo et al., 2010).

One can relate the density perturbations after recombination to the initial perturbations by (Mo et al., 2010):

$$\delta(k,t) = -\frac{k^2\Phi(k,t)}{4\pi G a^2\overline{\rho}} = -\frac{2}{3}\frac{K}{H_0^2\Omega_{m,0}}k^2\beta(k)T(k)D(t) \tag{1.84}$$

Therefore, one can write the power spectrum in density perturbations as (Mo et al., 2010):

$$P(k,t) = \left\langle|\delta(k,t)|^2\right\rangle = P_i(k)T^2(k)D^2(t) \tag{1.85}$$

where $P_i(k)$ is the initial power spectrum of density perturbations. In this way, the initial density perturbations after inflation are related to the density perturbations after recombination. The exact form of the transfer function can be calculated and is different for each cosmological model, e.g. depending on whether one has cold dark matter or warm dark matter. Calculating the exact transfer functions is a whole field of research in itself and we will not attempt to do it here.

1.5.5 The final state of large scale structure formation: The Cosmic Web

In the previous sections, we saw how from initial density perturbations created during inflation galaxies were able to form. In our description of structure formation until now we were only following the collapse of a single density perturbation, first in its dark matter content and then in its baryon content. However, if we look at the universe today we see not only a single galaxy but a myriad of galaxies assembled in groups, clusters, and lined up along filaments. This large-scale structure called the cosmic web forms from the collapse of the large-scale density field. In Fig. 1.4 we show the gas distribution in a high-resolution cosmological simulation and its collapse at four different redshifts. At $z = 10$ we can see that there is almost no structure yet and the gas is distributed almost uniformly, although overdensities and under densities in the gas distribution exist. At $z = 3$ the cosmic web with its nodes and filaments is already clearly visible, although the galaxies are still rather small. Also, in the regions that later become voids, there is still relatively much gas visible with many small filaments. However, at $z = 1$ and $z = 0$ the cosmic web is fully assembled and we can clearly see the web-like structure of galaxies, groups, and filaments. We will now describe in more detail the different components of this large-scale structure at $z = 0$ before describing in Sec. 1.6 the different processes that happen during its evolution.

Galaxy Clusters: Among the biggest structures we see today in the universe are galaxy clusters. For a formal definition of a galaxy cluster, we can use the criterion used by Abell in 1958 (Abell, 1958; Schneider, 2015). He defined a galaxy cluster as an overdensity of galaxies within a circular area using three criteria. First, there need to be at least 50 galaxies in the overdensity, i.e. $N \geq 50$. Second, these ≥ 50 galaxies need to be in a

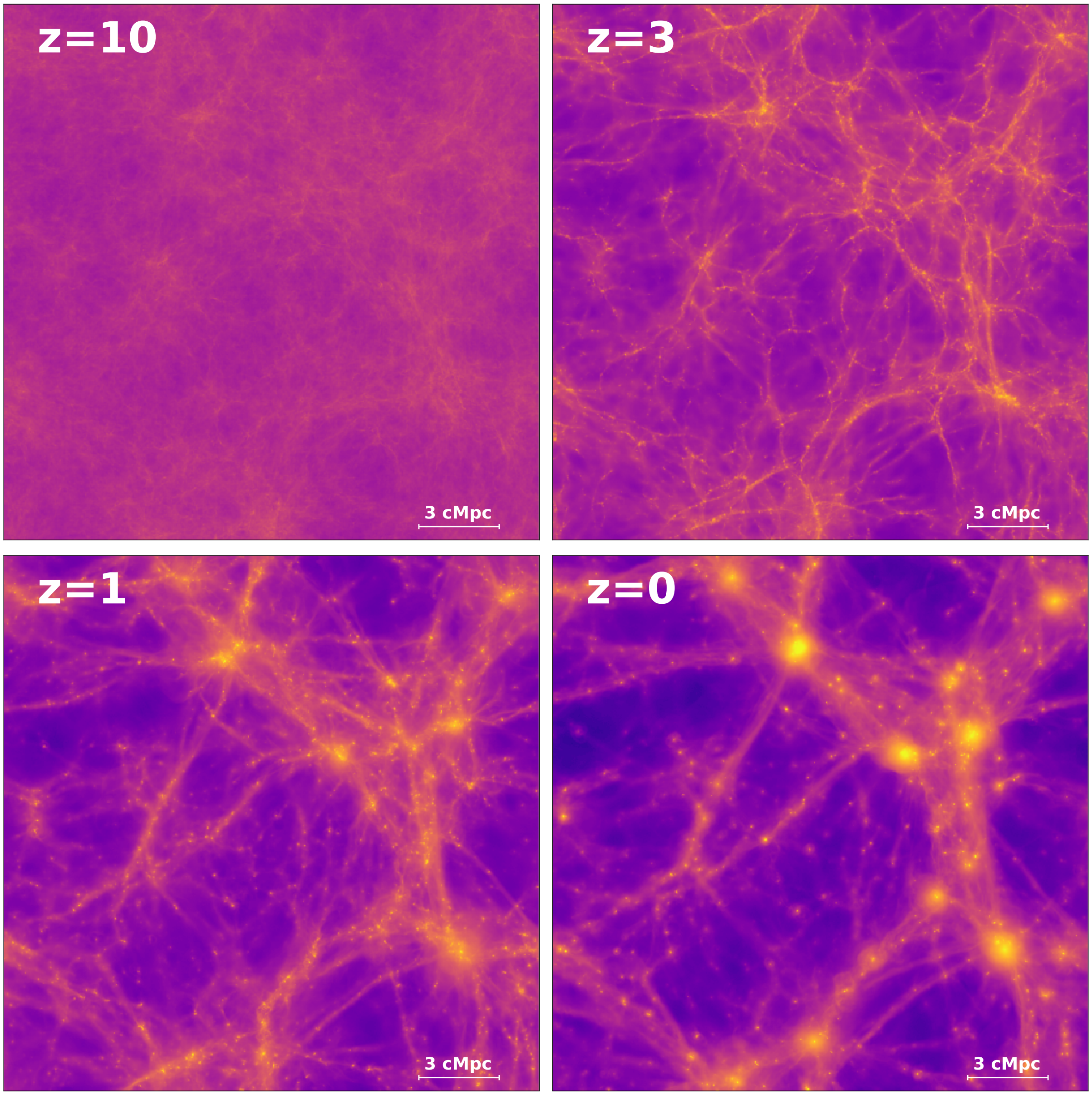

Figure 1.4: Gas distribution in a high-resolution cosmological simulation at four different redshifts. The simulation is the one we used for this thesis and is explained in detail in Sec. 2.4. In the top left panel, we show the gas distribution at $z = 10$ in the full simulation box. The cosmic web did not yet form, but instead one can see overdensities and under densities in the gas distribution. In the top right panel at $z = 3$, we can see already the filaments of the cosmic web and some galaxies as bright dots. In the two lower panels at $z = 1$ and $z = 0$ the cosmic web is fully assembled and galaxies can be found in groups and in isolation along filaments.

magnitude interval $m_3 < m < m_3 + 2$ with m_3 being the apparent magnitude of the third brightest galaxy in the cluster. Third, the circular area of the galaxy overdensity has an angular radius $\theta_A = \frac{1'.7}{z}$ with z being the redshift. This amounts to a radius of $R_A \approx 1.5h^{-1}$ Mpc in physical units. The masses of galaxy clusters are usually of the order $M \geq 3 \times 10^{14}$ $\mathrm{M}_\odot$ (Schneider, 2015; Mo et al., 2010).

Galaxy Groups: From the definition of clusters, we are now also able to define galaxy groups. In a very general way galaxy groups are overdensities of galaxies that do not fulfill the selection criteria of being a galaxy cluster. As for clusters, the definition of a group is in a way arbitrary, but usually, a group consists of at least three galaxies. Furthermore, its enhancement of the number density is of the order of 20 (Mo et al., 2010). The masses of galaxy groups are in the range $10^{12.5} - 10^{14}$ $\mathrm{M}_\odot$.

Isolated galaxies: Isolated galaxies, also called field galaxies, are galaxies that are not members of a galaxy group or galaxy cluster, i.e. they are in isolation in the field. Field galaxies are mostly undisturbed during their formation history and therefore the ideal testing bed for galaxy evolution. However, as we will show in Ch. 3 there exists a small subsample of galaxies that are isolated at $z = 0$, but that underwent environmental interactions in the past. We will show how environmental interactions can influence the final gas mass and halo mass of these galaxies.

Dwarf Galaxies: Dwarf galaxies are not a distinct part of the cosmic web, since they can be found both in isolation and in groups and clusters. Rather they are distinct class of galaxies that in a very handwaivy definition are just low mass galaxies. A more formal definition of dwarf galaxies classifies them according to their stellar mass with dwarf galaxies being all galaxies with $M_* \lesssim 10^9$ $\mathrm{M}_\odot$. One can further subdivide them into bright dwarfs, classic dwarfs and ultra-faint dwarfs. Bright dwarfs have stellar masses $M_* \approx 10^{7-9}$ $\mathrm{M}_\odot$, classic dwarfs $M_* \approx 10^{5-7}$ $\mathrm{M}_\odot$, and ultra-faint dwarfs $M_* \approx 10^{2-5}$ $\mathrm{M}_\odot$ (Bullock and Boylan-Kolchin, 2017). While for bright dwarfs the ratio of stellar mass to halo mass $M_*/M_{vir} \approx 10^{-3}$, this ratio becomes $\approx 10^{-4}$ for classic dwarfs and $\approx 10^{-5}$ for ultra-faint dwarfs (Bullock and Boylan-Kolchin, 2017). Therefore, the lower the mass of a dwarf galaxy, the more it is dominated by dark matter. Dwarf galaxies will be the subjects of study in Ch. 3.

Cosmic Web Filaments: Cosmic web filaments are the filamentary structures that connect galaxy groups, galaxy clusters, and isolated galaxies, as can be seen in Fig. 1.4. A more mathematical definition would be that filaments are "*[...] ascending 2-manifolds with their extremities plugged on to the maxima (peaks of the density field)*" (Kraljic et al., 2018, p. 551). This definition is adopted when using tools like `DisPerSE` (Sousbie, 2011; Sousbie et al., 2011) to extract the geometry of the cosmic web. However, as we will explain in more detail in Ch. 3 we will adopt a more qualitative approach instead of this formal mathematical one and define cosmic web filaments only as the gas that connects different galaxies and is outside their virial radii.

1.6 Environmental Interactions

As we have seen in Sec. 1.5.5 the large-scale structure of the universe is created by the collapse of the initial density field. Since most galaxies do not evolve in isolation, the galaxies that are formed, experience a variety of environmental interactions. The most important ones are mergers, which are a keystone of the hierarchical model of structure formation. However, there are also environmental interactions that do not necessarily lead to the merging of galaxies. We will present two of them, ram pressure stripping and tidal stripping here since we will encounter them later on in Chs. 3 and 5.

Mergers: In the hierarchical model of structure formation, the large-scale structure we see today is built from smaller structures. We have seen how dark matter halos and galaxies form from initial density perturbations. These collapsed dark matter halos and galaxies then grow in two ways. The first one is by continuous accretion of dark matter and gas. The second one is merging with other already collapsed larger structures, like other galaxies. If two galaxies merge to build a bigger galaxy, one can classify them into either minor or major mergers, depending on the mass ratio $q \equiv \frac{M_1}{M_2}$ of the two merging galaxies. If the masses of the two merging galaxies are similar with $q \lesssim 4$ one speaks of a major merger. On the other side, if the masses are different with $q \gtrsim 4$, it is classified as a minor merger (Schneider, 2015; Mo et al., 2010).

Ram Pressure stripping: During the build-up of the large-scale structure, when galaxies fall into groups, clusters, or in case of minor mergers into other bigger galaxies, they experience *ram pressure* (Gunn and Gott, 1972). Ram pressure is a hydrodynamical drag force that acts on gas clouds that are going through ambient gas. The ram pressure acting on a galaxy going through a cloud of gas is defined as (Mo et al., 2010):

$$P_{ram} = \rho_{amb} V_{rel}^2, \tag{1.86}$$

where ρ_{amb} is the density of the ambient gas it is going through, e.g. the intercluster medium, intergroup medium, the gaseous halo of another galaxy, or even a cosmic web filament, while V_{rel} is the relative velocity between the galaxy and the gas cloud it is plowing through. The restoring force is given by the gravitational potential of the galaxy going through the gas cloud and can be written as:

$$P_{gal} \propto \rho_{gal} V_c^2, \tag{1.87}$$

where ρ_{gal} is the gas density of the galaxy and $V_c^2 = \frac{GM}{r}$ its circular velocity. If the ram pressure is much higher than the restoring force, i.e.

$$P_{gal} \ll P_{ram}, \quad \text{or} \quad \frac{\rho_{gal} V_c^2}{\rho_{amb} V_{rel}^2} = \frac{P_{gal}}{P_{ram}} \ll 1 \tag{1.88}$$

then the gas gets stripped from the galaxy by ram pressure. Ram pressure stripping has been observed in clusters and groups (Boselli et al., 2023, 2016, 2022; Rasmussen et al., 2006) and theoretical studies suggest that it can also happen in cosmic web filaments (Benítez-Llambay et al., 2013).

Tidal interactions: A second class of interactions that can remove mass from a galaxy are tidal interactions. Opposite to ram pressure stripping that only acts on the gas, tidal stripping can also affect the dark matter and stellar content of a galaxy. Mass removal by tidal forces happens if the tidal acceleration $\frac{2GMr}{R^3}$ of the host exceeds the restoring force $\frac{Gm}{r^2}$ of the system that is stripped. Here M is the mass of the host, R is the distance from the host to the system that is stripped, r is the radius of the system that is stripped, and m is its mass. However, not all the mass is removed, but only the mass that is outside the tidal radius r_t that for a circular motion of a satellite around its host is given by (Mo et al., 2010):

$$r_t = \left[\frac{m/M}{(3 + m/M)}\right]^{1/3} R. \tag{1.89}$$

In the real universe, satellites are rarely on circular orbits, but galaxies that fall into a host are usually on eccentric orbits. In this case eq. (1.89) gets modified and one gets as a crude approximation (Mo et al., 2010):

$$r_t = \left[\frac{m(r_t)/M(R_0)}{2 + \frac{\Omega^2 R_0^3}{GM(R_0)} - \frac{\mathrm{d}\ \ln M}{\mathrm{d}\ \ln R}|_{R_0}}\right]^{1/3} R_0 \tag{1.90}$$

where R_0 is the pericentric distance and Ω the angular speed. However, in this thesis, we will not attempt to calculate the tidal forces acting on different systems but rather observe and describe its results during the evolution of dwarf field galaxies in Ch. 3 .

1.7 Research Question

We have seen until now how large-scale structure in the universe forms by the collapse of dark matter haloes and the subsequent collapse of gas that leads to star formation within these haloes. The galaxies that form in this way over time are assembling into the cosmic web we observe today. During this process of the formation of the cosmic web, galaxies can undergo interactions with their environment. Two environmental mechanisms, ram pressure stripping, and tidal stripping, do not necessarily destroy a galaxy but can leave it intact only changing its properties. Furthermore, these interactions also alter the properties of the host that are responsible for the stripping by adding material to the host and to the larger-scale structure where the stripping happens. The general question that therefore arises is how the environment and interactions with it influence galaxies and the large-scale structure they are embedded in.

This question can be further split into two parts. First, how do environmental interactions, like ram pressure stripping and tidal stripping influence the evolution and final properties of galaxies? We are especially interested in how the low mass end of the galaxy population is affected and will therefore focus on dwarf galaxies. Furthermore, since ram pressure stripping is more effective in low-mass galaxies, we want to investigate the role of cosmic web filaments in the gas stripping of dwarf galaxies. We will explore these questions in Ch. 3 where we investigate the influence of ram pressure stripping and tidal stripping on the gas content of simulated field dwarf galaxies. In Ch. 4 we then turn to the question, whether environmental interactions can produce dark matter deficient galaxies.

Second, we want to understand how environmental interactions change the large-scale environment in which a galaxy is embedded. The material that is removed from galaxies by ram pressure stripping has to be deposited somewhere. One of the sinks is the circumgalactic medium that links the interstellar medium to the cosmic web filaments. Therefore, environmental processes should also manifest themselves in changes to the circumgalactic medium. Since there is mounting evidence from observations that the large-scale structure a galaxy is embedded in has an influence on its CGM, we want to know in Ch. 5, whether these environmental interactions can change the composition of the circumgalactic medium in which a galaxy is stripped and whether the large-scale structure a galaxy is embedded in has any influence on its circumgalactic medium. The second part of the thesis therefore is the first attempt to systematically model the influence of environmental processes on the CGM. We are investigating all these questions using a high-resolution cosmological simulation, which we will explain next.

Chapter 2

Cosmological Simulations

As we have seen in Sec. 1.5 the formation of large-scale structure in the universe is a non-linear process impossible to follow analytically apart from a few very idealized examples. Therefore, we need numerical methods to investigate the formation of large-scale structure in the non-linear regime (Schneider, 2015). Several different types of simulations have been developed to investigate the formation of dark matter halos and galaxies. First, there are so-called dark matter-only simulations (Angulo and Hahn, 2022; Somerville and Davé, 2015). These simulations do not model baryonic physics with gas dynamics and star formation, but only the formation of dark matter halos and how they assemble in the large-scale structure of the universe. Examples of these simulations are the `millenium simulation` (Lemson and Virgo Consortium, 2006) or `PKDGRAV3` (Potter et al., 2017) which is used as a reference simulation for *Euclid*. Both of these simulations assume dark matter to be cold, but there exist also dark matter-only simulations for warm dark matter (Bose et al., 2017) and for the more exotic fuzzy dark matter (May and Springel, 2023).

The second class of simulations widely used today are semi-analytic models. In a semi-analytic model, one takes the output of a dark matter-only simulation and then puts an analytic model of galaxy formation on top to decide which dark matter halo is populated by which kind of galaxy. In these models, one makes assumptions about the accretion of gas on the halo, the cooling of gas and its transformation into stars as well as feedback processes from supernovae and black holes (Somerville and Davé, 2015). Semi-analytic models today are for example used to estimate the stochastic gravitational wave background from massive black hole binaries (Izquierdo-Villalba et al., 2022) or the properties of the hosts of massive black holes (Izquierdo-Villalba et al., 2023) and for a plethora of galaxy evolution studies (e.g. De Lucia et al., 2017, 2019, 2024; Gonzalez-Perez et al., 2014; Koutsouridou and Cattaneo, 2022).

Finally, there are also fully hydrodynamical simulations, which not only follow the collapse and formation of dark matter halos but also include baryons and baryonic physics. In contrast to semi-analytic models, fully hydrodynamical simulations are explicitly solving the equations (1.76) to (1.78) for the gas component. Furthermore, they have prescriptions for the heating and cooling of gas and when stars form out of cool gas clouds. Finally, they usually also include feedback from supernovae and supermassive black holes (Somerville and Davé, 2015).

One can further divide simulations based on the way they are solving the equations for gravity and gas dynamics. For the gravity part, one can either solve the differential form of the Poisson equation, $\nabla^2\Phi(\mathbf{r}) = 4\pi G\rho(\mathbf{r})$, leading to mesh-based methods (Vogelsberger et al., 2020). Or one tries to solve the integral form of the Poisson equation given by

$$\Phi(\mathbf{r}) = -G\int \mathrm{d}\mathbf{r}'\frac{\rho(\mathbf{r}\prime)}{|\mathbf{r}-\mathbf{r}'|}. \tag{2.1}$$

The most straightforward way to solve the integral form is to replace the integral by a direct sum leading to a particle-particle scheme which is of order $\mathcal{O}(N^2)$ with N being the number of particles. Adapting a so-called tree approach can reduce the computational cost to $\mathcal{O}(N\log N)$ (Vogelsberger et al., 2020).

Similarly, also for the gas dynamics there exist two main ways to solve the equations. First, by Eulerian methods which divide the volume into cells and calculate the flux between the cells. And second, by Lagrangian methods that follow individual fluid particles. An example of such a Lagrangian method is called *smoothed particle hydrodynamics*, where one calculates a weighted sum over neighboring particles (Somerville and Davé, 2015; Vogelsberger et al., 2020). The simulation we are using adopts a tree approach for the gravitational force and smoothed particle hydrodynamics for the gas. We will now explain the simulation and all the numerical techniques used in more detail.

2.1 Gravity with N-body simulations

Due to its long-range nature, the main force in large-scale structure formation is gravity which affects all matter components of the universe equally. If the patch of the universe one is simulating is small enough, one can neglect the effects of General Relativity and instead approximate gravity by the Newtonian version, while accounting for the expansion of the universe using the Friedmann equations (Somerville and Davé, 2015). For collisionless systems, the equations one needs to solve are the collisionless Boltzmann equation given in eq.(1.73) together with the Poisson equation given by eq. (1.48). However, when calculating the gravitational force numerically a more practical approach is to sample the phase space with particles and calculate directly the force exerted on each particle by all other particles in the system. The most direct way to do that is by (Mo et al., 2010)

$$\mathbf{F}_i = -\sum_{j\neq i} Gm\frac{\mathbf{r}_i-\mathbf{r}_j}{|\mathbf{r}_i-\mathbf{r}_j|^3}, \tag{2.2}$$

to then move them forward in time according to the force acting on them. However, such a direct force calculation for a system of N particles is of order $\mathcal{O}(N^2)$ and therefore not feasible.

Several methods exist to speed up the force calculation for the gravity part. One of them is the so-called *Tree algorithm*. The basic idea of the tree algorithm is that when calculating the gravitational force exerted on particle n_i, particles that are far away from particle n_i are grouped together and one only calculates the gravitational force between n_i and the center of mass of each of these groups, while for particles that are close to n_i one does the direct calculation as in eq. (2.2).

A standard implementation of the tree algorithm was developed by Barnes and Hut (1986). They divided the whole simulation volume into cells. Whenever a cell contains more than one particle it is subdivided into 8 smaller cells, so that at the end each cell only contains one particle. This construction leads to a tree structure of cells. For each particle, a distance criterion decides whether one goes all the way down the branch to the single particle for the force calculation or whether one stops higher up in the branch and calculates the force only approximately by using the center of mass of all the particles in the parent cell. With this implementation, the force calculation for gravity scales as $N\log(N)$ instead of N^2 (Barnes and Hut, 1986).

Another approach to speed up the calculation for the gravity part is the so-called *Particle-Mesh (PM) algorithm.* In this approach the simulation volume is first divided into mesh cells to then assign a mass to each of the grid points depending on the mass distribution of the simulation. Next, one solves the Poisson equation in Fourier space to get the gravitational force at each of the grid points. The gravitational force for the single particles is then obtained by interpolating the gravitational force from closeby grid points to the position of the particles. This method scales with the number N of the particles in the simulation (Mo et al., 2010). What is implemented in the simulation used in this thesis is a combination of the two methods called *TreePM* (Springel, 2005).

The tree and particle mesh methods allow us to simplify and speed up the force calculation when dealing with gravity in the long range. However, there is an effect one has to account for when calculating the motion of particles due to gravity in short-range interactions. Since due to eq. (2.2) the gravitational force diverges if two particles are very close to each other which can lead to unrealistic scattering events (Mo et al., 2010), one implements a so-called *softening length* for example by (Mo et al., 2010):

$$F = G\frac{m^2}{r^2} \quad \rightarrow \quad F = G\frac{m^2}{r^2+\epsilon^2} \tag{2.3}$$

where ϵ is the softening length. This makes the force always finite, but also restricts the scales that can be resolved. In general, the smallest scales that can be resolved in a particle simulation are given by two factors. First, the particle masses define the mass scales that can be resolved, and second, the softening length which tells you about the spatial scales which can be resolved.

After knowing how to calculate the force that is acting on each particle we can move the particles forward in time. We need to update both, their positions and their velocities, which requires numerical integration. The method of choice for gravitational n-body simulations is the so-called *leapfrog scheme* due to the long-term stability of the solutions (Springel, 2005). In the standard leapfrog scheme we first need to define the positions $\mathbf{r}_i$ at a time step $t_{n+1/2}$ (Mo et al., 2010):

$$\mathbf{r}_i'(t_{n+1/2}) = \mathbf{r}_i(t_n) + \mathbf{u}_i(t_n)\Delta t_n/2. \tag{2.4}$$

Using $\mathbf{r}'_i(t_{n+1/2})$ to calculate the force $\mathbf{F}_i(t_{n+1/2})$ at the halved time step $t_{n+1/2}$ we can then update the positions, velocities and time step as (Mo et al., 2010):

$$\mathbf{u}_i(t_{n+1}) = \mathbf{u}_i(t_n) + \mathbf{F}_i(t_{n+1/2})\Delta t_n, \tag{2.5}$$

$$\mathbf{r}_i(t_{n+1}) = \mathbf{r}_i(t_n) + \frac{\Delta t_n}{2}[\mathbf{u}_i(t_n) + \mathbf{u}_i(t_{n+1})], \tag{2.6}$$

$$t_{n+1} = t_n + \Delta t_n. \tag{2.7}$$

This standard leapfrog scheme requires that all particles are moved with the same time step. However, evolving all particles with the same time step wastes resources since particles in low-density regions do not need as small time steps as high-density regions (Springel, 2005). Therefore, the leapfrog integration used in the simulation is written in terms of kick and drift operators in a way that allows for variable time steps (Springel, 2005).

There are two components in cosmological simulations that only interact due to gravity and therefore are collisionless. These are dark matter particles and star particles. If our simulation would only contain these two types of particles the physics and numerics presented until here would be sufficient to run the simulation. However, our simulation is a fully hydrodynamical simulation also containing gas particles. Since gas does not only interact due to gravity but additionally also experiences hydrodynamical interactions these interactions also need to be implemented in the simulation. We will therefore now discuss the numerical implementation of the hydrodynamical equations.

2.2 Hydrodynamics in Lagrangian Formulation

When implementing hydrodynamics into a cosmological simulation one uses either the Eulerian formulation or the Lagrangian formulation depending on the numerical method one uses to solve the equations. Since the simulation we are using is based on smoothed-particle hydrodynamics where one is following single fluid elements, one needs to write the equations in the Lagrangian formulation. We already encountered these equations for hydrodynamics in Sec. 1.5.3 when discussing the collapse of baryons in dark matter halos. There we gave them in terms of physical coordinates, that is the locations in space are fixed and the fluid flows through them. However, our simulation discretizes the equations for gas dynamics in terms of particles. Therefore, we need to rewrite the equations for fluid dynamics in a frame where the coordinates are moving with the particles themselves. This is the Lagrangian formulation of hydrodynamics given by the following equations (Mo et al., 2010):

$$\frac{\mathrm{d}\rho}{\mathrm{d}t} + \rho\nabla\cdot\mathbf{u} = 0, \tag{2.8}$$

$$\frac{\mathrm{d}\mathbf{u}}{\mathrm{d}t} = -\frac{\nabla P}{\rho} - \nabla\phi, \tag{2.9}$$

$$\frac{\mathrm{d}\epsilon}{\mathrm{d}t} = -\frac{P}{\rho}\nabla\cdot\mathbf{u} - \frac{\mathcal{C}-\mathcal{H}}{\rho}. \tag{2.10}$$

Here ρ is again the density, P the pressure, $\mathcal{C}$ and $\mathcal{H}$ are the heating and cooling rate per unit volume and $\mathbf{u}$ is the velocity, while $\frac{\mathrm{d}}{\mathrm{d}t} \equiv \frac{\partial}{\partial t} + \mathbf{u}\nabla$ is the Lagrangian derivative (Vogelsberger et al., 2020). To close the set of equations one needs the Poisson equation given in eq. (2.1) and an equation of state which is given by (Mo et al., 2010):

$$P = (\gamma - 1)\rho\epsilon \tag{2.11}$$

where γ is the adiabatic index. This set of equations has to be solved numerically. We will now continue to explain how this is done using smoothed-particle hydrodynamics.

2.3 SPH - Smoothed Particle Hydrodynamics

Smoothed-Particles Hydrodynamics (SPH) was originally invented to deal with problems in stellar physics (Lucy, 1977; Gingold and Monaghan, 1977). The main idea is to discretize the equations one wants to solve using particles that carry the information about mass, density, velocity, entropy, and other physical quantities. To compute the change of these quantities one is summing over neighboring particles and weighting the sum with a *smoothing kernel*.

In a more formal definition of SPH one starts from the integral representation of a function which is given by (Liu and Liu, 2003):

$$f(x) = \int_\Omega f(x')\delta(x - x')dx', \tag{2.12}$$

where Ω is the volume containing x. This gives an exact representation of the function $f(x)$. However, one can replace the delta function $\delta(x - x')$ by a smoothing kernel $W(x - x', h)$ to give an approximation $\langle f(x)\rangle$ to the function $f(x)$ (Liu and Liu, 2003):

$$\langle f(x)\rangle = \int_\Omega f(x')W(x - x', h)dx'. \tag{2.13}$$

Here h is the smoothing length that tells us about the radius of the volume that is used for the approximation which is also called the support domain. Outside the support domain the smoothing kernel $W(x, h) = 0$. The integral representation of a derivative of a function is given by (Liu and Liu, 2003):

$$\langle \nabla f(x)\rangle = -\int_\Omega f(x') \cdot \nabla W(x - x', h)dx'. \tag{2.14}$$

Therefore, in the integral representation, the derivative of a function is given by the values of the function times the derivative of the smoothing kernel (Liu and Liu, 2003).

The next step in arriving at the SPH formulation is to replace the integral with a summation over the particles that carry the information about mass, density, velocity, and entropy. For each particle, the infinitesimal volume dx' is replaced by the volume ΔV_j

where the subscript j denotes the particle for which the calculation is done. In that case the mass m_j is given by (Liu and Liu, 2003):

$$m_j = \Delta V_j \rho_j \tag{2.15}$$

where ρ_j is the density of the particle. With that, we can rewrite eqs. (2.13) and (2.14) as (Liu and Liu, 2003):

$$\langle f(x) \rangle = \sum_{j=1}^{N} \frac{m_j}{\rho_j} f(x_j) W(x - x_j, h) \tag{2.16}$$

$$\langle \nabla f(x) \rangle = -\sum_{j=1}^{N} \frac{m_j}{\rho_j} f(x_j) \cdot \nabla W(x - x_j, h) \tag{2.17}$$

Finally, it follows that the density ρ_j in the SPH approximation is given by (Liu and Liu, 2003):

$$\rho_j = \sum_{j=1}^{N} m_j W(x - x_j, h). \tag{2.18}$$

In all these equations $j = 1$ ... N are the particles within the support domain.

With these approximations, we can now write the set of equations (2.8) to (2.10) as (Mo et al., 2010):

$$\frac{\mathrm{d}\rho_i}{\mathrm{d}t} = \sum_{j=1}^{N} m_j (\mathbf{u}_i - \mathbf{u}_j) \nabla_i W(\mathbf{r}_i - \mathbf{r}_j, h), \tag{2.19}$$

$$\frac{\mathrm{d}\mathbf{u}_i}{\mathrm{d}t} = -\sum_{j=1}^{N} m_j \left(\frac{P_i}{\rho_i^2} + \frac{P_j}{\rho_j^2} \right) \nabla_i W(\mathbf{r}_i - \mathbf{r}_j, h) - \nabla \phi, \tag{2.20}$$

$$\frac{\mathrm{d}\epsilon_i}{\mathrm{d}t} = \frac{1}{2} \sum_{j=1}^{N} m_j \left(\frac{P_i}{\rho_i^2} + \frac{P_j}{\rho_j^2} \right) (\mathbf{u}_i - \mathbf{u}_j) \cdot \nabla_i W(\mathbf{r}_i - \mathbf{r}_j, h) - \frac{\mathcal{C} - \mathcal{H}}{\rho}. \tag{2.21}$$

This is the most straightforward implementation of hydrodynamics given by eqs. (2.8) to (2.10) in the SPH formalism. However, current cosmological SPH codes usually use a different formulation of the three hydrodynamic equations presented here. First, they need to add an artificial viscosity term in order to capture shocks (Somerville and Davé, 2015). Second, they might replace the energy equation (2.21) with an entropy equation to mitigate the overcooling problem and avoid unphysical solutions if feedback is implemented by depositing all the energy into one particle (Springel and Hernquist, 2002). We will discuss the exact SPH implementation of hydrodynamics for the simulation used in this thesis in the following section.

2.4 A high-resolution cosmological simulation

We used a high-resolution cosmological hydrodynamical simulation to investigate the influence of the environment on the evolution and final properties of galaxies as well as the circumgalactic medium. As we will discuss in Sec. 3.1, the resolution of this simulation presented in Sec. 2.4.3 allows for the first time the study of dwarf galaxies in a cosmological context. We present the results of this research in Chs. 3, 4, and 5. The simulation used for this thesis is the one that was originally presented in Benitez-Llambay and Frenk (2020). We now want to present this simulation in more detail.

The simulation was run using `gadget3` which is a modified version of `gadget2` (Springel, 2005). While the gravity part was run with the original `gadget2` tools, the modifications concern the SPH part, the time stepping, and the subgrid physics which was replaced by the `EAGLE` model of galaxy formation (Schaye et al., 2015). We discuss the gravity part in Sec. 2.4.1, while the entropy formulation of SPH used in the simulation is discussed in Sec. 2.4.2. The `EAGLE` model of galaxy formation is presented in Sec. 2.4.5. The initial conditions for the simulation were created using `MUSIC` (Hahn and Abel, 2011) which we discuss in detail in Sec. 2.4.4. At redshift $z = 11.5$ a UV-background based on (Haardt and Madau, 2001) is switched on. We will discuss the implementation of this UV-backround in Sec. 2.4.5. Bound structures such as dark matter halos and subhalos have been identified using `HBT+` (Han et al., 2018), which also allows the tracking of galaxies through time to construct mass accretion histories. This will be discussed in detail in Sec. 2.5. The whole simulation employs the cosmological parameters from the 2013 results of the `Planck` collaboration (Planck Collaboration et al., 2014) which we already presented in Sec. 1.4. Finally, for visualizations and the measurement of column densities, we used the `py-SPHviewer` tool (Benitez-Llambay, 2015) which we briefly present in Sec. 2.7.

2.4.1 Gravitational interactions and the TreePM algorithm

When sampling the phase space of gravitational interactions in an expanding universe with particles their dynamics are described by the following Hamiltonian (Springel, 2005):

$$H = \sum_i \frac{\mathbf{p}_i^2}{2m_i a(t)^2} + \frac{1}{2}\sum_{ij} \frac{m_i m_j \varphi(\mathbf{x}_i - \mathbf{x}_j)}{a(t)} \tag{2.22}$$

with $\mathbf{x}_i$ being the comoving coordinates, $\mathbf{p}_i = a(t) m_i \dot{\mathbf{x}}_i$ the canonical momenta and $\varphi(\mathbf{x})$ is the interaction potential. The scale factor $a(t)$ accounts for the expansion of the universe and therefore introduces a time dependence in the Hamiltonian (Springel, 2005). In the case of periodic boundary conditions of a cubic box of size, L^3 the equation with the mean density subtracted (Springel, 2005):

$$\nabla^2 \varphi(\mathbf{x}) = 4\pi G \left[-\frac{1}{L^3} + \sum_n \tilde{\delta}(\mathbf{x} - \mathbf{n}L) \right], \tag{2.23}$$

where $\tilde{\delta}(\mathbf{x})$ is the single particle density distribution function, is solved by the interaction potential $\varphi(\mathbf{x})$. If one has a system where the mean density is subtracted, i.e. a system with the Poisson equation as $\nabla^2\phi(\mathbf{x}) = 4\pi[\rho(\mathbf{x}) - \overline{\rho}]$, the potential that solves that system is the peculiar potential. Since $\varphi(\mathbf{x})$ is the solution to a Poisson equation with the mean density subtracted, we can use it to define the peculiar potential $\phi(\mathbf{x})$ as (Springel, 2005):

$$\phi(\mathbf{x}) = \sum_i m_i \varphi(\mathbf{x} - \mathbf{x}_i) \tag{2.24}$$

Finally, $\tilde{\delta}(\mathbf{x})$ is set to be $\tilde{\delta}(\mathbf{x}) = W(|\mathbf{x}|, 2.8\epsilon)$ with $W(r)$ being (Springel, 2005):

$$W(r,h) = \frac{8}{\pi h^3} \begin{cases} 1 - 6\left(\frac{r}{h}\right)^2 + 6\left(\frac{r}{h}\right)^3, & 0 \le \frac{r}{h} \le \frac{1}{2}, \\ 2\left(1 - \frac{r}{h}\right)^3, & \frac{1}{2} < \frac{r}{h} \le 1, \\ 0 & \frac{r}{h} > 1. \end{cases} \tag{2.25}$$

With these equations, the movement of particles in an expanding universe can be calculated. However, note that the second part in the Hamiltonian in eq. (2.22) which is the contribution due to gravitational attraction, still contains a double sum, and therefore the computational effort is of oder $\mathcal{O}(N^2)$. Therefore, `gadget2` includes a simple tree algorithm and a more sophisticated *TreePM* algorithm to speed up the gravitational force calculations.

Tree algorithm in `gadget2`: Since we already described the basic idea of the tree code algorithm in Sec. 2.1, we will now only specify the way the algorithm is implemented in `gadget2`. In the same way, as in the original formulation by Barnes and Hut (1986) the subdivision of space in `gadget2` is done in terms of an oct-tree, i.e. each cell of side length L is split into eight smaller cells of side length $\frac{L}{2}$ if there is more than one particle in a cell. While in tree code algorithms it is possible to go to higher multipole moments in the force calculation, in `gadget2` only the monopole moments are used, which means that for each node they only use the mass and the center-of-mass coordinate vector (Springel, 2005). One of the advantages of only using the monopole moment is that the tree can be dynamically updated when different time steps of particles are required. Finally, whether a node is used or opened depends on an opening criterion. If M is the mass of the node, l its side length, and r the distance of the node to the particle under consideration, then the node is used if (Springel, 2005):

$$\frac{GM}{r^2}\left(\frac{l}{r}\right)^2 \leqslant \alpha|\mathbf{a}|, \tag{2.26}$$

where α is some tolerance parameter and $|\mathbf{a}|$ the total acceleration obtained in the last time step (Springel, 2005). Otherwise, the node is opened and each subnode is probed with the same criterion.

The TreePM algorithm: In the *TreePM* method the tree algorithm as described above is used to calculate the gravitational force on the short range. However, for the long-range gravitational force, a particle-mesh method is used. First, the peculiar potential given in eq. (2.24) is split into a long-range and a short-range part by (Springel, 2005):

$$\phi_{\mathbf{k}} = \phi_{\mathbf{k}}^{\text{long}} + \phi_{\mathbf{k}}^{\text{short}}. \tag{2.27}$$

The long-range part is then given by (Springel, 2005):

$$\phi_{\mathbf{k}}^{\text{long}} = \phi_{\mathbf{k}} \exp\left(-\mathbf{k}^2 r_s^2\right), \tag{2.28}$$

where r_s is the distance where the force split happens. Mesh-based Fourier methods are then used to calculate the long-range part (Springel, 2005). The short-range part of the potential in eq. (2.24) is given by (Springel, 2005):

$$\phi_{\mathbf{k}}^{\text{short}} = -G \sum_i \frac{m_i}{r_i} \text{erfc}\left(\frac{r_i}{2r_s}\right), \tag{2.29}$$

where $r_i = \min(|\mathbf{x} - \mathbf{r}_i - \mathbf{n}L|)$. Since for distances above r_s in eq. (2.29) the contribution to the force is suppressed, the short-range part is calculated using the tree method discussed above (Springel, 2005).

2.4.2 Entropy formulation of SPH

In Sec. 2.3 we described the most straightforward way to implement SPH numerically by using the density, velocity, and energy of the particles as the equations that are discretized and solved numerically. However, this implementation has a number of problems, like the inability to capture shocks and processes of fluid mixing (Hopkins, 2013). Therefore, modern cosmological simulations usually employ different versions of SPH. For example, in the simulation used for this thesis the formulation of SPH is based on the pressure-entropy formulation of (Hopkins, 2013). It has been briefly described in (Schaye et al., 2015) and (Schaller et al., 2015), but the paper aimed at a full description (Dalla Vecchia et al., in preparation) has not been published. Here we will just give the most important equations of this version of the pressure-entropy formulation as outlined in (Schaye et al., 2015; Schaller et al., 2015).

First, the equation of motion is written as (Schaye et al., 2015; Schaller et al., 2015):

$$\frac{\mathrm{d}\mathbf{v}_i}{\mathrm{d}t} = -\sum_{j=1}^{N} m_j \left[\frac{A_j^{1/\gamma}}{A_i^{1/\gamma}} \frac{\bar{P}_i}{\bar{\rho}_i^2} f_{ij} \nabla_i W_{ij}(h_i) + \frac{A_i^{1/\gamma}}{A_j^{1/\gamma}} \frac{\bar{P}_j}{\bar{\rho}_j^2} f_{ji} \nabla_i W_{ij}(h_j) \right], \tag{2.30}$$

where f_{ij} is given by (Schaye et al., 2015; Schaller et al., 2015):

$$f_{ij} = 1 - \frac{1}{A_j^{1/\gamma}} \left(\frac{h_i}{n_D \rho_i} \frac{\partial \bar{P}_i^{1/\gamma}}{\partial h_i} \right) \left[1 + \frac{h_i}{n_D \rho_i} \frac{\partial \rho_i}{\partial h_i} \right]^{-1}, \tag{2.31}$$

where n_D are the spatial dimensions and h_i the smoothing length. The quantities $\bar{\rho}_i$ and $\bar{P}_i$ are the weighted density and weighted pressure. The weighted density is given by (Schaller et al., 2015):

$$\bar{\rho}_i = \frac{1}{A_i^{1/\gamma}} \sum_j m_j A_j^{1/\gamma} W\left(|\mathbf{x}_i - \mathbf{x}_j|, h_i\right) \tag{2.32}$$

while the weighted pressure is simply (Schaller et al., 2015):

$$\bar{P}_i = A_i \bar{\rho}_i^{\gamma}, \tag{2.33}$$

where γ is the polytropic index. The weighted density should not be used as a physical quantity, since it is only an intermediate quantity for the equation introduced to deal with spurious pressure jumps (Schaller et al., 2015). The physical density is given as in the standard SPH formulation by (Schaye et al., 2015; Schaller et al., 2015):

$$\rho_i = \sum_j m_j W_{ij}(h_i). \tag{2.34}$$

In all the equations above A_i is the entropic function (Schaye et al., 2015; Schaller et al., 2015). Furthermore, the smoothing kernel from `gadget2` given in eq. (2.25) is changed to the C_2 kernel given by (Schaller et al., 2015):

$$W(r,h) = \frac{21}{2\pi h^3} \begin{cases} \left(1 - \frac{r}{h}\right)^4 \left(1 + 4\frac{r}{h}\right) & \text{if} \quad 0 \leq r \leq h \\ 0 & \text{if} \quad r > h. \end{cases}$$

The smoothing length h is defined by (Schaller et al., 2015):

$$\frac{4\pi}{3} h_i^3 = N_{ngb} \tilde{V}_i \tag{2.35}$$

where the number of neighboring particles N_{ngb} is chosen to be 58 (Schaller et al., 2015), The particle volume $\tilde{V}_i$ is given by (Schaller et al., 2015):

$$\tilde{V}_i = \frac{m_i}{\rho_i} = \frac{m_i}{\sum_j m_j W_{ij}(h_i)}. \tag{2.36}$$

Furthermore, as already mentioned in Sec. 2.3, each version of SPH needs to implement some artificial viscosity, if it wants to capture shocks. In this formulation of SPH, this is done by assigning a viscosity coefficient α_i to each particle. One then has an additional differential equation for α_i which one has to solve together with eq. (2.30) (Schaller et al., 2015). In the last step, the individual viscosities are combined and then enter the equation of motion.

Apart from artificial viscosity to capture shocks, this version of SPH also includes some entropy diffusion between particles. This solves the numerical problem that SPH by construction does not have diffusion and therefore might not have the right mixing between gas phases (Schaller et al., 2015). Therefore, the differential equation for the entropic function becomes (Schaller et al., 2015):

$$\frac{\mathrm{dA_i}}{\mathrm{dt}} \overset{\mathrm{diff.}}{=} \frac{1}{\bar{\rho}^{\gamma-1}} \sum_j \alpha_{\mathrm{diff},ij} v_{\mathrm{diff},ij} \frac{m_j}{\rho_i + \rho_j} (\frac{\bar{P}_i}{\bar{\rho}_i} - \frac{\bar{P}_j}{\bar{\rho}_j}) \overline{W}_{ij}, \tag{2.37}$$

where $v_{\mathrm{diff},ij}$ is the diffusion velocity and $\alpha_{\mathrm{diff},ij}$ the diffusion coefficient.

2.4.3 Resolution of simulation

We already mentioned in Sec. 2.1 that the resolution of a simulation based on particles is set by two factors. The first one is the mass of the particles and the second one is the gravitational softening. In the simulation used for this thesis, the masses of gas particles are $m_{gas} \approx 4.5 \times 10^4$ M$_\odot$. Star particles are born with the same mass, but then lose some of this mass over their lifetime due to feedback processes (Schaye et al., 2015). Dark matter particles have a mass of $m_{DM} \approx 2.4 \times 10^5$ M$_\odot$. If one requires about 1000 dark matter particles for a dark matter halo to be well resolved, we can resolve dwarf galaxies with a halo mass down to about $m_{halo} \approx 10^8$ M$_\odot$. Therefore, this high-resolution simulation for the first time allows us to study the dwarf galaxy regime in a cosmological context and is thus the perfect choice for the research goals of this thesis. Finally, the Plummer equivalent gravitational softening ϵ is 195 pc for both gas and dark matter particles. It was chosen in a way that it is always below 1% of the mean interparticle separation (Benitez-Llambay and Frenk, 2020).

This mass and gravitational force resolution make the simulation used in this thesis one of the highest-resolution cosmological-hydrodynamical simulations currently available. Compared to the standard `EAGLE` boxes (Schaye et al., 2015) the mass resolution in this simulation is about ~ 100 times better. The `TNG50` box has mass resolution of $m_{baryon} = 8.5 \times 10^4$ M$_\odot$ and $m_{DM} = 4.5 \times 10^5$ M$_\odot$ (Pillepich et al., 2019; Nelson et al., 2019), which makes the simulation used in this thesis still by a factor of 2 better in resolution. Finally, a similar resolution has been obtained by the `FIRE2` simulation which has a mass resolution of $m_{baryon} = 6.3 \times 10^4$ M$_\odot$ and $m_{DM} = 3.3 \times 10^5$ M$_\odot$ (Moreno et al., 2022).

2.4.4 Initial Conditions

To start a cosmological simulation we need to generate the initial conditions from which the particles are then moved forward at each time step according to the gravitational and hydrodynamical forces acting on them. As we discussed in Sec. 1.5.4, we cannot directly start from the initial fluctuations generated during inflation, since to arrive at the CMB the universe is undergoing epochs that need high energy physics to be described correctly. Instead, the simulation starts at a later time after the creation of the CMB, but when the growth of density perturbations is still in the linear regime. However, to arrive there we need to link the initial Gaussian perturbations created during inflation to the perturbations at the redshift where the simulation is started, which in our case is $z = 127$. This can be done using the transfer function $T(k)$ and the growth factor $D(t)$ as described in Sec. 1.5.4.

To start the simulation we need two kinds of perturbations. First, we need to know the perturbations in the density field, that is the displacement of the particles from a uniform distribution to know where to spawn the dark matter and gas particles. And second, we also need to know the perturbations in the velocity field for the initial velocities of the particles. The perturbations need to be generated separately for the baryonic and the dark matter components since the transfer functions for baryons and dark matter have different shapes. This is especially important for scales smaller than ~ 10 kpc/h (Hahn and Abel, 2011). Using the code `MUSIC` (Hahn and Abel, 2011) to generate these perturbations at $z = 127$ a simulation box of 20 Mpc side length and periodic boundary conditions is filled with 2×1024^3 dark matter and gas particles (Benitez-Llambay and Frenk, 2020). Starting from $z = 127$ the simulation is run all the way to $z = 0$ employing the `EAGLE` model of galaxy formation, which we will explain next.

2.4.5 Subgrid Physics: The `EAGLE` model of galaxy formation

In Sec. 2.1 we briefly discussed that the particle masses and the gravitational softening ϵ set the resolution of the simulation, while in Sec. 2.4.3 we discussed the values for ϵ and the particle masses adopted in the simulation used for this thesis. Although with $\epsilon = 195$ pc and particle masses of $\sim 10^4$ $M_\odot$ for baryons this simulation is one of the highest resolution cosmological simulations currently existing, there are still many processes important for large-scale structure formation which happen below the simulation resolution. For example, star formation happens in giant molecular clouds which have masses of about $10^4 - 10^6$ $M_\odot$ and an extend of several tens of parsec (Kenyon, 2023), while the stars that form have masses that are orders of magnitude lower. Since this is below the resolution limit of the simulation, all the processes connected to star formation as well as their life cycle, that is feedback from stellar winds and supernovae, have to be implemented by subgrid prescriptions. Furthermore, the accretion disc of supermassive black holes at the center of galaxies has an extent of about $\sim 10^{15}$ cm (Crain and van de Voort, 2023), which is about 6 orders of magnitude below the spatial scales we can resolve with $\epsilon = 195$ pc. Therefore, also black hole growth as well as AGN feedback has to be modelled with subgrid physics. Finally, the first stars and AGNs started to ionize the surrounding gas. These ionized patches gradually grew until they overlapped such that the whole universe was reionized creating the so-called UV-background (Kenyon, 2023). However, this gradual ionization cannot be modeled in a large cosmological simulation, since this would require radiative transfer calculations during the evolution of the simulation and knowledge of the escape fraction of Lyman limit photons (Haardt and Madau, 2001). Therefore also the UV background has to be treated with a simplified recipe. We will now discuss these processes that cannot be captured directly by the simulation in more detail.

Star Formation

Star formation is modeled similarly to the standard `EAGLE` prescription, which follows (Schaye and Dalla Vecchia, 2008) in their numerical implementation. In a first step the empirical Kennicutt-Schmidt law for the star formation rate in eq. (1.82) is rewritten into a pressure law (Schaye and Dalla Vecchia, 2008) which is given by (Schaye et al., 2015; Crain et al., 2015):

$$\dot{m}_* = m_{gas} A (1 \mathrm{M}_\odot \mathrm{pc}^{-2})^{-n} \left(\frac{\gamma}{G} f_g P \right)^{(n-1)/2} . \tag{2.38}$$

In this equation m_{gas} is the mass of the gas particle, G is the gravitational constant, $\gamma = \frac{5}{3}$ is the ratio of the specific heats, f_g the gas mass fraction and P the pressure. A and n are parameters which are determined by observations. They take the values $A = 1.515 \times 10^{-4}$ $\mathrm{M}_\odot \mathrm{yr}^{-1} \mathrm{kpc}^{-2}$ and $n = 1.4$ if $n_H < 10^3$ cm^{-3}, while $n = 2$ if $n_H > 10^3$ cm^{-3} (Schaye et al., 2015). The pressure-dependent star formation rate from eq. (2.38) is implemented stochastically. That means that at each time step Δt a gas particle is turned into a star particle with a probability given by (Schaye et al., 2015):

$$\mathrm{Prop} = \min \left(\frac{\dot{m}_* \Delta t}{m_{gas}}, 1 \right) . \tag{2.39}$$

To trigger star formation a density threshold needs to be exceeded. While in the standard `EAGLE` version, this density threshold depends on the metallicity (Schaye et al., 2015), the density threshold for the simulation used in this thesis is independent of metallicity and takes the value $n_{H,thr} = 1.0$ cm^{-3} (Benitez-Llambay and Frenk, 2020). This different density threshold is the only difference in the implementation of star formation between the standard `EAGLE` simulation and the simulation used in this thesis.

Black Holes

Another part in structure formation that has to be modeled with subgrid physics are supermassive black holes (SMBHs) at the center of galaxies. While the stellar mass black holes that form at the end of the life of massive stars can be ignored, the SMBHs and the accretion onto them as well as their feedback have to be included, since AGN feedback is one way to quench star formation in massive galaxies (Mo et al., 2010). It is currently still unclear how the SMBHs at the center of galaxies form, with several competing theories trying to explain it (Schaye et al., 2015; Kocsis and Loeb, 2014). Since the formation of SMBHs and accretion onto them happens on spatial scales several orders of magnitude below the resolution of modern cosmological simulations, all one has to do is to seed the SMBHs with a recipe and then model their growth and feedback. We will now explain in more detail how black hole formation is modeled in `EAGLE`.

A black hole is seeded in each dark matter halo that does not yet contain a black hole and has a halo mass $M_{halo} > 10^{10}$ $\mathrm{M}_\odot h^{-1}$. For the seeding, the gas-particle with the highest density is converted into a black hole particle with a subgrid mass $m_{BH} = 10^5$ $\mathrm{M}_\odot h^{-1}$, while the BH particle mass is the same as the mass of the gas particle. In the standard `EAGLE` model the subgrid mass m_{BH} is below the gas-particle mass, i.e. also the BH particle mass. Therefore, there are two different black hole masses. While the BH particle mass is used to calculate gravitational interactions, the subgrid black hole mass m_{BH} is used to calculate the accretion rate. Only when m_{BH} reaches the particle mass, the black hole particle can start to accrete neighboring SPH particles. From there on m_{BH} and the black hole particle mass are the same (Schaye et al., 2015; Crain et al., 2015). All black hole particles created in this way are treated as collisionless.

For the growth of black holes, the accretion of stars and dark matter is neglected and instead, the black hole grows only by gas accretion. How fast a black hole can accrete gas and grow depends on a number of factors, among them the gas density and temperature, the black hole mass and the angular momentum as well as the relative velocity of the ambient gas towards the BH (Schaye et al., 2015). The accretion onto a black hole can be modeled by (Schaye et al., 2015):

$$\dot{m}_{accr} = \dot{m}_{Bondi} \times min\left(C_{visc}^{-1}(c_s/V_\phi)^3, 1\right), \tag{2.40}$$

where c_s is the speed of sound, V_ϕ is the rotation speed of gas around the black hole, C_{visc} a parameter related to the viscosity of the accretion disc and $\dot{m}_{Bondi}$ is the Bondi and Hoyle accretion rate given by (Schaye et al., 2015):

$$\dot{m}_{Bondi} = \frac{4\pi G^2 m_{BH}^2 \rho}{(c_s^2 + v^2)^{3/2}}. \tag{2.41}$$

where ρ is the ambient density and v is the relative velocity between the black hole and the gas. The accretion rate of black holes in this model is limited by a maximum accretion rate, which is given by the Eddington rate (Springel et al., 2005):

$$\dot{m}_{Edd} = \frac{4\pi G m_{BH} m_p}{\epsilon_r \sigma_T c}. \tag{2.42}$$

Here m_p is the proton mass, σ_T the Thomson cross-section, c the speed of light and $\epsilon_r = 0.1$ is the radiative efficiency of the accretion disk (Schaller et al., 2015): Finally, the black hole grows at a rate given by (Schaye et al., 2015):

$$\dot{m}_{BH} = (1 - \epsilon_r)\dot{m}_{accr} \tag{2.43}$$

Additionally to the growth by gas accretion black holes in the simulation can also grow due to merging. For two black hole particles to merge two criteria need to be fulfilled. First, the distance between the two black holes needs to be smaller than the smoothing kernel h_{BH} of the two black holes and smaller than three gravitational softening lengths. Second, their relative velocity needs to smaller than $v_{rel} < \sqrt{G m_{BH} h_{BH}^{-1}}$, which is the circular velocity at the distance h_{BH}.

Feedback processes

Both, star formation and black hole growth lead to feedback processes that return energy to the surrounding gas. During their life stars return energy and mass due to stellar winds and at the end of their life they can explode into supernovae. Black holes at the center of galaxies contribute in a different way since they are the engines for active galactic nuclei (AGNs). Both these processes happen on scales much smaller than what can be directly resolved in the simulation and therefore again have to be implemented by subgrid prescriptions. The implementation of these kinds of feedback processes into cosmological simulations was crucial to regulate gas cooling as well as star formation and to produce realistic galaxies (Crain and van de Voort, 2023).

Since the mass of each star particle by far exceeds the mass of individual stars, a star particle is not treated as a single star, but rather as a stellar population with initial mass function (IMF) in the range $0.1 - 100$ $\mathrm{M}_\odot$ based on (Chabrier, 2003). The stellar populations undergo an evolution and lose mass due to stellar winds and supernovae. Furthermore, heavier elements are synthesized and returned to the ambient gas with the stellar winds and supernovae Type Ia (SNIa). The model to calculate the mass loss is based on (Wiersma et al., 2009b), the lifetimes of stars on (Portinari et al., 1998) and the amount of heavy elements synthesized follows (Marigo, 2001; Portinari et al., 1998).

The mass that is lost during the evolution of a star particle is returned to neighboring gas particles. The mass that a particle k receives is calculated by (Schaye et al., 2015):

$$m_{received} = \frac{\frac{m_{gas}}{\rho_k} W(r_k, h)}{\sum_i \frac{m_{gas}}{\rho_i} W(r_i, h)} \tag{2.44}$$

where r_k is the distance to the star particle, h the smoothing length and W the kernel. Furthermore, a transfer in mass also leads to a change in momentum and energy, which is taken into account (Schaye et al., 2015). Finally, the number of SNIa that occur per unit initial stellar mass is given by (Schaye et al., 2015):

$$\dot{N}_{SNIa} = \nu \frac{\mathrm{e}^{-t/\tau}}{\tau}, \tag{2.45}$$

where $\nu = 2 \times 10^{-3}$ $\mathrm{M}_\odot^{-1}$ is the total number of SNIa per unit initial stellar mass and $\exp(-t/\tau)/\tau$ is an empirical delay time distribution function with $\tau = 2$ Gyrs (Schaye et al., 2015). Same as with the stellar winds above, the mass that is lost at each time step by SNIa events is distributed among the neighbors of the star particle.

Additionally to increasing the metallicity and mass of neighboring gas particles, the feedback processes from star formation also insert energy into the surrounding gas. In the `EAGLE` model this is done by stochastically heating gas particles. For that, first, the temperature increase ΔT for the gas particles is specified. Then f_{th}, the fraction of the energy budget available for feedback, is calculated by (Schaye et al., 2015):

$$f_{th} = f_{th,min} + \frac{f_{th,max} - f_{th,min}}{1 + \left(\frac{Z}{0.1 Z_\odot}\right)^{n_Z} \left(\frac{n_{H,birth}}{n_{H,0}}\right)^{-n_n}}, \tag{2.46}$$

where $Z_\odot = 0.0127$ is the solar metallicity, $n_Z = n_n = \frac{2}{\ln 10}$, $f_{th,max} = 3$ and $f_{th,min} = 0.3$. The value of $n_{H,0}$ depends on the resolution of the simulation (Schaye et al., 2015). Finally, $n_{H,birth}$ is the density the gas particle had when it was converted into the star particle for which the feedback is calculated. This f_{th} determines the probability that a star particle is heated following (Dalla Vecchia and Schaye, 2012). To decide whether a gas particle is heated by a star particle a random number r between 0 and 1 is drawn and if $r \leq p$, where $p \sim f_{th}$, the gas particle is heated by ΔT (Dalla Vecchia and Schaye, 2012).

Apart from stellar feedback, also AGN feedback is able to heat up the surrounding gas. While other models make a distinction between 'quasar' and 'radio' modes of AGN feedback, the `EAGLE` model does not make this difference and injects feedback only thermally and stochastically, similar to the way the stellar feedback works. The rate with which energy is injected by AGN feedback is given by (Schaye et al., 2015):

$$\text{injection rate} = \epsilon_f \epsilon_r \dot{m}_{accr} c^2 \tag{2.47}$$

where $\epsilon_r = 0.1$ is again the radiative efficiency of the accretion disk and $\epsilon_f = 0.15$ is the fraction of the radiated feedback coupled to the ISM. At each time step Δt an energy reservoir E_{BH} at each black hole is increased by $\epsilon_f \epsilon_r \dot{m}_{accr} c^2 \Delta t$. To trigger the heating by an amount ΔT_{AGN} there needs to be enough energy to heat at least n_{heat} particles. If that is the case, the probability for each neighboring gas particle to be heated is given by (Schaye et al., 2015):

$$P = \frac{E_{BH}}{\Delta\epsilon_{AGN} N_{ngb} \langle m_{gas} \rangle}, \tag{2.48}$$

where N_{ngb} is the number of gas neighbors of the BH, $\langle m_{gas} \rangle$ the mean mass of the neighboring gas particles and ϵ_{AGN} is the increase in internal energy, which has been calculated from ΔT_{AGN} (Schaye et al., 2015).

UV Background

While in the real universe, reionization started from the first stars and AGNs gradually ionizing the whole universe, the UV background in this cosmological simulation is implemented spatially uniform at a certain redshift. The goal of modeling the UV background is to arrive at a broad agreement with the measurements of the thermal history of the intergalactic gas (Schaye et al., 2015). To achieve that two components, hydrogen and helium, have to be heated. Following the implementation of (Haardt and Madau, 2001) the UV-background is turned on in the whole simulation at a redshift of $z = 11.5$ and 2 eV per proton mass are inserted into the gas to heat it up to $T = 10^4$ K. For hydrogen the insertion of energy happens instantaneously at $z = 11.5$, while for helium it is smeared out in time with a Gaussian centering at $z = 3.5$ and $\sigma(z) = 0.5$ (Schaye et al., 2015).

The existence of a UV background has important implications for galaxy formation. Due to the ionizing background and the higher temperature of the intergalactic gas, star formation is shut down in galaxies with a halo mass that is too low for gas cooling (Somerville and Davé, 2015). In other words, for star formation to happen a certain halo mass has to be exceeded, because otherwise, the gas cannot cool down. This critical mass for star formation is dependent on the redshift and makes a jump when the UV background is turned on (Benitez-Llambay and Frenk, 2020). Therefore, after reionization a higher halo mass is needed for star formation to proceed and galaxies with a halo mass below the critical mass lose the ability to form stars.

Cooling

As we saw before, to form stars, gas has to cool down to collapse under gravity. Also, this cooling has to be implemented by subgrid prescriptions, which is done in the simulation according to (Wiersma et al., 2009a). They calculate cooling for 11 elements (H, He, C, N, O, Ne, Mg, Si, S, Ca, Fe) from tables as a function of temperature, density, and redshift. The tables have been pre-generated using `CLOUDY` (Ferland et al., 1998), assuming ionization equilibrium for the gas which is exposed to both, the CMB and the UV-background from (Haardt and Madau, 2001).

The `EAGLE` model and high resolutions

Originally, the `EAGLE` model of galaxy formation was designed for particle masses of $m_{gas} \approx 2 \times 10^6$ M$_\odot$ and $m_{DM} \approx 10^7$ M$_\odot$ (Schaye et al., 2015). The application of the same model to higher particle resolutions, i.e. lower particle masses, can create problems when trying to match the resulting galaxy population to observables. For example, in the simulation we use (Benitez-Llambay and Frenk, 2020) there is a mismatch between the predictions from abundance matching and the galaxy population of the simulation in the stellar mass-halo mass relation at high galaxy masses. We show this mismatch in Fig. 3.1. Such a mismatch does not pose a problem if one only considers the part of the sample that matches the predictions from abundance matching, as we do in Ch. 3 where we deal with dwarf galaxies, or if one only considers the gas around the galaxies, as we do in Ch. 5 where we solely consider the CGM.

2.5 Halo Finders and Merger trees

When using cosmological simulations to investigate interactions of galaxies with their environment, it is first necessary to define and identify what counts as a galaxy in the simulation. This is done by running a halo finder on the simulation data, which identifies bound structures in the simulation output. A galaxy is then defined as a bound structure that also contains star particles. There exist many different halo finders like `Rockstar` (Behroozi et al., 2013), `HSF` (Maciejewski et al., 2009) or `SUBFIND` (Springel et al., 2001) each of them with their own advantages and shortcomings (Knebe et al., 2011a). This simulation uses `HBT+` (Han et al., 2018) to find bound structures and substructures and to link them between simulation snapshots, which allows the tracking of bound structure through time. We will now explain in more detail how `HBT+` finds bound structures and links them between simulation snapshots.

2.5.1 Finding substructure and linking it through time

Since `HBT+` needs a catalogue of friend-of-friend halos as input, the first step consists in creating this catalogue. In general, a friends-of-friends (FoF) algorithm works the following way: first, one has to choose a linking length b and then starting from one particle check which other particles are within the linking length. Continuing from these "friends" one checks, whether there are any other particles within the linking length of these friends or any other newly found friends until no further particles are found. This is done for all the particles in the simulation. Particles that are linked together in this way are then said to be part of a FoF halo (Schneider, 2015). When the linking length is chosen as $b = 0.2 \times \sqrt{1/n}$, where $\sqrt{1/n}$ is the mean interparticle separation with $n = N/L^3$ the number density of particles, then the halos constructed in this way have a density about 200 times the critical density, which roughly corresponds to the value for virialized objects as mentioned in Sec. 1.5.2 (Schneider, 2015). One can construct this required catalogue of FoF halos either with the algorithm implemented in `HBT+` or any other halo finder.

Having a list of FoF halos at each snapshot, `HBT+` then determines which of these halos are subhalos of bigger halos and how these halos are linked between different snapshots. Starting from the snapshot at the highest redshift, `HBT+` determines for each halo existing at z_n, which is the corresponding halo at snapshot z_{n+1}, by taking the bound particles from the halos at snapshot z_n and looking for the corresponding halo at snapshot z_{n+1}. If more than two halos are linked to another halo the main progenitor is determined by taking the most massive halo at the previous snapshot. If several halos have a similar mass as the most massive progenitor, then the progenitor with the lowest kinetic energy with respect to the bulk motion of the host halo is chosen as the main progenitor. Furthermore, each of the halos is assigned a unique track ID which then allows the easy tracking of each halo through time and the construction of merger trees (Han et al., 2018).

For the `HBT+` algorithm to work one needs to determine the bound particles of each halo at each snapshot. This is done by an unbinding procedure, where all particles with a kinetic energy bigger than the potential energy of the halo are removed. After the removal of all the unbound particles the potential energy of the halo is updated and the unbinding procedure starts again. This process has to be repeated until the mass of the halo converges (Han et al., 2018).

2.5.2 Mass accretion histories

The construction of merger trees also allows one to construct *mass accretion histories* of galaxies. A mass accretion history shows the growth of a dark matter halo and how the different components of dark matter, gas, and stars contribute to the total virial mass. We show an example of a mass accretion history in Fig. 2.1. The galaxy is born when the universe is less than 1 Gyr old and quickly reaches a halo mass of $M_h \sim 5 \times 10^9$ $\mathrm{M}_\odot$. From there it continues to grow until it reaches a halo mass of $M_h \sim 10^{10}$ $\mathrm{M}_\odot$ and a stellar mass of $M_* \sim 10^7$ $\mathrm{M}_\odot$ at the present day. Such mass accretion histories can be used to analyze the evolution of galaxies as done in Ch. 3, and to identify problems in the tracking and

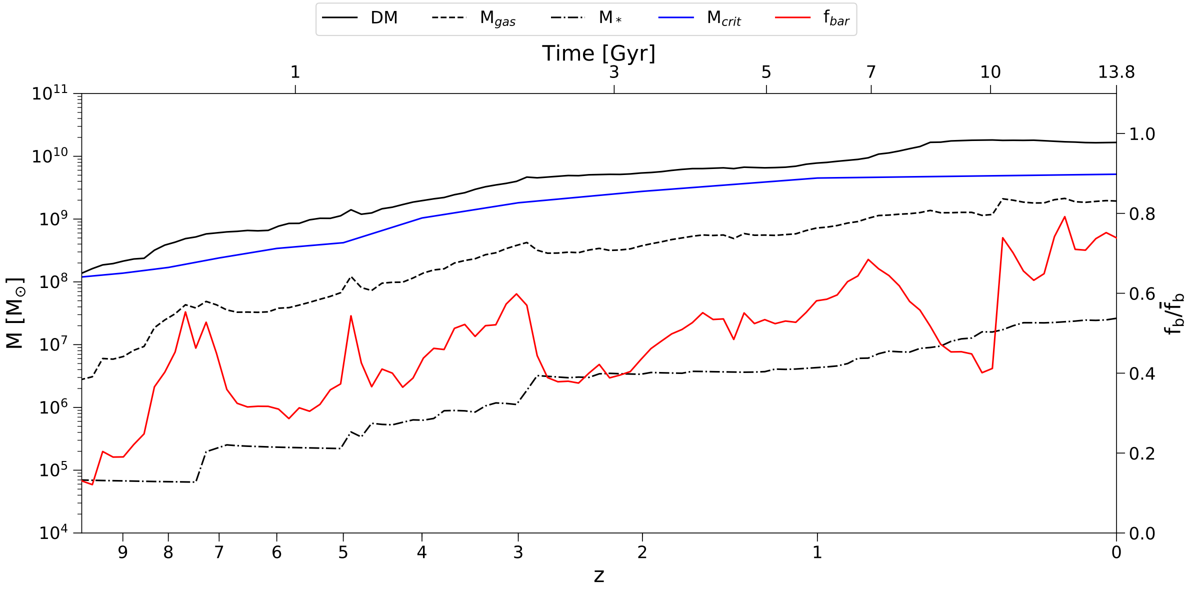

Figure 2.1: Mass accretion history of a galaxy. The solid black line shows the dark matter mass, the dashed line is the gas mass and the dotted line is the stellar mass. The blue line is the critical mass that needs to be exceeded for star formation to happen. The red line is the baryon fraction. The galaxy is born at around ~ 0.5 Gyrs and reaches a halo mass of $\sim 5 \times 10^9$ M$_\odot$ after about 2 Gyrs. From there the galaxy slowly continues to grow and at the present day it has a halo mass of $\sim 10^{10}$ M$_\odot$ and a stellar mass of $M_* \sim 10^7$ M$_\odot$. Since the halo mass is always above the critical mass for star formation, this galaxy continues to form stars until the present day.

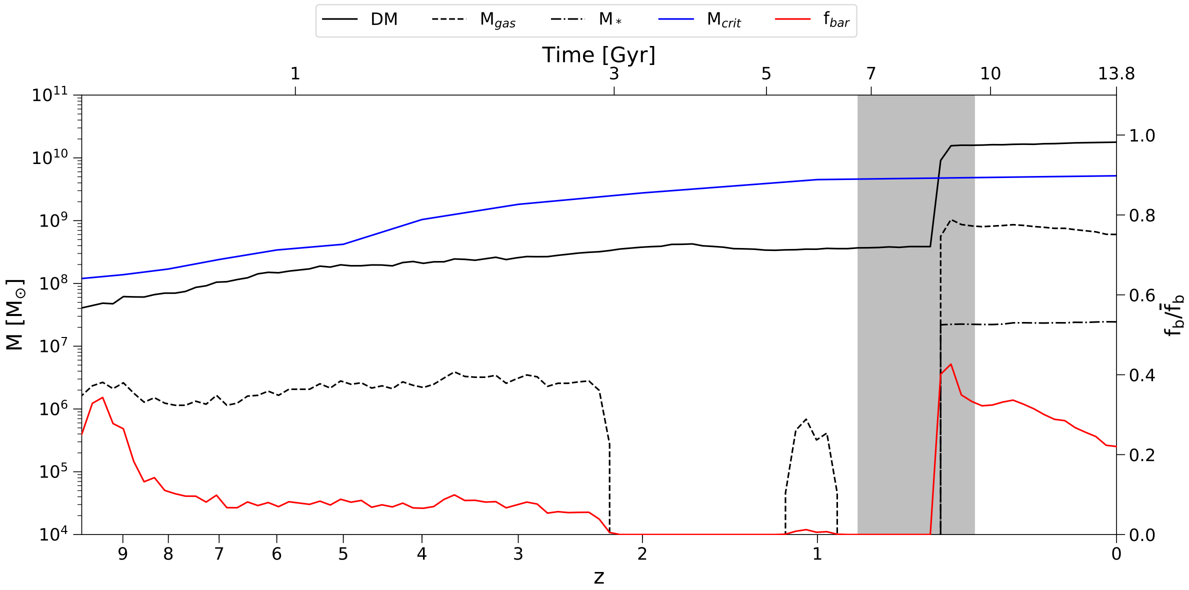

Figure 2.2: Mass accretion history of a galaxy where the wrong galaxy was selected as the main progenitor. The black solid line is the dark matter mass, the dashed line is the gas mass, and the dotted line is the stellar mass. The blue line shows the critical mass necessary for star formation and the red line is the baryon fraction. At a time of around 8 Gyrs, there is a sharp jump in all the tracked masses. This is because here the tracking went wrong and a low-mass halo was chosen as the main progenitor. We show a visualization of this jump from the starless dark matter halo to the galaxy in Fig. 2.3. The grey-shaded area corresponds to the timespan shown in the visualization.

unbinding algorithm of the halo finder.

During the analysis of the simulation, we were able to identify three main problems of the halo catalogue produced by `HBT+`: first, the incorrect identification of the main progenitor that leads to a wrong tracking of the galaxy; second, the association of gas particles to dark matter halos that are not heavy enough to accrete gas; and third, the association of freely floating star particles to dark matter halos that never formed stars, sometimes only for a few snapshots, which incorrectly turns them into “galaxies”. We will now discuss all three problems and how they can be ameliorated in more detail.

Incorrect identification of the main progenitor

In Sec. 2.5.1 we discussed how `HBT+` is constructing the merger trees and finding the main progenitors. However, in the construction of these merger trees not always the right main progenitor is found which leads to a wrong tracking. This can be seen for example in the mass accretion history if there are unexpected large jumps in the bound components of the tracked galaxy. We show an example of such a mass accretion history where the wrong main progenitor was selected in Fig. 2.2. At around 8 Gyrs there is a sharp jump in all

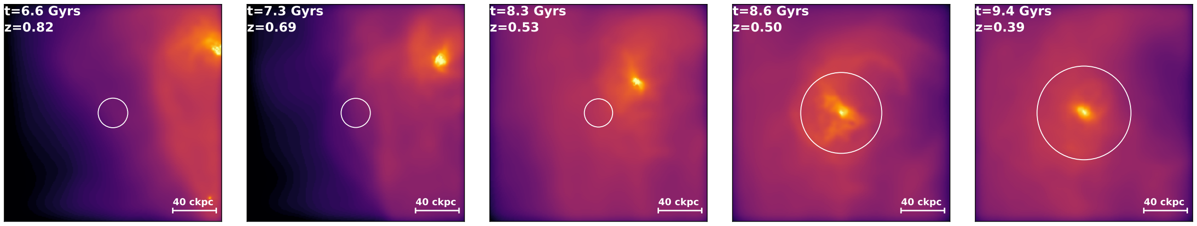

Figure 2.3: Visualization of the jump from the star less dark matter halo to the galaxy. The first three panels show the star less dark matter halo that has been wrongly identified as the main progenitor as it approaches a more massive galaxy. In panel four and five the halo finder identified the right galaxy as the main galaxy. These wrong identifications of the main progenitor happen for about 10% of the field galaxies and need to be corrected if one is interested in the evolution of the galaxy sample.

the masses tracked which is due to the selection of a low mass halo as the main progenitor. We show a visualization of this galaxy in Fig. 2.3. The first three panels show a starless dark matter halo with a low mass traveling towards a galaxy. In panel four the star-less dark matter halo merged with the galaxy, the bound components in the mass accretion history make a jump and the halo finder centers now on the galaxy. One can see that the more massive galaxy should have been selected as the main progenitor by `HBT+` instead of the starless dark matter halo. About 10% of all the field galaxies show this behavior which has to be corrected by selecting the most massive galaxy as the main progenitor if one is interested in the environmental interactions of a galaxy during its evolution.

Incorrect association of “bound” gas particles

When determining which particles count as bound particles to a dark matter halo `HBT+` relies on an unbinding procedure as described before. However, this procedure can fail in certain cases and produce results that have to be corrected in post-processing. Especially, if a galaxy is undergoing environmental interactions as described in Sec. 1.6 which manage to remove all the gas from a galaxy, the halo finder can incorrectly associate gas particles with the galaxy afterward. We see an example of such a mass accretion history in Fig. 2.4, where after a stripping event that removed all the gas from the galaxy, there is a spike in the gas mass shortly after 6 Gyrs and later after 10 Gyrs an apparent accretion of gas. However, when looking at the visualization of this galaxy at five different snapshots in Fig. 2.5 one can see that the gas that is associated with the galaxy after the stripping event, should not be counted as bound gas. In the first panel before the stripping event the gas is concentrated inside the galaxy. The second and third panels show snapshots of the galaxy when there is no gas bound to the galaxy according to `HBT+`. One can see that the halo finder correctly identified the gas inside the galaxy as belonging to the ambient gas. Finally, the fourth and fifth panels show the galaxy at snapshots when `HBT+` associates gas with them. However, as in the two panels before, there is no gas concentrated in the

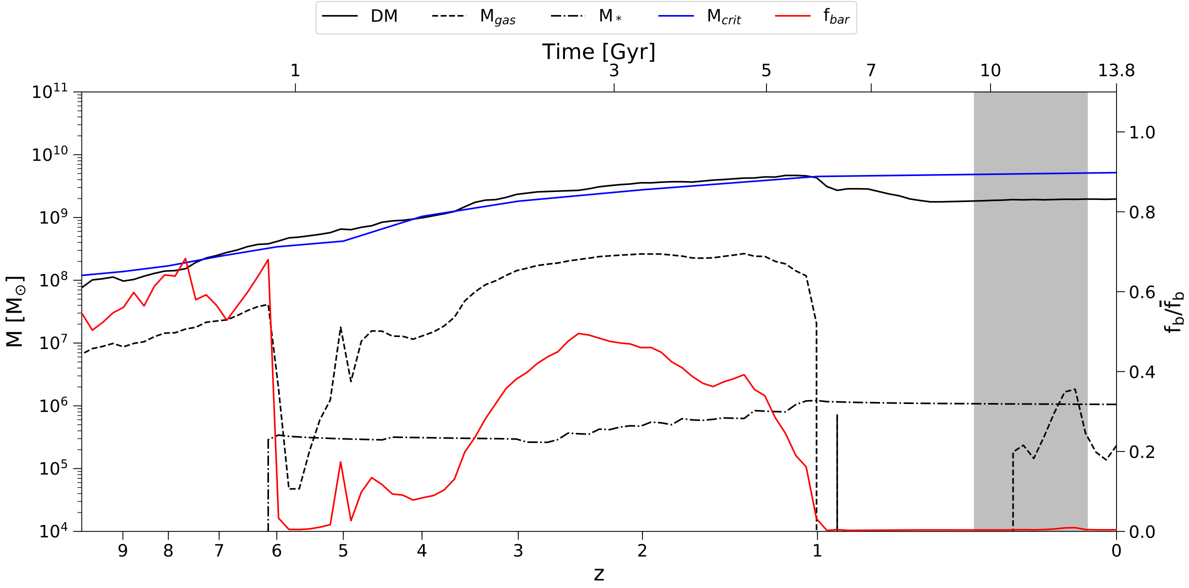

Figure 2.4: Mass accretion history of a galaxy where gas particles are wrongly associated with the halo. The lines show the same as before. At around 6 Gyrs the galaxy undergoes an environmental interaction that removes some of its dark matter and all of its gas. Shortly after 6 Gyrs, we can see a spike in the gas mass and after 10 Gyrs it seems like the galaxy is accreting some gas again. However, this is only due to a failure of the unbinding procedure in `HBT+` that wrongly associates gas particles with this dark matter halo, while traveling through ambient gas. We show a visualization of this galaxy before stripping and in the timespan marked by the grey-shaded area in Fig. 2.5.

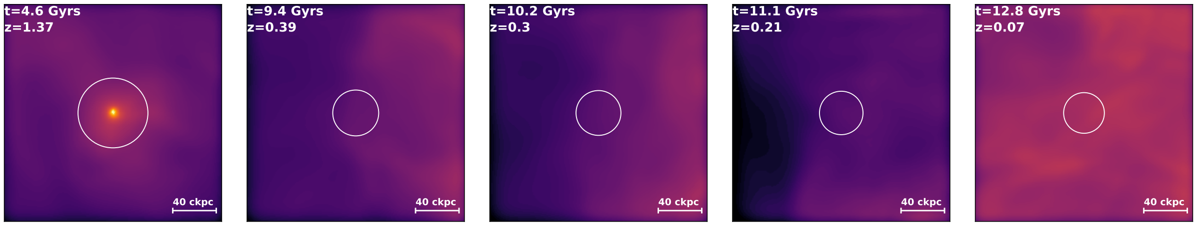

Figure 2.5: Visualization of the galaxy that wrongly has gas particles associated with it by `HBT+`. In the first panel, we see the galaxy before the stripping event with the gas concentrated in the center. In the next four panels, we see the galaxy after the stripping event, where the second and the third panels show the galaxy at snapshots where `HBT+` did not associate gas particles with them, while the fourth and the fifth panels show the galaxy at snapshots with gas associated with them by `HBT+`. Since there is no gas concentrated at the center of the galaxy, and one can rather only see the ambient gas, one has to correct the gas mass by hand and set it to zero.

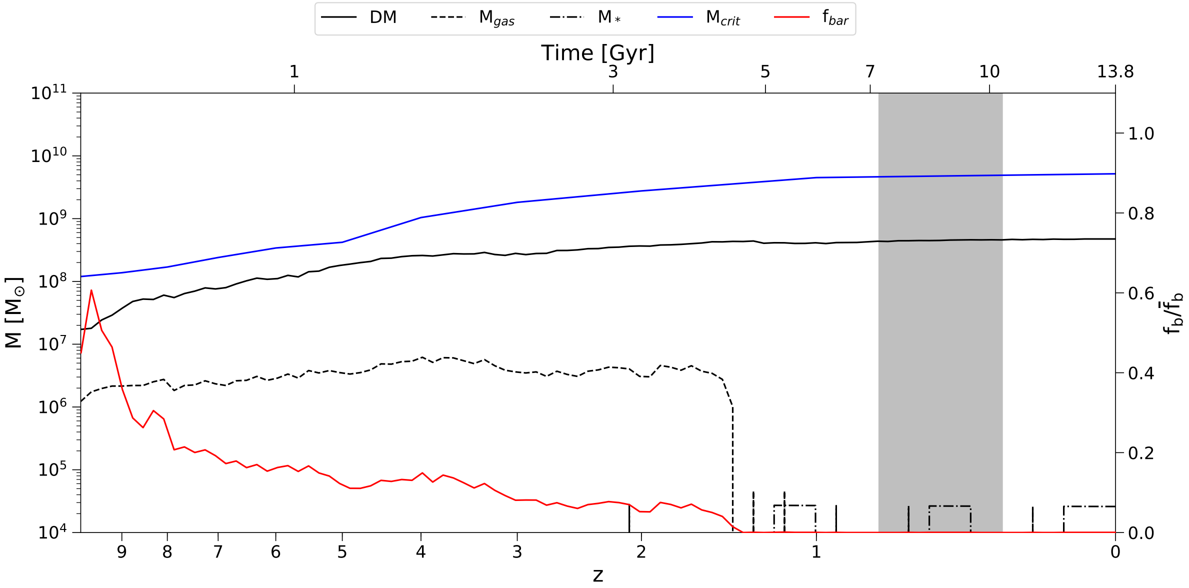

Figure 2.6: Mass accretion history of a galaxy where a freely floating star particle is wrongly associated with the dark matter halo. We see that the stellar mass seems to oscillate, i.e. it seems like the galaxy forms stars and loses stars several times. However, since the gas mass is zero, even before the first star is acquired, this star particle cannot come from the transformation of a gas particle into a star particle. Instead, it captures a freely floating star particle that has been formed somewhere else, whenever the stellar mass is non-zero.

center of the galaxy. Instead, the gas that happens to be inside the galaxy belongs to the ambient gas structure. Therefore, it should not be counted as gas belonging to the galaxy and if galaxies show this kind of behaviour, one has to correct it and set the gas mass to zero after the stripping event. Out of a ≈ 2280 field galaxies, 78 had to be corrected in this way.

Incorrect association of freely floating star particles

Due to tidal stripping events, it is possible that star particles are removed from galaxies and then are freely floating in the simulation volume. It can happen that such a star particle is crossing an otherwise empty dark matter halo and that `HBT+` is wrongly associating this star particle to the dark matter halo as a bound particle. These "galaxies" show a mass accretion history where the stellar mass seems to oscillate or where star formation seems to happen without a loss in gas mass, i.e. without the transformation of gas particles into stellar particles as prescribed by the subgrid physics model discussed in Sec. 2.4.5. We show such a mass accretion history in Fig. 2.6 where we can see that an increase in stellar mass happens without a loss in gas mass. Furthermore, the dark matter mass of this "galaxy" is its whole life below the minimum mass for star formation that is marked in blue. Therefore, the star particles that are associated with the "galaxy" by `HBT+` have to

Figure 2.7: Visualization of a “galaxy” that has captured a freely floating star particle. In each panel, we mark the virial radius of the “galaxy” by a white circle, and the star particles close to the galaxy with white stars. In the first panel, there are four star particles, and although one is at the edge of the virial radius of the galaxy, it is not counted as a bound particle by `HBT+`. In the second and fourth panels, the star particle is counted as bound, while in the third and fifth panels, it is again not bound to the galaxy.

come from somewhere else. In Fig. 2.7 we show a visualization of the “galaxy” and mark the freely floating star particles with white stars. We can see that the transformation of the dark matter halo into a “galaxy” is due to a glitch of `HBT+` that is associating a freely floating star particle to the dark matter halo. Such a behavior is a problem, especially at the low stellar mass end of galaxies, and can be ameliorated by requiring a minimum number of ~ 5 stellar particles bound to a dark matter halo for the halo to count as a galaxy. However, if one wants to include also galaxies with only one or a few star particles in the sample because one is interested in the behavior of low-mass galaxies, one has to identify these example galaxies and remove them from the sample. In our case we had to remove 9 galaxies out of ≈ 2280 to this reason from the sample we use in Ch. 3.

2.6 Virial Quantities

We discussed the virial theorem and how to derive it in Sec. 1.5.2. When studying the spherical collapse and subsequent virialization of a spherical density perturbation in a universe with $\Omega_m = 1$ and $\Omega_\Lambda = 0$ one finds that a collapsed density perturbation has an average density ~ 178 times the background density (Somerville and Davé, 2015). Virial quantities in simulations are therefore defined by rounding up to 200 and taking the mass that is enclosed in a sphere with an average density 200 times the critical density $\rho_{crit} = 3H^2/8\pi G$ as the virial mass. The radius of this sphere is then the virial radius and the virial temperature can be calculated using eq. (1.80).

The definition of virial quantities in terms of an enclosed mass means that for satellite galaxies, virial quantities are not well defined. The closer a satellite galaxy is to the center of its host, the higher the background density of the satellite. Therefore, when calculating the virial mass by means of an enclosed mass the sphere that has an average density of $200 \times \rho_{crit}$ will be smaller the closer the satellite is to the center of the host halo. This dependence of virial quantities on the location inside the host halo makes them ill-defined for satellites and one has to choose a different approach when dealing with satellite galaxies.

A suitable workaround is to use the half-mass radius which is the radius that contains half the bound mass of the galaxy. This is independent of the location within the halo of the host. Since our sample in Ch. 5 also includes satellite galaxies, we use this approach instead of the virial radius.

2.7 Visualization, Movies, and Calculation of Column Densities

Visualization of the simulation output as seen for example in Fig. 1.4 is done with the `py-SPHviewer` tool (Benitez-Llambay, 2015). By giving the masses, positions, and smoothing lengths of all particles in a certain region as input, py-SPHviewer can render the scene of this region and produce images that can be used for scientific interpretation. In this process `py-SPHviewer` takes the density field in a 3D region and projects it onto a 2D plane. Therefore, each pixel of an image can also be interpreted as the column density of gas along this sight line. In Ch. 5 we use py-SPHviewer to calculate the column densities of different gas phases.

Often the simple visualization of the simulation output together with mass accretion histories is not sufficient to understand what is happening in the simulation. Therefore, one often has to resort to following the evolution history by examining movies of the simulation output, especially when one is interested in the evolution of galaxies and the processes that happen during this evolution. Such movies can be easily created by gluing together the visualizations of the simulation output at different snapshots.

Chapter 3

Galaxies and their Interactions with the Environment

In Ch. 1 we discussed how galaxies form inside dark matter halos by a collapse of gas that is transformed into stars. In this idealized picture of galaxy formation, where galaxies are not undergoing any interaction with their environment or other galaxies, but rather evolve in isolation, the gas content of galaxies is set by a balance between gas infall and outflows due to feedback processes. However, this only applies, if there are feedback processes due to star formation or AGNs that are driving these outflows. If this is not the case, the gas content is rather set by the balance between the pressure of the intergalactic medium and the gravitational potential and can be described by a simple model (Benitez-Llambay and Frenk, 2020). The distinction between star-forming and quiescent galaxies depends on their halo mass and is described by a critical mass. The critical mass is the minimum halo mass necessary for starformation and therefore also galaxy formation (Benitez-Llambay and Frenk, 2020).

However, these models do not account for environmental interactions, that galaxies can undergo during their evolution. Among these interactions are ram pressure stripping and tidal stripping as we presented them in Sec. 1.6. These interactions have been studied in high density environments like clusters and groups (Boselli et al., 2023, 2016, 2022; Rasmussen et al., 2006). Since deep galaxy surveys like the *MUSE Ultra Deep Field (MUDF)* (Lusso et al., 2019; Fossati et al., 2019) will be able to observe low stellar mass galaxies located in the field, there is the need to model environmental interactions of dwarf galaxies in less dense environments like cosmic web filaments. We now want to investigate how environmental interactions in low density environments are shaping the final properties like the dark matter mass and gas mass of field dwarf galaxies.

3.1 The need for a cosmological representative sample

There have been already theoretical studies investigating the influence of environmental interactions on field dwarf galaxies.. For example, (Benítez-Llambay et al., 2013) found that isolated dwarf galaxies can undergo ram pressure stripping in cosmic web filaments ("cosmic-web stripping") removing the gas and shutting down star formation. However, since the simulation they used in (Benítez-Llambay et al., 2013) was a local group simulation containing a biased subsample of the overall galaxy population, it was not possible to give an estimate on the importance of this process on cosmological scales.

We wanted to ameliorate this problem and investigate the importance of environmental interactions and especially cosmic web stripping for the gas content of isolated galaxies using a cosmologically representative sample. This required, first, a simulation that has a particle resolution high enough to properly resolve dwarf galaxies. For a dark matter halo to be properly resolved, we need about 1000 dark matter particles in the halo. Therefore, to resolve low mass dwarf galaxies, i.e. galaxies with a halo mass of $\sim 10^8$ $\mathrm{M}_\odot$ we need a simulation with a dark matter particle mass of $\sim 10^5$ $\mathrm{M}_\odot$. And second, the simulation box had to be big enough to get a representative sample of galaxies. The high-resolution hydrodynamical cosmological simulation we are using and that we presented in Sec. 2.4 is one of the first simulations that fulfills both criteria so that this research is possible. The results of that research have been published in (Herzog et al., 2023) and are presented below:

3.2 The present-day gas content of simulated field dwarf galaxies

We examine the gas content of field dwarf galaxies in a high-resolution cosmological simulation. In agreement with previous work, we find that galaxies inhabiting dark matter haloes with mass below a critical value, $M_{200} \lesssim M_{\mathrm{crit}} \approx 5 \times 10^9$ $M_\odot$, are quiescent at the present day. The gas content of these galaxies is thus insensitive to feedback from evolving stars. Almost half of these quiescent systems today have gas masses much smaller than that expected for their mass. We find that gas-deficient galaxies originate from 1) past interactions with massive hosts, in which a dwarf loses gas and dark matter via tidal and ram-pressure forces; and 2) from hydrodynamic interactions with the gaseous filaments and sheets of the cosmic web, in which a dwarf loses gas via ram-pressure. We refer to these systems as "flybys" and "COSWEBs". Flybys locate in high-density regions, tracing the location of the most massive galaxies in the simulation. In contrast, COSWEBs are dispersed throughout the volume and trace the cosmic web. For sub-critical systems, $M_{200} < M_{\mathrm{crit}}$, the fraction of COSWEB galaxies can be as high as 35%, and much higher for flybys, which make up 100 per cent of the galaxies with $M_{200} < 3 \times 10^8$ $\mathrm{M}_\odot$. The deficit of gas caused by these mechanisms may preclude the detection of a large fraction of field dwarfs in future H I surveys. For galaxies inhabiting halos with mass $M_{200} > M_{\mathrm{crit}}$, we find that cosmic web stripping, on average, shuts down star formation in more than 70% of the affected systems.

3.2.1 Introduction

Within the Λ Cold Dark Matter (ΛCDM) paradigm of structure formation, galaxies form from gas that condenses to turn into stars in the centre of gravitationally-bound dark matter haloes (White and Rees, 1978). The amount of baryons that reside in these haloes depends, however, on the considered mass and cosmic time scales.

At early times, for example, before the epoch of cosmic reionization, dark matter haloes sufficiently massive to overcome the entropy of the intergalactic medium can accumulate gas copiously, reaching gas mass fractions similar to the cosmic mean, $f_{\rm b} \sim \Omega_{\rm b}/\Omega_{\rm m}$ (e.g. Naoz et al., 2009). The gas in these haloes is, however, quickly pressurised through shocks and cannot collapse further to the centre of the majority of systems to form stars. This is because galaxy formation at early times proceeds predominantly in atomic cooling (AC) haloes, i.e., those haloes with virial[1] temperature $T_{200} \gtrsim 10^4\ K$,[2] for which gas can lose its pressure support via radiative cooling (see, e.g., a review by Bromm and Yoshida, 2011). Once galaxies form in the centre of these haloes, the efficient expulsion of gas by baryonic processes associated with stellar evolution, including radiative, thermal, and kinetic feedback, affects their baryon content dramatically, and numerical hydrodynamical simulations are required to follow their gas content in detail, which is largely determined by the net balance between gas infall and outflows.

At later times, after the epoch of reionization ($z < z_{\rm re}$), the presence of the ionizing UV background (UVB) radiation field prevents gas accretion onto haloes less massive than a present-day mass, $M_{200} \lesssim M_{\rm crit} \approx 5 \times 10^9\ M_\odot$, a mass-scale that exceeds that imposed by the AC limit by roughly a factor of 5.[3] By cutting out their gas supplies, the photoheating associated with the UVB inhibits further star formation in the already existing galaxies that inhabit these low-mass haloes (e.g. Efstathiou, 1992; Thoul and Weinberg, 1996; Quinn et al., 1996; Weinberg et al., 1997; Babul and Rees, 1992; Bullock et al., 2000; Benson et al., 2002, and references therein), and prevents the formation of galaxies in starless haloes less massive than $M_{\rm crit}$. Although the majority of baryons are indeed pushed out from these low-mass systems, an increasingly small fraction of gas remains bound to dark matter haloes down to a present-day virial mass, $M_{200} \gtrsim 10^6\ M_\odot$, below which dark matter haloes become baryon-free (Benitez-Llambay and Frenk, 2020, hereafter BL20). The gas content of haloes in the mass range $10^6 \lesssim M_{200}/M_\odot \lesssim 5\times 10^9$ is thus established by the balance between the gravitational potential and the pressure of the intergalactic medium (Rees, 1986; Ikeuchi, 1986; Benítez-Llambay et al., 2017), and it is insensitive to the stellar content of the halo because the gravitational contribution of stars in these low-mass systems can be largely neglected. On the other hand, the baryon content of haloes with virial mass $M_{200} > M_{\rm crit}$, for which gas cannot remain in hydrostatic equilibrium, is affected by feedback associated

---

[1] We identify virial quantities with a 200 subscript. These quantities correspond to those measured within a sphere for which the mean enclosed density is 200 times the critical density of the Universe, $\rho_{\rm crit} = 3H^2/8\pi G$.

[2] The virial temperature is defined as $T_{200} = 36(V_{200}/{\rm km\ s^{-1}})^2$ K, where V_{200} is the halo virial circular velocity, $V_{200} = (GM_{200}/R_{200})^{1/2}$, and we assume a mean molecular weight $\mu = 0.6$.

[3] Note that at $z = 0$, the AC limit corresponds to halo virial mass $M_{200} \sim 10^9\ M_\odot$.

with star formation, and simulations are required to track the gas content of these haloes.

It is thus clear that the baryon content of galaxy haloes is largely regulated by the balance between gas infall and outflows, but only for haloes more massive than the AC limit before cosmic reionization, and for haloes more massive than $M_{\rm crit}$ afterwards. In the present-day halo mass range, $10^6 \lesssim M_{200}/M_\odot \lesssim M_{\rm crit} \approx 5 \times 10^9$, for which gas is stable against gravitational collapse (and therefore unable to foster star formation), the small amount of gas left inside these haloes remains in hydrostatic equilibrium (BL20).

The previous picture strictly applies to systems that form and evolve in relative isolation, as the gas content of galaxy haloes may be affected, in turn, by external environmental processes. For example, it is well known that hydrodynamic and gravitational interactions can remove gas from galaxy haloes and cut off their gas supplies, and similarly to the previous mechanisms, their impact on the gas content is exacerbated for low-mass haloes. These interactions affect predominantly satellite galaxies that fall into groups and clusters (e.g., Gunn and Gott, 1972; Moore et al., 1996; Abadi et al., 1999; McCarthy et al., 2008, and references therein), and are thought to be responsible for the environmental dichotomy observed within our Local Group (e.g., van den Bergh, 1994), in which the majority of satellites of the Milky Way (MW) and Andromeda (M31) are devoid of gas and are not forming stars at the present day, whereas the fraction of gas-rich dwarfs increases dramatically further out from the host galaxies (see, e.g., a recent compilation by Putman et al., 2021).

The existence of the environmental dichotomy in gas mass observed today in the Local Group constitutes perhaps the strongest argument in favour of the idea that isolated galaxies represent true examples of how galaxies form and evolve in the absence of environmental processes. However, the existence of nearby dwarfs in relative isolation that exhibit particularly low gas-to-stellar mass ratios (e.g. Karachentsev et al., 2014) seem to challenge this idea. Moreover, using high-resolution numerical simulations, (Benítez-Llambay et al., 2013, hereafter BL13) have shown that isolated dwarf galaxies may be subject to "cosmic-web stripping", a process that can either suppress star formation by removing gas from dwarf galaxy haloes in the case of strong interactions between the galaxy gaseous halo and the cosmic web or reignite star formation by compressing the gas for the case of weaker interactions (e.g. Wright et al., 2019; Genina et al., 2019). The efficiency of this process in shaping the present-day gas content of the cosmological population of dwarfs is, however, difficult to assess, as the simulations considered by these authors encompass, in all cases, very limited (and biased) cosmological volumes.

The goal of our paper is thus to revisit the importance of the environment, and in particular of cosmic-web stripping, in establishing the present-day gas content of isolated dwarf galaxies. To this end, we use a hydrodynamic simulation with sufficiently high resolution to track the gas content of dwarf galaxy haloes and with sufficient large volume to understand the importance of this process over cosmological scales. We describe our simulation and galaxy sample in Sec. 3.2.2. We then present and discuss our results in Sec. 3.2.3 and Sec. 3.2.4, respectively, and conclude with a summary of our results in Sec. 3.2.5.

3.2.2 Methods

The simulation

We use a Smoothed-Particle-Hydrodynamics (SPH) cosmological simulation evolved with the `P-Gadget3` code (Springel, 2005) and the `EAGLE` model of galaxy formation (Schaye et al., 2015; Crain et al., 2015). The simulation is the same introduced by BL20 and consists of a random realisation of a periodic cubic volume of side length 20 Mpc filled with 1024^3 gas and dark matter particles. The gas and dark matter particle mass are, respectively, $m_{\rm gas} \approx 4.5 \times 10^4$ M$_\odot$, and $m_{\rm dm} \approx 2.4 \times 10^5$ M$_\odot$, which ensures the simulated volume is at the mean density of the Universe. The initial conditions were carried out at redshift, $z = 127$, with the publicly-available code `MUSIC` (Hahn and Abel, 2011). The Plummer-equivalent gravitational softening, ϵ, adopted in our simulation never exceeds 1% of the mean interparticle separation. This gives $\epsilon \sim 195$ pc for both the gas and the dark matter particles. This value is much smaller than the radius below which the 2-body relaxation timescale equals the age of the Universe for our simulation (Power et al., 2003). The structure of the haloes in our simulation is thus not limited by the choice of ϵ, but by the number of particles. We list here the simulation details relevant to our study, and we refer the reader to the original papers for further details.

Star formation is implemented in the simulation by turning gas particles into stars at the same Kennicutt–Schmidt rates adopted in the EAGLE simulations, but only for gas particles that exceed a density threshold $\rho_{\rm th} = 1.0$ cm^{-3}. This high threshold ensures that the gas is self-gravitating in the centre of the haloes before turning into stars (Benítez-Llambay et al., 2019). Unlike the original `EAGLE` model, the density threshold for star formation in our simulation does not depend on metallicity. The simulation includes gas cooling and heating by the external UVB, which is turned on at the redshift of reionization, $z_{\rm re} = 11.5$, and corresponds to that of Haardt and Madau (2001). We assume cosmological parameters consistent with early Planck results (Planck Collaboration et al., 2014).

Our mass resolution is ~ 100 higher than that of the original EAGLE suite, making our simulation particularly well-suited to resolve dwarf galaxy haloes with several hundred DM particles. The star particles have a mass identical to that of the gas particles, imposing a minimum galaxy mass in our model, $M_\star \sim 4.5 \times 10^4 \ M_\odot$. Dark matter haloes are identified in the simulation with the `HBT+` code (Han et al., 2018), which uses a catalogue of Friend-of-Friends (FoF) haloes constructed with a percolation length $b = 0.2$, in units of the mean interparticle separation, to carry out an unbinding procedure based on the gravitational binding energy of the particles. `HBT+` returns a catalogue of gravitationally-bound haloes, together with a list of particles (dark matter, stars, and gas) bound to each halo. `HBT+` also classifies haloes as either “centrals” or “satellites” based on whether the halo is the more massive substructure of the FoF group or not, respectively. We refer the reader to the original `HBT+` paper for extensive details on the algorithm.

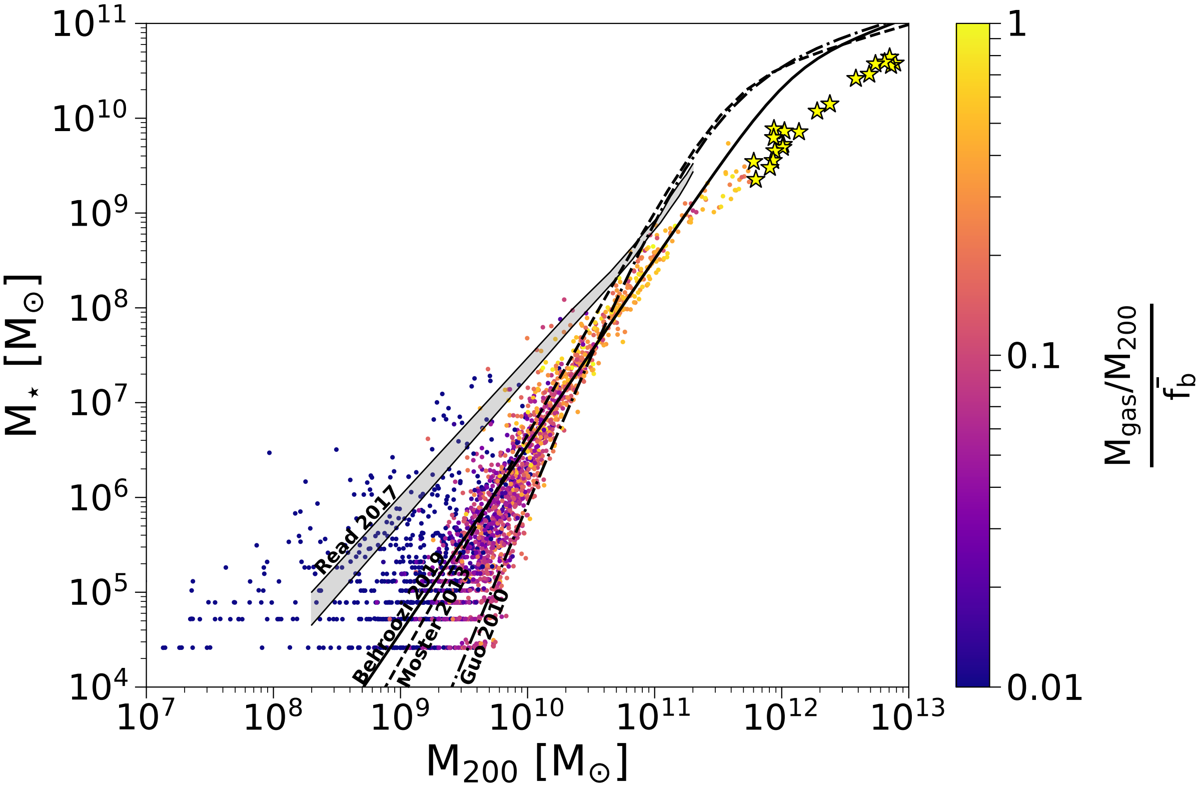

Figure 3.1: Present-day stellar mass, $M_\star$, as a function of virial mass, M_{200}, for the isolated galaxies identified in the simulation. Galaxies are coloured according to their virial gas mass fraction, $M_{\rm gas}/M_{200}$, relative to the universal baryon fraction, $\bar{f}_{\rm b} = \Omega_b/\Omega_m$. The various lines display different abundance matching expectations, as labelled. Yellow stars show the galaxies inhabiting the 20 most massive haloes of the simulation.

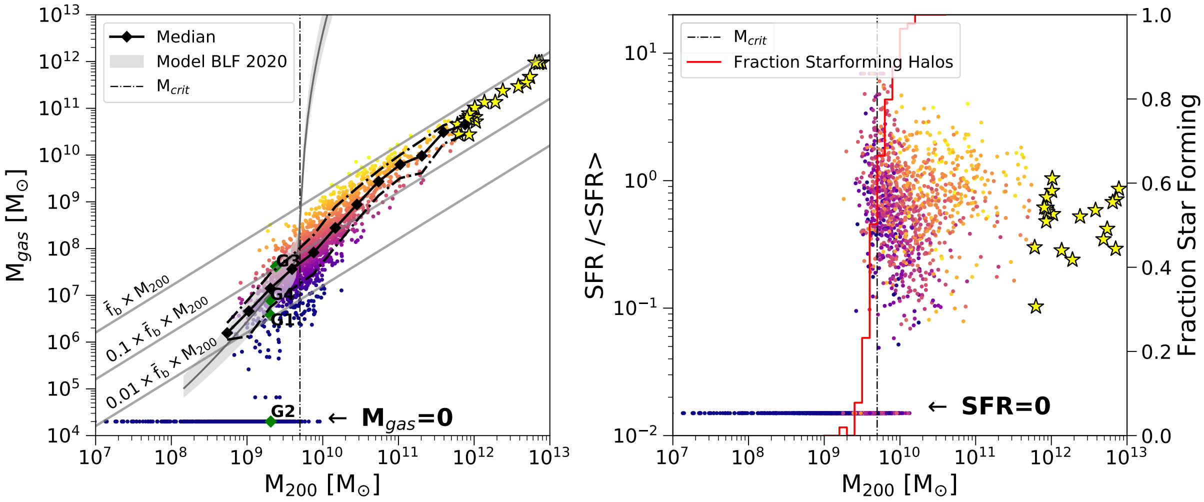

Figure 3.2: The left panel shows the present-day gas mass as a function of halo mass for our galaxy sample. We display galaxies with $M_{\rm gas} = 0$ with an arbitrarily low value (horizontal arrow). Galaxies are coloured as in Fig. 3.1, i.e., according to their gas mass fraction relative to the universal baryon fraction. The solid black line indicates the running median of the distribution for galaxies with $M_{\rm gas} > 0$, and the dot-dashed lines indicate the 16-84th percentiles, as measured in bins equally spaced logarithmically in mass (black symbols). The grey line and shaded region show the gas mass that results from applying the BL20 model. The vertical dot-dashed line indicates the critical virial mass above which gas cannot remain in hydrostatic equilibrium according to this model. The oblique lines display the universal baryon fraction, $\bar{f}_{\rm b} = \Omega_b/\Omega_m$, 10 per cent, and 1 per cent of this value. The green diamonds indicate four example galaxies (G1, G2, G3, and G4) that inhabit halos of the same mass today but contain very different gas masses. The right panel shows the star formation rate (SFR), in units of the past average, as a function of present-day halo mass. The red histogram shows the fraction of systems for which SFR>0 (scale on the right). We display galaxies with SFR $= 0$ with an arbitrarily low value (horizontal arrow). Galaxies less massive than the BL20 critical mass are quiescent, as expected. In both panels, the yellow stars indicate the 20 most massive systems in the simulation.

Sample selection

Our goal is to examine the current gas content of isolated dwarf galaxies. Therefore, we restrict our galaxy sample to systems labelled as "centrals" by `HBT+` at the present day. As opposed to satellite systems, central galaxies do not reside within the virial radius of more massive counterparts, by definition. In addition to the isolation criterion, we require the haloes to contain a galaxy, i.e., to have at least one bound stellar particle. These two conditions yield a population of central galaxies resolved with more than ~ 100 dark matter particles. After a detailed inspection of the galaxies' individual mass accretion histories, we removed 14 galaxies that were wrongly identified by `HBT+`. Our selection criteria thus result in 2268 galaxies that span the stellar mass range, $10^4 \lesssim M_\star/M_\odot \lesssim 10^{11}\ M_\odot$, and the halo mass range, $10^7 \lesssim M_{200}/M_\odot \lesssim 10^{13}$. As shown in Fig. 3.1, the stellar vs halo mass relation of the simulated galaxies is broadly consistent with abundance matching (AM) expectations from Moster et al. (2013), Read et al. (2017), Behroozi et al. (2019) and Guo et al. (2010) but only at low masses. Our simulated galaxies form too few stars compared to AM at high masses. This mismatch, however, does not preclude the results that follow, as we are interested in dwarf galaxies only.

3.2.3 Results

Present-day gas content of isolated simulated galaxies

The left panel of Fig. 3.2 shows the present-day bound gas mass of our galaxy sample as a function of virial mass. Galaxies are coloured according to their gas mass fraction, $f_{\rm b} = M_{\rm gas}/M_{200}$, relative to the universal mean, $\bar{f}_{\rm b} = \Omega_b/\Omega_m$ (shown by the top solid oblique line in the same panel). The black symbols indicate the running median and the 16-84th percentiles of the distribution (but only for galaxies for which $M_{\rm gas} > 0$). Except for a few systems, most galaxies in our simulation do not retain the universal baryon budget within their virial boundaries. Indeed, more than half of the systems at all masses have lost more than 2/3 of their baryons at $z = 0$[4]. For massive systems ($M_{200} >> 10^{10}\ M_\odot$), the loss of baryons is largely due to the effect of the efficient supernova feedback (see, e.g., Wright et al., 2020; Mitchell and Schaye, 2022, and references therein for a recent study on the baryon content of massive haloes in the EAGLE simulations). For less massive systems, the loss of baryons is exacerbated by their shallower potential wells and by the presence of the external UVB radiation field (e.g. Okamoto et al., 2008).

Supernova feedback is responsible, too, for the removal of baryons in low-mass systems, but only for haloes more massive than $M_{\rm crit} \approx 5 \times 10^9\ M_\odot$, for which gas becomes self-gravitating in the centre and forms stars (see Sec. 3.2.1, and the work of Pereira Wilson et al., 2022). For haloes with mass $M_{200} \lesssim M_{\rm crit}$ this is not the case, as we demonstrate in the right-hand panel of the same figure, where we show the star formation rate (SFR) of our galaxy sample, in units of the past average, as a function of present-day halo mass.

---

[4] Note that the contribution of the stars can be largely neglected to the virial baryonic budget (see Fig. 3.1).

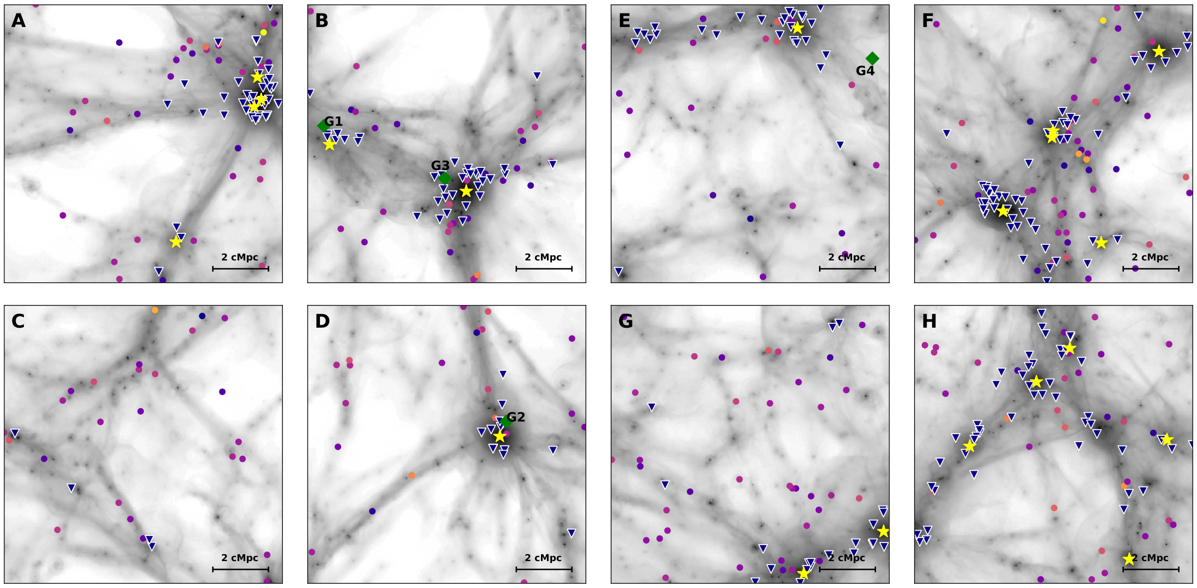

Figure 3.3: Spatial distribution of simulated galaxies spanning the narrow range in virial mass, $10^9 < M_{200}/M_{\odot} < 3 \times 10^9$, in cubic regions of 10 Mpc side length equally spaced to cover the entire simulated volume. Panels A, B, C, and D may be combined to form a slice spanning the coordinates range, $(x, y, z) = (0-20, 0-20, 0-10)$ Mpc, whereas panels E, F, G, and H may be combined to cover the remaining half of the box, i.e., $(x, y, z) = (0-20, 0-20, 10-20)$ Mpc. As in Fig. 3.2, we colour galaxies according to their present-day gas fraction relative to the universal baryon fraction. Yellow stars indicate the location of the 20 most massive galaxies in the simulation. The colour map in the background displays the projected gas density. Gas-deficient galaxies (blue triangles with white edges) cluster either along the filaments of the cosmic web or close to massive systems, in sharp contrast with the other galaxies in the same halo mass range. The strongly clustered distribution of gas-deficient galaxies thus points to the role of the environment in shaping their present-day gas content.

The star formation rate is simply defined as $\Delta M/\Delta t$, i.e., the ratio between the mass of stars formed within the galaxy radius, $R_{\rm gal} = 0.2 \times R_{200}$, in the last $\Delta t = 2$ Gyrs, and Δt. The past average is defined as $< \rm SFR >= M_{gal}/t_H$, where $t_{\rm H}$ is the Hubble time. We show galaxies that have not formed stars in this time interval with an arbitrarily low value indicated by the arrow at the bottom right of the same panel. The red solid line shows the fraction of galaxies, as a function of halo mass, for which SFR > 0 (scale on the right). This rough definition of SFR indicates that, on average, massive systems in the simulation have formed stars at a constant rate in the past few billion years. Galaxies inhabiting haloes with masses $M_{200} \lesssim M_{\rm crit}$, on the other hand, have not formed stars in the same time interval. Thus, the systematic reduction in their gas content compared to more massive systems cannot be due to the effect of supernova feedback. The transition between star-forming and quiescent dwarfs occurs close the BL20 critical mass (shown by the vertical dot-dashed line), below which gas remains in hydrostatic equilibrium.

The thin grey solid line in the left-hand side panel of Fig. 3.2 shows the gas mass as a function of halo mass that results from the BL20 model. This model derives the gas mass of a dark matter halo after assuming that the gas is in thermal equilibrium with the external UVB and in hydrostatic equilibrium with a Navarro-Frenk-White (NFW; Navarro et al. 1996, 1997) halo. To derive the gas mass, the model further assumes that the gas pressure sufficiently far from the system is that of the intergalactic medium at the mean density of the Universe, $\bar{\rho}_{\rm b}$. The grey shaded region shows the expected gas mass for haloes embedded in an environment three times over/under-dense (top/bottom envelopes). The agreement between the median gas mass of galaxies with $M_{\rm gas} > 0$ and the model demonstrates that the gas mass of galaxies inhabiting haloes with mass, $M_{200} \lesssim M_{\rm crit}$, is indeed established by the effect of the external photoheating background,[5] and offers the physical explanation as to why these galaxies have not been forming stars for such a long time. Interestingly, some of these quiescent galaxies do not contain gas bound to them (see the left panel in Fig. 3.2), or when they do, their gas content departs significantly from that expected for isolated galaxies. The gas mass of these galaxies is thus neither established by the external UVB nor by supernova-driven winds.

Defining gas-deficient systems as galaxies whose present-day gas fraction is $M_{\rm gas}/M_{200} < 0.01 \times \bar{f}_{\rm b} = 0.01 \times \Omega_b/\Omega_m$, does a good job at splitting our galaxy sample between normal systems (those galaxies whose gas mass is well-understood in terms of the BL20 model), and gas-deficient systems. Therefore, we shall adopt this definition in what follows. We address the origin of these gas-deficient galaxies next.

Role of environment in establishing the present-day gas content of field dwarf galaxies

Fig. 3.3 provides clues to the origin of the population of isolated, quiescent, and gas-deficient galaxies. Here we show the spatial distribution of dwarfs inhabiting the narrow range in halo mass, $10^9 \lesssim M_{200}/M_\odot \lesssim 3 \times 10^9$, in cubic regions of 10 Mpc side length

---

[5] We note that the gas mass of subcritical halos depends weakly on the assumed photoheating background (see, e.g., Benítez-Llambay et al., 2017).

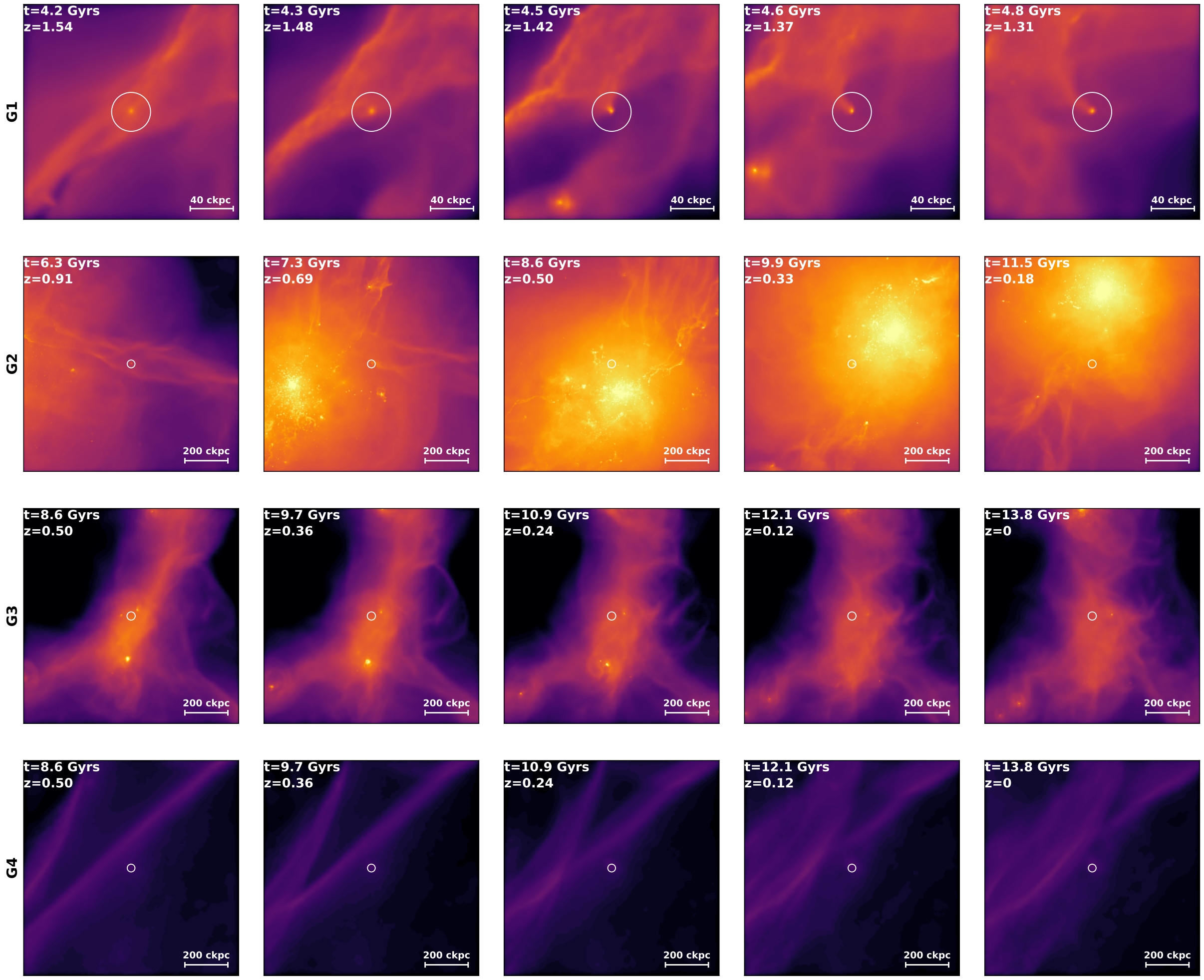

Figure 3.4: Time evolution of 4 individual simulated dwarf galaxies. Different rows show the projected gas density around each dwarf at various times. The white circle indicates the virial radius of the galaxy. The first row shows the evolution of G1, which loses its gas by cosmic web stripping. The second row displays G2, which, although an isolated system today, approached a massive system in the past and lost gas and dark matter via tidal and ram pressure forces. The third row shows the evolution of G3, a galaxy embedded in a dense but otherwise isolated environment, in contrast to G4 (fourth row), which evolves in a less dense but isolated environment.

taken from the parent volume. We colour galaxies as in Fig. 3.2 (i.e., according to their gas fraction relative to the cosmic mean). The colour map in the background shows the projected gas density.

Interestingly, gas-free dwarfs (blue triangles with white edges) cluster preferentially in the surroundings of massive systems (shown by yellow stars), albeit further away from their virial radius, by construction. In contrast, the rest of the galaxies reside further away from the overdense regions depicted by the most massive systems in the volume. Consider, for example, panel C of Fig. 3.3, where we can hardly identify gas-free haloes. This particular region of our simulation lacks massive galaxies and prominent large-scale gaseous structures. A similar analysis applies to panel G, where only very few gas-free dwarfs are found at the bottom right corner of the volume, a region that contains two massive galaxies and a prominent filament that connects them. If we focus on panel H, we see that gas-free galaxies cluster around the five massive galaxies present in this volume or depict the location of dense gaseous filaments. The rest of the normal galaxies in terms of their gas fraction, i.e., those whose gas mass is roughly consistent with simple analytic expectations, lie further away from overdense regions. A similar analysis holds to the remaining volumes. Thus, it is tempting to ascribe the dichotomy in the gas mass to the characteristic environment surrounding each dwarf. In the next section, we analyse four individual examples in detail.

Individual examples

To demonstrate how the different environments, together with the past evolution of field galaxies, shape their current gas mass, we shall consider four individual examples that exhibit disparate present-day gas contents. These are labelled G1, G2, G3, and G4. As shown by the green diamonds in the left panel of Fig. 3.2, these galaxies are selected to inhabit dark matter haloes with virtually the same mass today but with very different gas mass.

Past encounter with a massive system: First, consider galaxy G2, which inhabits a halo currently devoid of gas. This galaxy locates, similarly to the rest of the gas-free galaxies, in the surroundings of a more massive companion (see panel D in Fig. 3.3). The second row from the top in Fig. 3.4, which shows the evolution of G2 since redshift, $z = 0.91$, makes it clear that the galaxy formed in relative isolation until $z \sim 0.5$, when it encountered a massive companion. This close encounter is responsible for removing, via both ram-pressure and tidal stripping, the gas content of G2. G2 is thus an example of a system usually referred to as “flyby” or “backsplash” galaxy in the context of galaxy clusters (see, e.g., Balogh et al., 2000; Mamon et al., 2004; Gill et al., 2005, for earlier discussions on these galaxies), but which are known to be associated with smaller systems as well (e.g. Sales et al., 2007; Knebe et al., 2011b). These are galaxies that have interacted with a massive system in the past and are now on very eccentric orbits that may reach apocentric distances several virial radii away from their host.

We show the evolution of G2 quantitatively in the top right panel of Fig. 3.5. The dark matter, gas and stellar mass are displayed by the black solid, dashed, and dot-dashed lines, respectively. The red line indicates the baryon fraction in units of the cosmic mean (scale on the right). The grey shaded region displays the time interval shown in Fig. 3.4. As G2 forms stars early on, the combined effect of supernova feedback and the UVB removes roughly 80 per cent of the baryons from the system. As G2 approaches the massive companion at around $z = 1$, it starts losing dark matter and the remaining gas. Some of the gas compresses during the interaction, leading to the formation of stars. G2 thus ends up being devoid of gas at $z = 0$. We conclude that the interaction with a massive companion at around $z = 1$ is responsible for G2's extreme deficit of gas relative to the rest of the dwarfs in the similar virial mass range.

Cosmic Web Stripping: We now focus on galaxy G1, which inhabits a gas-deficient halo whose gas mass departs significantly from the value expected for its halo mass (see Fig. 3.2). Unlike G2, galaxy G1 is much further away from a massive companion than galaxy G2. A close inspection of the evolution of this galaxy reveals the origin of its current deficit of gas compared to other galaxies of similar virial mass. The top row of Fig. 3.4 shows that galaxy G1 formed in relative isolation until it was swept by a gaseous filament or sheet at $z \sim 1.5$. The ram pressure exerted on G1 by this gaseous structure removes most of G1's gas, which is left in a prominent tail behind the galaxy. Note, however, that G1 does not lose all its gas. Even after the interaction, a small amount of dense gas remains deep in the centre of G1, which is however unable to form stars. G1 is thus an example of a galaxy undergoing cosmic web stripping, as described by BL13.

In the top left panel of Fig. 3.5 we show the evolution of the dark matter, gas, and stellar content of G1. The gas mass fraction of G1 is roughly consistent with the universal mean, $\bar{f}_{\rm b} = \Omega_b/\Omega_m$, prior to cosmic reionization. However, the gas is quickly pushed away from the halo as the universe undergoes reionization and the interstellar medium is photoheated. This is expected, as G1 inhabits a dark matter halo less massive than the BL20 critical mass (shown by the blue line). As G1 approaches a dense filament, its gas compresses, enabling G1 to form stars even though G1 inhabit a halo less massive than the critical mass (see Wright et al., 2019; Pereira Wilson et al., 2022, for similar examples). This star formation episode is responsible for the sudden loss of baryons observed between $z = 3$ and $z = 2$, in which G1 loses almost half of its baryons. As G1 crosses the filament at around $z \sim 2$, it loses more than 3/4 of the remaining gas. The lack of star formation after $z \sim 2$ indicates that the loss of gas after this time is not associated with supernova feedback but with the encounter of the dense filament or sheet of the cosmic web seen in Fig. 3.4. After the relatively abrupt loss of gas during the interaction with the dense filament, G1 continues to lose gas steadily as it moves through the ambient gas until the present day.

The impact of the ambient density: Finally, galaxies G3 and G4 have gas masses roughly consistent with that expected for their halo mass, but G3 has retained more gas than G4 to the present day. As shown in Fig. 3.4, the difference between the two galaxies may be ascribed to their environment. Both dwarfs have evolved in relative isolation, away from the massive galaxies of the simulated volume. However, G3 resides in a denser environment than that of G4[6]. As shown by BL20, the environment that surrounds a sub-

---

[6] The colour scale is the same for G3 and G4. Therefore, it is possible to visually asses the relative

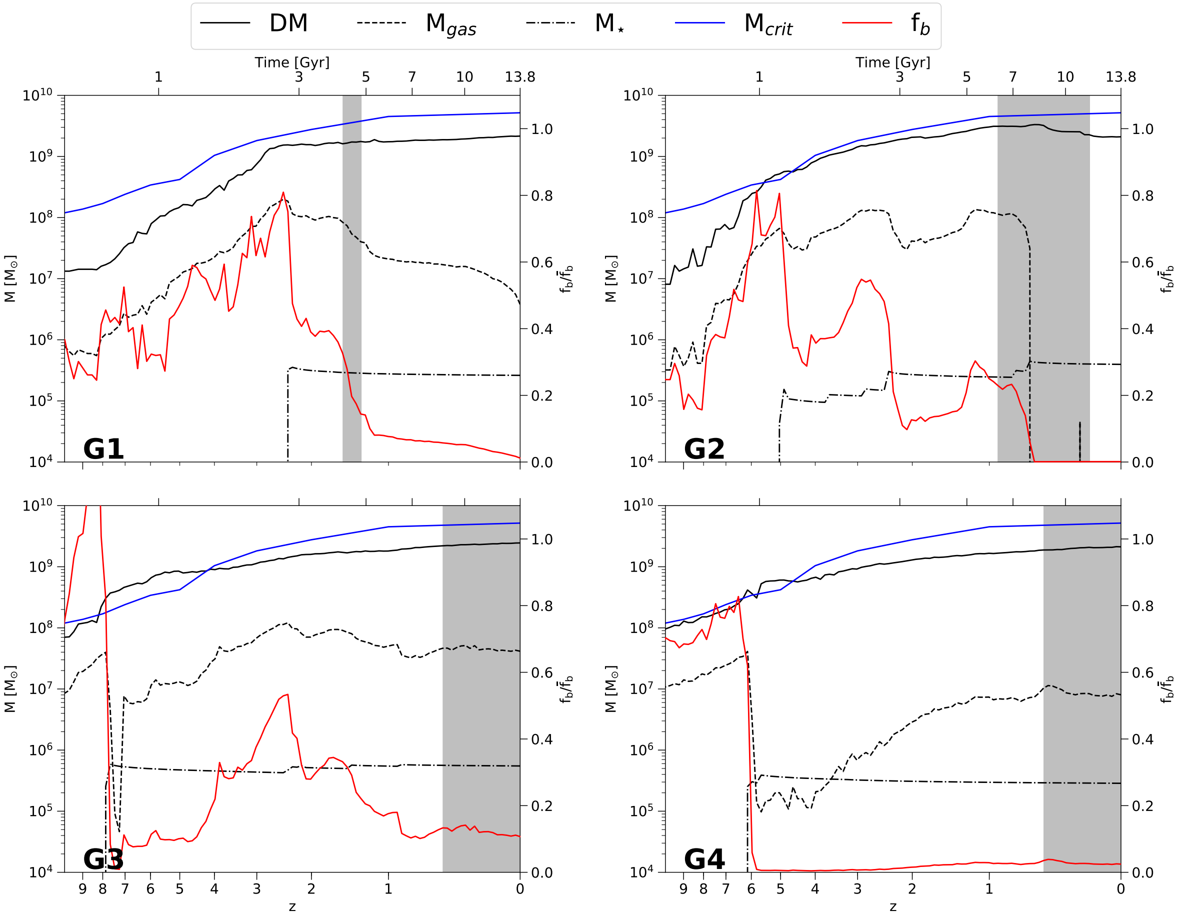

Figure 3.5: Mass assembly histories of the four individual dwarfs shown in Fig. 3.4. The black-solid, dashed, and dot-dashed lines show the dark matter (DM), gas, and stellar mass, respectively. The blue line corresponds to the critical mass for the onset of star formation, as predicted by the BL20 model. The red line shows the baryon fraction, $M_{\rm gas}/M_{200}$, in units of the universal baryon fraction (scale on the right). The grey shaded area spans the time interval shown for each dwarf in Fig. 3.4.

critical halo with mass, $M_{200} \lesssim M_{\rm crit}$, impacts its inner gas content (see Eq. 5 in BL20). Therefore, sub-critical haloes that form and evolve in denser environments have more gas at a fixed halo mass than similar haloes residing in underdense regions. The shaded region in the left panel of Fig. 3.2 shows the gas mass that results from applying the BL20 model but assuming a universe that is over/underdense by a factor of 3. We have verified in our simulation that the inner gas content of the haloes correlates with the mean density outside the haloes, indicating that the scatter in gas mass is due, to some extent, to the ambient pressure around the haloes (see Ch. 3.2.4). The observed scatter around the median gas mass at fixed halo mass for sub-critical haloes is thus likely due to fluctuations of the ambient gas density relative to the mean.

The lower panels of Fig. 3.5 show that G3 and G4 undergo an initial burst of star formation after which both galaxies lose most of their baryons. As galaxy G3 inhabits a denser environment than G4, it can accrete more gas after the initial episode of star formation. At around $z \sim 3$, a further star formation event removes some gas from the galaxy. The gas mass of G3 finally stabilises at about $M_{\rm gas} \sim 5 \times 10^7\ M_\odot$, a higher value than that expected for its halo mass. Note that G3 has maintained this configuration for roughly half of the Hubble time, implying that its current gas mass is not related to its past star formation, but to its environment, and the balance between the gas pressure and the halo gravity. Focusing on G4, we see that its initial star formation drives most of the baryons out of the system. Although some gas recovers secularly over a long timescale, the gas mass equilibrates at $M_{\rm gas} \sim 10^7$ at around $z \sim 1.5$ and remains constant until the present day. Therefore, as both galaxies have identical virial masses and have been quiescent for most of their lifetimes, their different present-day gas masses must stem from the different environments they inhabit today.

Flyby galaxies

The clustering of gas-deficient galaxies around massive companions shown in Fig. 3.3 together with the time evolution of G2 shown in the second row of Fig. 3.4 suggests that a significant fraction of gas-deficient galaxies must be flybys.

As shown in Fig. 3.5, a distinctive feature of these flyby galaxies is that they lose both gas and dark matter as they approach a massive companion. Indeed, galaxy G2 has lost all its gas and ~ 30 per cent of its dark matter.

Empirically, we find that flybys can be told apart from other galaxies in our simulation by requiring them to be present-day central galaxies that have lost dark matter in the past. Furthermore, we find that all these flybys were closer than $d < 1.5 \times R_{200}$ of the eventual host, in good agreement with previous work (see, e.g., Behroozi et al., 2014). Given these arguments, we define flyby galaxies in our simulation as present-day central systems that have lost more than 20 per cent of their dark matter and that were within $1.5 \times R_{200}$ of another galaxy at some point during their evolution. These criteria yield 328 galaxies that, similarly to G2, have had a relatively strong interaction with a massive system in the past.

---

difference in the ambient density each dwarf resides.

Fig. 3.6 shows that our classification criteria have interesting consequences. The top panel of this figure shows the present-day gas mass as a function of halo mass for our galaxy sample. We show flyby galaxies with open cyan circles. Interestingly, at a fixed stellar mass flybys inhabit lower mass haloes than non-flyby counterparts. This dark matter deficit originates from the tidal interaction between the flybys and the eventual host. Secondly, as shown in the bottom panel of the same figure, most flybys have lost all the gas. Thirdly, flybys cluster today near massive systems, as shown in Fig. 3.7. This figure is analogue to Fig. 3.3, but we only display the location of the flyby galaxies that result from our selection criteria. Flybys depict well the location of the 20 most massive systems of our simulation, shown by yellow stars. Finally, a minority of flybys lie well beyond the virial radius of massive systems. For example, towards the top left corner of panel H in Fig. 3.7 we find a flyby galaxy located beyond 2 Mpc from all massive hosts in the simulation, making it difficult to associate this flyby to a host from its present-day location. In a recent work, Benavides et al. (2021) reported similar examples.

We thus conclude that a significant number of simulated isolated gas-deficient galaxies are flybys that have interacted with a massive companion in the past. We will quantify the contribution of these galaxies to the population of gas-deficient galaxies in Sec. 3.2.4.

Cosmic-Web Stripped (COSWEB) galaxies

Having established the reason behind the gas deficit for a significant fraction of the sample of gas-deficient galaxies, we now focus on the remaining gas-deficient galaxies that are not flybys. We show these systems with red open circles in Fig. 3.8. This figure, which is analogue to Fig. 3.6 but in which we removed flybys, demonstrates that not all the gas-deficient galaxies are flybys. Indeed, after removing flybys, there is still a sizeable population of 231 gas-deficient systems that have not interacted with massive systems in the past. The gas deficit of most of these galaxies cannot be due to the effect of supernova feedback. Indeed, most of these systems inhabit sub-critical dark matter haloes, implying they have been quiescent for a long time (see right panel of Fig. 3.2). These systems, albeit gas deficient today, are similar to other simulated systems in terms of their stellar mass (see the top panel). What is the reason behind the deficit of gas for these dwarfs?

Fig. 3.9 shows the spatial distribution of the gas-deficient galaxies that are not flybys. Interestingly, these galaxies cluster less than flybys towards the massive systems of our simulation, and they predominantly depict the location of the filaments and sheets of the cosmic web (see, e.g., panels D, E, H). Galaxies visually close to a massive host in our simulation are typically on their first infall, so they have not yet lost dark matter via tidal stripping. A visual inspection of the evolution of these systems through movies of their surrounding gas distribution made with the Py-SPHViewer code (Benitez-Llambay, 2015), together with the analysis of their individual mass assembly histories, revealed that they are all analogues of galaxy G1 (shown in the first row of Fig. 3.4), i.e. these are systems that have lost their gas through hydrodynamic interactions with the cosmic web and denser gaseous structures which are not obviously associated with gaseous galaxy haloes. The only exception are ten galaxies that become gas-deficient due to SN feedback. We, therefore,

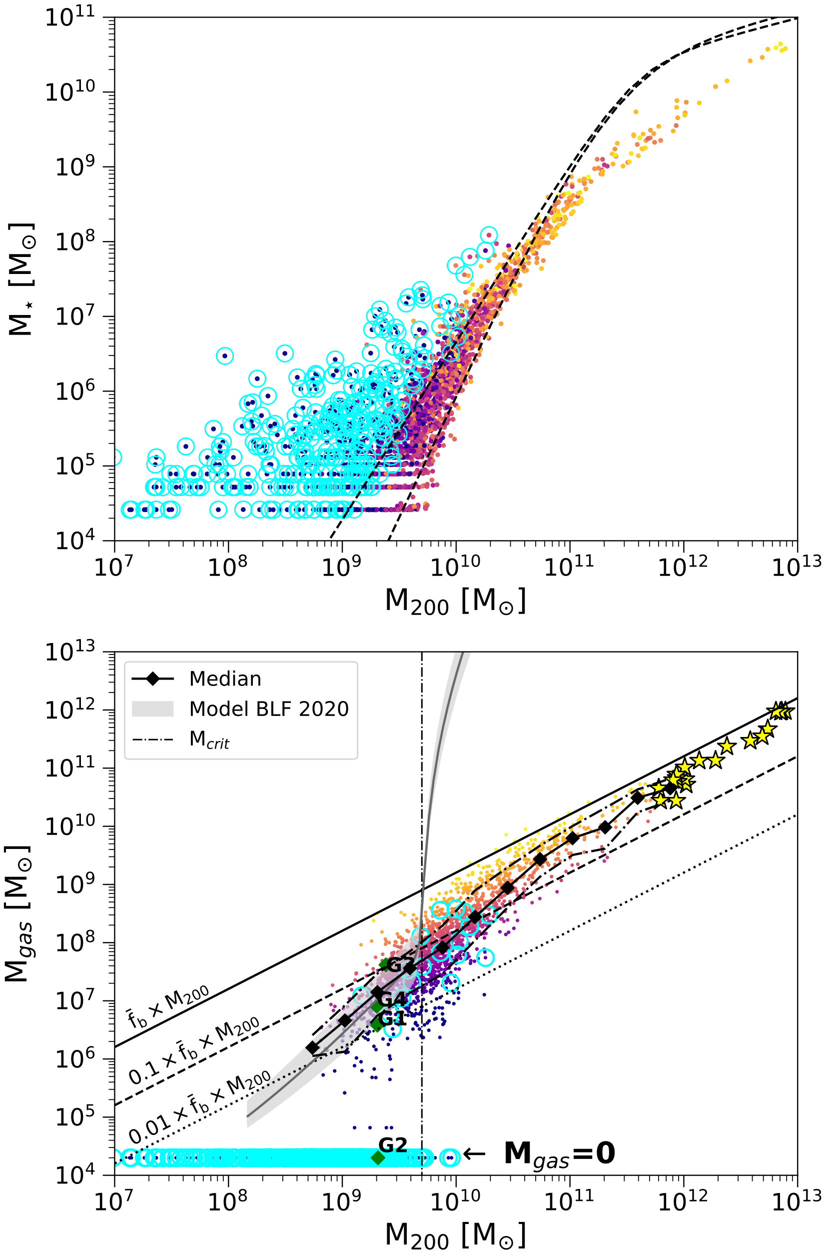

Figure 3.6: The top panel, analogous to Fig. 3.1, shows the present-day stellar mass versus halo mass for our galaxy sample. The cyan circles indicate flyby galaxies, as defined in Sec. 3.2.3. Interestingly, flybys scatter off the stellar mass versus halo mass relation followed by non-flybys. The lower panel, analogous to Fig. 3.2, shows the current gas mass as a function of halo mass. As in Fig. 3.2, we show gas-free galaxies with an arbitrary gas mass value, $M_{\rm gas} = 2 \times 10^4$ $M_\odot$. The majority of flybys (cyan circles) are essentially devoid of gas.

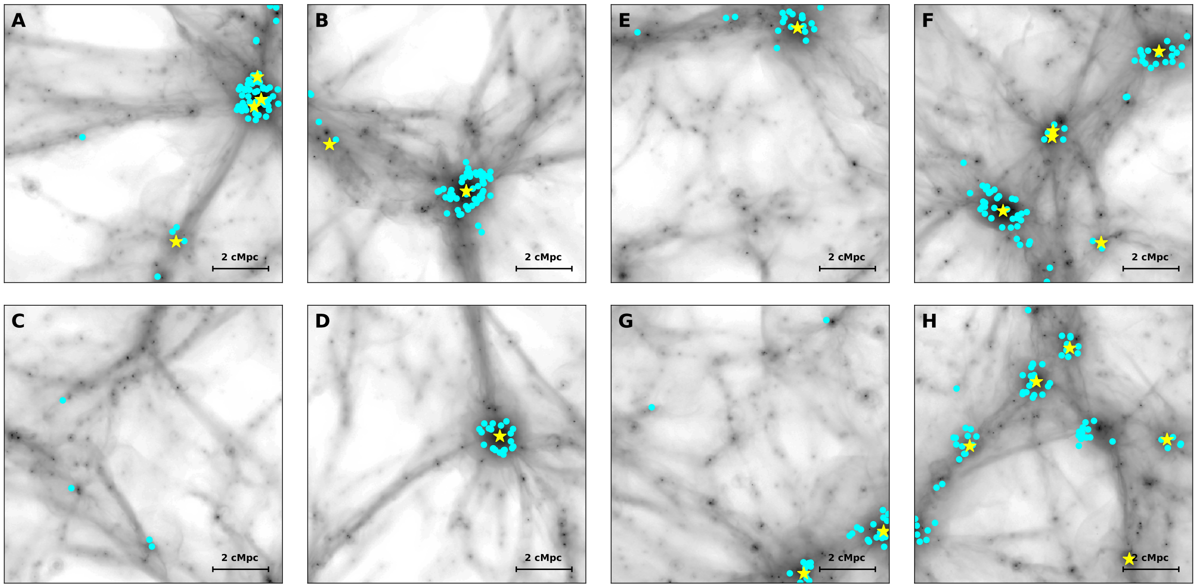

Figure 3.7: Analogous to Fig. 3.3, but we now display the spatial distribution of flyby galaxies (cyan symbols), as defined in Sec. 3.2.3. Flyby galaxies exhibit a characteristic clustering pattern towards the more massive systems of the simulation (yellow stars).

conclude that our methodology captures the underlying physics responsible for removing gas from the system well. Because of this, we shall define cosmic-web-stripped (COSWEB) galaxies as gas-deficient galaxies that have lost their gas via ram pressure in the past and are far from other halos. This definition results in 221 COSWEB galaxies (i.e., all but 10 gas-deficient galaxies that are not flybys).

3.2.4 Discussion

In the previous sections, we demonstrated that the present-day population of field gas-deficient galaxies originates from either a close interaction with a massive host in the past (flybys) or ram-pressure stripping with the cosmic web (COSWEBs). The difference between flybys and COSWEBs becomes evident in their clustering properties. Flybys cluster towards the most massive galaxies present in our simulation. COSWEBs, on the other hand, are more dispersed throughout the simulation volume, preferentially depicting the location of the gaseous filaments and sheets of the cosmic web. What is the relative contribution of flybys and COSWEBs to the population of present-day gas-deficient galaxies, i.e., galaxies whose gas mass fraction is $M_{\rm gas}/M_{200} < 0.01 \times \Omega_b/\Omega_m$?

In Fig.3.10 we show the fraction of gas-deficient galaxies (black line) as a function of halo mass. The fraction of gas-deficient galaxies reaches unity below the halo mass $M_{200} \lesssim 5 \times 10^8\ M_\odot$ because the gas mass of every dark matter halo eventually falls below $M_{\rm gas} < 0.01\,(\Omega_b/\Omega_m)\,M_{200}$, which is the maximum gas mass below which galaxies become

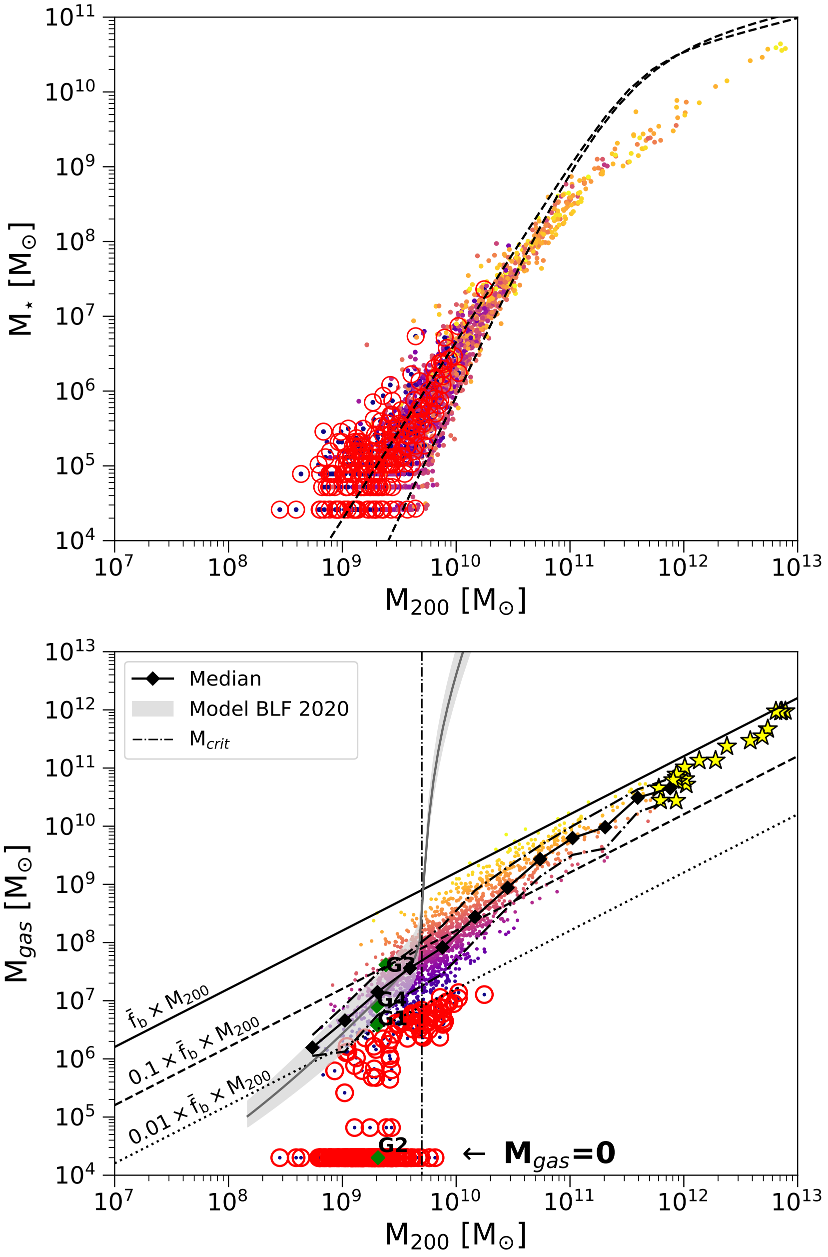

Figure 3.8: The top panel, analogous to Fig. 3.1, but in which we removed flyby galaxies, shows the present-day stellar mass as a function of halo mass for our galaxy sample. The red circles indicate COSWEB galaxies, as defined in Sec. 3.2.3. The lower panel, analogous to Fig. 3.2, shows the gas mass as a function of halo mass for all galaxies but flybys. As in the top panel, we show COSWEBs with red circles. Gas-free galaxies are indicated with a lower gas mass, $M_{\rm gas} = 2 \times 10^4$ $M_\odot$.

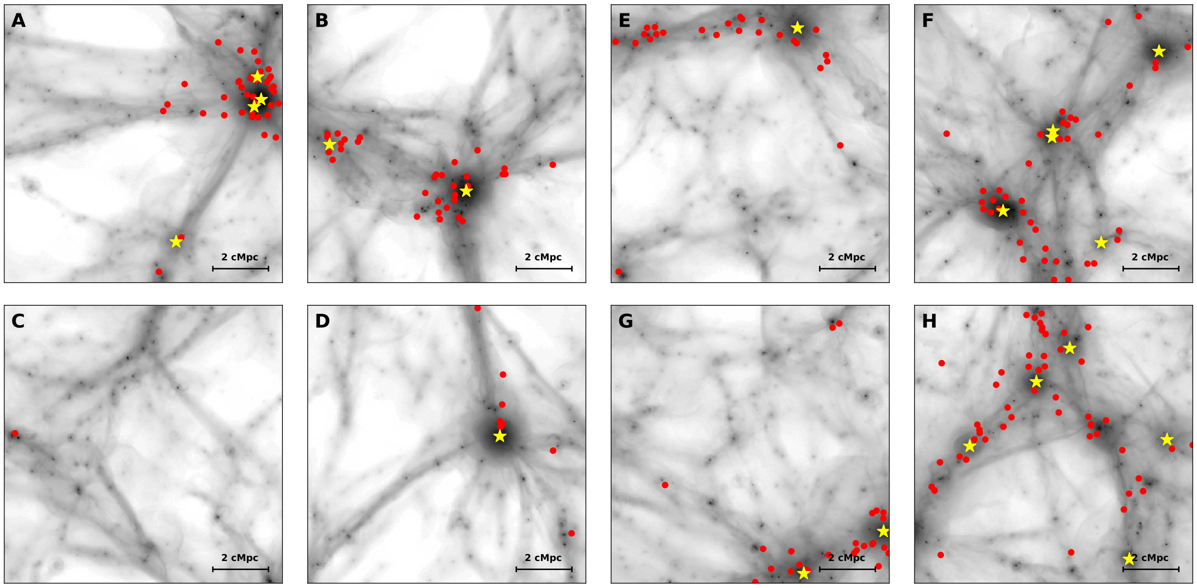

Figure 3.9: Analogous to Fig. 3.3, but we now display the spatial distribution of COSWEB galaxies only (red symbols), as defined in Sec. 3.2.3. COSWEBs exhibit much less clustering towards massive systems (yellow stars) than flybys (see Fig. 3.7), and they depict the location of the filaments of the cosmic web well. We have verified that those COSWEB galaxies close to a massive system today are approaching the host for the first time. These galaxies have been stripped of their gas several virial radii away from the massive systems, so their gas removal is not directly related to ram-pressure exerted by the host's hot gaseous halo.

gas-deficient in our definition. In addition, the limited resolution of our simulation makes the gas content of halos with mass $M_{200} \lesssim 10^9\ M_\odot$ only marginally resolved. Indeed, the BL20 model indicates that the average gas mass of dark matter halos of mass $M_{200} \sim 10^9\ M_\odot$ is $M_{\rm gas} \sim 10^6\ M_\odot$, or ~ 20 gas particles in our simulation, so we caution not to overinterpret results in this regime. However, for masses $M_{200} > 10^9\ M_\odot$, we expect the fraction of gas-deficient galaxies to be robust.

Next, we quantify the relative contribution of flybys and COSWEBs to the population of present-day gas-deficient galaxies. We show this in Fig. 3.10, where the fraction of flybys and COSWEBs, relative to the population of gas-deficient galaxies, are indicated by the blue and red histograms, respectively. COSWEBs dominate over flybys at higher masses. However, less than 10 per cent of the field galaxies (but essentially all gas-deficient galaxies) are COSWEBs today for halo masses $M_{200} \gtrsim 5 \times 10^9\ M_\odot$, as only a negligible fraction of galaxies are flybys within the same mass range. The lack of massive flybys is not surprising, as these galaxies, unlike COSWEBs, have all lost dark matter, thus biasing the population of flybys towards lower masses. The contribution of COSWEBs peaks at around $M_{200} \sim 10^9 M_\odot$, making up roughly 35 per cent of the field galaxies (and half of the gas-deficient galaxies) at that mass before vanishing below a halo mass $M_{200} \lesssim 3 \times 10^8\ M_\odot$, which is the limit where galaxies stop forming in our simulation (Benitez-Llambay and Frenk, 2020; Benitez-Llambay and Fumagalli, 2021). In contrast, the contribution of flybys becomes more relevant with decreasing halo mass, which is not surprising. Indeed, galaxies can form in our simulation only in haloes that exceed the atomic cooling limit, which imposes a minimum halo mass to host a galaxy today of $M_{200} \gtrsim 3 \times 10^8\ M_\odot$. The only way a galaxy can inhabit a halo less massive than this critical mass in our simulation is by decreasing the halo mass, as is the case for flybys.

The details of our analysis may be influenced, to some extent, by the specifics of our definitions or the modelling included in our simulation. Indeed, some of our COSWEB galaxies could be classified as flybys if we made our classification criteria less stringent. However, this would only reduce the number of COSWEBs galaxies in our simulation. Thus, we can safely and robustly conclude that cosmic web stripping affects the gas content of less than 10 per cent of the simulated galaxies that would otherwise be able to foster star formation. These are galaxies with virial mass $M_{200} \gtrsim 5 \times 10^9\ M_\odot$, above which gas, if available, can collapse and form stars. Also, although cosmic web stripping is a rare process for massive dwarfs, it dramatically affects the gas fraction and the ability to form stars in most affected dwarfs. We have verified that more than 70 per cent of massive COSWEBs that inhabit haloes that could sustain star formation today, i.e. those with $M_{200} \gtrsim 5 \times 10^9\ M_\odot$, are quiescent at the present day due to the lack of gas. These are the systems shown with zero SFR to the right of the critical mass (vertical line) in the right panel of Fig. 3.2. It is interesting to see that essentially none of the massive COSWEB galaxies lose all the gas after interacting with the cosmic web. In all cases, a small amount of gas remains in the centre. This remnant originates after cosmic web stripping removes the outer low-density gas, causing the gradual expansion of the inner dense star-forming gas. Thus, the lack of a cold molecular phase in our simulation does not prevent the gas from reaching high enough densities and resisting the ram pressure. However, assessing the importance of the cold phase to the present-day properties of the COSWEB dwarfs requires dedicated simulations that include the explicit treatment of molecular cooling.

The scarcity of massive COSWEBs contrasts sharply with the 80 per cent fraction found by BL13 within a similar halo mass range in a simulation of the formation of the Local Group. The low fraction of massive COSWEBs in our simulation thus indicates that the effect of cosmic web stripping is small over cosmological scales, affecting roughly 1 in 10 massive dwarfs in the field. We note, however, that the BL13 results may indicate that cosmic web stripping is a more frequent process nearby biased regions, such as the Local Group, whereas our results asses the average importance over cosmological scales. Fig. 3.9, together with Fig. 3.7 and Fig. 3.3, reveal that the sheer number of COSWEBs and flybys really depends on the environment. However, we do not find any region in our simulation containing a fraction of COSWEB as high as that found by BL13. Therefore, we believe that the discrepancies largely arise from the biased region studied by these authors, which is constrained and departs from a random ΛCDM realisation, together with the reduced number of dwarfs they consider.

Also, it is interesting to see that cosmic web stripping can promote star formation in some systems, at least for some time. We do not quantify this, but our simulation contains example dwarfs inhabiting haloes with mass under the critical mass whose gas is compressed by the cosmic web, thus triggering star formation. Galaxy G1 is an example (see Fig. 3.5). Using simulations of the formation of the Local Group, Pereira Wilson et al. (2022) have recently pointed out similar examples. These results agree qualitatively with Wright et al. (2019), who find that interactions with the cosmic web can promote star formation in dwarf galaxies.

For less massive dwarfs, cosmic web stripping becomes a more frequent process. However, we expect it to have only a minor impact on the galaxy, as these galaxies have already lost most of their gas due to the effect of the UVB radiation field. The remaining small amount of gas is in hydrostatic equilibrium and unable to condense to the centre to form stars. Although the loss of gas in these low-mass galaxies has little importance for their evolution, it may have observational implications for their detection in the next-generation HI surveys. Benítez-Llambay et al. (2017) have shown that these small haloes can contain HI masses $M_{\rm HI} \gtrsim 10^3~M_\odot$, and reach column densities $N_{\rm HI} \gtrsim 10^{18}~{\rm cm}^{-2}$. This value is below current threshold limits for detectability but may well be reached in the future with upcoming instruments.

Environment

To investigate the reason for the scatter in gas mass for galaxies that are neither flybys nor COSWEBs, we now consider the “ambient” gas density. We define the “ambient” gas density as the mean density of a shell centred at each galaxy, and located between $2 \times R_{200}$ to $3 \times R_{200}$. The left panel of Fig. 3.11 shows the gas mass, as a function of halo mass, for our galaxy sample, colouring galaxies according to their “ambient” density relative to the mean baryon density of the Universe. Interestingly, at fixed halo mass, galaxies with higher gas mass display higher values of “ambient” density, whereas the opposite is true

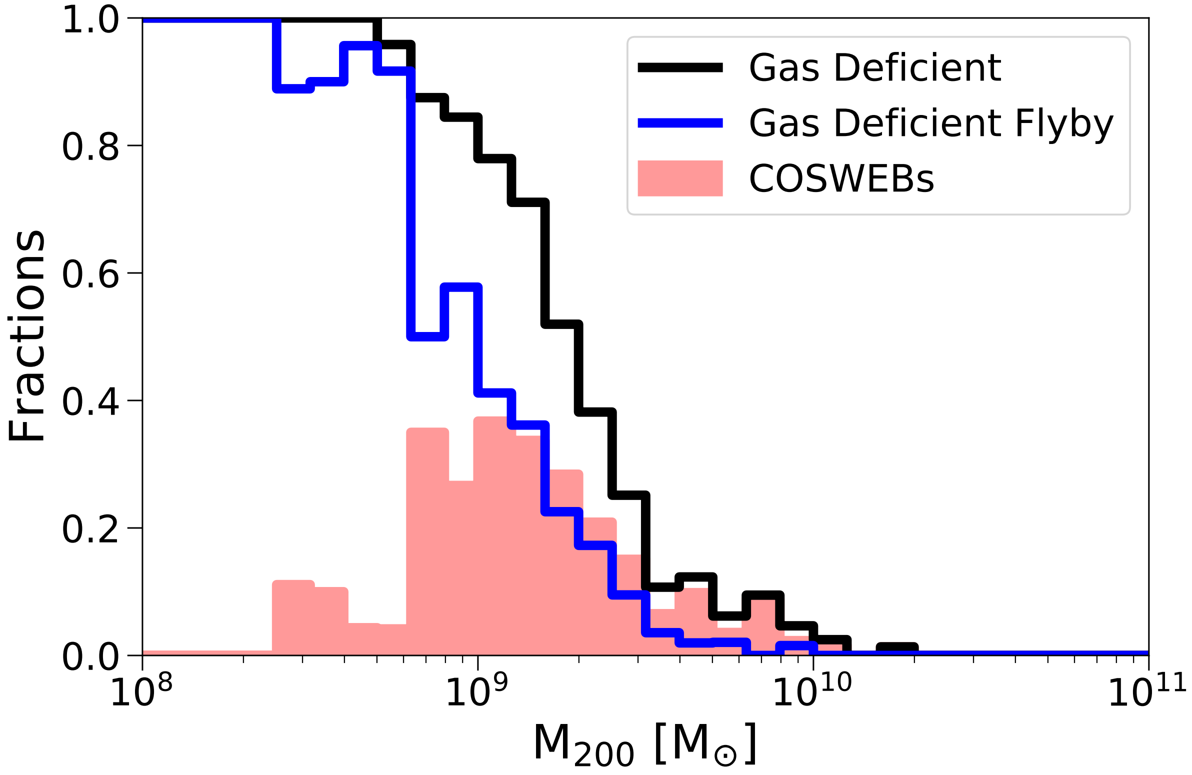

Figure 3.10: Fraction of gas-deficient (black line), flyby (blue line), and COSWEB (red area) galaxies, as a function of halo mass. We define gas-deficient galaxies as those whose virial gas mass fraction is under 1% of the universal baryon fraction, $\bar{f}_{\rm b} = \Omega_{\rm b}/\Omega_m$. For consistency, we only considered those flyby galaxies that are also gas-deficient. We, therefore, excluded only 17 flybys that do not fulfil this requirement. Below a halo mass, $M_{200} \sim 5 \times 10^8$ $\mathrm{M}_\odot$, all galaxies become gas deficient (see text for a discussion on this). Below a halo mass, $M_{200} \sim 3 \times 10^8$ $\mathrm{M}_\odot$, all gas-deficient galaxies become flybys.

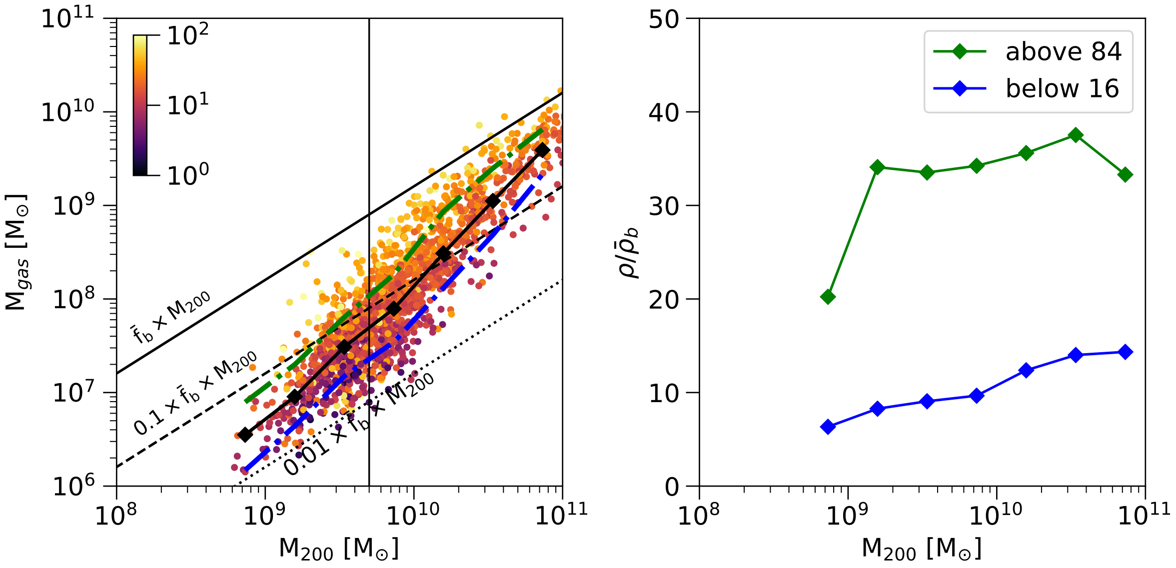

Figure 3.11: The left panel shows the gas mass as a function of halo mass for our galaxy sample, excluding gas-deficient galaxies. Galaxies are coloured according to their "ambient" density, i.e., the mean gas density within a shell between 2 to 3 times the virial radius of the systems, in units of the mean density of the Universe. The coloured lines show the median and the 16-84th percentiles of the distribution. The oblique lines show the expected gas mass for haloes that have retained the universal baryon fraction (solid line), 10% of this value (dashed line), and 1% (dotted line). The vertical line shows the BL20 critical mass. The right panel shows the median "ambient" density relative to the mean baryon density of the Universe, as a function of halo mass, for galaxies whose gas mass is above the 84th percentile (green line), and for galaxies whose gas mass is under the 16th percentile (blue line). The difference in "ambient" density between gas-rich and gas-poor galaxies indicates that the gas mass of these halos is affected, to some extent, by the amount of gas located beyond the virial radius of the systems.

for galaxies with low gas mass.

In the right panel of Fig. 3.11, we quantify the difference in the "ambient" gas density between gas-rich and gas-poor galaxies as a function of halo mass. To this end, we display the median "ambient" density relative to the mean baryon density of the Universe for the galaxies with gas mass above the 84th percentile (green line in the top panel), and for those with gas masses below the 16th percentile (blue line in the top panel). The median "ambient" density for galaxies with a high gas mass almost triples that of low gas mass galaxies. This factor, albeit smaller than the scatter in gas mass, indicates that the gas mass within the haloes is determined, to some extent, by the environment that surrounds the haloes, as expected from the simple arguments of Benitez-Llambay and Frenk (2020).

Comparison with Observations

So far our model of galaxy evolution makes the following predictions: i) galaxies can become ram pressure-stripped in cosmic web filaments, in galaxy groups and massive galaxies; ii) there exists a population of flyby galaxies that is gas deficient and lost parts of their dark matter halo. We now want to check whether these predictions of our model are supported by observations.

There is ample evidence for ram pressure stripping in groups. For example, Vulcani et al. (2018) analyse four galaxies of an assembling group and conclude that one of these galaxies experienced ram pressure stripping inside the group environment. Lin et al. (2023) study ram pressure stripping in the NGC 4636 group and find that 72% of all non-merging satellites that are detected in H I are undergoing ram pressure stripping within the group. Some of them show signs of ram pressure stripping already outside the virial radius of the group which is in accordance with what we see in our simulation. Furthermore, Roberts, I. D. et al. (2021) analyse a set of jellyfish galaxies and find that ram pressure stripping is acting also on jellyfish galaxies in groups, although the stripping is weaker compared to jellyfish galaxies found in clusters.

Also for ram pressure stripping in cosmic web filaments, some observational evidence exists. For example, Lin et al. (2023) identified some galaxies that are getting ram pressure stripped, but are outside the virial radius of the group NGC 4636. In our classification, these galaxies would count as COSWEB galaxies. Furthermore, Cattorini et al. (2023) find that there are more H I deficient galaxies in cosmic web filaments compared to the normal field galaxy population. Although Cattorini et al. (2023) do not explicitly identify the physical mechanisms, this could point to ram pressure stripping in cosmic web filaments.

The population of flyby galaxies is undergoing two kinds of interactions. First, ram pressure stripping of its gas content which we already discussed and tidal stripping of the dark matter halo. While we cannot directly observe tidal interactions on the dark matter content, we can look for tidal interactions on the gas of a galaxy. If tidal interactions act on the gas content of a galaxy, also its less-bound dark matter halo at the outskirts should be affected by tidal forces. For example, Lin et al. (2023) find that 49% of non-merging galaxies in NGC 4636 that are detected in H I are undergoing tidal interactions. Furthermore, there are also several candidates for flyby (or backsplash) galaxies (c.f. Santos-Santos et al., 2023; Casey et al., 2023; Carleton et al., 2024), while Bhattacharyya et al. (2023) find strong evidence for the existence of a whole backsplash population.

Our model of galaxy evolution makes predictions on ram pressure stripping in cosmic web filaments, large galaxies and galaxy groups as well as tidal stripping of the dark matter halo. A first comparison with existing literature shows that these predictions are supported by observational evidence. However, future work should bring together observations and simulations more systematically to explicitly check the predictions made from simulations. For example, to test whether the relative numbers we give for the different processes happening to dwarf galaxies are right, more dedicated large-scale surveys targeting the dwarf galaxy population in the field are necessary.

3.2.5 Summary and Conclusions

We examined the gas content of simulated field galaxies identified in a high-resolution cosmological hydrodynamical simulation. We showed that the simulated galaxies are naturally split into quiescent and star-forming (those that have/have not formed stars during the last 2 Gyrs, respectively) based on how the mass of their haloes compares to a well-understood critical mass. In agreement with previous work, we find that galaxies residing in haloes more massive than the present-day value of the BL20 critical mass are largely star-forming, whereas those galaxies inhabiting lower mass haloes are quiescent.

Of the quiescent galaxies, we find that those that contain gas today follow the BL20 remarkably well. This indicates that, on average, the gas mass of luminous galaxies that inhabit sub-critical dark matter haloes depends on the balance between the gas pressure and the halo gravity and not on feedback from evolving stars. This fact is not minor, as this allowed us to use the BL20 model to target galaxies with a reduced gas content while ruling out supernova feedback as the main culprit for their gas deficit. These are the only galaxies whose current gas content could have been severally affected by an external process.

Our conclusions may be summarised as follows:

- Galaxies inhabiting sub-critical dark matter haloes, namely haloes with mass, $M_{200} \lesssim M_{\rm crit} \sim 5 \times 10^9\ M_\odot$, are quiescent today, and they have been so for a long time. This is because the gas in these haloes is in hydrostatic equilibrium and unable to undergo gravitational collapse and form stars in the centre. The gas mass of the galaxies that inhabit these low-mass haloes is thus well understood and can be calculated in detail by the simple BL20 model (see Fig. 3.2).

- We find that the ambient density around our galaxy sample is of the same order as the fluctuations in the galaxys' gas mass (at a fixed halo mass). This indicates that the scatter in gas mass for sub-critical haloes at fixed halo mass is due to the environment and unrelated to past events of star formation (see Ch. 3.2.4, Fig. 3.4 and Fig. 3.5).

- A non-negligible number of galaxies inhabiting sub-critical haloes today are gas-deficient, meaning their gas mass falls well below the value (and the scatter) expected for their halo mass. The exacerbated gas deficit in these galaxies cannot stem from the effect of supernova feedback or the external UVB. The origin of these gas-deficient galaxies relates to their present-day environment and their past evolution (see Fig. 3.3 and Fig. 3.4).

- Most simulated gas-deficient galaxies originate from past interactions with the most massive galaxies that form in our volume. Although our galaxy sample considers central galaxies today, we find that many field galaxies are, in fact, "flybys" that lost their gas (and also dark matter) in past interactions with massive hosts. Most simulated flybys do not contain gas today, and they cluster towards the most massive galaxies of our volume (see, e.g., Fig. 3.4 and Fig. 3.7).

- A substantial number of gas-deficient galaxies are not flybys. Close inspection of their evolution and clustering properties reveals that these systems have lost their gas through hydrodynamic interactions with the gaseous filaments and sheets of the cosmic web. We refer to these as cosmic-web stripped (COSWEBs) galaxies (see Fig. 3.8).

- Flyby galaxies make up 100 per cent of the gas-deficient galaxies below the present-day halo mass of $M_{200} \lesssim 3 \times 10^8 \ M_\odot$, as galaxy formation only proceeds in haloes more massive than the atomic cooling limit in our simulation. Galaxies inhabiting haloes less massive than this limit must have formed in haloes that underwent heavy dark matter stripping in the past, as flybys do.

- COSWEBs are more frequent than flybys at high halo masses ($M_{200} \gtrsim 5 \times 10^9 \ M_\odot$). This mass dependence originates from the loss of dark matter by flybys. We find that cosmic web stripping affects less than 10 per cent of the simulated galaxies that could otherwise sustain star formation today. These are galaxies that inhabit dark matter haloes more massive than the critical mass, $M_{200} \gtrsim M_{\rm crit} \sim 5 \times 10^9 \ M_\odot$. Cosmic web stripping thus affects, on average, only a small fraction of the cosmological population of star-forming dwarfs.

- More than 70 per cent of COSWEB galaxies inhabiting haloes with mass $M_{200} > M_{\rm crit}$ are quiescent today. This indicates that cosmic web stripping, albeit of low frequency, is an efficient process at shutting off star formation in dwarfs that would otherwise be able to form stars today.

- The fraction of COSWEB galaxies increases for sub-critical haloes, peaking at ~ 35 per cent at $M_{200} \sim 10^9 \ M_\odot$. The small gas content of galaxies inhabiting these sub-critical haloes cannot collapse to make stars in their centre, so cosmic web stripping has a negligible impact on the properties of these galaxies. Although the loss of gas in these low-mass galaxies has little importance for their evolution and present-day properties, it may have observational implications for their detection in upcoming HI surveys. Simple analytic and numerical considerations (see e.g., Benítez-Llambay et al., 2017), indicate that these galaxies may contain over $10^3 - 10^4 \ M_\odot$ of neutral hydrogen, and reach column densities, $N_{\rm HI} \gtrsim 10^{18}$ cm^{-2}. The removal of gas in these low-mass systems may thus add up to the expected diversity in the HI mass of dwarf galaxies (Rey et al., 2022), and preclude the future detection of a large number of faint dwarfs in future blind HI surveys.

Our analysis demonstrates, for the first time, that cosmic-web stripping affects only a low fraction of dwarfs massive enough to sustain star formation at the present day. The classification of gas-deficient galaxies into flybys or COSWEBs becomes ambiguous for galaxies that have not undergone strong gravitational interactions with a host in the past, or for those that may be approaching a massive companion for the first time today. Our estimates of the importance of cosmic-web stripping thus constitute an upper limit of the significance of this process over cosmological scales. Although the exact numbers we derive in our analysis may be sensitive to the particularities of our definitions, we note that the existence of a significant number of gas-deficient galaxies is a robust result of our analysis. Our study reveals the important role of the environment in shaping the gas content of field dwarf galaxies over cosmological scales.

Chapter 4

Dark-Matter-Deficient Galaxies

We explained in Sec. 1.5.3 how in the current model of structure formation, galaxies form when gas collapses within dark matter halos. These first galaxies grow by continued accretion of gas and dark matter as well as mergers. The final galaxies that form in this scenario are always dominated by dark matter. However, recently isolated galaxies that seem to lack dark matter have been observed (van Dokkum et al., 2018b, 2019a). The existence of such galaxies lacking dark matter seems to contradict the current model of galaxy formation unless it is possible to form them within the current model. We now want to investigate the possibility of dark-matter-deficient galaxies in our simulation.

4.1 Introduction

In the ΛCDM model of structure formation, the present-day structure is formed hierarchically from smaller structures White and Rees (1978); Planelles et al. (2015). In the first step, dark matter haloes are formed which then grow by accretion of dark matter and mergers with other dark matter haloes. When a critical mass is exceeded, gas can cool down, sink to the center of the halo, and form the first stars Benitez-Llambay and Fumagalli (2021). These first galaxies then continue to grow by accretion of dark matter and gas as well as mergers with other galaxies. In this model, the final galaxy that forms is always dominated by dark matter.

However, recently, some galaxies have been discovered that seem to lack dark matter. By measuring the velocity dispersion of globular clusters around the ultra-diffuse galaxies NGC1052-DF2 and NGC1052-DF4 van Dokkum et al. (2018b, 2019a) concluded that both of these galaxies are dark matter deficient. Since the inferred mass of the two galaxies crucially depends on our distance to these galaxies it was suggested that this apparent lack of dark matter could be explained by wrong distance measurements of the galaxies (Trujillo et al., 2019). However, (van Dokkum et al., 2018a) and (van Dokkum et al., 2019b) argue that the distance measurement was correct and the assessment as dark-matter-deficient galaxies stands. Furthermore, there has been another claimed dark-matter-deficient galaxy where the dark matter mass was estimated from Jeans modeling (Comerón et al., 2023).

Since the existence of such dark-matter-deficient galaxies poses a challenge to the current standard model of structure formation, the question arises about whether galaxies lacking dark matter can be produced within the ΛCDM model or whether our reference model needs to be adapted.

In principle, there are two ways to explain dark-matter-deficient galaxies within the ΛCDM paradigm. First, these galaxies could have formed within dark matter halos but then got stripped of their dark matter content ending up as dark-matter-deficient galaxies. Second, there could be a formation channel for bound stellar structure that does not include cooling and star formation within dark matter haloes, i.e. dark-matter-deficient galaxies formed outside dark matter haloes.

Both of these avenues have already been explored using numerical simulations. For example, Moreno et al. (2022) find a total of 8 dark-matter-deficient galaxies in their 21 cMpc box that uses the `FIRE2` feedback model. They were looking for galaxies that resemble NGC1052-DF2 and NGC1052-DF4 in their internal properties as well as their distance to the closest massive galaxy. All of these 8 dark-matter-deficient galaxies have been produced by close encounters with massive galaxies in the past. A different approach was taken by Shin et al. (2020) who showed that dark-matter-deficient galaxies can also form as relics of high-velocity collisions between galaxies. Using idealized high-resolution simulations they show that such high-velocity collisions can separate the DM from the warm disk gas which due to compression forms stars outside a dark matter halo. These stars then form a gravitationally bound structure, i.e., a galaxy. This kind of formation scenario was also proposed by van Dokkum et al. (2022) as the most likely scenario for the formation of NGC1052-DF2 and NGC1052-DF4. We now want to explore, whether we can find dark-matter-deficient galaxies in our simulation box. We show the results of this search in Sec. 4.2, before we summarize and discuss them in Sec. 4.3.

4.2 Results

We showed in Sec. 3.2 that the flyby processes can remove dark matter from a galaxy due to tidal stripping and that some of these flyby galaxies are found far away from the hosts responsible for the stripping. During the most violent stripping events, a galaxy can lose more than an order of magnitude of its dark matter content. This happens when a galaxy is not just stripped by a single host, but rather undergoes n-body interactions in an assembling group. Here, n-body interaction refers to the process where a galaxy interacts with several hosts instead of just one and travels in a random orbit between them. During this interaction, it gets tidally stripped by the hosts and ultimately receives a kick that lets it leave the assembling group. Most of these galaxies undergoing n-body interactions at $z = 0$ reside several hundred kpc away from the group that stripped them. However, it is also possible that a galaxy undergoing n-body interactions completely leaves the gravitational field of its host, since it can be slingshotted out during the process. We show such a galaxy that is undergoing n-body interactions and is subsequently slingshotted out in Fig. 4.1. In the first two panels, the galaxy is still inside the assembling group undergoing

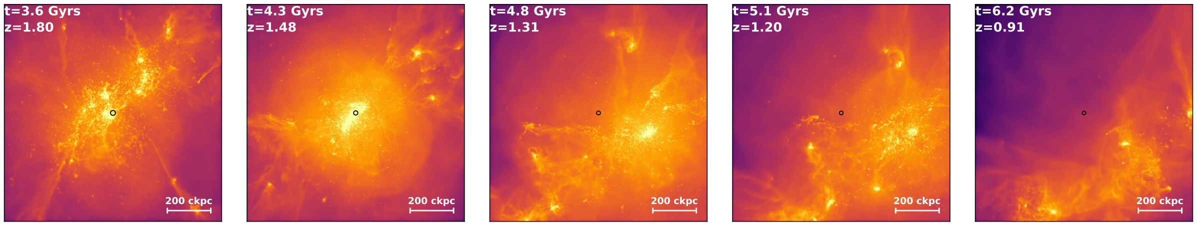

Figure 4.1: Time evolution of a galaxy that is undergoing n-body interactions in an assembling group and is subsequently slingshotted out. Each panel shows the projected gas density around the galaxy in a cube of 1 cMpc side length. The virial radius of the galaxy that is stripped is marked with a black circle. In the first and second panel, the galaxy is inside an assembling group and is losing dark matter due to tidal interactions. In the third panel, the galaxy received a kick due to n-body interactions and is leaving the gravitational field of its host. In the fourth and fifth panel, the galaxy is then travelling again through the simulation volume.

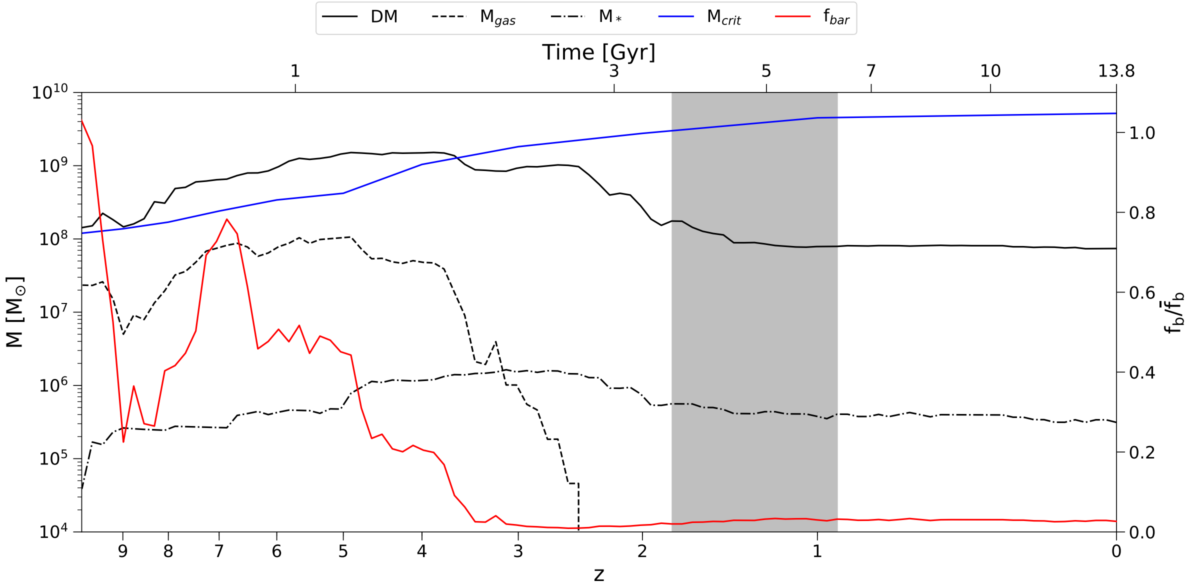

Figure 4.2: Mass accretion history of a galaxy undergoing n-body interactions and which subsequently is slingshotted out. The black solid line shows the dark matter mass, the dashed line is the gas mass, and the dashed-dotted line is the stellar mass. We marked by a grey shaded area the timespan shown in Fig. 4.1. During the n-body process, which starts around $z = 4$ and ends around $z = 1.5$ the galaxy loses more than an order of magnitude of its dark matter mass. The tidal interactions are so strong, that even part of the stellar mass is lost due to the stripping.

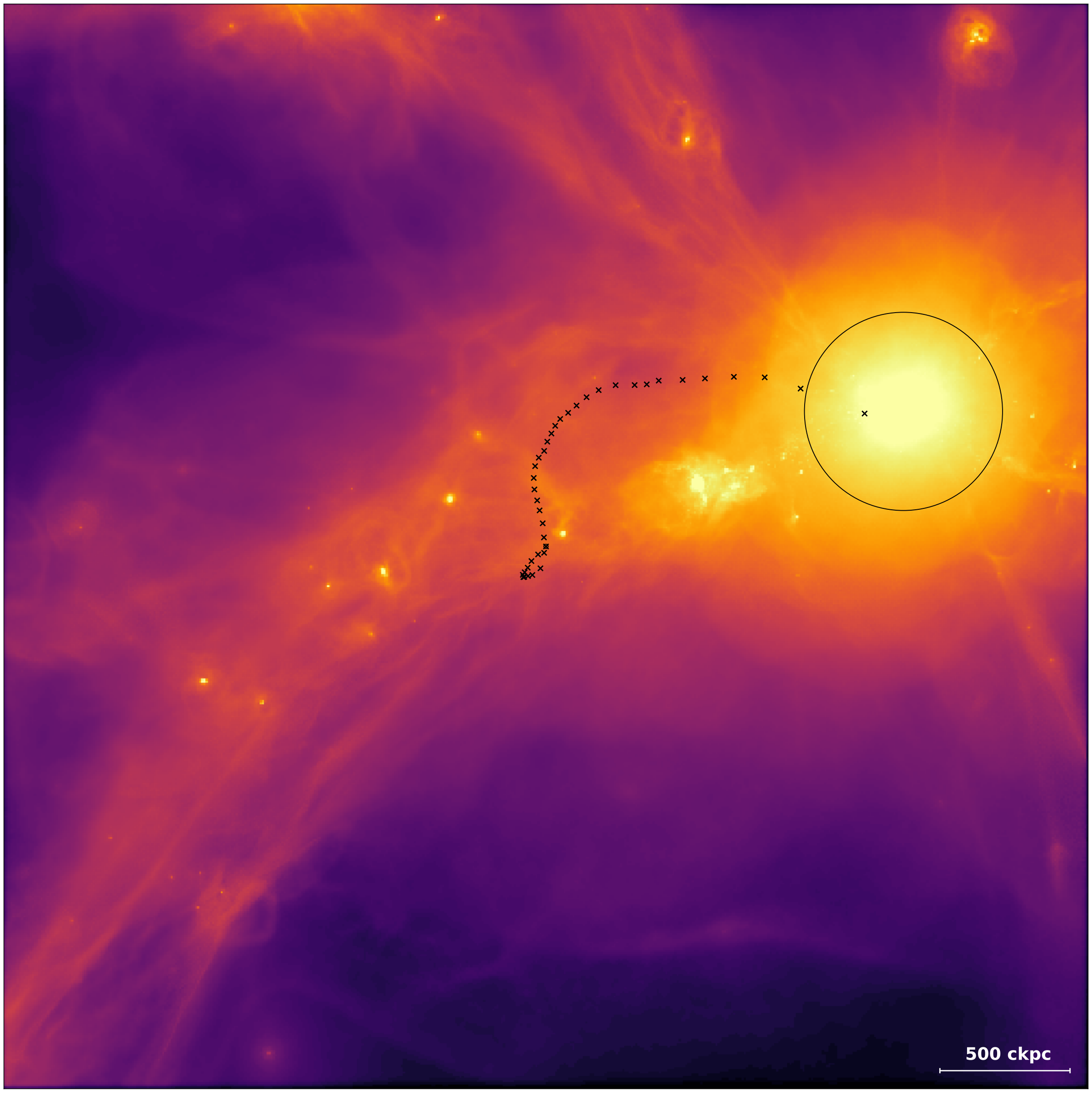

Figure 4.3: Path of the galaxy in the simulation volume after it experiences n-body interactions. We show the gas distribution at $z = 0$ and mark the virial radius of the host that was responsible for the stripping with a black circle. Additionally, we mark the path of the galaxy that gets slingshotted out by black crosses. The $z = 0$ position of the galaxy that got slingshotted out is at the center of the picture. We can see that the galaxy after receiving the kick quickly leaves the gravitational field of the host. Towards $z = 0$ it makes another turn-around, which is due to the collision with another galaxy. At $z = 0$ the distance between the host and the galaxy that got slingshotted out is about 1.6 Mpc.

n-body interactions during which it loses dark matter. In the third panel, it received a kick that lets it leave the gravitational field of its host and subsequently travel through the simulation volume, which we see in panels four and five. The associated mass accretion history can be found in 4.2, where we can see that the n-body process starts around $z = 4$ and ends around $z = 1.5$. During this process, the galaxy loses more than an order of magnitude of its dark matter mass and even part of its stellar mass due to the strong tidal forces. After this interaction, the dark matter and stellar component do not change much anymore, since the galaxy travels through mostly empty space in the simulation volume due to the kick it received during the n-body process. Only at around $t \approx 10$ Gyrs, it loses some more dark matter which is due to another galaxy that it encounters in a high-velocity face-on collision.

We show the path after the interaction overplotted over the gas distribution at $z = 0$ in Fig. 4.3. There we can see that after the n-body interaction, it quickly leaves the gravitational field of the host, where we marked the virial radius of the host with a black circle. Later on, when the galaxy that was slingshotted out encounters another galaxy in a face-on collision, another change of trajectory happens. At $z = 0$, the galaxy is then about 1.6 Mpc away from the host that was responsible for the stripping. This example shows, that in the most violent cases of tidal stripping the mass loss can be more than an order of magnitude, and n-body interactions can launch galaxies on trajectories that lead them far away from their hosts. Therefore, the flyby processes would be a natural explanation for dark-matter-deficient galaxies that are found in isolation.

A second way to explain dark-matter-deficient galaxies within the ΛCDM paradigm would be to find a formation channel for bound stellar structure, that is not dependent on formation within dark matter halos. Using simulations, it has been shown that bound stellar structure can form through high-velocity collisions between galaxies (Shin et al., 2020). Furthermore, van Dokkum et al. (2022) argued that the dark-matter-deficient galaxies DF2 and DF4 in the NGC 1052 group are actually remainders of such a high-velocity collision. We identified some of these high-velocity collisions between field galaxies in our simulation. For example, the galaxy we showed in Fig. 4.1 later encounters another galaxy in a face-on collision. However, since the galaxy that was slingshotted out due to n-body interactions is completely stripped of gas as can be seen in Fig. 4.2, we did not expect star formation to happen and therefore did not investigate whether this collision triggered star formation that eventually developed into a bound stellar structure outside a dark matter halo. Nevertheless, it shows that high-velocity collisions between galaxies do happen even in relatively small simulation volumes.

Having observed both mechanisms by which dark-matter-deficient galaxies in isolation in principle can be produced, we wanted to investigate whether isolated dark-matter-deficient galaxies exist in our simulation box. Since Jackson et al. (2021) already showed that dark-matter-deficient satellite galaxies can be produced by stripping in a more massive host, we restricted ourselves to a search for dark-matter-deficient field galaxies, that is dark-matter-deficient galaxies that are not satellites of another bigger dark matter halo. We split our search into two parts. First, we used the halo catalogue provided by `HBT+` together with the particle data to check whether any of the flyby galaxies is dark matter deficient at any point during its evolution. Although at some snapshots some of the galaxies would be baryon-dominated at the center, none of the flyby galaxies was dark matter deficient at any point during their evolution, when taking all the matter within the virial radius into account.

Since `HBT+` needs a catalogue of FoF halos as input, in a second step we considered the case that `HBT+` might have missed bound stellar structure that exists outside dark matter FoF halos. We performed an in-depth search of the whole simulation volume at $z = 0$, whether any bound stellar structures are not contained in the catalog provided by `HBT+`. Also, this search turned out to be negative. In the following, we now want to describe in detail the search strategy that brought up the null result of not finding isolated dark-matter-deficient galaxies in the simulation volume.

First, we were checking all of the flyby galaxies undergoing stripping in n-body interactions, since these galaxies are the ones most likely to be dark matter deficient due to the heavy mass loss. We followed each of these galaxies from before the stripping until redshift $z = 0$ and calculated the radial mass profiles for dark matter, gas, stars, and total baryonic mass at each snapshot. Marking the virial radius and $0.1 \times R_{vir}$ we then checked whether the total baryonic mass is higher than the dark matter mass at some point during their evolution. Although some of the galaxies were baryon-dominated at the center at some snapshots, none of the galaxies was dark matter deficient when considering the mass within $0.1 \times R_{vir}$. We therefore concluded that none of the flyby galaxies, even the ones undergoing the most violent stripping events, is dark matter deficient at any point during their evolution.

We then applied the following search strategy when looking for bound stellar structure at $z = 0$ that might have been missed by `HBT+`. First, we checked for each star particle in the simulation, whether it is inside the virial radius of a field galaxy or outside. All star particles that were not inside the virial radius of a field galaxy, were considered for the moment freely floating star particles. For each star particle that was classified as freely floating in this way, we then checked how many other freely floating star particles are within a radius of 10 kpc. If more than 20 star particles were within a radius of 10 kpc, we set a distance threshold of 1.1 R_{vir} to the center of the closest field galaxy, i.e. we required that the collection of star particles has to be at least 0.1 R_{vir} outside the virial radius of the closest galaxy. We chose the threshold of $n = 20$ star particles since we were picking up collections of randomly scattered star particles too often when using a threshold of 5 or 10 star particles. We chose the distance threshold to make sure that they are not part of a satellite that is on the edge of the dark matter halo of the host. However, since satellite galaxies may be found outside the virial radius of their hosts with some found up to $2 \times R_{vir}$ away from the main galaxy we had to refine our search strategy.

We then verified whether the star particles that were preliminarily flagged as freely floating are also outside the dark matter halos of all the satellites. If we still found star particles outside the dark matter halo of all field galaxies and satellites, we performed a visual inspection of the collection of star particles in the simulation by plotting the dark matter content and the gas content in the simulation and overplotting it with star particles. We show an example in Fig. 4.4 where we find two collections of star particles

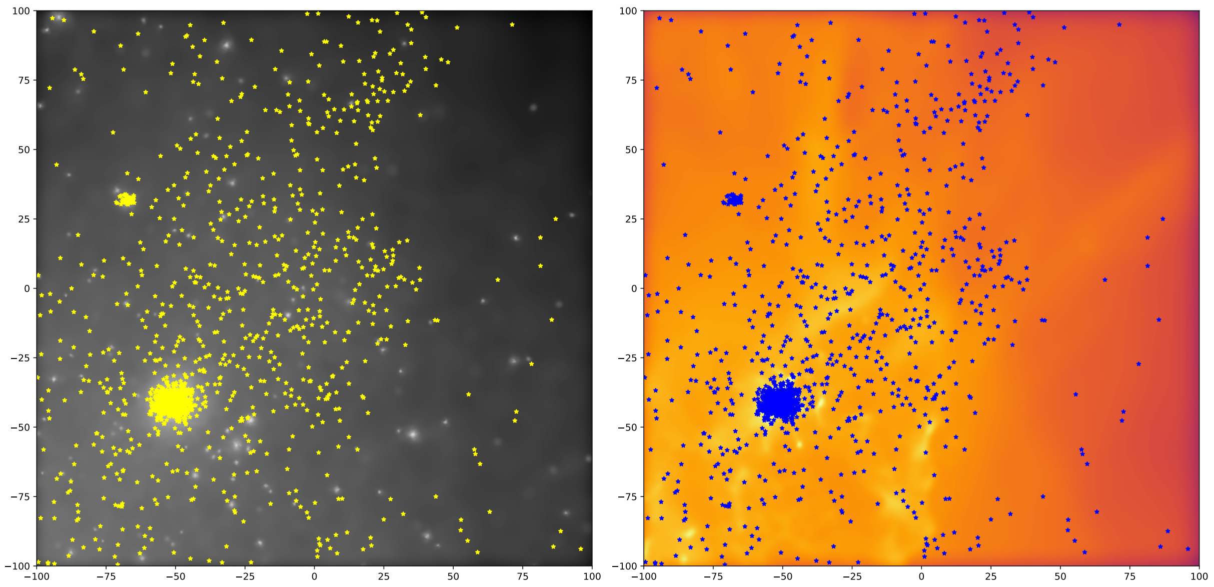

Figure 4.4: Dark matter map (left panel) and gas map (right panel) of a region where we preliminarily identified a collection of more than 20 freely floating star particles. The dark matter and gas map is overplotted with all the star particles in the region marked yellow stars in the left panel and blue stars in the right panel. We can see two collections of star particles that seem to be gravitationally bound, a big one towards the lower left corner and a small one towards the upper right corner. When calculating the mass profiles around these clusters of star particles they were dark matter dominated. Apart from the two clusters of star particles, many star particles seem to be scattered around the volume without being gravitationally bound. We had to introduce the threshold of $n = 20$ star particles because otherwise, we picked up too often random collections of such freely floating particles that were not gravitationally bound.

that seem to be gravitationally bound, but also many seemingly freely floating particles. We then measured the dark matter, stellar, gas, and total baryonic mass profiles of each of the collection of star particles that met our selection criteria the same way as before. None of the collection of seemingly freely floating star particles that met our selection criteria was baryon-dominated. Therefore we concluded that there are no bound stellar structures outside dark matter halos that have been missed by `HBT+` and therefore also no dark-matter-deficient field galaxies.

4.3 Discussion and Summary

In this chapter, we explored whether there are any dark-matter-deficient galaxies in our simulation box. We identified two possible processes that can lead to galaxies lacking dark matter. The first one is tidal stripping of the dark matter halo during n-body interactions with other galaxies, while the second one is the formation of bound stellar structure after high-velocity collisions. Since both, n-body interactions between galaxies and high-velocity collisions exist in our simulation, we searched for dark-matter-deficient galaxies in our simulation box. However, this search did not turn up any galaxy lacking dark matter.

Our results are interesting in so far as there has been previous work that finds dark-matter-deficient galaxies in a similar simulation volume. Using the `FIRE2` simulation Moreno et al. (2022) looked for galaxies that resemble the dark-matter-deficient galaxies DF2 and DF4 within their simulation box. Their simulation is a periodic cubic box with 21 Mpc side length and particle masses of $m_{baryon} = 6.3 \times 10^4$ M$_\odot$ and $m_{DM} = 3.3 \times 10^5$ M$_\odot$. In their approach, they did not differentiate between satellite galaxies and isolated field galaxies but rather looked for galaxies that resembled DF2 and DF4 in their internal properties as well as their distance to the closest massive galaxy. They found a total of 8 dark-matter-deficient galaxies in their simulation box, with some of them closely resembling the internal properties of DF2 and DF4. All these dark-matter-deficient galaxies were created by close encounters with massive hosts that removed the dark matter from the galaxies by tidal stripping (Moreno et al., 2022).

Since Moreno et al. (2022) found a total of 8 dark-matter-deficient galaxies in their simulation box which is about 1 dark-matter-deficient galaxy per 10 cMpc^3, while we did not find a single one in our box that has a similar size and a similar resolution, the question is where this difference comes from. The most likely reason is the different methodology that we applied. While we were looking for dark-matter-deficient galaxies that are truly isolated, i.e. excluding all galaxies that have been labeled satellites by `HBT+`, Moreno et al. (2022) do not make this restriction. They include all galaxies in the simulation volume irrespective of whether they are labeled as centrals or satellites. They then count a dark-matter-deficient galaxy as isolated if it is found at a similar distance to its host as the two dark-matter-deficient galaxies DF2 and DF4.

Apart from a different methodology, there is a second difference, which one has to take into account when comparing the results. This difference concerns the structure that is formed in the two simulation boxes. The biggest structure that we form in our simulation is of the order of $M_{vir} \sim 8 \times 10^{12}$ $M_\odot$, while in the simulation of Moreno et al. (2022) they form structures with $M_{vir} \geq 10^{13}$ $M_\odot$. In fact, six out of their 8 dark-matter-deficient galaxies are hosted in such halos with $M_{vir} \geq 10^{13}$ $M_\odot$. Since the tidal acceleration and therefore the strength of the tidal stripping is proportional to the mass of the host where a galaxy gets stripped, the different structures formed in the two simulations might also contribute to explaining the different results between the two simulations. However, for a final conclusion, a thorough study is needed that compared the results in several similar simulation boxes with different highest mass structure formed.

Finally, also the employed subgrid physics in the simulation might play a role in the number of dark-matter-deficient galaxies formed. If in the simulation of Moreno et al. (2022) the transformation of gas into stars is more efficient compared to our simulation, then this can lead to more stellar mass formed per unit dark matter mass, especially if the star formation is induced due to compression of gas particles when a galaxy moves inside the gaseous halo of a host. We have already seen in Sec. 3.2 that this induced star formation happens for example during the flyby process. However, also for this question of how different efficiencies in transforming gas particles into star particles influence the results one needs to compare different simulation boxes, but this time the boxes need to be run with different subgrid prescriptions.

A final answer on the expected number of isolated dark-matter-deficient galaxies as well as their formation mechanism in ΛCDM is highly desirable since the number of dark-matter-deficient galaxies found per unit volume as well as the formation channel could be used to further test the ΛCDM model of structure formation. Especially, since the original assessment of the two galaxies NGC1052-DF2 and NGC1052-DF4 by van Dokkum et al. (2018b, 2019a) could be confirmed by independent means after the initial discussion about the right distance measurement (Trujillo et al., 2019; van Dokkum et al., 2018a, 2019b). For example, Danieli et al. (2019) used stellar kinematics data instead of globular clusters to confirm that NGC1052-DF2 is lacking dark matter, while Shen et al. (2023) confirmed the lack of dark matter in NGC1052-DF4 using the stellar velocity dispersion. Further independent evidence for the lack of dark matter in NGC1052-DF2 and NGC1052-DF4 comes from Keim et al. (2022) who showed that both galaxies are tidally distorted pointing to a dark matter halo mass that is not much greater than their stellar mass. That a population of dark-matter-deficient galaxies exists is further supported by Guo et al. (2020) who find 14 baryon-dominated galaxies in isolation. With the existence of dark-matter-deficient galaxies firmly established and two viable scenarios that can produce these galaxies, where Moreno et al. (2022) showed that they can reproduce galaxies like NGC1052-DF2 and NGC1052-DF4 in their simulation by close encounters with massive galaxies, while van Dokkum et al. (2022) argues for the formation of these dark-matter-deficient galaxies through a high-velocity collision (Silk, 2019; Shin et al., 2020), the number dark-matter-deficient galaxies per unit volume predicted from ΛCDM compared with the observed number can be used to test the current model of structure formation.

Chapter 5

The influence of large-scale structure on galaxy properties

In the previous chapters, we showed how the environment can influence the evolution of galaxies. We found two distinct processes which we termed flyby and cosmic web stripping. The first one removes both dark matter due to tidal stripping and gas due to ram pressure stripping, while the second one only affects the gas content of a galaxy again by ram pressure forces. While we observed the consequences of these processes at $z = 0$, both of them acted at higher redshift during the evolution of the affected galaxies. Now we want to turn to a different question and ask how the environment a galaxy is embedded in influences its properties. This question is driven by several observations that show that galaxies embedded in a group environment have an enhanced covering fraction of Mg II, C IV and H I in their circumgalactic medium (CGM) compared to galaxies in isolation (see e.g. Dutta et al., 2020, 2021; Lofthouse et al., 2023; Galbiati et al., 2023).

5.1 The circumgalactic medium and the galaxy environment

The circumgalactic medium (CGM) is the gaseous halo in which galaxies are embedded. It acts both as the reservoir from which it can accrete gas to continue star formation and as the sink into which the metal-enriched gas is deposited by feedback processes. It is observed and predicted to be “multiphase” since different gas phases exist alongside each other. The differentiation into different phases can be made according to the temperature which then also corresponds to a difference in density. The hot phase describes gas with a temperature $T > 10^6$ K, the warm-hot phase has a temperature of $10^{5.5} - 10^6$ K and the cool phase has a temperature of $\sim 10^4$ K (Tumlinson et al., 2017). There is no universally agreed definition for the spatial extent of the CGM and the distance from a galaxy up to which gas is considered to be part of the CGM can vary significantly. For example, Tumlinson et al. (2017) only considers gas up to $1 \times R_{vir}$ as part of the CGM, while in other studies even the gas up to $4 \times R_{vir}$ is counted as part of the CGM (Dutta et al., 2021).

Recent work by Wilde et al. (2023) takes a middle ground and determined the transition between CGM and IGM to be at $R \approx 2.0 \pm 0.6 \times R_{vir}$.

The CGM is studied both in absorption (Dutta et al., 2021; Galbiati et al., 2023) as well as emission (Tumlinson et al., 2017). In absorption line studies light from a background quasar on its way to the telescope goes through several gas clouds, where absorption happens according to the atoms and ions present. If one of these absorptions happens sufficiently close to a galaxy the gas is associated with this galaxy and counted as part of its CGM. While the distance to the galaxy in the xy-plane is measured in real space, the distance in the z-direction has to be taken in velocity space. Typical values in velocity space to associate an absorption line to a galaxy are on the order of $\Delta v = \pm 500$ km/s (Dutta et al., 2021; Galbiati et al., 2023; Lofthouse et al., 2023).

When observing the CGM using these absorption line studies many different ionic species are found alongside each other in the same CGM. Since each atom requires specific densities and temperatures to be ionized into different ionic species, the ions one finds can be used to draw conclusions about phases of the CGM. For example Mg II is ionized in gas with temperatures of $T \approx 10^4 - 10^5$ K and densities $-4 \lesssim \log n_H \lesssim 1$ cm^{-3}, while C IV needs temperatures of $T \approx 10^5 - 10^{5.5}$ K and densities of $-5 \lesssim \log n_H \lesssim -3$ cm^{-3} (Tumlinson et al., 2017). Therefore, Mg II traces the cold phase, while C IV traces the warm-hot phase.

When having a sample of galaxies with quasar sightlines one can calculate the covering fraction of different absorbers. The covering fraction f_c of an ion can be calculated as n_{ion} divided by n_{tot}, where n_{ion} is the number of sightlines that detect an ion and n_{tot} is the total number of sightlines up to a radius R, i.e.:

$$f_c = \frac{n_{ion}(r < R)}{n_{tot}(r < R)}. \tag{5.1}$$

This means that the covering fraction is a measure of how often a certain ion is found and therefore also for the abundance of the gas phase it is tracing, i.e. keeping the column density necessary for a detection fixed a higher covering fraction of a certain ion means that there is more mass of the gas phase this ion is tracing.

When doing these kinds of absorption line studies it has been found that the covering fraction of different ions depends on the environment the galaxies are embedded in (Dutta et al., 2020, 2021; Lofthouse et al., 2023; Galbiati et al., 2023). Here environment refers to whether a galaxy is found in a group or whether it is found in isolation. A galaxy is considered to be in a group, if there is at least one other galaxy within a certain distance. If this is not the case, it is considered to be in isolation. They have to rely on this crude assessment of the environment due to the small datasets available. What Dutta et al. (2020), Dutta et al. (2021), Lofthouse et al. (2023), and Galbiati et al. (2023) find is that group galaxies have higher covering fractions of Mg II, C IV and H I compared to isolated galaxies, which means that there is more gas in the cold phase as well as the warm-hot phase in group galaxies compared to isolated galaxies.

There are several approaches that try to explain the increased covering fraction in group galaxies. First, galaxies in groups are getting ram pressure stripped and are depositing gas in the CGM in this way increasing the amount of gas in different gas phases. Second, when probing galaxies in groups the CGMs of group galaxies are overlapping and one is not just probing one CGM but several CGMs with a single sightline thus increasing the probability of finding ions in groups. Third, when probing the CGM of group galaxies observers are also picking up gas that is outside the CGM in some intergroup medium. We now wanted to explore the mechanisms that could be behind the increased covering fraction in group galaxies using the high-resolution simulation presented in Sec. 2.4. The results of this study are presented in the next section, and are part of a paper in preparation.

5.2 The Influence of the Environment on the CGM of galaxies

5.2.1 Introduction

In the hierarchical model of structure formation small structures like galaxies form first, while bigger structures like massive galaxies, groups, and clusters grow over time by mergers and accretion of smaller galaxies (Planelles et al., 2015). Therefore, most galaxies do not evolve in isolation for their entire life but will undergo a myriad of processes like mergers, ram pressure stripping in clusters, groups, and cosmic web filaments as well as tidal interactions. All these interactions influence the evolution and final properties of galaxies and lead to a difference between galaxies found in groups and galaxies found in isolation.[1]

For example, ram pressure stripping in groups and clusters can remove gas from infalling galaxies leading not only to a shutdown of star formation but also to a transformation to elliptical galaxies for low-mass systems (Boselli et al., 2022). Therefore, galaxies in overdense regions tend to be spheroidal and red, which means that star formation stopped a long time ago, while galaxies in isolation are usually disk galaxies and have ongoing star formation even today (c.f. Blanton and Moustakas, 2009; Naab and Ostriker, 2017). Furthermore, galaxies in overdense regions are also subject to tidal interactions that can not only affect the gas and the stellar content of galaxies but also remove parts of the dark matter halo. Although it is possible that also isolated galaxies were affected by environmental interactions in the past that led to the removal of gas and dark matter as well as a shutdown of star formation, only a minority of isolated galaxies are affected, especially in the dwarf galaxy regime (c.f. Applebaum et al., 2021; Benavides et al., 2021; Herzog et al., 2023). From the point of view of galaxies, it has therefore long been established that the environment a galaxy is found in has a considerable influence on its properties like shape, star formation rate, or the age of the stellar population.

---

[1] In this paper *galaxies in groups* will denote all galaxies that are not found in isolation, i.e. irrespective whether the accumulation of galaxies would be classified as a galaxy group or a galaxy cluster due to its halo mass. We describe the group finder algorithms that we use to define galaxies as isolated or residing in groups in detail in Sec. 5.2.3.

However, recent observations point in the direction that not only galaxies themselves are affected by the environment they reside in, but also their circumgalactic medium (CGM). The CGM is a gaseous halo around galaxies and connects the interstellar medium (ISM) with the intergalactic medium (IGM) and the filaments of the cosmic web. For galaxies to sustain star formation they need to accrete gas which they do from the CGM and the cosmic web filaments. Therefore, the CGM serves on the one hand as a source to replenish the gas in the ISM. On the other hand, it also serves as a sink where feedback processes like supernovae and stellar winds deposit metal-enriched gas. Therefore, the CGM plays a crucial role in the evolution of galaxies (Tumlinson et al., 2017; Péroux and Howk, 2020). Now when a galaxy undergoes an interaction with the environment like ram pressure stripping in a galaxy cluster or group, the gas that is removed has to be deposited somewhere with one of the possible sinks being the CGM of the host. Now the question arises, whether such interactions with the environment predominantly observed in groups and clusters influence the CGM of galaxies residing in these groups and clusters.

There is indeed mounting evidence that there is a difference between the CGM of galaxies in groups and galaxies found in isolation. For example, Bordoloi et al. (2011) find a more extended Mg II absorption around group galaxies compared to isolated galaxies, but argued that this can be explained by the superposition of several absorbing galaxies. Using Lyα absorption to study the effect of the environment on H I both Yoon and Putman (2013) and Burchett et al. (2018) find that in cluster environments the CGM is depleted of neutral hydrogen. Using absorption from O IV Pointon et al. (2017) found that the covering fraction in of O IV in group environments is lower than in isolated environments arguing against the superposition model of Bordoloi et al. (2011) and instead proposing that the virial temperature of the halos in groups is high enough to ionize O IV to higher states. Finally, also Burchett et al. (2016) found an environmental dependence of the CGM using C IV absorption. For galaxies with $M_* > 10^{9.5}$ $\mathrm{M}_\odot$ more than half the isolated galaxies had C IV absorption, while non of the group galaxies showed C IV. However, the sample in this study was rather small.

With the sensitive IFU capabilities of the Multi Unit Spectroscopic Explorer (MUSE) at the VLT (Bacon et al., 2006, 2010) unbiased studies of the galaxy environment became possible. Fossati et al. (2019) found higher Mg II absorption in group galaxies at $z \approx 1$ compared to isolated galaxies attributing it to gravitational interactions within the group that strip gas from galaxies and distribute it in the intergroup medium. Similar results were found by Dutta et al. (2020) showing a higher Mg II absorption in group galaxies compared to isolated galaxies. Comparing the absorption of C IV and Mg II in (Dutta et al., 2021) the previous results for Mg II were confirmed and an environmental dependence of C IV absorption with a higher C IV covering fraction in group galaxies compared to isolated galaxies was found as well. Furthermore, at higher redshift Lofthouse et al. (2023) and Galbiati et al. (2023) found a similar behavior with a higher H I and C IV covering fraction in group environments. The exact physical mechanism that is causing the higher covering fraction in groups is still unclear with possible explanations ranging from environmental interactions like ram pressure stripping, over the superposition of several CGMs, to the additional probing of the intergroup medium.

The systematic differences between galaxies in groups and galaxies in isolation have been observed at different redshifts from low redshifts of $z \approx 1$ (Dutta et al., 2020), over intermediate redshift with $z < 2$ (Dutta et al., 2021) to high redshifts of $z = 3{-}4$ (Lofthouse et al., 2023; Galbiati et al., 2023). However, when looking at the redshift evolution of these differences the picture is still somewhat unclear and the effect of the environment seems to depend both on the redshift and the gas phase in question. For the warm-hot phase at $z < 0.5$ there is a lack of C IV (Burchett et al., 2016) and weaker and narrower O VI (Pointon et al., 2017) in denser environment. However, the sample sizes of these studies are too small to draw definitive conclusions. At $z \approx 1$ one finds more C IV in denser environments (Dutta et al., 2021), but the results are not statistically significant. On the other hand, at high redshifts of $z \approx 3.5$ the covering fraction of C IV around group galaxies is found to be higher (Galbiati et al., 2023; Muzahid et al., 2021; Banerjee et al., 2023). Considering the cool and low-ionized phase traced by Mg II there are several studies at $z < 2$ pointing towards environmental effects on the CGM (Bordoloi et al., 2011; Fossati et al., 2019; Dutta et al., 2020; Nielsen et al., 2018). Thus, the observations converge on the fact that the environment a galaxy is embedded in influences the abundance of the ions that trace the different gas phases. However, until now there is almost no theoretical basis to guide the interpretation of the observational results and several open questions connected to the influence of the environment on the CGM exist.

First, how does the environment affect the different gas phases? Are the different gas phases affected differently as observations suggest? Second, does the interplay between the environment and the CGM evolve with redshift? The observational results discussed above indicate that this is indeed the case, but they are not yet conclusive. Third, it is still under debate what is the physical mechanism that drives the difference in covering fractions between galaxies in groups and galaxies in isolation. Currently, there exist several approaches to explain the observed difference: i) *environmental interactions:* interactions with the environment like ram pressure or tidal stripping in groups distribute the gas over a bigger area leading to a more frequent detection of Mg II, C IV or H I in groups; ii) *superposition of several CGMs:* when probing galaxies in groups one is not only probing one CGM, but in fact several overlapping CGMs from different group galaxies along the line of sight which leads to a more frequent detection of the ions in groups compared to galaxies in isolation; iii) *intergroup medium:* for galaxies that reside in groups the intergroup medium, i.e. the gas that is outside their CGM but between the various group galaxies, might also contain a significant amount of ions. Therefore, when probing the CGM of galaxies in groups one might also pick up a signal from the intergroup medium that combined with the signal from the CGM itself leads to a more frequent detection of ions in groups (c.f. Dutta et al., 2020). Since from observations it is unclear which of these approaches to explain the increased covering fraction of group galaxies is right, or whether it is a combination of them, the environmental influence on the CGM needs to be investigated in more detail with models.

The CGM and its properties have been studied in simulations and compared to observations. For example, Suresh et al. (2015) studied the influence of AGN feedback on metal enrichment of the CGM, Fumagalli et al. (2011), Turner et al. (2017), and Hafen et al. (2017) used simulations and comparison with observations to study inflows and their effects on observational tracers, and Oppenheimer et al. (2018) study the metal content of the multiphase CGM. However, none of these studies took the cosmological context and how the CGM might depend on the large-scale structure in which a galaxy is embedded into account. This paper therefore is a first attempt to model the effect of the environment on the multiphase CGM in a cosmological context using a high-resolution cosmological simulation based on the `EAGLE` model of galaxy formation (Schaye et al., 2015; Crain et al., 2015). Using a cosmological simulation to understand the origin of the observed difference in the CGM between group galaxies and isolated galaxies has two advantages. First, we can track our sample of galaxies through time which allows us to study the redshift evolution of the observed difference not only for a sample of galaxies but for each individual galaxy. Furthermore, this allows us also to explicitely check whether environmental interactions are the cause of the difference. Second, in simulations, we have the 3D position of the absorbing gas with respect to the galaxy and know exactly which gas particles are bound to the galaxy. Therefore, instead of relying on a window of about ±400 km/s in velocity space for the association of gas to a galaxy, as is done in observations and which can amount to several Mpc in real space depending on the redshift (Knobel et al., 2009), one can select exactly the gas one is interested in when working with simulations. This, in combination with the ability to track each galaxy through time, allows us to test the different physical scenarios that have been proposed to explain the observed difference in the covering fraction of gas around galaxies in groups and galaxies found in isolation.

This paper is structured as follows: In Sec. 5.2.2 we describe the simulation, how we select our sample and create a matched sample out of it, how we split galaxies into group and isolated galaxies as well as the calculation of column densities and covering fractions. In Sec. 5.2.4 we present our results. First, we compare central galaxies in groups to central galaxies in isolation in Sec. 5.2.4. Second, in Sec. 5.2.4, we compare isolated central galaxies to satellite galaxies. Finally, in Sec. 5.2.4 we test several methods used in observations and whether they have an influence on the results. In Sec. 5.2.5 we discuss our results and potential caveats, before we end with our conclusions in Sec. 5.2.6.

5.2.2 Methods

5.2.3 Simulation

For our investigation of the influence of the environment on the CGM we use the same simulation that we already presented in Sec. 3.2.2. Here we discuss in a bit more detail how star formation is implemented since this is important for our analysis.

For star formation to proceed, the gas has to cool down and exceed a density threshold of $\rho_{th} = 1.0$ cm^{-3}. Gas cooling and heating are implemented following Wiersma et al. (2009a). When ρ_{th} is exceeded, gas particles are stochastically transformed into star particles of a mass of $M_* \approx 4.5 \times 10^4$ M$_\odot$ following the Kennicutt-Schmidt law. Star-forming gas is put on an artificial equation of state $T(\rho) = T_0(\rho/\rho_{th})^{\gamma-1}$, where $\gamma = 4/3$ and $T_0 = 8000$ K, to prevent the formation of extremely high density gas. Since this affects only star-forming gas found only in the center of galaxies, this does not affect directly our analysis of the CGM.

Group Finders

In order to divide our galaxy sample into group galaxies and isolated galaxies we need a group finder algorithm that tells us which galaxies are bound to another galaxy, i.e. are group galaxies, and which galaxies are in isolation. In this paper we will use three group finder algorithms in order to make the distinction between group galaxies and isolated galaxies. First, we will use the results of the simulation group finder `HBT+` that comes with the simulation output in order to divide our galaxy sample into central galaxies and satellite galaxies. Furthermore, we use `HBT+` also to check which gas particles are bound to a galaxy and which are not. Second, we use a distance criterion to assess which central galaxies are group galaxies and which central galaxies are isolated galaxies. And third, we will use an observational group finder that follows the friends-of-friends algorithm used in observational studies (c.f. Knobel et al., 2009, 2012; Dutta et al., 2021).

Simulation Group Finder: In the simulation `HBT+` (Han et al., 2018) is used as a group finder. We already discussed how `HBT+` works in Sec. 3.2.2. Here we just want to repeat that `HBT+` returns a catalogue of centrals and subhalos with a list of particles (DM, stars, gas) that are bound to these halos as well as several halo properties like virial mass, bound stellar mass, bound gas mass, virial radius, half mass radius as well as the position and average physical velocity of the halo. Furthermore, we want to stress that `HBT+` sets the most massive galaxy of a dark matter halo as the central galaxy, while galaxies that are gravitationally bound to the central are listed as subhaloes or satellites. These satellites are inside the dark matter halo of the central galaxy, i.e. their host.

Distance Criterion: In order to divide the central galaxies in our sample into galaxies in groups and galaxies in isolation we apply a distance criterion. For each galaxy with $M_* > 10^8$ $\mathrm{M}_\odot$ that is the central galaxy of its dark matter halo as identified by `HBT+` we check whether there is another central galaxy within 750 kpc. If yes, both the galaxy and all the companions that are within 750 kpc are classified as group galaxies. If no, we check whether there is another central galaxy within $5 \times R_{200}$. If yes, again both the galaxy and all the companions that are within $5 \times R_{200}$ are classified as group galaxies. If there is no galaxy within 750 kpc or within $5 \times R_{200}$, then the galaxy is flagged as an isolated galaxy for the moment. If at a later step it is identified as being within $5 \times R_{200}$ of another bigger galaxy, i.e. if it is the companion of another galaxy, it will be put into the sample of group galaxies. If not, it is an isolated galaxy. Therefore, group galaxies are all galaxies that 1) have another galaxy within 750 kpc; 2) or have another galaxy within $5 \times R_{200}$; 3) or are within $5 \times R_{200}$ of another galaxy. All other galaxies are isolated galaxies.

Observational Group Finder: While in simulations we have the full 3D information of the positions and velocities of each particle, which allows for the construction of groups based on their location, in observations we lack exact information for one of the three coordinates. In observations, the x and y coordinates can be retrieved from the position in the sky. However, for the z coordinate one has to resort to the redshift z, i.e. the position in velocity space, which is a combination of the Hubble flow as well as the peculiar velocity. The x and y coordinates as well as the line-of-sight velocity are then used to construct FoF groups.

Since we want to compare the simulation with observations, we construct the same group finder as is used in Dutta et al. (2021) for our simulation. Dutta et al. (2021) run a FoF algorithm (Knobel et al., 2009, 2012; Diener et al., 2013) with linking lengths $\Delta r = \sqrt{(\Delta x)^2 + (\Delta y)^2} = 500$ kpc and $\Delta v = 500$ km s^{-1}. We adopt the same values for the observational group finder for the simulation. For the x and y coordinates we feed into the algorithm we take the x and y coordinates of the most bound positions calculated by `HBT+` for each galaxy in our sample. The line-of-sight velocity of each galaxy we calculate by assuming the observer at the edge of the box looking into the z-direction. We take the z-value of the physical average velocity of each galaxy as the peculiar velocity calculated by `HBT+` and then add the Hubble flow assuming the observer at the x and y position of the galaxy at the edge of the box, i.e. the full Hubble flow of each galaxy goes into the z-direction. This gives us a list of galaxies that are in groups and galaxies that are in isolation. Note that the groups `HBT+` finds are gravitationally bound, while for the groups from the observational group finder, this is not necessarily the case. We compare the three group finders in sec. 5.2.3.

Sample Selection and Classification

In order to be consistent with the observational approach by Dutta et al. (2020) we select our sample in the same way. At the snapshot we analyze we select all galaxies which `HBT+` classified as having a bound stellar mass of $M_* > 10^8$ M$_\odot$, irrespective of whether they are labeled as central galaxies or satellites. The cut in stellar mass corresponds to the typical stellar mass completeness limit at $z \approx 1$ of the MUSE studies. All other galaxies are disregarded in our analysis, both for calculating the covering fractions as well as for determining whether a galaxy is in a group or in isolation.

This way of selecting the galaxies gives us a sample of 289 galaxies at redshift $z = 0$, with 163 of them being classified as central galaxies and 126 as satellite galaxies by `HBT+`. Using the distance criterion described in Sec. 5.2.3, we split the central galaxies into galaxies in groups and galaxies in isolation, giving us 52 group galaxies and 111 isolated galaxies. However, when using the observational group finder and giving all 289 galaxies as input we get 204 group galaxies and 85 isolated galaxies. The 204 group galaxies are divided into 35 groups containing between 2 and up to 28 galaxies per group. Since each galaxy that is classified as a satellite by `HTB+` ends up in a group by the observational group finder, all isolated galaxies are central galaxies of their dark matter halo, when applying the observational group finder. Furthermore, in each of the 35 groups the most massive galaxy in terms of stellar mass is always a central galaxy as defined by `HBT+`. Therefore, when following the approach of observers and picking the most massive galaxy as the central galaxy in the group, one compares again galaxies that are the main galaxies of their dark matter halo, when comparing central galaxies in groups with galaxies in isolation.

Matched Samples

To ensure that differences between group galaxies and isolated galaxies are not just due to differences in the secular properties of the galaxies, we create matched samples for our analysis to account for different masses. Since in simulations we have the advantage of knowing both the halo mass and the stellar mass of each system in our sample, we take advantage of that and create two kinds of matched samples. First, taking advantage of the simulation where we know the exact halo mass of each system, we create a sample that is matched in both stellar mass and halo mass in order to test whether any differences are due to the environment or just due to different virial temperatures. When matching in stellar mass and halo mass we are choosing two bins in the stellar mass halo mass plane with a width of 0.5 dex such that the amount of group galaxies and isolated galaxies in these bins is maximized in order to get a good statistics. The two bins we are choosing are $\log_{10}\mathrm{M}_* = [8, 8.5]$ $\mathrm{M}_\odot$ and $\log_{10}M_h = [10.6, 11.1]$ $\mathrm{M}_\odot$ for Bin1 and $\log_{10}\mathrm{M}_* = [8.5, 9]$ $\mathrm{M}_\odot$ and $\log_{10}\mathrm{M}_h = [10.8, 11.3]$ $\mathrm{M}_\odot$ for Bin2.

We show the sample we are using in our analysis in Fig. 5.1. The sample consists of all galaxies in the simulation with a stellar mass $M_* > 10^8$ $\mathrm{M}_\odot$. We marked the two bins we are analyzing as black rectangles. For the halo mass, we use the total bound mass of each galaxy as identified by `HBT+` instead of the virial mass M_{200}, since the virial mass is not well defined for satellite galaxies. Using the total bound mass instead of M_{200} leads to slightly higher halo masses for all galaxies, but does not affect the subsequent analysis. In the left panel of Fig. 5.1 we marked all galaxies classified as group galaxies by our distance criterion with blue stars, while all the isolated galaxies are marked with red stars. The satellite galaxies are shown as grey dots. Since we are maximizing the number of group and isolated galaxies, we are left with only two mass bins with $\mathrm{M}_* < 10^9$ $\mathrm{M}_\odot$, because at stellar masses above 10^9 $\mathrm{M}_\odot$ we cannot find an area in the stellar mass-halo mass plane where there are more than 10 group and isolated galaxies within ±0.5 dex in stellar mass and halo mass. In the right panel of Fig. 5.1 we marked the satellite galaxies as green dots and the isolated centrals as red dots. The hosts of the satellites are marked as black stars. For analyzing the influence of the satellites we take the galaxies in the same stellar mass-halo mass bin as before and mark it with a black rectangle. To construct the matched sample in this way for the satellite galaxies we used the halo mass at $z = 0$.

Additionally, since in observations, one has to resort to stellar mass due to a lack of knowledge of the exact halo mass, in the next step we mimic the observational approach and create a sample matched only in stellar mass. To create the matched sample in stellar mass we take a central galaxy of the group galaxies and look for all isolated galaxies within ± 0.3 dex in M_*. We then randomly selected one of them and put both galaxies, the isolated one and the group galaxy into the matched sample. If no match can be found, the group galaxy is discarded and not considered in the analysis. When using this method to create a matched sample we input the full sample of galaxies. Therefore, while each galaxy in the matched sample has a match within 0.3 dex in stellar mass, the galaxies in the matched sample itself span several orders of magnitude in stellar mass.

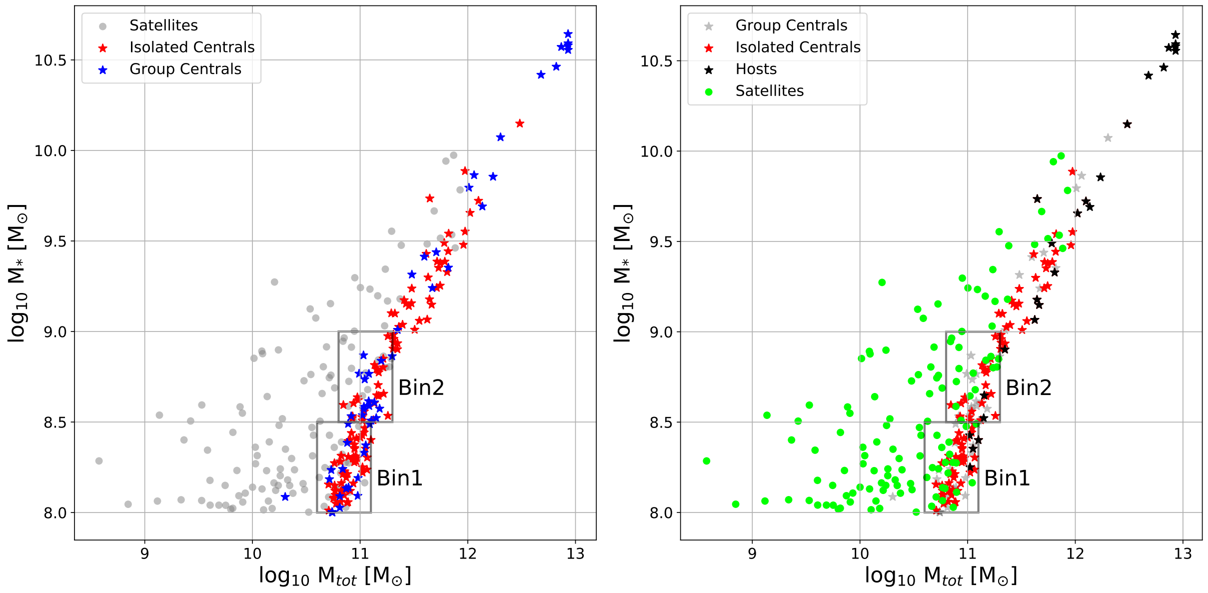

Figure 5.1: Stellar mass plotted against the halo mass for all galaxies in our sample, where for the halo mass we took the total bound mass for each galaxy. In the left panel, we mark galaxies that are classified as group galaxies as blue stars while galaxies that are classified as isolated galaxies are marked as red stars. Satellite galaxies are marked as grey dots. In the right panel, we show again the stellar mass-halo mass relation for all the galaxies in our sample with isolated centrals being marked as red stars, satellite galaxies as green dots, and the hosts of the satellites within Bin1 and Bin2 as black stars. All other group galaxies are marked as grey stars. We chose two bins in stellar mass and halo mass marked by the rectangles spanning the area of $\log_{10}\mathrm{M}_* = [8, 8.5]$ $\mathrm{M}_\odot$ and $\log_{10} M_{200} = [10.6, 11.1]$ $\mathrm{M}_\odot$ in the stellar mass-halo mass plane for Bin1 and $\log_{10}\mathrm{M}_* = [8.5, 9]$ $\mathrm{M}_\odot$ and $\log_{10}\mathrm{M}_{200} = [10.8, 11.3]$ $\mathrm{M}_\odot$ in the stellar mass-halo mass plane for Bin2. At low halo and stellar masses, we find both isolated and group galaxies, while at intermediate halo and stellar masses, isolated galaxies dominate. At very high halo masses we find only group galaxies. Therefore, we cannot analyze a bin at intermediate or high halo and stellar masses, since there is no area in the stellar mass-halo mass plane with sufficient group as well as isolated galaxies to do a proper comparison.

Definition of hot, warm and cold phase

When studying the CGM in observations one uses various ionization states of metals as tracers for the different gas phases (Dutta et al., 2021; Lofthouse et al., 2023; Galbiati et al., 2023). For example, Mg II is used for the cool ($T \approx 10^4$ K) phase, while C IV for the cool and warm ($T \approx 10^4 - 10^5$ K) phases. Although the simulation also tracks several metals and among them are also Carbon and Magnesium, it does not calculate the ionization states of these metals. Therefore, we used the ION_BALANCE module of `TRIDENT` (Hummels et al., 2017) with the ionization table implementing the UV background of Haardt and Madau (2012) to calculate the mass per SPH particle of the ions we are interested in. Trident calculates the ionization fractions as a function of temperature, density and redshift using `CLOUDY` (Ferland et al., 2013). This calculation is done on the original SPH particles to avoid errors from smoothing temperature or density fields (Hummels et al., 2017). Calculating the column densities for Mg II and C IV with the Py-SPHViewer code (Benitez-Llambay, 2015) we were not able to correctly reproduce observables, like the number density of absorbers per redshift. This is due to the simulation not being calibrated on the metals and least the ionization states of the metals. Therefore, we choose another approach to test the different gas phases of the CGM and instead make a cut in the temperature. We define the cold phase as gas with $T < 10^5$ K, the warm phase as the gas with 10^5 K $< T < 10^6$ K and the hot phase as gas with $T > 10^6$ K. Gas below a temperature of $T = 10^4$ K in our simulation is for the most part star forming gas on an artificial equation of state (see. Sec. 5.2.3). Although this gas is included in the cold phase we remove it from the calculation of covering fractions by neglecting the innermost part of the galaxies (see. Sec. 5.2.3) where the star forming gas sits.

Calculation of Column Densities

We analyze the gas around the galaxies in our sample by calculating the column densities of different gas phases in a disk with $r = 10 \times R_{half}$ around the galaxy in the xy-plane, where R_{half} is the half mass radius of the galaxy. Since R_{200} is not well defined for satellites[2], we chose to do the analysis in terms of R_{half} instead of the virial radius R_{200}, in order to be consistent with the other parts of our analysis when investigating the influence of satellites. We will calculate the column densities in two ways, once by selecting the gas in real space and once by selecting the gas in velocity space.

When selecting the gas in real space we pick the gas for each gas phase in a sphere of radius $r = 10 \times R_{half}$ around the galaxy. [3] We then calculate the column densities for pixels of the size of 1 kpc/h out to $10 \times R_{half}$ by collapsing all the gas in the sphere along the z-axis using the Py-SPHViewer code of Benitez-Llambay (2015). In this way each pixel

---

[2] The virial radius R_{200} is the radius of the sphere with a mean enclosed density of 200 times the critical density of the universe. For a satellite that lies within the halo of a host galaxy this radius depends on the location within the host halo.

[3] We chose to do the analysis up to a radius of $r = 10 \times R_{half}$, since for central galaxies $R_{half}/R_{200} \approx 0.4$, i.e. probing the gas until $10 \times R_{half}$ is to probe the gas until about $4 \times R_{200}$, one of the standard definitions for the CGM.

constitutes a sightline where sightlines close to the galaxy intersect almost the full CGM, while sightlines near the edge of the sphere only intersect a smaller part of the CGM. The choice of pixel size is about a factor of 3 better in spatial resolution than what is used in observations and resolves the lowest mass central galaxies in our sample with more than 300 pixels within $1 \times R_{half}$.

When selecting the gas in velocity space, we use all the gas in a window of ±500 km/s along the z-direction to calculate the column densities. We make this choice to mimic observations, since absorbers are typically found to cluster around galaxies in this window (Dutta et al., 2021; Galbiati et al., 2023; Lofthouse et al., 2023). In order to calculate for each galaxy in our sample which gas particles along the z-direction are within the window of ±500 km/s we place the observer at the x and y position of the galaxy at the edge of the box. We then calculate the line-of-sight velocity of the galaxy the same way as when running the observational group finder algorithm, i.e. it is the peculiar velocity in the z-direction together with the Hubble flow from the edge of the box to the position of the galaxy. Next, we calculate the line-of-sight velocity for each gas particle combining again the peculiar velocity in the z-direction with the Hubble flow. Note, that this time we need to project the Hubble flow onto the z-direction, since the observer is not centered at the gas particles. We then take all the gas that is within a circle of radius $r = 10 \times R_{half}$ in the xy-plane and within a window of ±500 km/s around the line-of-sight velocity of the galaxy in the z-direction. We calculate again the column density in pixels of 1 kpc/h using the Py-SPHViewer code of Benitez-Llambay (2015) by collapsing all the gas along the z-direction. This time the amount of gas that is intersected by each sightline is not necessarily smaller when we go to bigger distances from the galaxy, since it is dependent on the position of the gas in velocity space and not in real space.

Calculation of Covering Fractions

We calculate the covering fractions by counting for each galaxy the number of pixels above a detection threshold in an annulus with an inner radius of $r_{in} = 0.25 \times R_{half}$ and an outer radius $r_{an} > r_{in}$ and dividing it by the total number of pixels within this annulus. Neglecting the innermost disc with $r = 0.25 \times R_{half}$ means that we are carving out the innermost part where the ISM of the central galaxy sits. To calculate the number of pixels above the detection threshold we impose the following thresholds for observations: i) $n_{th}(cold) > 10^{20}$ n/cm^2 for cold gas, ii) $n_{th}(warm) > 10^{19}$ n/cm^2 for warm gas and iii) $n_{th}(hot) > 10^{18}$ n/cm^2 for hot gas. These thresholds are arbitrary and chosen in a way that we neither have a detection at each pixel nor no detection at all, but rather a falling covering fraction from inside out. Since we are only interested in the relative difference of the covering fractions between group and isolated galaxies and in a possible change of the covering fraction when changing our approach to the analysis, we are safe to use this arbitrary detection thresholds. We vary the radius r_{an} in steps of $0.25 \times R_{half}$ from $r_{an} = 0.5 \times R_{half}$ to $r_{an} = 10 \times R_{half}$ and thus get the covering fraction for increasingly larger annulai for each galaxy. To calculate the covering fractions for different samples of galaxies we then take the median and the 16/84 percentiles of their covering fractions to get the covering fraction of a certain subsample of galaxies.

5.2.4 Results

Observers consistently find an excess in covering fraction no matter whether they compare group centrals to isolated centrals, satellites in groups to isolated centrals or mix the two and compare group galaxies (both satellites and centrals) to isolated centrals (see e.g. Dutta et al., 2020, 2021; Lofthouse et al., 2023; Galbiati et al., 2023). In order to assess what is causing this excess in covering fraction of galaxies in groups we split the analysis in three parts. First, in Sec. 5.2.4 we want to know the covering fractions for group galaxies and isolated galaxies, if the galaxies are matched in all relevant properties, i.e. stellar mass, halo mass and them being the central galaxies of the DM halo, and additionally, if one is only probing the CGM of the galaxies in question. In a second step in Sec. 5.2.4 we want to know how the covering fractions change if we compare satellites in groups to isolated centrals of the same stellar mass and halo mass bin, i.e. we try to assess the effect on the covering fraction of satellite galaxies in the sample. These first two parts will tell us what observers should see if they can perfectly match their sample in stellar mass and halo mass and additionally only probe the CGM of the galaxies in question. This allows us to go to the third part in Sec. 5.2.4 where we can check the effect on the covering fraction when using the tools of observers one by one: i) taking not only the gas of the CGM but the gas in a window of ± 500 km/s in velocity space; ii) finding a matched sample using only the stellar mass of the galaxy; iii) defining group galaxies and isolated galaxies with the same group finder as in observations.

Comparing Centrals in Groups to Centrals in Isolation

When comparing centrals in groups to centrals in isolation only galaxies that have been identified as the main galaxies in a DM halo by `HBT+` are part of our subsample. To divide this subsample into group and isolated centrals we cannot rely on `HBT+`, since each central is by definition in a different group. Relying on a criterion based on whether a central has a satellite in our sample as defined by `HBT+` is also arbitrary, since we are doing a cut in stellar mass at $M_* = 10^8$ $\mathrm{M}_\odot$ and a different cut in stellar mass would lead to a different definition of group and isolated galaxies. Therefore, we split our subsample into group and isolated galaxies based on a distance criterion. Each central galaxy that is within $5{\times}\mathrm{R}_{200}$ of another central galaxy or, if that is not the case, within 750 kpc of another central galaxy is classified as a group galaxy. All other galaxies are classified as isolated galaxies. We explain the algorithm of this group finder in more detail in Sec. 5.2.3.

This definition of group galaxies and isolated galaxies traces the overdensities in our simulation fairly well as can be seen in Fig. 5.2 where we show the spatial distribution of our sample of simulated galaxies in the simulation volume. Each panel shows the gas distribution in grey as well as the galaxies in a subcube of 10 Mpc side length projected onto the xy-plane. Central galaxies classified as group galaxies are marked as blue stars, while central galaxies classified as isolated galaxies are shown as red stars. Additionally,

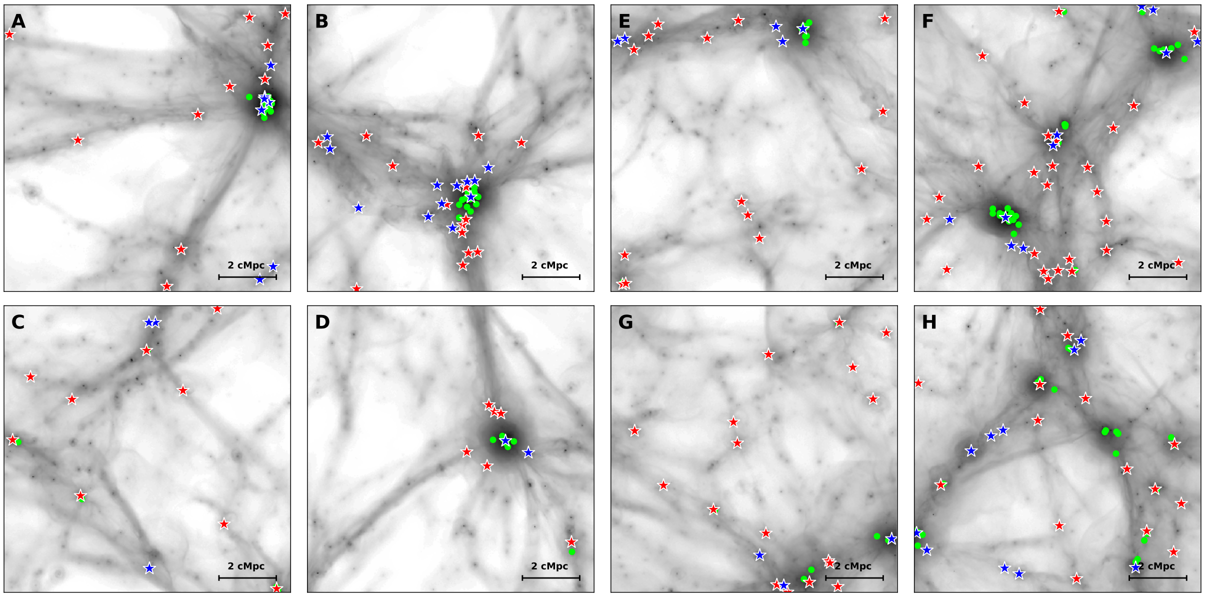

Figure 5.2: Spatial distribution of simulated galaxies with $M_* > 10^8\ M_\odot$ in the simulation volume. In panels A, B, C and D the gas within a slice $0 < z < 10000$ kpc is projected onto the xy-plane, while in panels E, F, G and H it is the gas within $10000 < z < 20000$ kpc, i.e. panels A, B, C and D can be moved directly above panels E, F, G and H to span the full cube. Blue stars mark central galaxies that are in a group environment, red stars are central galaxies that are in isolation and green dots are satellite galaxies as identified by `HBT+`. We split the sample of central galaxies into group and isolated galaxies by means of a distance criterion (see text). Group galaxies reside in denser environments marked by the darker color of the underlying gas structure in the simulation Although some isolated galaxies seem to cluster in groups or seem to be group galaxies like for example in the lower part of panel F, these galaxies fulfill the isolation condition and the apparent clustering is just a projection effect.

we also show the distribution of satellite galaxies by green dots. We can see that group galaxies are mostly clustering around the nodes of the cosmic web shown in dark grey in the gas distribution, while isolated galaxies are mostly found along filaments. Note, that some isolated galaxies seem to cluster in groups, like in the lower part of panel F or G. However, due to our classification due to a distance criterion, we can confidently say that this is only due to projection effects since we are projecting all the gas and all galaxies within 10 Mpc onto the xy-plane. Therefore, we can conclude that the way we split our sample into group galaxies and isolated galaxies traces the different environments in the simulation fairly well and we can use it as the starting point for our analysis.

To analyze the influence of the environment on the gas around galaxies and the measured covering fraction, we take the galaxies in the two bins in stellar mass and halo mass as explained in Sec. 5.2.3. In Bin1 there are 17 group galaxies and 48 isolated galaxies, while in Bin2 there are 16 group galaxies and 23 isolated galaxies. In each bin, we take all available group galaxies and all available isolated galaxies as our subsamples. For these two subsamples, we then calculate the radial density and temperature profiles.We calculate the radial density profile by calculating the mass density of the total gas in spherical shells around each galaxy in our sample and then take the median of the densities. For the temperature profiles we take again the gas in spherical shells around the galaxies in our sample and take the median temperature of the gas particles in each shell. For the radial temperature profile we then take the median of the median temperatures. We show all radial profiles for the comparison of group galaxies and isolated galaxies in Fig. 5.3.

There we can see that in both mass bins the density profiles for group galaxies (blue) and isolated galaxies (red) are the same all the way out to 10 half mass radii. The temperature profiles for group and isolated galaxies are the same all the way to about $6\times\mathrm{R}_{half}$ where the group galaxies seem to have a slightly higher temperature. However, this difference is not significant since the percentiles still overlap. Therefore, we can conclude that galaxies in groups and galaxies in isolation do not show any difference in the gas surrounding them if the gas is selected in real space and if they are exactly matched in all relevant properties, that is in stellar mass, halo mass and them being the central galaxy of the dark matter halo. Since there is no difference in any of the properties that is relevant for calculating the covering fraction, also the covering fraction of group galaxies and isolated galaxies should be the same.

We calculated the covering fractions for the hot ($T > 10^6$ K), warm ($10^5 < T < 10^6$ K) and cold ($T < 10^5$ K) gas phase for Bin1 and Bin2 following the recipies presented in Secs. 5.2.3 and 5.2.3 by first selecting all the gas within a sphere of radius $r = 10\times R_{half}$ and dividing it into hot, warm and cold gas according to the temperature of the gas particles. We then collapsed the gas for the three gas phases along the z-axis onto the xy-plane and calculated the column density in pixels of 1 kpc/h with SPHViewer (Benitez-Llambay, 2015). Then we checked how many pixels in an annulus between $r = 0.25 \times R_{half}$ and $r = r_{an}$ are above the detection limit of $n_{th}(cold) > 10^{20}$ n/cm^2 for cold gas, $n_{th}(warm) > 10^{19}$ n/cm^2 for warm gas and $n_{th}(hot) > 10^{18}$ n/cm^2 for hot gas where r_{an} goes from $0.5 \times R_{half}$ to $10 \times R_{half}$ in steps of $0.25 \times R_{half}$, i.e. we are neglecting the ISM from the calculation of the covering fractions. The number of pixels above the detection limit for each disc with

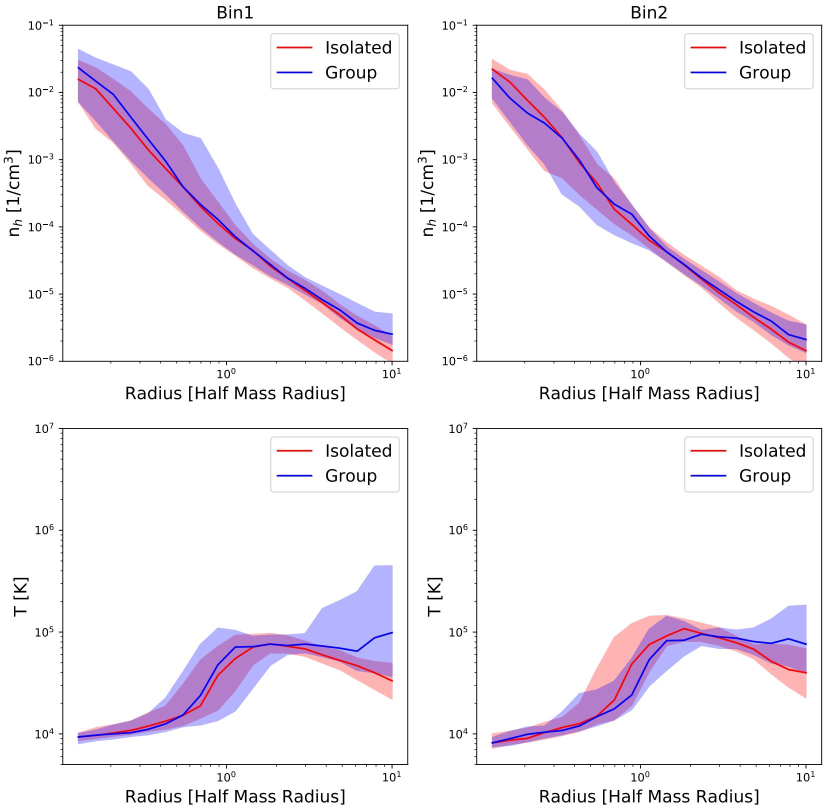

Figure 5.3: Radial profiles of density and temperature for Bin1 (left column) and Bin2 (right column). *Upper panels:* Radial profiles of the average gas density for group galaxies (blue) and isolated galaxies (red). The solid line is the median, while the shaded areas are the percentiles. Isolated galaxies and group galaxies do not show a difference in the density profile up to about $4 \times R_{half}$. After that a small difference is visible with group galaxies having a slightly higher gas density. *Lower panels:* Radial profile of average gas temperature for group galaxies (blue) and isolated galaxies (red). The solid line shows the median and the shaded area the 16/84 percentiles. The temperature profiles for isolated galaxies and group galaxies are the same up to about 4 half mass radii. Only at radii R> 4×R$_{half}$ the temperature of galaxies in groups is slightly higher compared to isolated galaxies.

radius r_{an} is the covering fraction $f_c(r < r_{an})$ for each of the galaxies.

And indeed, when calculating the covering fractions for the hot, warm and cold gas phases for Bin1 and Bin2 one does not find a difference between isolated galaxies and group galaxies as can be seen in Fig. 5.4, where we show the median and the 16/84 percentiles of the covering fractions for the group galaxies (blue) and isolated galaxies (red) for the three gas phases. For all three phases of Bin2 and the hot and the cold phase of Bin1 the covering fractions of group galaxies and isolated galaxies are exactly the same. Only for the warm phase of Bin1 the median of the covering fraction of group galaxies is higher than the median of isolated galaxies. However, for the warm phase the median of the isolated galaxies lies within 16/84 percentiles of the group galaxies which almost cover most of the area of the 16/84 percentiles of the isolated galaxies. Therefore, we cannot regard this difference in covering fraction for the warm phase of Bin1 as significant. Thus we can conclude that the gas around group galaxies and isolated galaxies is the same and should show the same observational signature if one only selects the gas in a sphere in real space around the galaxies and the galaxies of the sample are perfectly matched in all relevant parts, i.e. in stellar mass, halo mass and them being the main galaxy of the dark matter halo.

Comparing Satellites with Centrals

In simulations we have access to the exact information about stellar mass and halo mass of a galaxy and its position inside the dark matter halo, which allowed us to assess in Sec. 5.2.4 that galaxies in groups and galaxies in isolation are the same and show the same observational signature when matched in all relevant properties. However, in observations we do not have the same exact information as in simulations and to assess which galaxy is the main galaxy of the group, i.e. the main galaxy of a dark matter halo, one usually takes the galaxy with the highest stellar mass in a group as the central galaxy (c.f. Dutta et al., 2021). However, due to uncertainties in determining the stellar masses or if one did not observe the central galaxy of a group due to it being obscured by dust or too close to the quasar, one might end up classifying a satellite galaxy as the central galaxy in a dark matter halo. Therefore, we now turn to the question of what happens when we compare central galaxies in isolation to satellite galaxies instead of comparing central galaxies in isolation to central galaxies in groups. This means we still match in stellar mass, halo mass and select the gas in a sphere around the galaxy, but compare galaxies that are the central galaxies of a dark matter halo to galaxies that are not the central galaxy in their dark matter halo.

In order to make the results from this section comparable to the results from Sec. 5.2.4 we again pick the same bins in stellar mass and halo mass as in Sec. 5.2.4, but this time we compare centrals in isolation to satellites as identified by `HBT+`. We show the stellar mass-halo mass relation for satellites and centrals in the right panel of Fig. 5.1 where we marked centrals that have been identified as isolated galaxies by our distance criterion from Sec. 5.2.4 as red stars, galaxies that are classified as satellites by `HBT+` are shown as green dots, the hosts of the satellites within the two mass bins Bin1 and Bin2 are marked

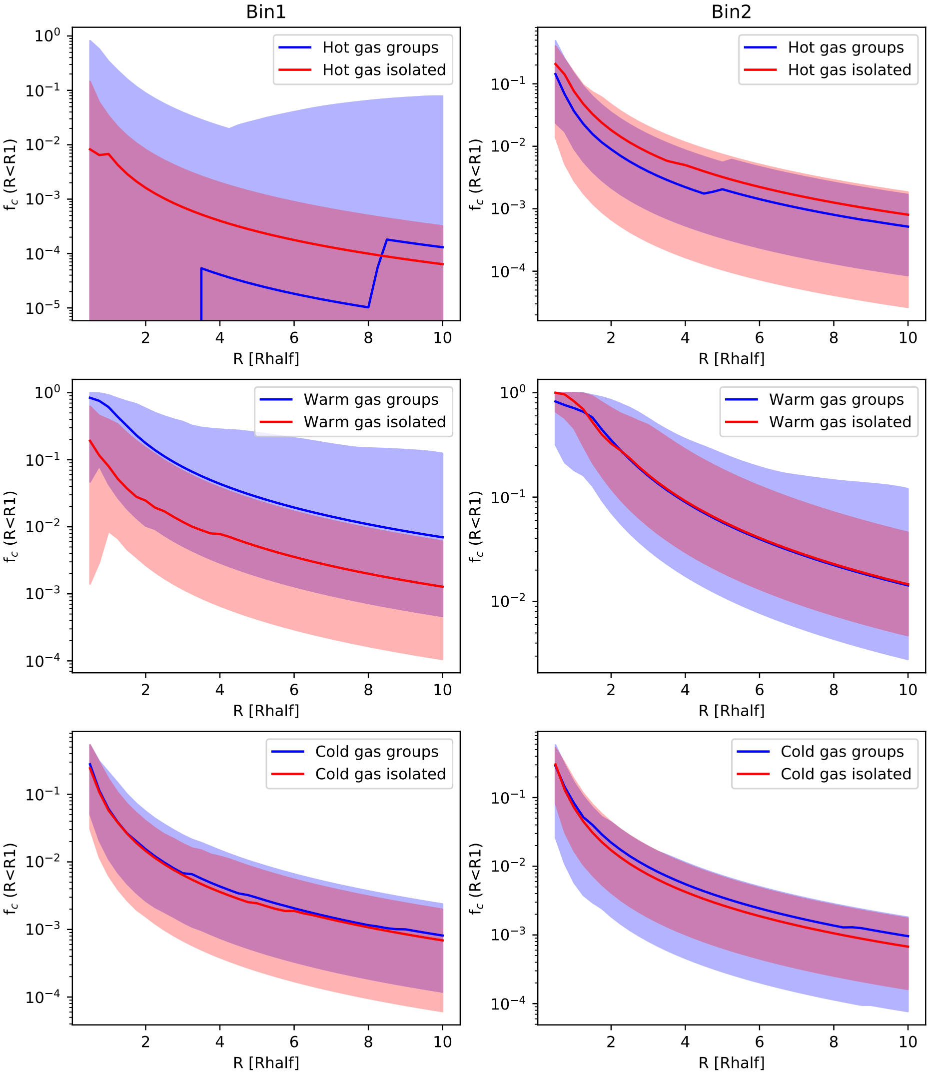

Figure 5.4: Covering fraction of hot (upper row), warm (middle row) and cold gas (lower row) for group galaxies (blue) and isolated galaxies (red). The left column is for Bin1 and the right column for Bin2. We can clearly see that if the gas around galaxies is selected in real space and the galaxies in the sample are exactly matched in stellar mass, halo mass and them being the central galaxies of their dark matter halo there is no difference in the covering fraction of different gas phases.

by black stars and the remaining central galaxies as grey stars. We can readily see that the majority of the hosts for the satellites within Bin1 and Bin2 are at stellar and halo masses way above the two mass bins we are actually testing. Furthermore, when looking at Fig. 5.2 we can see for example in panel C or D that there are isolated galaxies that are hosting satellites in our sample. In order to avoid that we have both a satellite and its host at the same time in our comparison, we exclude all those isolated centrals in Bin1 and Bin2 from our analysis that host a satellite in the same mass bin.

In Bin1 this gives us 21 satellites and 45 isolated galaxies that do not host a satellite of Bin1 or Bin2, while in Bin2 there are 22 isolated centrals not hosting satellites and 15 satellite galaxies. We show the temperature and density profiles for both mass bins in Fig. 5.5. We did the calculations for the average density and the average temperature the same way as in Sec. 5.2.4, with the only difference being that for satellites we did the calculation once for all the gas that is found within each shell and once for only the bound gas particles as defined by `HBT+`. Looking at the upper row of Fig. 5.5 we see a difference between the density profiles of satellites and centrals of the same stellar and halo mass bin. At all radii satellites have a higher density than isolated central galaxies of the same stellar mass-halo mass bin. At radii $r < 1 \times R_{half}$ the gas of satellite galaxies is dominated by bound gas, while at radii $r > 1 \times R_{half}$ the total gas mass is dominated by unbound gas. Therefore, the difference in the density at larger radii is mostly driven by unbound gas in the satellite, i.e., gas that belongs to the host of the satellite.

We can see a similar behavior when looking at the temperature profiles in the lower panels of Fig. 5.5. The profiles for satellites differ significantly from the profiles for isolated centrals in the same stellar mass-halo mass bin. While in the center the profiles of both satellites and isolated centrals are similar, they start to show a considerable difference at radii $r > 1 \times R_{half}$ where the temperature in satellites is about one order of magnitude higher than the temperature in central galaxies. This difference is again mostly driven by unbound gas, i.e. gas that belongs to the more massive host with a higher virial temperature. Combining the information we get from the temperature and the density profiles, we expect that the covering fraction for satellites is higher than the covering fraction of central galaxies of the same stellar mass-halo mass bin.

And that is indeed what can be seen in Figs. 5.6 and 5.7 where we show the covering fraction of satellite galaxies and isolated centrals in the two mass bins Bin1 and Bin2. The covering fraction has again been calculated as described in Sec. 5.2.4 for all the gas within a sphere of $10 \times R_{half}$ around the galaxy (upper rows), only the bound gas (middle rows) and only the unbound gas (lower rows) for the three gas phases hot, warm and cold. We can see in the upper rows of both figures that the covering fraction for satellites is much higher than the covering fraction of isolated centrals in all three gas phases, but especially for the hot and warm phase. However, if we would consider only the bound gas of each galaxy (middle row) the difference goes away entirely (warm gas Bin1 and 2 and cold gas Bin1) or is at least considerably diminished (hot gas Bin1 and 2 and cold gas Bin2). If we consider only the unbound gas (lower rows) we see a huge difference in the covering fraction between satellites and isolated centrals, showing that the difference is mostly driven by gas that does not belong to the satellite galaxies, but rather to their hosts. Therefore, we

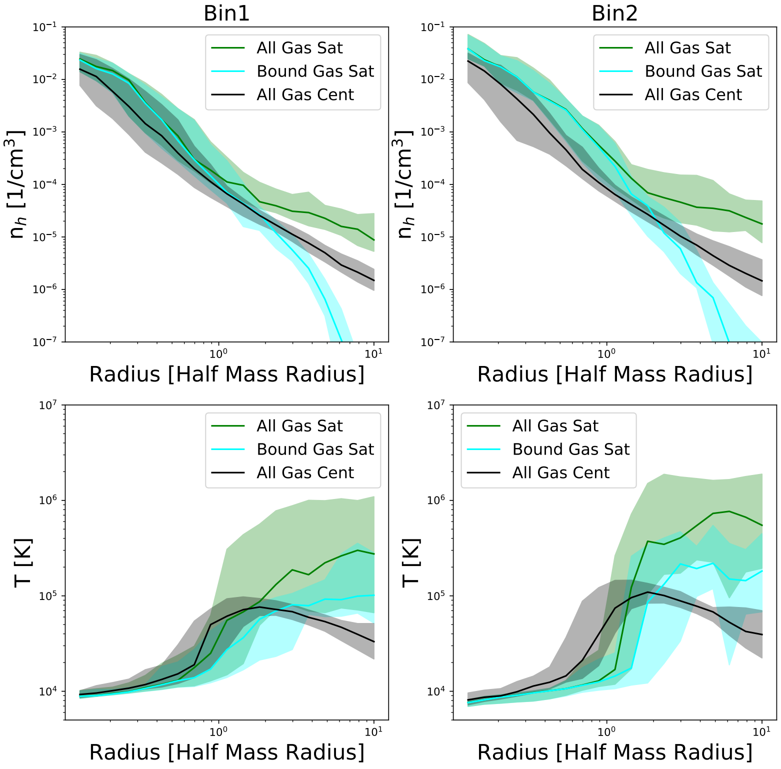

Figure 5.5: *Upper row:* Radial profile of the average gas density for all the gas in satellites (green), the bound gas of the satellites (cyan) and all the gas in isolated central galaxies (black) in Bin1 (left panel) and Bin2 (right panel). The solid lines are the medians, while the shaded areas are the percentiles. Satellites have a higher gas density than isolated centrals at each radius. Up to about 1 half mass radius the density profile for satellites is dominated by bound gas, while after 1 half mass radius it is dominated by unbound gas. Furthermore, at around 1 half mass radius also the difference in the densities between the gas around satellites and the gas around isolated central galaxies starts to increase which is due to the presence of gas belonging to the host in the case of satellites. *Lower row:* Radial profile of average gas temperature for all gas in satellite galaxies (green), only the bound gas in satellites (cyan) as well as all the gas in isolated central galaxies (black) for Bin1 (left panel) and Bin2 (right panel). The solid line shows the median and the shaded area the 16/84 percentiles. The temperature profiles for satellites and isolated centrals of the same stellar mass and halo mass bin differ significantly. At radii $R > 1 \times R_{half}$ the temperature profiles start to diverge with satellites reaching much higher temperatures than isolated centrals of the same mass bin. This is especially driven by unbound gas, i.e. gas that does not belong to the galaxy itself but to its more massive host galaxy.

found a way to observe a higher covering fraction in groups compared to isolated galaxies, namely if the sample of central galaxies is contaminated by satellites.

This can pose a problem in observations where one does not know which galaxy is the main galaxy of the dark matter halo and instead has to rely on picking the galaxy with the highest stellar mass. However, this process is open to errors, since the stellar masses of the central galaxy and the most massive satellite might be within each others error bars so that one might pick the wrong galaxy as the central galaxy. Furthermore, a massive central galaxy might not be observed at all or wrongly identified as several galaxies, since it might be obscured by dust. Finally, if there is a galaxy close to the quasar itself it might not show up in the data, if the quasar is brighter than the galaxy itself. If this galaxy close to the quasar is a massive galaxy, we might miss the main galaxy of the group in the data. All these ways can lead to a wrong identification of the central galaxy and to an increased covering fraction of galaxies in groups compared to galaxies in isolation, even when fixed in stellar mass and halo mass.

Mimicking Observations

In Sec. 5.2.4 we established that when galaxies are matched in all relevant properties, i.e. stellar mass, halo mass and being the central galaxy of a dark matter halo, and additionally the gas is selected in a sphere around the galaxy, there is no difference between galaxies in groups and galaxies in isolation. In Sec. 5.2.4 we changed one of the parameters and compared galaxies that are the central galaxies of their dark matter halos to galaxies that are satellites, while still matching in stellar mass, halo mass and selecting the gas in spheres around the galaxies. This change induced a difference between galaxies in groups (satellites) and galaxies in isolation (centrals) not only in the density and temperature profiles, but also in the observational traces, i.e. the covering fractions of different gas phases was higher in satellites compared to isolated centrals. Therefore, we were able to conclude that one way the observed difference in covering fractions between galaxies in groups and galaxies in isolation can come about even when only central galaxies are selected is that the sample of central galaxies in groups could be contaminated by satellite galaxies, which then leads to higher covering fractions for group galaxies.

We now want to test whether any other technique that is used in observations can lead to a similar result as in Sec. 5.2.4, i.e. an increased covering fraction for galaxies in groups compared to galaxies in isolation. There are three major differences in the approach of observers compared to simulations due to the limited information available to observers: i) since in observations one cannot simply select the gas in a sphere around a galaxy as in simulations, one has to rely on a certain window in velocity space to associate gas to a galaxy. A typical value for associating an absorption line to a galaxy would be a window of ±500 km/s in velocity space; ii) in observations one does not know the exact mass of the dark matter halo and instead of picking a sample of galaxies in a stellar mass-halo mass bin, they are creating a matched sample relying only on the stellar mass; iii) in simulations we have access to the exact x,y and z-positions of all particles and galaxies allowing us to define groups and isolated galaxies by a simple distance criterion. However, in observations one only has information of the x and y coordinates via the position on the sky, while for the z-coordinate on again has to rely on the location in velocity space. Therefore, group and isolated galaxies in observations are defined by a distance criterion in real space in the x and y coordinates and a distance criterion in velocity space for the z-coordinate. We will be testing the influence of i-iii) on the covering fraction by always altering just one aspect of the approach we took in Sec. 5.2.4.

Gas in velocity space: In order to test the influence of associating gas to a galaxy based on a window of ±500 km/s in velocity space we calculate again the covering fraction in the same way and using the same samples as in Sec. 5.2.4 with the only difference being that instead of selecting the gas in a sphere around the galaxies we select it in a window of ±500 km/s around the galaxy in velocity space. We show the results in Fig. 5.8 where the solid lines are again the medians of group galaxies (blue) and isolated galaxies (red) with the shaded areas being the 16/84 percentiles. Additionally we also show the medians of the same samples when the gas is selected in a sphere around the galaxies as we did it in Sec. 5.2.4 with the black solid line being for group galaxies while the dashed line is for isolated galaxies. In the lowest row where we show the covering fraction for cold gas we see that there is basically no change when selecting the gas in a velocity window of ±500 km/s compared to selecting the gas in a sphere around the galaxy. Since cold gas is mainly found in the center of galaxies we can conclude that there are no other galaxies in the line of sight that would increase the covering fraction of cold gas and that any processes able of removing gas from the galaxy, like ram pressure stripping or tidal interactions is either not present or not strong enough to lead to an increase of the covering fraction.

This result however changes when looking at the warm gas phase (middle row) in Fig. 5.8, where we can see a clear enhancement of the covering fraction compared to the selection in a sphere around the galaxy especially for galaxies in groups. While the covering fraction for isolated galaxies is also slightly increased, the increase for group galaxies is much higher and leads to a significant difference, especially in Bin1. A similar picture emerges for the hot phase (upper row) of Fig. 5.8 where there is no change to the covering fraction for galaxies in isolation when selecting the gas in velocity space, while group galaxies show a huge increase in Bin1 and a small increase mostly at larger radii for Bin2. Therefore, we can conclude that associating gas to galaxies in terms of a velocity window of ±500 km/s as is done in observations can lead to a difference in the covering fraction observed in group galaxies compared to isolated galaxies. However, this observed larger covering fraction for group galaxies is not due to an inherent difference of group galaxies and isolated galaxies, since we showed in Sec. 5.2.4 that they are the same when matched in all relevant properties and the gas is selected in a sphere around the galaxy. It is rather due to group galaxies being embedded in an environment where there is simply more gas present as can be seen in Fig. 5.2. When the gas is then selected in a velocity window in simulations, or associated to a galaxy in a velocity window in observations, one counts gas as belonging to a galaxy and its CGM which strictly speaking does not belong to the galaxy or its CGM. Therefore, it points to the intergroup medium or overlapping halos as the explanation for the observed difference in covering fractions between group galaxies and isolated galaxies.

However, there is also a caveat in this interpretation of the results. Although we see an enhancement in the hot and warm phase when associating gas to a galaxy by a window in ± 500 km/s in velocity space, it does not necessarily mean that this gas is also ionized. Since in observations one is not directly observing the hot or warm phase, but instead relies on the observation of different ions, like Mg II or C IV to trace the different phases, one would only see an enhancement in the observed covering fraction if the additional gas is also ionized. In the simulation we are using we are not able to properly model ionization and therefore cannot say whether the additional gas one is picking up is also ionized and would lead to a higher covering fraction in observations. In order to answer this question we need better simulations that are calibrated on the ionization.

Matched Sample in Stellar Mass: Due to a lack of information on the halo mass observers have to resort to match their galaxy sample in stellar mass only. Furthermore, they restrict this matching not only to a small bin in stellar mass as we do it with 0.5 dex, but match over several orders of magnitude in stellar mass. Since in Sec. 5.2.4 we showed that an increase in the covering fraction can be driven by mass when probing the gas of a more massive galaxy, we want to investigate whether matching the sample over several orders of magnitude in stellar mass has any influence on the results. We created a matched sample as described in Sec. 5.2.3 by matching in stellar mass with an allowed difference of 0.3 dex all the central galaxies classified as group and isolated galaxies using our distance criterion from Sec. 5.2.4. We then look again on the effect on the covering fraction using the same calculation for the covering fraction as in Sec. 5.2.4, i.e. we are selecting the gas in spheres with $r = 10 \times R_{half}$ around the galaxies. We show the results in Fig. 5.9 where we see that there is no difference between galaxies in groups and galaxies in isolation in the covering fraction when using the matched sample. Although we showed before that differences in covering fraction can arise due to differences in the halo masses probed, this does not pose a problem here since over the full sample this differences are averaged out and the average halo mass of the matched group galaxies is 11.12 $\mathrm{M}_{\odot}$ while the average halo mass of the matched isolated galaxies is 11.13 $\mathrm{M}_{\odot}$ a difference of only 0.01 dex. We can therefore conclude that using a matched sample in stellar mass with an allowed difference of 0.3 dex from a parent sample that stretches over several orders of magnitude in stellar mass does not lead to any differences in the covering fraction.

Observational Group finder: Last we want to investigate whether defining group and isolated galaxies the way observers do it has an influence on the observed covering fraction. We defined group and isolated galaxies as described in Sec. 5.2.3 giving all galaxies, central galaxies and satellites with $M_* > 10^8$ $\mathrm{M}_{\odot}$, as the input. Using the linking lengths of $\Delta r = 500$ kpc and $\Delta v = 500$ km/s we get 204 group galaxies in 35 groups and 85 isolated galaxies. From the group galaxies we pick only the most massive galaxies of each group, which are our 35 central galaxies. We checked that the galaxies that are the most massive galaxies in a group with the observational group finder are also central galaxies of their dark matter halo as defined by `HBT+`. Since all the isolated galaxies are also central galaxies of their dark matter halo, we are in essence comparing central galaxies in groups to central galaxies in isolation, as in Sec. 5.2.4.

Since the observational group finder only gives us 35 groups and therefore only 35 central group galaxies and since these central galaxies are spread over the whole stellar mass and halo mass range, it is not possible to find a bin with Δ 0.5 dex in stellar mass and halo mass where there are 10 or more group galaxies. Therefore, we cannot select bins in stellar mass and halo mass to do the comparison as we did in the previous sections, but have to use the full sample. Since we showed before, that using a matched sample in stellar mass over the full stellar mass range, does not lead to any difference between group and isolated galaxies, we can now use a matched sample in stellar mass to compare central galaxies in groups to central galaxies in isolation as classified by the observational group finder.

Creating a matched sample as described in Sec. 5.2.3 using central galaxies in groups and isolated galaxies as labeled by the observational group finder, we get a matched sample of 26 group and isolated galaxies. We calculated the covering fraction in the same way as described in Sec. 5.2.4 and show the results using the matched sample in Fig. 5.10. We can see again that there is no difference in the observational signal. Although the median for group galaxies is slightly higher than the one for isolated galaxies, the percentiles shown as the shaded area, almost perfectly overlap and the difference in the medians is not significant. Therefore, we can conclude that the use of the observational group finder where in the z-direction one uses the distance in velocity space, does not have any effect on the observed signature between group and isolated galaxies.

However, this conclusion hinges on the exact knowledge of the stellar masses of all galaxies so that the central galaxy can be identified without errors. This is not the case in observations. For example, in Dutta et al. (2021) in about 20% of the groups the difference in stellar mass between the most massive galaxy, which is taken as the central, and the second most massive is within 0.2 dex, the typical error in stellar mass estimates. This can lead to a misidentification of the central galaxy in the group. Second, the previous conclusion also hinges on the assumption that one has indeed observed all galaxies and is not missing the most massive galaxy which, for example, might be heavily obscured by dust or might be close to the quasar itself and therefore not observed at all. Also in this case one can wrongly identify a satellite as the central galaxy in the dark matter halo.

5.2.5 Discussion

When probing the gas around galaxies in absorption it has been continuously shown that the covering fraction of Mg II, C IV or H I tracing the various gas phases of the CGM is higher for galaxies in groups compared to galaxies in isolation (see e.g. Dutta et al., 2020, 2021; Lofthouse et al., 2023; Galbiati et al., 2023) with several competing theories like ram pressure stripping, the probing of overlapping halos or the existence of an intergroup medium trying to explain this phenomenon. While the influence of the environment, in which galaxies are located, on their CGM is an active area of research in observations, theoretical studies so far have focused on either highly idealized setups, simulations of single galaxies or zoom in simulations of galaxies located in the same environment. In these studies it was shown that ram pressure stripping can add cold gas to the CGM (Roy et al., 2023), that major mergers can increase the covering fraction of oxygen and trigger outflows that increase the metal covering fraction (Hani et al., 2018) or that metal

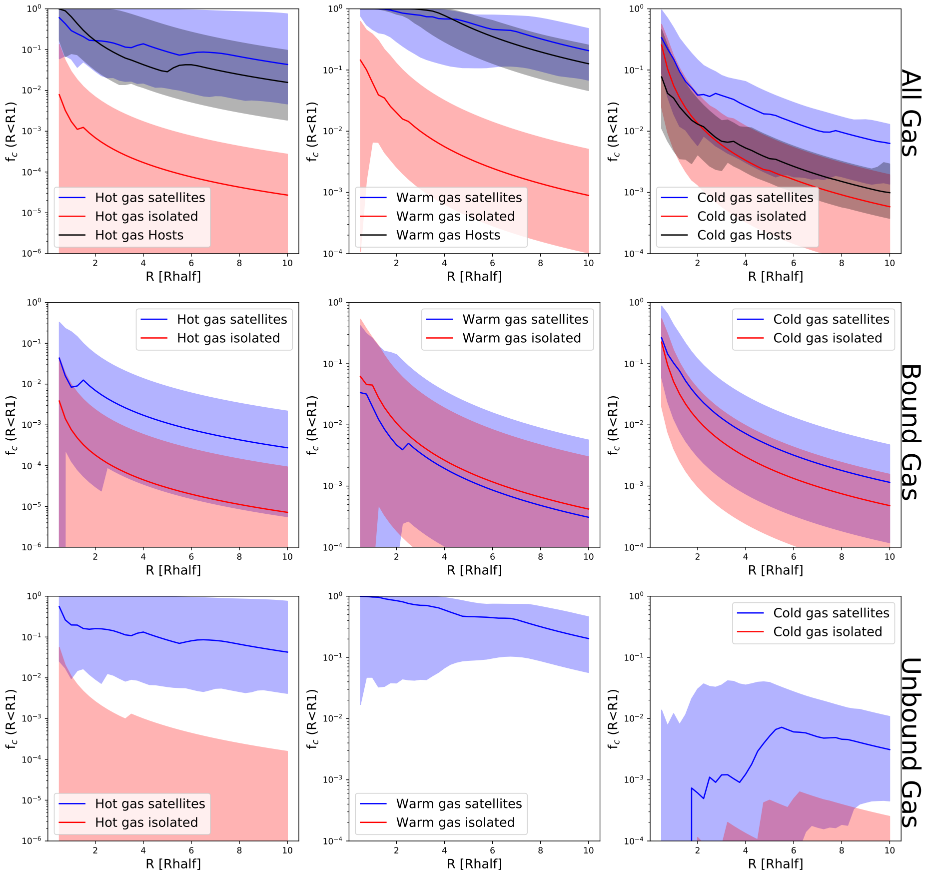

Figure 5.6: Covering fractions of all the gas (upper row), bound gas (middle row) and unbound gas (lower row) for satellite galaxies and isolated central galaxies in the stellar mass-halo mass Bin1. We show the median (solid line) and 16/84 percentiles (shaded area) for satellites (blue) and isolated centrals (red). In the upper row we also show the covering fraction of the hosts of the satellites (black). When looking at all the gas we see that satellites show a higher covering fraction compared to isolated centrals, especially for the warm and hot phase. Furthermore, the covering fraction of satellites for the warm and hot phase is comparable to the covering fraction of their hosts. The covering fraction for bound gas is similar for both satellites and isolated centrals while for unbound gas the covering fraction is much higher for satellite galaxies. This means that what we saw in the radial profiles is also true for the covering fraction, namely that the difference between satellites and isolated centrals is mostly driven by unbound gas in the satellites that belongs to their more massive hosts.

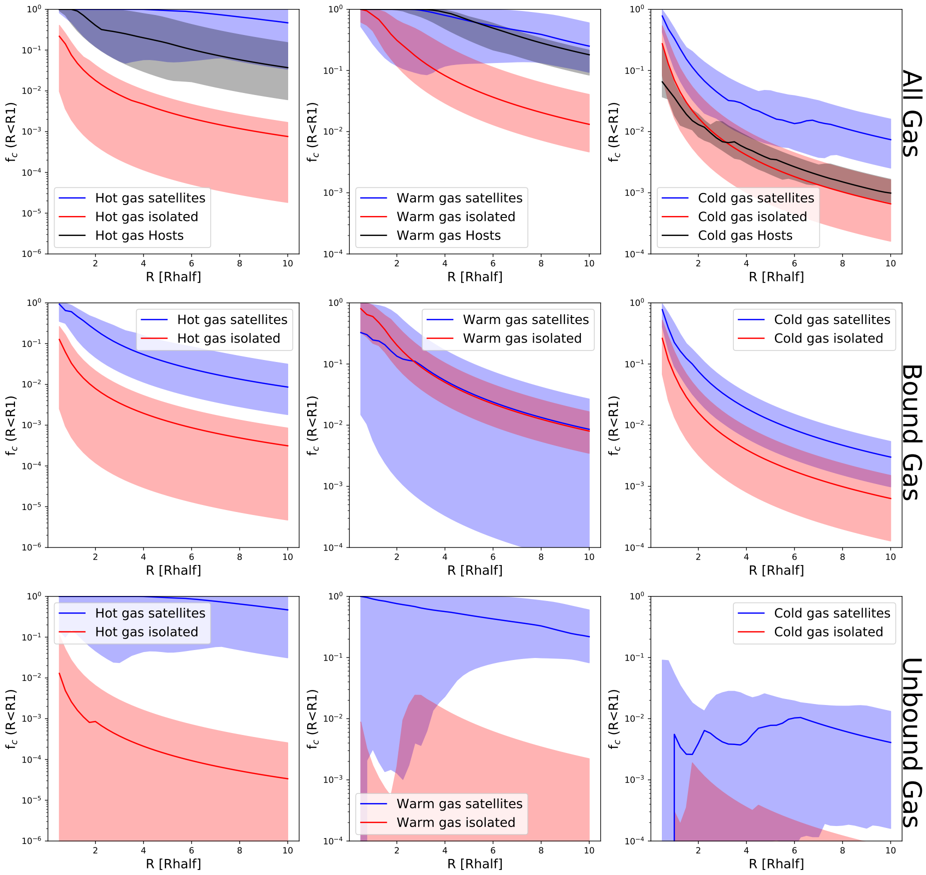

Figure 5.7: Same as in Fig. 5.6 but for Bin2. Again, satellites show a much higher covering fraction than isolated centrals and this difference is again mostly driven by the additional unbound gas in satellites, i.e. the gas that belongs to their hosts.

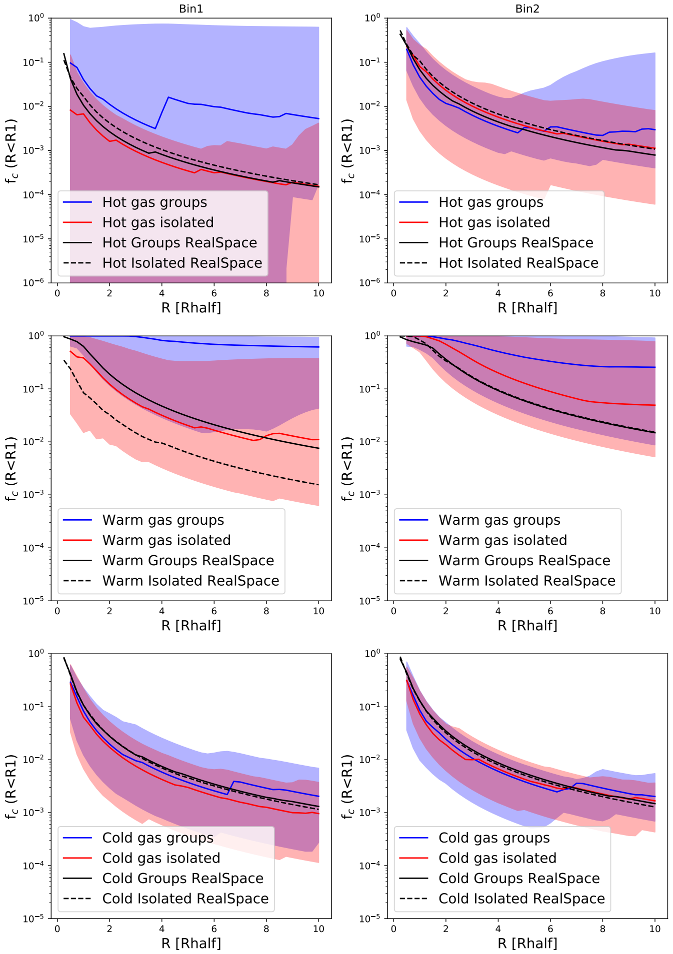

Figure 5.8: Covering fractions for hot, warm and cold gas when the gas is selected in a window of ±500 km/s in velocity space around the galaxy. We show the median (solid lines) and 16/84 percentiles (shaded area) of group galaxies (blue) and isolated galaxies (red) in the same stellar mass-halo mass bins as in Fig. 5.4. For better comparison we also show the medians of group galaxies (solid black line) and isolated galaxies (dashed black line) from Fig. 5.4 where the gas was selected in a sphere around the galaxies. Selecting the gas in velocity space has almost no effect on cold gas. The situation is different for the warm and hot phases where a difference between group and isolated galaxies emerges. This shows that associating gas to galaxies in a window of ±500 km/s in velocity space can artificially introduce a difference for the warm and hot phases.

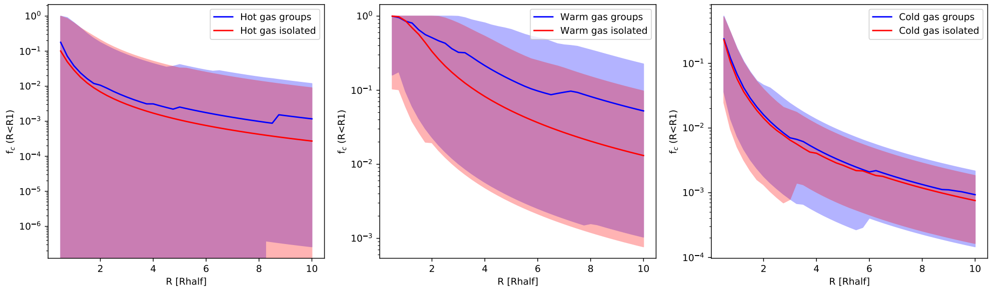

Figure 5.9: Covering fraction for hot (left panel), warm (middle panel) and cold gas (right panel) for group galaxies (blue) and isolated galaxies (red) when matching the sample in stellar mass with an allowed difference of 0.3 dex. Solid lines show the medians while shaded areas show the 16/84 percentiles. There is no difference between group and isolated galaxies for hot and cold gas with the medians and the percentiles almost perfectly overlapping. For warm gas the median in groups is slightly higher than the median for isolated galaxies. However, the median for groups lies within the 16/84 percentiles of isolated galaxies and the percentiles of both samples also almost perfectly overlap.

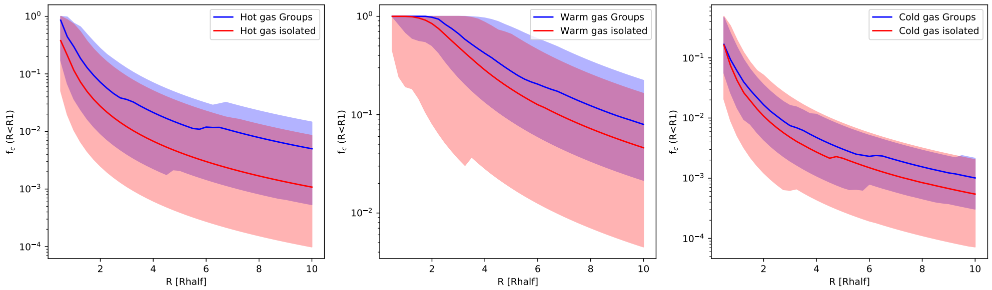

Figure 5.10: Covering fraction for hot (left panel), warm (middle panel) and cold gas (right panel) for group galaxies (blue) and isolated galaxies (red) as defined by the observational group finder and when matching the sample in stellar mass with an allowed difference of 0.3 dex. Solid lines show the medians while shaded areas show the 16/84 percentiles. While the medians of group galaxies are slightly higher than the medians of isolated galaxies, the percentiles overlap. Therefore, using the observational group finder that uses a window of ±500 km/s in velocity space to link in the z-direction is merely a complicated way of relabeling galaxies and does not significantly influence the observed covering fractions.

covering fractions correlate with internal properties such as the stellar mass or the disc fraction, but not with the specific star formation rate (Hani et al., 2019). Furthermore, there have been studies comparing the covering fractions of ions of simulated galaxies to observations (Marra et al., 2021; Appleby et al., 2021), and several studies looking at how an increased resolution in simulations influences the simulated CGM and its properties (Ramesh and Nelson, 2023; Peeples et al., 2019; van de Voort et al., 2019). However, there are no studies so far investigating the distribution of the CGM gas galaxies located in different environments taking the cosmological context into account. This paper is trying to bridge this gap in the literature by looking for the processes that are driving this observed difference in a high resolution cosmological simulation.

Since our simulation is not calibrated on the metallicity or the ionization states of metals, we resort to a cut in temperature to probe the different phases of the CGM. Furthermore, we were defining galaxies in groups and galaxies in isolation based on a distance criterion, with group galaxies being those central galaxies that have another central galaxy within 750 kpc or within $5 \times R_{200}$. Using this definition of group and isolated galaxies and taking a cut in temperature and defining i) cold gas as gas with $T < 10^5$ K, ii) warm gas as gas with 10^5 K $< T < 10^6$ K and iii) hot gas as gas with $T > 10^6$ K we found in Sec. 5.2.4 that there is no difference between galaxies in groups and galaxies in isolation if the gas is selected in a sphere around the galaxies and they are matched in all relevant properties, i.e. their stellar mass, their halo mass and them being the central galaxy of their dark matter halo. Since the covering fraction of the three gas phases is the same, we asked whether an increase in the covering fraction of group galaxies compared to isolated galaxies can be produced by any limitations in the observational techniques.

We then showed in Secs. 5.2.4 and 5.2.4 that such an increase in the covering fraction around group galaxies is indeed possible in two cases. First, if one mistakes satellite galaxies for the central galaxies of the dark matter halo one gets an increase in the covering fraction in all three phases, since one is probing the gas of the more massive host galaxy. That the covering fraction is mass driven is in accordance with other studies that find a positive correlation of covering fractions of different metals with stellar mass (Hani et al., 2019) and a positive correlation of cold gas tracers with halo mass (Nelson et al., 2020). Mistaking a satellite galaxy for the central galaxy in observations could occur due to uncertainties in stellar mass estimates and bias against detecting passive and dusty galaxies.Therefore, mistaking satellite galaxies as central galaxies is one likely channel for the observed increased covering fraction in group galaxies.

Second, if one is assigning gas to galaxies in a line-of-sight velocity window of ± 500 km/s as is the standard procedure in observations, one gets an increase in the covering fraction mostly for the warm and hot phase, since one is probing additional gas outside the CGM in group environments. However, due to the limitations of our simulation we do not know whether this additional gas would also show up as an increase in the covering fraction of different ions like Mg II and C IV in observations, since the gas is not necessarily ionized. Nevertheless, this forms a likely second channel for the observed increased covering fraction for group galaxies. That associating gas to galaxies within a window of ±500 km/s, as used in observations, can indeed increase the detection fraction of ions was shown in Ho et al. (2020), where they tested the effect of such a detection window on the measurement of corotating gas.

Furthermore, we also tested whether using a stellar mass-matched sample over $\approx 10^{8-11}$ $\mathrm{M}_{\odot}$ and whether defining groups and isolated galaxies through a group finder that uses velocity space in the z-direction influences the results of the covering fraction. For both of these methods we could not see an increase in covering fraction of group galaxies compared to isolated galaxies and therefore concluded that these observational techniques do not affect the original results from Sec. 5.2.4. However, these results crucially hinge on the exact knowledge of the stellar masses of our galaxies and that we are not missing any galaxies from our sample. Wrong stellar masses or missing massive galaxies from the sample can lead to the wrong identification of central galaxies or the creation of a sample that is not perfectly matched in stellar mass. However, this is not a problem of the group finder or the matched sample per se, but rather an observational limitation that can be addressed by infrared and radio observations to uncover the dusty galaxies.

In observations an increased covering fraction for group galaxies is found in both, C IV which is tracing the warm and hot phase, and Mg II which is tracing the cold gas phase. Since in our study the use of a window in velocity space increased the covering fraction mainly for the hot and warm phase, but probing satellites was also increasing the covering fraction in the cold phase, it is quite likely that in observations at least some contamination of the sample of central galaxies with satellite galaxies is happening. Although a recent study of idealized simulations has shown that also ram pressure stripping can add cold gas to the CGM (Roy et al., 2023), it is not clear whether in a cosmological context ram pressure stripping is relevant. We did not explicitly test or look for ram pressure stripped satellites in this sample, but the absence of an increased covering fraction in all phases, when all relevant parameters are matched, suggests that on a cosmological scale, ram pressure stripping is irrelevant as a mechanism to increase the covering fraction. In order to get a final answer on the relevance of ram pressure stripping in a cosmological context one would have to find host galaxies that have satellites that get ram pressure stripped, check whether that is increasing the covering fraction of any of the gas phases and then one would have to count how often these processes happen in the simulation volume, to get an estimate of its importance. However, this is beyond the scope of this paper and is left for future work.

In addition to not having ionization and not testing for ram pressure stripping explicitly, there is another caveat in this study. Since the simulation box we are using has only 20 Mpc side length and we are imposing a cut in stellar mass at $M_{*} = 10^{8}$ $\mathrm{M}_{\odot}$ our galaxy sample contains only 163 central galaxies, which we then divide into isolated and group galaxies by a distance criterion. Although we were able to find enough galaxies in two bins in stellar mass and halo mass in Sec. 5.2.4 to test for mass evolution when galaxies are matched exactly in stellar mass and halo mass, we are missing this exact comparison for galaxies with a stellar mass above 10^{9} $\mathrm{M}_{\odot}$ and a halo mass above $10^{11.3}$ $\mathrm{M}_{\odot}$. At these higher host halo masses, more massive galaxies with more gas can be stripped and therefore might be able to significantly increase the amount of gas in different phases leading to an increased covering fraction. This adds additional uncertainty on our conclusions on the importance of ram pressure stripping in a cosmological context. Furthermore, the low number of galaxies precluded us from doing the exact comparison in bins of stellar mass and halo mass when testing the influence of the observational group finder on the covering fraction in Sec. 5.2.4. Therefore, future studies should probe bigger simulation boxes in order to ameliorate this shortcoming.

Also, it was shown in Ramesh and Nelson (2023), Peeples et al. (2019), and van de Voort et al. (2019) that increasing the resolution in simulations not only affects the structures one can resolve in the CGM but also that the measured covering fractions increase with increased resolution. Since we are interested in the CGM in a cosmological context we have to use a galaxy sample taken from a cosmological simulation. Testing how CGM properties and covering fractions would change in a cosmological environment when increasing the resolution of the simulation would require rerunning a similar box at lower particle masses, which not only takes several millions of CPU hours to run but also requires a change in the subgrid physics. Considering that the simulation we are using in this study is already one of the highest resolution cosmological simulations that currently exist, a test of how the results change with an increase in resolution is therefore not feasible and we have to wait for the next generation of cosmological simulations to arrive.

Finally, we want to discuss how our results are influenced by the way the simulation was calibrated. Since this simulation is not calibrated on the metals that are returned to the gas by feedback mechanisms, any property that depends on metals, like the amount of different ions, is a prediction of the model, and hence it is not guaranteed to match observations. In this work, we take a more theoretical approach and circumvent possible differences in the ion content by directly probing the gas phases on which the simulation is calibrated instead of using Mg II and C IV as tracers. Therefore, our results are less affected by the details of the subgrid model. Yet, some dependencies are unavoidable. For example, the thermal state of the gas is set by a balance of heating and cooling, where the heating is linked to subgrid energy injection, while the cooling depends on metals, and hence on the star formation.

Furthermore, what can also influence the results is the physics that is included in the simulation. For example, the simulation used in this work does not include magnetic fields or cosmic rays. As van de Voort et al. (2021) showed, the inclusion of magnetic fields in a simulation significantly alters the properties of the CGM and leads to increased densities in the inner CGM, higher temperatures in the outer CGM, a higher pressure, a higher gas fraction and a higher metal mass fraction. The inclusion of cosmic rays leads to an overall cooler CGM (Butsky et al., 2022). Whether both these effects could also affect the CGM differently depending on the large-scale structure a galaxy is embedded in and therefore be the cause for the observed difference in covering fraction is unclear and needs to be tested with dedicated simulations. Additionally, our simulation does not resolve the small-scale structure of the CGM. Therefore, new simulations should also be of a higher resolution to resolve smaller scales in the CGM to test whether this influences our results.

5.2.6 Conclusions

In this work we made a detailed comparison of galaxies in groups and galaxies in isolation and how their location affects their CGM and their covering fractions of different gas phases as observational tracers of the CGM. We first compared central galaxies in groups to central galaxies in isolation, where the division into group and isolated galaxies was done by means of a distance criterion. Second, we investigated how the results change if one compares centrals in isolation to satellite galaxies. Finally, we also checked how the methods used in observation, i.e. selecting gas in a window of ± 500 km/s in velocity space, using a group finder that uses the location of galaxies in velocity space as the z-axis and comparing matched samples in stellar mass, are influencing the covering fractions.

Our main findings are:

- If galaxies are matched in all relevant aspects, that is they are the main galaxies of their dark matter halo, they have the same stellar mass and halo mass and if the gas is selected in a sphere around the galaxy, than there is no difference between galaxies in groups and galaxies in isolation.
- If one relaxes one condition of the previous comparison and instead compares galaxies that are the main galaxies of their dark matter halo to galaxies that are not the main galaxies, i.e. satellites, but still matches in stellar mass and halo mass and selects the gas in spheres around the galaxies, one finds a difference between the two samples. We showed that satellite galaxies reach higher densities and higher temperatures in their CGM than central galaxies of the same stellar and halo mass. This also translates to a higher covering fraction in all gas phases we were probing. The reason for that is that when probing the gas around satellite galaxies one is in fact probing the gas of their hosts reaching higher densities, temperatures and covering fractions. This is in accordance with other studies that show that an increase in galaxy mass also increases the covering fraction.
- Associating gas that is within a window of ± 500 km/s to a galaxy as is done in observations instead of selecting it in a sphere around the galaxy, also leads to an increase in covering fraction, especially for the hot and warm phase. Whether this additional gas would also show up as an increased covering fraction of different ions in observations is unclear, since we do not explicitly track the ionization states.
- Using a matched sample in stellar mass and using a group finder that uses the position of galaxies in velocity space as the z-coordinate does not have any effect on the observed covering fractions.

We therefore conclude that the increased covering fraction of group galaxies compared to isolated galaxies seen in observations is mainly due to systematics in the observations, either due to a contamination of the sample of central galaxies by satellites or due to additional gas that is associated to the galaxy when using a window of ±500 km/s. This mostly calls on observers to improve their methods for their surveys. However, we also need to improve the modelling in simulations for better predictions. One the one hand we need a bigger simulation box to have bigger galaxy sample to improve the statistics. On the other hand we also need a simulation that is calibrated on the metals and their ionization states to figure out whether the additional gas seen in the covering fractions of the different gas phases would also show up if one is probing the covering fraction of ions like Mg II or C IV. Finally, also an explicit study on the importance of ram pressure stripping in the host CGMs is necessary. Therefore, further works remains in order to decide what is driving the observed difference of covering fractions between group and isolated galaxies and to shed light on the importance of environmental processes on the CGM in a cosmological context.

5.3 Post-processing of ionization states and comparison with observations

In the previous section, we analyzed the influence of the environment a galaxy is embedded in on its CGM. We showed that there is a difference between group galaxies and isolated galaxies with group galaxies having more gas and therefore also a higher covering fraction in what we defined as the warm and hot phase. For this analysis, we relied on a definition of gas phases where we did a split in terms of temperature. We opted for this approach since the simulation allows us to directly access the information about gas phases which is only available through ions in observations. Therefore, we were able to investigate the influence of the environment on different gas phases circumventing the need for ions as tracers.

We also tried to model the results with the same tracers used in observation to be able to compare it to observational data. For that, we calculated the ionization states of Mg II and C IV during post-processing and used the abundances of these two ions for the analysis. However, this approach led to inconsistencies with data. We now want to explain in more detail the problems one encounters when using ionization states from post-processing for the analysis.

Post Processing of ionization states

Although the simulation tracks several metals among which are also Carbon and Magnesium, it does not calculate the ionization states of these metals. Therefore, if one wants to compare the simulation directly with observations one has to calculate the ionization states of the metals in the simulation as well as the fraction of each ionization state during post-processing. We used the ION_BALANCE module of `TRIDENT` (Hummels et al., 2017) with the ionization table implementing the UV background of Haardt and Madau (2012) to calculate the mass per SPH particle of the ions we are interested in. Trident calculates the ionization fractions as a function of temperature, density, and redshift using `CLOUDY` (Ferland et al., 2013). This calculation is done on the original SPH particles to avoid errors from smoothing temperature or density fields (Hummels et al., 2017). The results can be saved to a file and then be used in the analysis with the Py-SPHViewer code (Benitez-Llambay, 2015) to calculate the column densities of Mg II and C IV with the proper SPH approximation.

Results when using Mg II and C IV from postprocessing

When using the ionization states obtained during post-processing our results did not match observations. We first calculated the covering fractions for our sample and then compared them to observations. We show the covering fraction of Mg II for all galaxies in our sample with a stellar mass $10^8 < \mathrm{M}_*/\mathrm{M}_\odot < 10^{10}$ in Fig. 5.11 and the results for C IV in Fig. 5.12. As a detection limit for Mg II we used a column density of 10^{12} cm^{-2} per pixel, while for C IV we used a column density of 10^{13} cm^{-2} per pixel. In both plots we overplotted our results with the results of Dutta et al. (2021) for galaxies with a stellar mass $10^8 < \mathrm{M}_*/\mathrm{M}_\odot < 10^{10}$ in their sample. For Mg II the covering fraction seems to be in agreement with observations for radii $R > 200$ kpc, while at $R < 200$ kpc we see an upturn in the covering fraction in our simulation leading to covering fractions that are much too high compared with observations. On the other hand, for C IV the covering fraction for radii $R > 150$ kpc is too low. We again see an upturn in the covering fraction from our simulation at small radii, but this is not necessarily in contradiction to observations since for $EW = 0.03$ Å one reaches similar values. Since the covering fractions for both Mg II and C IV around galaxies with a stellar mass $10^8 < \mathrm{M}_*/\mathrm{M}_\odot < 10^{10}$ do not agree with observations, we performed a closer investigation on whether the total amount of ionized magnesium and carbon in the full simulation cube obtained through post-processing is in agreement with observations.

For that we were calculating $l(z)$, the number of absorbers per unit redshift as:

$$\frac{dN}{dz} = l(z) = \frac{N_{Ion}}{N_{tot}\Delta z}, \tag{5.2}$$

where N_{tot} is the total number of pixels of the simulation cube, Δz is the redshift interval and N_{Ion} is the number of pixels in the whole simulation box that have a detection of the respective ion, i.e. a column density higher than 10^{12} cm^{-2} for Mg II and a column density higher than 10^{13} cm^{-2} for C IV.

To calculate $l(z)$ in eq. (5.2) we also need to know the redshift interval Δz in which we detect our absorbers. In our case, this is the sidelength of our 20 cMpc simulation box translated to a distance in redshift. We use `astropy` to find the redshift interval that corresponds to a distance of 20 cMpc at $z = 0$, $z = 1$ and $z = 3$ in the `Planck13` cosmology. The values are $\Delta z = 0.0047$ at $z = 0$, $\Delta = 0.008$ at $z = 1$ and $\Delta z = 0.02$ at $z = 3$. The results of $l(z)$ are given in table 5.1, both for the detection limits of 10^{12} cm^{-2} for Mg II and a column density higher than 10^{13} cm^{-2} for C IV as well as one order of magnitude higher and lower. We did the variation of the detection limits to test the influence of our detection limits on $l(z)$.

For Mg II we show the results for $l(z)$ in Fig. 5.13 where we also compare with the parameterization of the observational results from Mathes et al. (2017). In Mathes et al.

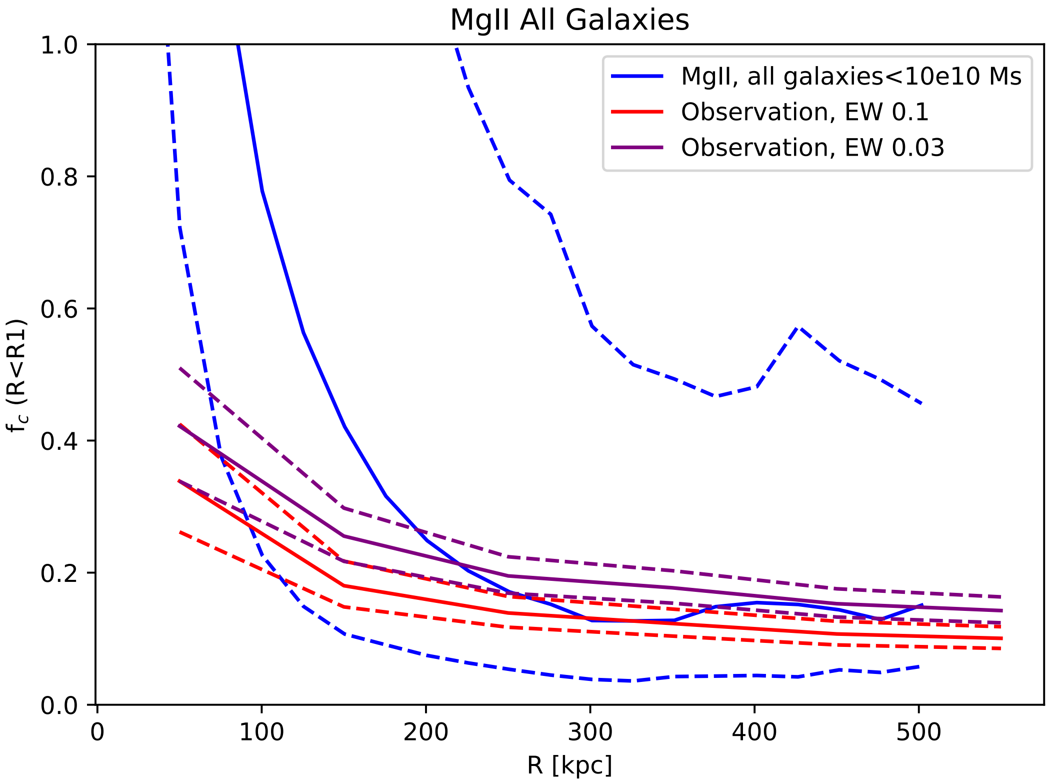

Figure 5.11: Covering fraction of Mg II in our simulation (blue lines) overplotted with the cumulative covering fractions of Mg II (solid lines) using an equivalent with of $EW = 0.1$ Å (red lines) and $EW = 0.03$ Å (purple lines) together with their 1σ errors (dashed lines) for all galaxies with $M_* < 10^{10}$ $M_\odot$ from Dutta et al. (2021). At radii $R < 200$ kpc our covering fractions are much too high compared to observations, while at radii $R > 200$ kpc the median seems to match observations. We used a column density of 10^{12} cm^{-2} per pixel as a threshold for detection in the simulation.

Mg II				C IV			
z	10^{11} cm^{-2}	10^{12} cm^{-2}	10^{13} cm^{-2}	z	10^{12} cm^{-2}	10^{13} cm^{-2}	10^{14} cm^{-2}
0	0.9	0.5	0.25	0	10.6	2.2	0.033
1	1.03	0.47	0.2	1	7.4	1.6	0.03
3	0.25	0.32	0.09	3	3.4	0.13	0.0002

Table 5.1: Values of $l(z)$ for Mg II and C IV at different redshifts for three different detection limits. We calculated $l(z)$ with eq. (5.2).

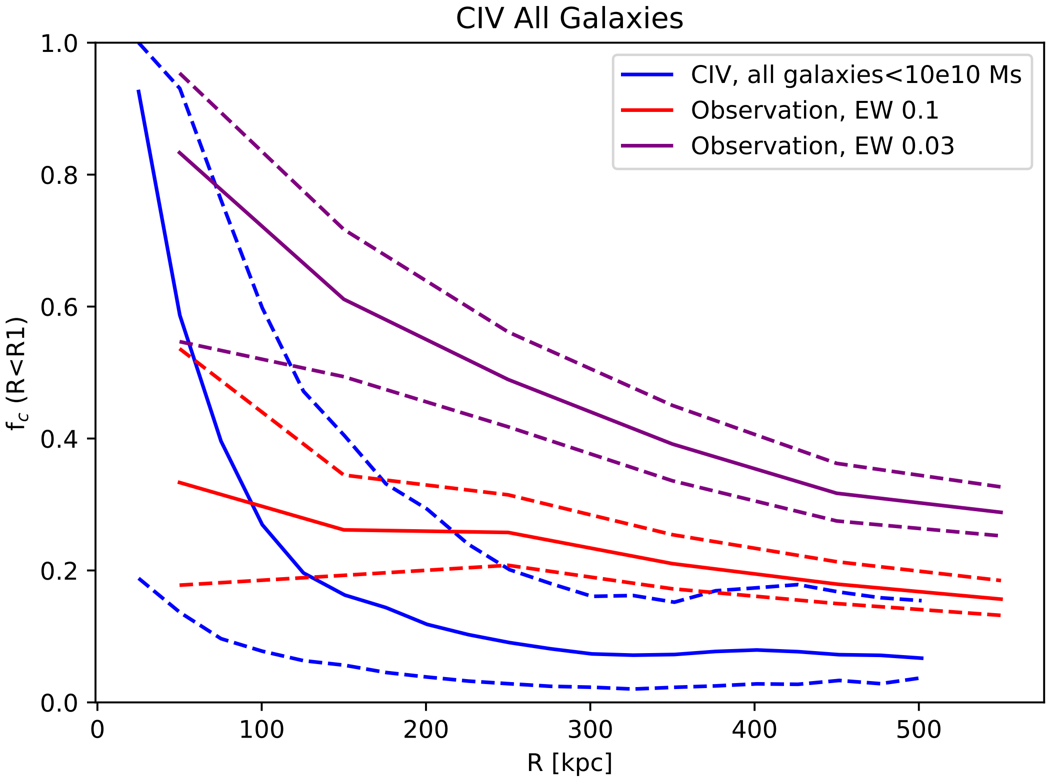

Figure 5.12: Covering fraction of C IV in our simulation (blue lines) overplotted with the cumulative covering fractions of C IV using an equivalent with of $EW = 0.1$ Å (red solid lines) and $EW = 0.03$ Å (purple solid lines) together with their 1σ errors (dashed lines) for all galaxies with $M_* < 10^{10}$ $\mathrm{M}_\odot$ from Dutta et al. (2021). At radii $R < 100$ kpc our covering fraction sees a sharp upturn which is not seen in observations, while at radii $R > 150$ kpc our covering fractions are too low. We used a column density of 10^{13} cm^{-2} per pixel as a threshold for detection in the simulation.

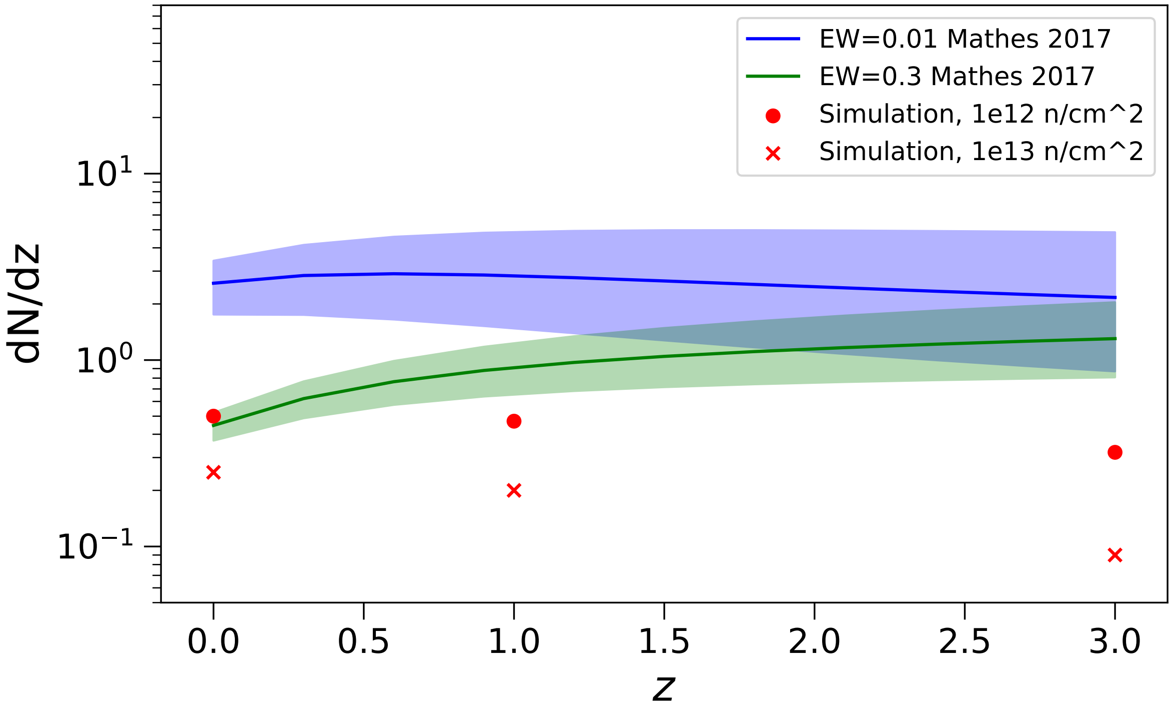

Figure 5.13: Mg II absorbers per unit redshift at different redshifts. We show the values from the simulation at $z = 0$, $z = 1$ and $z = 3$ for a detection limit of 10^{12} cm^{-2} and 10^{13} cm^{-2}. We compare it to the parametrization for dN/dz from Mathes et al. (2017) which we obtained by transforming their parametrization for dN/dX from their eq. (7) and their Table 1. We show the results for an equivalent width of $EW = 0.01$ Å which corresponds to a column density detection limit of 2.3×10^{11} cm^{-2} and $EW = 0.3$ Å which corresponds to a column density detection limit of 7×10^{12} cm^{-2}. Ideally, our results for a detection limit of 10^{12} cm^{-2} should lie between the two curves for $EW = 0.01$ Å and $EW = 0.3$ Å. However, apart from $z = 0$ which is on the line of $EW = 0.3$ Å all the other measurements are below that line and therefore too low. This means we do not have enough Mg II absorbers in our simulation volume.

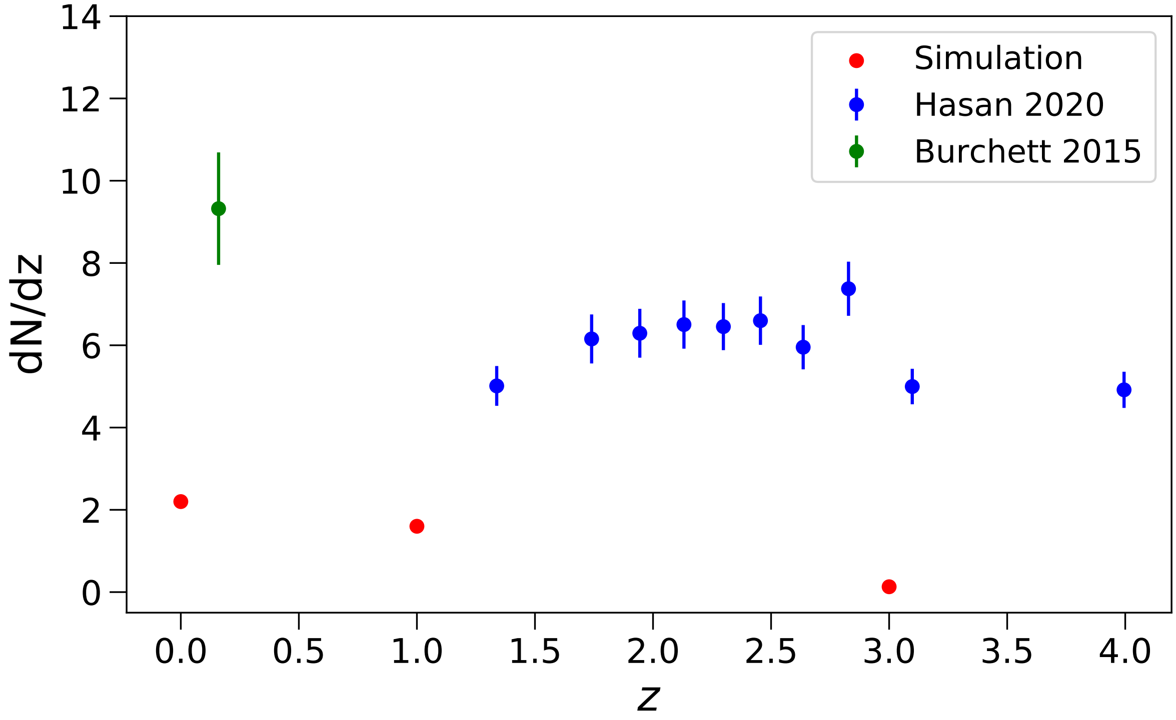

Figure 5.14: C IV absorbers per unit redshift for different redshifts. We show the values from the simulation at $z = 0$, $z = 1$ and $z = 3$ for a detection limit of 10^{13} cm^{-2} and compare them with the values from Hasan et al. (2020) and Burchett et al. (2015) for an equivalent width $EW = 0.05$ Å which corresponds to 1.24×10^{13} cm^{-2}. Since the values we get in the simulation are far below the values from observations, there are not enough C IV absorbers in our simulation.

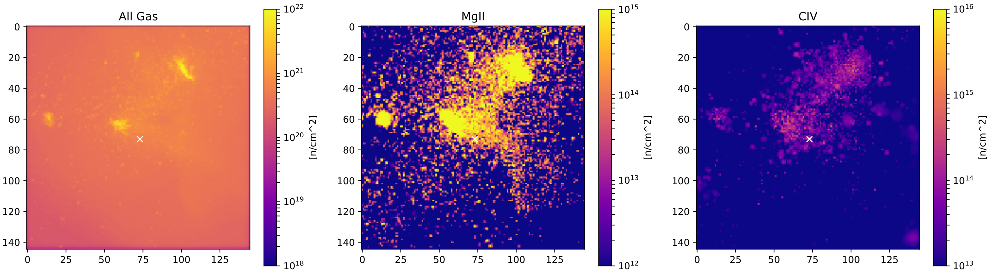

Figure 5.15: Column density of all the gas in the simulation (left panel), Mg II (middle panel) and C IV (right panel) where the ions have been obtained by using `TRIDENT` during post-processing. We can see that in the left panel, the column density of the total gas distribution is smooth. However, in the middle and right panel where the column density for the two ions is shown the column density seems to be very pixelated instead of smooth as we would expect. This let us suspect that something during the post-processing of the ionization states by `TRIDENT` went wrong.

(2017) they define dN/dX as:

$$dN/dX = f(z) \equiv \frac{c}{H_0} n_0 \sigma_0 (1+z)^{\epsilon}. \tag{5.3}$$

For an equivalent width of $EW = 0.01$ Å, the prefactor is parametrized as $\frac{c}{H_0} n_0 \sigma_0 = 2.583 \pm 0.827$ and $\epsilon = -1.04 \pm 0.38$, while for $EW = 0.3$ Å they have $\frac{c}{H_0} n_0 \sigma_0 = 0.446 \pm 0.076$ and $\epsilon = -0.14 \pm 0.21$ (Mathes et al., 2017). We then transform dN/dX to dN/dz by eq. (5.4). Looking at our results in Fig. 5.13 we can see that we do not have enough Mg II absorbers in our simulation.

In Fig. 5.14 we compare $l(z)$ for C IV from our simulation with the results from Hasan et al. (2020) and Burchett et al. (2015). They both give the results in terms of dN/dX which we have to transform to dN/dz using Hasan et al. (2020):

$$\frac{dN(z)}{dz} = \frac{dN(z)}{dX} \frac{dX}{dz}, \tag{5.4}$$

where dX/dz is defined as Hasan et al. (2020):

$$\frac{dX}{dz} = \frac{(1+z)^2}{\sqrt{\Omega_M (1+z)^3 + \Omega_\Lambda}}. \tag{5.5}$$

Looking at Fig. 5.14 we see the same result for C IV as we already had for Mg II. We are not able to reproduce observations and instead have too little C IV absorbers in our simulation.

Since also $l(z)$ did not match the results of observations we did a closer investigation on the distribution of ions around galaxies. For that we plotted the gas distribution as well as the distribution of Mg II and C IV around the simulated galaxies. We show an example galaxy in Fig. 5.15. We can see that the distribution of all the gas in the left panel is smooth, while the middle and the right panel showing the distribution of Mg II and C IV from post-processing are rather pixelated. Therefore, we were suspecting that something during the post-processing of the ionization states with `TRIDENT` went wrong. One reason for the behavior in Fig. 5.15 might be that we used the normal element abundances when doing the post-processing with `TRIDENT` instead of the smoothed element abundances. However, we did not explore any further whether the use of the smoothed element abundance improves the results and how this would change $l(z)$.

Another reason for the disagreement between $l(z)$ from our simulation and $l(z)$ from observations might be that the simulation we used is not calibrated to give the right element abundances. Therefore, we cannot guarantee that we get the right amount of ions during post-processing with `TRIDENT`, since this of course depends on the element abundances. In other words, we might get the right abundance just by chance or we might be off. Therefore, a direct comparison between simulation and observations using metals and their ionization states can easily lead to wrong conclusions. The uncertainty about the right element abundances together with the problem of not being able to reproduce $l(z)$ or the covering fractions for Mg II and C IV in our galaxy sample let us abandon the approach to use ionization states from post-processing for our analysis. Instead, we used a split into different gas phases. These results were presented in Sec. 5.2.

Chapter 6

Conclusions and Future Research

In this thesis, we wanted to know how the environment influences galaxies. We split this question into two parts. First, we wanted to know how interactions with the environment like ram pressure stripping and tidal stripping affect the gas and dark matter content of galaxies. In Ch. 3 we investigated the influence of such interactions on the final gas and dark matter mass of field dwarf galaxies, while in Ch. 4 we checked whether such interactions can produce dark matter deficient galaxies in isolation. Second, we wanted to know whether ram pressure stripping changes the CGM of the host and whether that can explain the observed dependence of a galaxies CGM on the large-scale structure in which the galaxy is embedded.

Using a high-resolution hydrodynamical cosmological simulation we found in Ch. 3 that two distinct processes can influence the evolution and final properties of field dwarf galaxies. The first one termed "cosmic web stripping", removes gas from galaxies by hydrodynamical interactions when ploughing through cosmic web filaments. This process can shut down star formation in galaxies and makes them gas-deficient at $z = 0$. About 10% of the total sample is undergoing this process, while it is more important for dwarf galaxies.

The second process that we termed "flyby" process removes from galaxies both, gas due to hydrodynamic interactions and dark matter due to tidal interactions when close to a more massive host. After this interaction, they leave the host and are again found in isolation at $z = 0$. Almost all galaxies undergoing the flyby process are devoid of gas after the interaction. Furthermore, these galaxies are scattered off the stellar mass-halo mass relation due to the loss of dark matter. This allows the creation of galaxies with a halo mass below the minimum mass for star formation. About 15% of the total sample are flyby galaxies, with the majority of them being dwarf galaxies. Furthermore, below a halo mass of about 3×10^8 $\mathrm{M}_\odot$ all galaxies are flyby galaxies implying that any isolated galaxy with a halo mass below that limit must have undergone the flyby process.

Since we found a process that not only can remove dark matter from galaxies but lets them also be isolated at $z = 0$, we wanted to know in Ch. 4 whether we can find dark matter deficient field galaxies in our simulation. After a thorough search, we concluded that there are no dark matter-deficient galaxies in our simulation.

We then turned to the question of how the large-scale environment a galaxy is embedded in influences its CGM in Ch. 5. In a first attempt to model that systematically in a cosmological context, we found that galaxies in groups have slightly more gas in their CGM compared to galaxies in isolation. This effect is strongly enhanced if one includes satellite galaxies in the sample. Furthermore, also the use of a velocity window to assign gas to galaxies can increase the measured gas mass around a galaxy. Additionally, we checked whether ionization states from post-processing can be used to make a direct comparison with observations. However, since we were not able to reproduce several observable, we concluded that this is not possible with our simulation.

Although some progress was made in understanding the connection between the environment and the evolution of galaxies, some questions remained open. First, we could not assess whether there are galaxies in our simulation that only resemble the dark matter deficient galaxies found by van Dokkum et al. (2018b) and van Dokkum et al. (2019a) instead of being truly dark matter deficient. Second, we were not able to determine, whether ram pressure stripping plays a role in the enhanced covering fractions of Mg II and C IV. Both these questions are worth a deeper investigation but is left for future work.

Additionally, this thesis also opened up new research questions. For example, how would a change in the dark matter model influence the results of tidal stripping? A naive expectation would be that both with warm dark matter and self-interacting dark matter the stripping is more efficient, since in the case of warm dark matter it is less bound, while in the case of self-interacting dark matter, a ram pressure like force would also act on the dark matter particles. Furthermore, it would be worth investigating whether the change in the underlying dark matter model then allows the creation of dark matter-deficient field galaxies. Another open question is how tidal stripping of dark matter halos influences the shapes of these haloes. Since the shape of a dark matter halo is one of the necessary pieces of information when using Jeans modelling codes, a systematic study comparing the shapes of haloes before and after stripping is desireable. These are the questions which I hope to adress in my future research.

Bibliography

Abadi, M. G., Moore, B., and Bower, R. G. (1999). Ram pressure stripping of spiral galaxies in clusters. *MNRAS*, 308(4):947–954.

Abell, G. O. (1958). The Distribution of Rich Clusters of Galaxies. *ApJS*, 3:211.

Albrecht, A. and Steinhardt, P. J. (1982). Cosmology for Grand Unified Theories with Radiatively Induced Symmetry Breaking. *Phys. Rev. Lett.*, 48(17):1220–1223.

Angulo, R. E. and Hahn, O. (2022). Large-scale dark matter simulations. *Living Reviews in Computational Astrophysics*, 8(1):1.

Applebaum, E., Brooks, A. M., Christensen, C. R., Munshi, F., Quinn, T. R., Shen, S., and Tremmel, M. (2021). Ultrafaint Dwarfs in a Milky Way Context: Introducing the Mint Condition DC Justice League Simulations. *ApJ*, 906(2):96.

Appleby, S., Davé, R., Sorini, D., Storey-Fisher, K., and Smith, B. (2021). The low-redshift circumgalactic medium in SIMBA. *MNRAS*, 507(2):2383–2404.

Arbey, A. and Mahmoudi, F. (2021). Dark matter and the early Universe: A review. *Progress in Particle and Nuclear Physics*, 119:103865.

Babul, A. and Rees, M. J. (1992). On dwarf elliptical galaxies and the faint blue counts. *MNRAS*, 255:346–350.

Bacon, R., Accardo, M., Adjali, L., Anwand, H., Bauer, S., Biswas, I., Blaizot, J., Boudon, D., Brau-Nogue, S., Brinchmann, J., Caillier, P., Capoani, L., Carollo, C. M., Contini, T., Couderc, P., Daguisé, E., Deiries, S., Delabre, B., Dreizler, S., Dubois, J., Dupieux, M., Dupuy, C., Emsellem, E., Fechner, T., Fleischmann, A., François, M., Gallou, G., Gharsa, T., Glindemann, A., Gojak, D., Guiderdoni, B., Hansali, G., Hahn, T., Jarno, A., Kelz, A., Koehler, C., Kosmalski, J., Laurent, F., Le Floch, M., Lilly, S. J., Lizon, J. L., Loupias, M., Manescau, A., Monstein, C., Nicklas, H., Olaya, J. C., Pares, L., Pasquini, L., Pécontal-Rousset, A., Pelló, R., Petit, C., Popow, E., Reiss, R., Remillieux, A., Renault, E., Roth, M., Rupprecht, G., Serre, D., Schaye, J., Soucail, G., Steinmetz, M., Streicher, O., Stuik, R., Valentin, H., Vernet, J., Weilbacher, P., Wisotzki, L., and Yerle, N. (2010). The MUSE second-generation VLT instrument. In McLean, I. S., Ramsay, S. K., and Takami, H., editors, *Ground-based and Airborne Instrumentation* *for Astronomy III*, volume 7735 of *Society of Photo-Optical Instrumentation Engineers (SPIE) Conference Series*, page 773508.

Bacon, R., Bauer, S., Boehm, P., Boudon, D., Brau-Nogué, S., Caillier, P., Capoani, L., Carollo, C. M., Champavert, N., Contini, T., Daguisé, E., Dallé, D., Delabre, B., Devriendt, J., Dreizler, S., Dubois, J., Dupieux, M., Dupin, J. P., Emsellem, E., Ferruit, P., Franx, M., Gallou, G., Gerssen, J., Guiderdoni, B., Hahn, T., Hofmann, D., Jarno, A., Kelz, A., Koehler, C., Kollatschny, W., Kosmalski, J., Laurent, F., Lilly, S. J., Lizon, J., Loupias, M., Lynn, S., Manescau, A., McDermid, R. M., Monstein, C., Nicklas, H., Parès, L., Pasquini, L., Pécontal-Rousset, A., Pécontal, E., Pello, R., Petit, C., Picat, J. P., Popow, E., Quirrenbach, A., Reiss, R., Renault, E., Roth, M., Schaye, J., Soucail, G., Steinmetz, M., Stroebele, S., Stuik, R., Weilbacher, P., Wozniak, H., and de Zeeuw, P. T. (2006). Probing unexplored territories with MUSE: a second generation instrument for the VLT. In McLean, I. S. and Iye, M., editors, *Ground-based and Airborne Instrumentation for Astronomy*, volume 6269 of *Society of Photo-Optical Instrumentation Engineers (SPIE) Conference Series*, page 62690J.

Balogh, M. L., Navarro, J. F., and Morris, S. L. (2000). The Origin of Star Formation Gradients in Rich Galaxy Clusters. *ApJ*, 540(1):113–121.

Banerjee, E., Muzahid, S., Schaye, J., Johnson, S. D., and Cantalupo, S. (2023). MUSEQuBES: the relation between Ly α emitters and C IV absorbers at z $\approx$ 3.3. *MNRAS*, 524(4):5148–5165.

Barnes, J. and Hut, P. (1986). A hierarchical O(N log N) force-calculation algorithm. *Nature*, 324(6096):446–449.

Behroozi, P., Wechsler, R. H., Hearin, A. P., and Conroy, C. (2019). UNIVERSEMACHINE: The correlation between galaxy growth and dark matter halo assembly from z = 0-10. *MNRAS*, 488(3):3143–3194.

Behroozi, P. S., Wechsler, R. H., Lu, Y., Hahn, O., Busha, M. T., Klypin, A., and Primack, J. R. (2014). Mergers and Mass Accretion for Infalling Halos Both End Well Outside Cluster Virial Radii. *ApJ*, 787(2):156.

Behroozi, P. S., Wechsler, R. H., and Wu, H.-Y. (2013). The ROCKSTAR Phase-space Temporal Halo Finder and the Velocity Offsets of Cluster Cores. *ApJ*, 762(2):109.

Benavides, J. A., Sales, L. V., Abadi, M. G., Pillepich, A., Nelson, D., Marinacci, F., Cooper, M., Pakmor, R., Torrey, P., Vogelsberger, M., and Hernquist, L. (2021). Quiescent ultra-diffuse galaxies in the field originating from backsplash orbits. *Nature Astronomy*, 5:1255–1260.

Benitez-Llambay, A. (2015). Py-Sphviewer: Py-Sphviewer V1.0.0. Zenodo.

Benitez-Llambay, A. and Frenk, C. (2020). The detailed structure and the onset of galaxy formation in low-mass gaseous dark matter haloes. *MNRAS*, 498(4):4887–4900.

Benítez-Llambay, A., Frenk, C. S., Ludlow, A. D., and Navarro, J. F. (2019). Baryon-induced dark matter cores in the EAGLE simulations. *MNRAS*, 488(2):2387–2404.

Benitez-Llambay, A. and Fumagalli, M. (2021). The tail of late-forming dwarf galaxies in Λcdm. *The Astrophysical Journal Letters*, 921(1):L9.

Benítez-Llambay, A., Navarro, J. F., Abadi, M. G., Gottlöber, S., Yepes, G., Hoffman, Y., and Steinmetz, M. (2013). Dwarf Galaxies and the Cosmic Web. *ApJ*, 763(2):L41.

Benítez-Llambay, A., Navarro, J. F., Frenk, C. S., Sawala, T., Oman, K., Fattahi, A., Schaller, M., Schaye, J., Crain, R. A., and Theuns, T. (2017). The properties of 'dark' ΛCDM haloes in the Local Group. *MNRAS*, 465(4):3913–3926.

Benson, A. J., Lacey, C. G., Baugh, C. M., Cole, S., and Frenk, C. S. (2002). The effects of photoionization on galaxy formation - I. Model and results at z=0. *MNRAS*, 333(1):156–176.

Bhattacharyya, J., Peter, A. H. G., Martini, P., Mutlu-Pakdil, B., Drlica-Wagner, A., Pace, A. B., Strigari, L. E., Cheng, Y. T., Roberts, D., Tanoglidis, D., Aguena, M., Alves, O., Andrade-Oliveira, F., Bacon, D., Brooks, D., Carnero Rosell, A., Carretero, J., da Costa, L. N., Pereira, M. E. S., Davis, T. M., Desai, S., Doel, P., Ferrero, I., Frieman, J., García-Bellido, J., Giannini, G., Gruen, D., Gruendl, R. A., Hinton, S. R., Hollowood, D. L., Honscheid, K., James, D. J., Kuehn, K., Marshall, J. L., Mena-Fernández, J., Miquel, R., Palmese, A., Pieres, A., Plazas Malagón, A. A., Sanchez, E., Santiago, B., Schubnell, M., Sevilla-Noarbe, I., Smith, M., Suchyta, E., Swanson, M. E. C., Tarle, G., Vincenzi, M., Walker, A. R., Weaverdyck, N., and Wiseman, P. (2023). Environmental Quenching of Low Surface Brightness Galaxies near Milky Way mass Hosts. *arXiv e-prints*, page arXiv:2312.00773.

Birrer, S. et al. (2020). TDCOSMO - IV. Hierarchical time-delay cosmography – joint inference of the Hubble constant and galaxy density profiles. *Astron. Astrophys.*, 643:A165.

Blakeslee, J. P., Jensen, J. B., Ma, C.-P., Milne, P. A., and Greene, J. E. (2021). The Hubble Constant from Infrared Surface Brightness Fluctuation Distances. *Astrophys. J.*, 911(1):65.

Blanton, M. R. and Moustakas, J. (2009). Physical Properties and Environments of Nearby Galaxies. *ARA&A*, 47(1):159–210.

Blumenthal, G. R., Faber, S. M., Primack, J. R., and Rees, M. J. (1984). Formation of galaxies and large-scale structure with cold dark matter. *Nature*, 311:517–525.

Bordoloi, R., Lilly, S. J., Knobel, C., Bolzonella, M., Kampczyk, P., Carollo, C. M., Iovino, A., Zucca, E., Contini, T., Kneib, J. P., Le Fevre, O., Mainieri, V., Renzini, A., Scodeggio, M., Zamorani, G., Balestra, I., Bardelli, S., Bongiorno, A., Caputi, K., Cucciati, O., de la Torre, S., de Ravel, L., Garilli, B., Kovač, K., Lamareille, F., Le Borgne, J. F., Le Brun, V., Maier, C., Mignoli, M., Pello, R., Peng, Y., Perez Montero, E., Presotto, V., Scarlata, C., Silverman, J., Tanaka, M., Tasca, L., Tresse, L., Vergani, D., Barnes, L., Cappi, A., Cimatti, A., Coppa, G., Diener, C., Franzetti, P., Koekemoer, A., López-Sanjuan, C., McCracken, H. J., Moresco, M., Nair, P., Oesch, P., Pozzetti, L., and Welikala, N. (2011). The Radial and Azimuthal Profiles of Mg II Absorption around 0.5 ¡ z ¡ 0.9 zCOSMOS Galaxies of Different Colors, Masses, and Environments. *ApJ*, 743(1):10.

Bose, S., Hellwing, W. A., Frenk, C. S., Jenkins, A., Lovell, M. R., Helly, J. C., Li, B., Gonzalez-Perez, V., and Gao, L. (2017). Substructure and galaxy formation in the Copernicus Complexio warm dark matter simulations. *MNRAS*, 464(4):4520–4533.

Boselli, A., Cuillandre, J. C., Fossati, M., Boissier, S., Bomans, D., Consolandi, G., Anselmi, G., Cortese, L., Côté, P., Durrell, P., Ferrarese, L., Fumagalli, M., Gavazzi, G., Gwyn, S., Hensler, G., Sun, M., and Toloba, E. (2016). Spectacular tails of ionized gas in the Virgo cluster galaxy NGC 4569. *A&A*, 587:A68.

Boselli, A., Fossati, M., and Sun, M. (2022). Ram pressure stripping in high-density environments. *A&ARv*, 30(1):3.

Boselli, A., Serra, P., de Gasperin, F., Vollmer, B., Amram, P., Edler, H. W., Fossati, M., Consolandi, G., Côté, P., Cuillandre, J. C., Ferrarese, L., Gwyn, S., Postma, J., Boquien, M., Braine, J., Combes, F., Gavazzi, G., Hensler, G., Miville-Deschenes, M. A., Murgia, M., Roediger, J., Roehlly, Y., Smith, R., Zhang, H. X., and Zabel, N. (2023). ViCTORIA project: MeerKAT H I observations of the ram pressure stripped galaxy NGC 4523. *A&A*, 676:A92.

Bosma, A. (1981). 21-cm line studies of spiral galaxies. II. The distribution and kinematics of neutral hydrogen in spiral galaxies of various morphological types. *AJ*, 86:1825–1846.

Boveia, A., Berkat, M., Chen, T. Y., Desai, A., Doglioni, C., Drlica-Wagner, A., Gardner, S., Gori, S., Greaves, J., Harding, P., Harris, P. C., Lippincott, W. H., Monzani, M. E., Pachal, K., Prescod-Weinstein, C., Rybka, G., Shakya, B., Shelton, J., Slatyer, T. R., Steinhebel, A., Tanedo, P., Toro, N., Tsai, Y.-T., Williams, M., Winslow, L., Yu, J., and Yu, T.-T. (2022). Snowmass 2021 Dark Matter Complementarity Report. *arXiv e-prints*, page arXiv:2211.07027.

Bromm, V. and Yoshida, N. (2011). The First Galaxies. *ARA&A*, 49(1):373–407.

Brout, R., Englert, F., and Gunzig, E. (1978). The creation of the Universe as a quantum phenomenon. *Annals of Physics*, 115:78–106.

Bullock, J. S. and Boylan-Kolchin, M. (2017). Small-Scale Challenges to the ΛCDM Paradigm. *ARA&A*, 55(1):343–387.

Bullock, J. S., Kravtsov, A. V., and Weinberg, D. H. (2000). Reionization and the Abundance of Galactic Satellites. *ApJ*, 539(2):517–521.

Burchett, J. N., Tripp, T. M., Bordoloi, R., Werk, J. K., Prochaska, J. X., Tumlinson, J., Willmer, C. N. A., O'Meara, J., and Katz, N. (2016). A Deep Search for Faint Galaxies Associated with Very Low Redshift C IV Absorbers. III. The Mass- and Environment-dependent Circumgalactic Medium. *ApJ*, 832(2):124.

Burchett, J. N., Tripp, T. M., Prochaska, J. X., Werk, J. K., Tumlinson, J., O'Meara, J. M., Bordoloi, R., Katz, N., and Willmer, C. N. A. (2015). A Deep Search For Faint Galaxies Associated With Very Low-redshift C IV Absorbers. II. Program Design, Absorption-line Measurements, and Absorber Statistics. *ApJ*, 815(2):91.

Burchett, J. N., Tripp, T. M., Wang, Q. D., Willmer, C. N. A., Bowen, D. V., and Jenkins, E. B. (2018). Warm-hot gas in X-ray bright galaxy clusters and the H I-deficient circumgalactic medium in dense environments. *MNRAS*, 475(2):2067–2085.

Butsky, I. S., Werk, J. K., Tchernyshyov, K., Fielding, D. B., Breneman, J., Piacitelli, D. R., Quinn, T. R., Sanchez, N. N., Cruz, A., Hummels, C. B., Burchett, J. N., and Tremmel, M. (2022). The Impact of Cosmic Rays on the Kinematics of the Circumgalactic Medium. *ApJ*, 935(2):69.

Carleton, T., Ellsworth-Bowers, T., Windhorst, R. A., Cohen, S. H., Conselice, C. J., Diego, J. M., Zitrin, A., Archer, H. N., McIntyre, I., Kamieneski, P., Jansen, R. A., Summers, J., D'Silva, J. C. J., Koekemoer, A. M., Coe, D., Driver, S. P., Frye, B., Grogin, N. A., Marshall, M. A., Nonino, M., Pirzkal, N., Robotham, A., Ryan, R. E., Ortiz, Rafael, I., Tompkins, S., Willmer, C. N. A., Yan, H., and Holwerda, B. W. (2024). PEARLS: A Potentially Isolated Quiescent Dwarf Galaxy with a Tip of the Red Giant Branch Distance of 30 Mpc. *ApJ*, 961(2):L37.

Casey, K. J., Greco, J. P., Peter, A. H. G., and Davis, A. B. (2023). Discovery of a red backsplash galaxy candidate near M81. *MNRAS*, 520(3):4715–4729.

Cattorini, F., Gavazzi, G., Boselli, A., and Fossati, M. (2023). A complete spectroscopic catalogue of local galaxies in the northern spring sky: Gas properties and nuclear activity in different environments. *A&A*, 671:A118.

Chabrier, G. (2003). Galactic Stellar and Substellar Initial Mass Function. *PASP*, 115(809):763–795.

Comerón, S., Trujillo, I., Cappellari, M., Buitrago, F., Garduño, L. E., Zaragoza-Cardiel, J., Zinchenko, I. A., Lara-López, M. A., Ferré-Mateu, A., and Dib, S. (2023). The massive relic galaxy NGC 1277 is dark matter deficient. From dynamical models of integral-field stellar kinematics out to five effective radii. *A&A*, 675:A143.

Crain, R. A., Schaye, J., Bower, R. G., Furlong, M., Schaller, M., Theuns, T., Dalla Vecchia, C., Frenk, C. S., McCarthy, I. G., Helly, J. C., Jenkins, A., Rosas-Guevara, Y. M., White, S. D. M., and Trayford, J. W. (2015). The EAGLE simulations of galaxy formation: calibration of subgrid physics and model variations. *MNRAS*, 450(2):1937–1961.

Crain, R. A. and van de Voort, F. (2023). Hydrodynamical Simulations of the Galaxy Population: Enduring Successes and Outstanding Challenges. *ARA&A*, 61:473–515.

Dalla Vecchia, C. and Schaye, J. (2012). Simulating galactic outflows with thermal supernova feedback. *MNRAS*, 426(1):140–158.

Danieli, S., van Dokkum, P., Conroy, C., Abraham, R., and Romanowsky, A. J. (2019). Still Missing Dark Matter: KCWI High-resolution Stellar Kinematics of NGC1052-DF2. *ApJ*, 874(2):L12.

Davis, M., Efstathiou, G., Frenk, C. S., and White, S. D. M. (1985). The evolution of large-scale structure in a universe dominated by cold dark matter. *ApJ*, 292:371–394.

De Lucia, G., Fontanot, F., and Hirschmann, M. (2017). AGN feedback and the origin of the α enhancement in early-type galaxies - insights from the GAEA model. *MNRAS*, 466(1):L88–L92.

De Lucia, G., Fontanot, F., Xie, L., and Hirschmann, M. (2024). Tracing the Quenching Journey across Cosmic Time. *arXiv e-prints*, page arXiv:2401.06211.

De Lucia, G., Hirschmann, M., and Fontanot, F. (2019). Nature versus nurture: what regulates star formation in satellite galaxies? *MNRAS*, 482(4):5041–5051.

Dekel, A. and Silk, J. (1986). The Origin of Dwarf Galaxies, Cold Dark Matter, and Biased Galaxy Formation. *ApJ*, 303:39.

Diener, C., Lilly, S. J., Knobel, C., Zamorani, G., Lemson, G., Kampczyk, P., Scoville, N., Carollo, C. M., Contini, T., Kneib, J. P., Le Fevre, O., Mainieri, V., Renzini, A., Scodeggio, M., Bardelli, S., Bolzonella, M., Bongiorno, A., Caputi, K., Cucciati, O., de la Torre, S., de Ravel, L., Franzetti, P., Garilli, B., Iovino, A., Kovač, K., Lamareille, F., Le Borgne, J. F., Le Brun, V., Maier, C., Mignoli, M., Pello, R., Peng, Y., Perez Montero, E., Presotto, V., Silverman, J., Tanaka, M., Tasca, L., Tresse, L., Vergani, D., Zucca, E., Bordoloi, R., Cappi, A., Cimatti, A., Coppa, G., Koekemoer, A. M., López-Sanjuan, C., McCracken, H. J., Moresco, M., Nair, P., Pozzetti, L., and Welikala, N. (2013). Proto-groups at 1.8 ¡ z ¡ 3 in the zCOSMOS-deep Sample. *ApJ*, 765(2):109.

Dutta, R., Fumagalli, M., Fossati, M., Bielby, R. M., Stott, J. P., Lofthouse, E. K., Cantalupo, S., Cullen, F., Crain, R. A., Tripp, T. M., Prochaska, J. X., Arrigoni Battaia, F., Burchett, J. N., Fynbo, J. P. U., Murphy, M. T., Schaye, J., Tejos, N., and Theuns, T. (2021). Metal-enriched halo gas across galaxy overdensities over the last 10 billion years. *MNRAS*, 508(3):4573–4599.

Dutta, R., Fumagalli, M., Fossati, M., Lofthouse, E. K., Prochaska, J. X., Arrigoni Battaia, F., Bielby, R. M., Cantalupo, S., Cooke, R. J., Murphy, M. T., and O'Meara, J. M. (2020). MUSE Analysis of Gas around Galaxies (MAGG) - II: metal-enriched halo gas around z $\sim$ 1 galaxies. *MNRAS*, 499(4):5022–5046.

Efstathiou, G. (1992). Suppressing the formation of dwarf galaxies via photoionization. *MNRAS*, 256(2):43P–47P.

Einstein, A. (1915). Die Feldgleichungen der Gravitation. *Sitzungsberichte der Königlich Preussischen Akademie der Wissenschaften*, pages 844–847.

Einstein, A. (1916). Die Grundlage der allgemeinen Relativitätstheorie. *Annalen der Physik*, 354(7):769–822.

Eisenstein, D. J. and Hu, W. (1998). Baryonic Features in the Matter Transfer Function. *ApJ*, 496(2):605–614.

Eisenstein, D. J. and Hu, W. (1999). Power Spectra for Cold Dark Matter and Its Variants. *ApJ*, 511(1):5–15.

ESA, Euclid-Consortium, N. (2023). Euclid's view of perseus cluster. image processing by J.-C. Cuillandre (CEA Paris-Saclay), G. Anselmi, CC BY-SA 3.0 IGO from https://www.esa.int/ESA_Multimedia/Images (Last accessed 23 January 2023), Licence: https://creativecommons.org/licenses/by-sa/3.0/igo/.

Faber, S. M. and Gallagher, J. S. (1979). Masses and mass-to-light ratios of galaxies. *ARA&A*, 17:135–187.

Ferland, G. J., Korista, K. T., Verner, D. A., Ferguson, J. W., Kingdon, J. B., and Verner, E. M. (1998). CLOUDY 90: Numerical Simulation of Plasmas and Their Spectra. *PASP*, 110(749):761–778.

Ferland, G. J., Porter, R. L., van Hoof, P. A. M., Williams, R. J. R., Abel, N. P., Lykins, M. L., Shaw, G., Henney, W. J., and Stancil, P. C. (2013). The 2013 Release of Cloudy. *Rev. Mex. Astron. Astrofis.*, 49:137–163.

Fossati, M., Fumagalli, M., Lofthouse, E. K., D'Odorico, V., Lusso, E., Cantalupo, S., Cooke, R. J., Cristiani, S., Haardt, F., Morris, S. L., Peroux, C., Prichard, L. J., Rafelski, M., Smail, I., and Theuns, T. (2019). The MUSE Ultra Deep Field (MUDF). II. Survey design and the gaseous properties of galaxy groups at 0.5 ¡ z ¡ 1.5. *MNRAS*, 490(1):1451–1469.

Frenk, C. S., White, S. D. M., Efstathiou, G., and Davis, M. (1985). Cold dark matter, the structure of galactic haloes and the origin of the Hubble sequence. *Nature*, 317(6038):595–597.

Friedmann, A. (1922). Über die Krümmung des Raumes. *Zeitschrift fur Physik*, 10:377–386.

Friedmann, A. (1924). Über die Möglichkeit einer Welt mit konstanter negativer Krümmung des Raumes. *Zeitschrift fur Physik*, 21(1):326–332.

Fumagalli, M., Prochaska, J. X., Kasen, D., Dekel, A., Ceverino, D., and Primack, J. R. (2011). Absorption-line systems in simulated galaxies fed by cold streams. *MNRAS*, 418(3):1796–1821.

Galbiati, M., Fumagalli, M., Fossati, M., Lofthouse, E. K., Dutta, R., Prochaska, J. X., Murphy, M. T., and Cantalupo, S. (2023). MUSE Analysis of Gas around Galaxies (MAGG) – V: Linking ionized gas traced by CIV and SiIV absorbers to Lyα emitting galaxies at $z \approx 3.0 - 4.5$. *arXiv e-prints*, page arXiv:2302.00021.

Genina, A., Frenk, C. S., Benítez-Llambay, A., Cole, S., Navarro, J. F., Oman, K. A., and Fattahi, A. (2019). The distinct stellar metallicity populations of simulated Local Group dwarfs. *MNRAS*, 488(2):2312–2331.

Gill, S. P. D., Knebe, A., and Gibson, B. K. (2005). The evolution of substructure - III. The outskirts of clusters. *MNRAS*, 356(4):1327–1332.

Gingold, R. A. and Monaghan, J. J. (1977). Smoothed particle hydrodynamics: theory and application to non-spherical stars. *MNRAS*, 181:375–389.

Gonzalez-Perez, V., Lacey, C. G., Baugh, C. M., Lagos, C. D. P., Helly, J., Campbell, D. J. R., and Mitchell, P. D. (2014). How sensitive are predicted galaxy luminosities to the choice of stellar population synthesis model? *MNRAS*, 439(1):264–283.

Gunn, J. E. and Gott, J. Richard, I. (1972). On the Infall of Matter Into Clusters of Galaxies and Some Effects on Their Evolution. *ApJ*, 176:1.

Guo, Q., Hu, H., Zheng, Z., Liao, S., Du, W., Mao, S., Jiang, L., Wang, J., Peng, Y., Gao, L., Wang, J., and Wu, H. (2020). Further evidence for a population of dark-matter-deficient dwarf galaxies. *Nature Astronomy*, 4:246–251.

Guo, Q., White, S., Li, C., and Boylan-Kolchin, M. (2010). How do galaxies populate dark matter haloes? *MNRAS*, 404(3):1111–1120.

Guth, A. H. (1981). Inflationary universe: A possible solution to the horizon and flatness problems. *Phys. Rev. D*, 23(2):347–356.

Haardt, F. and Madau, P. (2001). Modelling the UV/X-ray cosmic background with CUBA. In Neumann, D. M. and Tran, J. T. V., editors, *Clusters of Galaxies and the High Redshift Universe Observed in X-rays*, page 64.

Haardt, F. and Madau, P. (2012). Radiative Transfer in a Clumpy Universe. IV. New Synthesis Models of the Cosmic UV/X-Ray Background. *ApJ*, 746(2):125.

Hafen, Z., Faucher-Giguère, C.-A., Anglés-Alcázar, D., Kereš, D., Feldmann, R., Chan, T. K., Quataert, E., Murray, N., and Hopkins, P. F. (2017). Low-redshift Lyman limit systems as diagnostics of cosmological inflows and outflows. *MNRAS*, 469(2):2292–2304.

Hahn, O. and Abel, T. (2011). Multi-scale initial conditions for cosmological simulations. *MNRAS*, 415(3):2101–2121.

Han, J., Cole, S., Frenk, C. S., Benitez-Llambay, A., and Helly, J. (2018). HBT+: an improved code for finding subhaloes and building merger trees in cosmological simulations. *MNRAS*, 474(1):604–617.

Hani, M. H., Ellison, S. L., Sparre, M., Grand, R. J. J., Pakmor, R., Gomez, F. A., and Springel, V. (2019). The diversity of the circumgalactic medium around z = 0 Milky Way-mass galaxies from the Auriga simulations. *MNRAS*, 488(1):135–152.

Hani, M. H., Sparre, M., Ellison, S. L., Torrey, P., and Vogelsberger, M. (2018). Galaxy mergers moulding the circum-galactic medium - I. The impact of a major merger. *MNRAS*, 475(1):1160–1176.

Hasan, F., Churchill, C. W., Stemock, B., Mathes, N. L., Nielsen, N. M., Finlator, K., Doughty, C., Croom, M., Kacprzak, G. G., and Murphy, M. T. (2020). Evolution of C IV Absorbers. I. The Cosmic Incidence. *ApJ*, 904(1):44.

Herzog, G., Benítez-Llambay, A., and Fumagalli, M. (2023). The present-day gas content of simulated field dwarf galaxies. *MNRAS*, 518(4):6305–6317.

Ho, S. H., Martin, C. L., and Schaye, J. (2020). Morphological and Rotation Structures of Circumgalactic Mg II Gas in the EAGLE Simulation and the Dependence on Galaxy Properties. *ApJ*, 904(1):76.

Hobson, M. P., Efstathiou, G. P., and Lasenby, A. N. (2006). *General Relativity: An Introduction for Physicists*. Cambridge University Press.

Hopkins, P. F. (2013). A general class of Lagrangian smoothed particle hydrodynamics methods and implications for fluid mixing problems. *MNRAS*, 428(4):2840–2856.

Hubble, E. (1929). A Relation between Distance and Radial Velocity among Extra-Galactic Nebulae. *Proceedings of the National Academy of Science*, 15(3):168–173.

Hummels, C. B., Smith, B. D., and Silvia, D. W. (2017). Trident: A Universal Tool for Generating Synthetic Absorption Spectra from Astrophysical Simulations. *ApJ*, 847(1):59.

Ikeuchi, S. (1986). The baryon clump within an extended dark matter region. *Ap&SS*, 118(1-2):509–514.

Izquierdo-Villalba, D., Sesana, A., Bonoli, S., and Colpi, M. (2022). Massive black hole evolution models confronting the n-Hz amplitude of the stochastic gravitational wave background. *MNRAS*, 509(3):3488–3503.

Izquierdo-Villalba, D., Sesana, A., and Colpi, M. (2023). Unveiling the hosts of parsec-scale massive black hole binaries: morphology and electromagnetic signatures. *MNRAS*, 519(2):2083–2100.

Jackson, R. A., Kaviraj, S., Martin, G., Devriendt, J. E. G., Slyz, A., Silk, J., Dubois, Y., Yi, S. K., Pichon, C., Volonteri, M., Choi, H., Kimm, T., Kraljic, K., and Peirani, S. (2021). Dark matter-deficient dwarf galaxies form via tidal stripping of dark matter in interactions with massive companions. *MNRAS*, 502(2):1785–1796.

Karachentsev, I. D., Kaisina, E. I., and Makarov, D. I. (2014). Suites of Dwarfs around nearby Giant Galaxies. *AJ*, 147(1):13.

Katz, N., Weinberg, D. H., and Hernquist, L. (1996). Cosmological Simulations with TreeSPH. *ApJS*, 105:19.

Kazanas, D. (1980). Dynamics of the universe and spontaneous symmetry breaking. *ApJ*, 241:L59–L63.

Keim, M. A., van Dokkum, P., Danieli, S., Lokhorst, D., Li, J., Shen, Z., Abraham, R., Chen, S., Gilhuly, C., Liu, Q., Merritt, A., Miller, T. B., Pasha, I., and Polzin, A. (2022). Tidal Distortions in NGC1052-DF2 and NGC1052-DF4: Independent Evidence for a Lack of Dark Matter. *ApJ*, 935(2):160.

Kennicutt, Robert C., J. (1998). The Global Schmidt Law in Star-forming Galaxies. *ApJ*, 498(2):541–552.

Kenyon, I. R. (2023). *Introduction to General Relativity and Cosmology (Second Edition)*. 2514-3433. IOP Publishing.

Kirshner, R. P. (2004). Hubble's diagram and cosmic expansion. *Proceedings of the National Academy of Science*, 101(1):8–13.

Knebe, A., Knollmann, S. R., Muldrew, S. I., Pearce, F. R., Aragon-Calvo, M. A., Ascasibar, Y., Behroozi, P. S., Ceverino, D., Colombi, S., Diemand, J., Dolag, K., Falck, B. L., Fasel, P., Gardner, J., Gottlöber, S., Hsu, C.-H., Iannuzzi, F., Klypin, A., Lukić, Z., Maciejewski, M., McBride, C., Neyrinck, M. C., Planelles, S., Potter, D., Quilis, V., Rasera, Y., Read, J. I., Ricker, P. M., Roy, F., Springel, V., Stadel, J., Stinson, G., Sutter, P. M., Turchaninov, V., Tweed, D., Yepes, G., and Zemp, M. (2011a). Haloes gone MAD: The Halo-Finder Comparison Project. *MNRAS*, 415(3):2293–2318.

Knebe, A., Libeskind, N. I., Knollmann, S. R., Martinez-Vaquero, L. A., Yepes, G., Gottlöber, S., and Hoffman, Y. (2011b). The luminosities of backsplash galaxies in constrained simulations of the Local Group. *MNRAS*, 412(1):529–536.

Knobel, C., Lilly, S. J., Iovino, A., Kovač, K., Bschorr, T. J., Presotto, V., Oesch, P. A., Kampczyk, P., Carollo, C. M., Contini, T., Kneib, J. P., Le Fevre, O., Mainieri, V., Renzini, A., Scodeggio, M., Zamorani, G., Bardelli, S., Bolzonella, M., Bongiorno, A., Caputi, K., Cucciati, O., de la Torre, S., de Ravel, L., Franzetti, P., Garilli, B., Lamareille, F., Le Borgne, J. F., Le Brun, V., Maier, C., Mignoli, M., Pello, R., Peng, Y., Perez Montero, E., Silverman, J., Tanaka, M., Tasca, L., Tresse, L., Vergani, D., Zucca, E., Barnes, L., Bordoloi, R., Cappi, A., Cimatti, A., Coppa, G., Koekemoer, A. M., López-Sanjuan, C., McCracken, H. J., Moresco, M., Nair, P., Pozzetti, L., and Welikala, N. (2012). The zCOSMOS 20k Group Catalog. *ApJ*, 753(2):121.

Knobel, C., Lilly, S. J., Iovino, A., Porciani, C., Kovač, K., Cucciati, O., Finoguenov, A., Kitzbichler, M. G., Carollo, C. M., Contini, T., Kneib, J. P., Le Fèvre, O., Mainieri, V., Renzini, A., Scodeggio, M., Zamorani, G., Bardelli, S., Bolzonella, M., Bongiorno, A., Caputi, K., Coppa, G., de la Torre, S., de Ravel, L., Franzetti, P., Garilli, B., Kampczyk, P., Lamareille, F., Le Borgne, J. F., Le Brun, V., Maier, C., Mignoli, M., Pello, R., Peng, Y., Perez Montero, E., Ricciardelli, E., Silverman, J. D., Tanaka, M., Tasca, L., Tresse, L., Vergani, D., Zucca, E., Abbas, U., Bottini, D., Cappi, A., Cassata, P., Cimatti, A., Fumana, M., Guzzo, L., Koekemoer, A. M., Leauthaud, A., Maccagni, D., Marinoni, C., McCracken, H. J., Memeo, P., Meneux, B., Oesch, P., Pozzetti, L., and Scaramella, R. (2009). An Optical Group Catalog to z = 1 from the zCOSMOS 10 k Sample. *ApJ*, 697(2):1842–1860.

Kocsis, B. and Loeb, A. (2014). Menus for Feeding Black Holes. *Space Sci. Rev.*, 183(1-4):163–187.

Koutsouridou, I. and Cattaneo, A. (2022). Probing the link between quenching and morphological evolution. *MNRAS*, 516(3):4194–4211.

Kraljic, K., Arnouts, S., Pichon, C., Laigle, C., de la Torre, S., Vibert, D., Cadiou, C., Dubois, Y., Treyer, M., Schimd, C., Codis, S., de Lapparent, V., Devriendt, J., Hwang, H. S., Le Borgne, D., Malavasi, N., Milliard, B., Musso, M., Pogosyan, D., Alpaslan, M., Bland-Hawthorn, J., and Wright, A. H. (2018). Galaxy evolution in the metric of the cosmic web. *MNRAS*, 474(1):547–571.

Lemaître, G. (1931a). A homogeneous universe of constant mass and increasing radius accounting for the radial velocity of extra-galactic nebulae. *MNRAS*, 91:483–490.

Lemaître, G. (1931b). The Beginning of the World from the Point of View of Quantum Theory. *Nature*, 127(3210):706.

Lemaître, G. (1931c). The expanding universe. *MNRAS*, 91:490–501.

Lemson, G. and Virgo Consortium, t. (2006). Halo and Galaxy Formation Histories from the Millennium Simulation: Public release of a VO-oriented and SQL-queryable database for studying the evolution of galaxies in the LambdaCDM cosmogony. *arXiv e-prints*, pages astro–ph/0608019.

Lin, X., Wang, J., Kilborn, V., Peng, E. W., Cortese, L., Boselli, A., Liang, Z.-Z., Lee, B., Yang, D., Catinella, B., Deg, N., Dénes, H., Elagali, A., Kamphuis, P., Koribalski, B. S., Lee-Waddell, K., Rhee, J., Shao, L., Spekkens, K., Staveley-Smith, L., Westmeier, T., Wong, O. I., Bekki, K., Bosma, A., Du, M., Ho, L. C., Madrid, J. P., Verdes-Montenegro, L., Wang, H., and Wang, S. (2023). FAST-ASKAP Synergy: Quantifying Coexistent Tidal and Ram Pressure Strippings in the NGC 4636 Group. *ApJ*, 956(2):148.

Linde, A. D. (1982). A new inflationary universe scenario: A possible solution of the horizon, flatness, homogeneity, isotropy and primordial monopole problems. *Physics Letters B*, 108(6):389–393.

Liu, G. R. and Liu, M. B. (2003). *Smoothed Particle Hydrodynamics.* WORLD SCIENTIFIC.

Lofthouse, E. K., Fumagalli, M., Fossati, M., Dutta, R., Galbiati, M., Arrigoni Battaia, F., Cantalupo, S., Christensen, L., Cooke, R. J., Longobardi, A., Murphy, M. T., and Prochaska, J. X. (2023). MUSE Analysis of Gas around Galaxies (MAGG) - IV. The gaseous environment of z 3-4 Ly α emitting galaxies. *MNRAS*, 518(1):305–331.

Lucy, L. B. (1977). A numerical approach to the testing of the fission hypothesis. *AJ*, 82:1013–1024.

Lusso, E., Fumagalli, M., Fossati, M., Mackenzie, R., Bielby, R. M., Arrigoni Battaia, F., Cantalupo, S., Cooke, R., Cristiani, S., Dayal, P., D'Odorico, V., Haardt, F., Lofthouse, E., Morris, S., Peroux, C., Prichard, L., Rafelski, M., Simcoe, R., Swinbank, A. M., and Theuns, T. (2019). The MUSE Ultra Deep Field (MUDF) - I. Discovery of a group of Lyα nebulae associated with a bright z $\approx$ 3.23 quasar pair. *MNRAS*, 485(1):L62–L67.

Maciejewski, M., Colombi, S., Springel, V., Alard, C., and Bouchet, F. R. (2009). Phase-space structures - II. Hierarchical Structure Finder. *MNRAS*, 396(3):1329–1348.

Mamon, G. A., Sanchis, T., Salvador-Solé, E., and Solanes, J. M. (2004). The origin of H I-deficiency in galaxies on the outskirts of the Virgo cluster. I. How far can galaxies bounce out of clusters? *A&A*, 414:445–451.

Marigo, P. (2001). Chemical yields from low- and intermediate-mass stars: Model predictions and basic observational constraints. *A&A*, 370:194–217.

Marra, R., Churchill, C. W., Kacprzak, G. G., Vander Vliet, R., Ceverino, D., Lewis, J. G., Nielsen, N. M., Muzahid, S., and Charlton, J. C. (2021). Spatial Distribution of O VI Covering Fractions in the Simulated Circumgalactic Medium. *ApJ*, 907(1):8.

Massey, R., Kitching, T., and Richard, J. (2010). The dark matter of gravitational lensing. *Reports on Progress in Physics*, 73(8):086901.

Mathes, N. L., Churchill, C. W., and Murphy, M. T. (2017). The Vulture Survey I: Analyzing the Evolution of Mg II Absorbers. *arXiv e-prints*, page arXiv:1701.05624.

May, S. and Springel, V. (2023). The halo mass function and filaments in full cosmological simulations with fuzzy dark matter. *MNRAS*, 524(3):4256–4274.

McCarthy, I. G., Frenk, C. S., Font, A. S., Lacey, C. G., Bower, R. G., Mitchell, N. L., Balogh, M. L., and Theuns, T. (2008). Ram pressure stripping the hot gaseous haloes of galaxies in groups and clusters. *MNRAS*, 383(2):593–605.

Mitchell, P. D. and Schaye, J. (2022). Baryonic mass budgets for haloes in the EAGLE simulation, including ejected and prevented gas. *MNRAS*, 511(2):2600–2609.

Mo, H., van den Bosch, F., and White, S. (2010). *Galaxy Formation and Evolution*. Cambridge University Press.

Moore, B., Katz, N., Lake, G., Dressler, A., and Oemler, A. (1996). Galaxy harassment and the evolution of clusters of galaxies. *Nature*, 379(6566):613–616.

Moreno, J., Danieli, S., Bullock, J. S., Feldmann, R., Hopkins, P. F., çatmabacak, O., Gurvich, A., Lazar, A., Klein, C., Hummels, C. B., Hafen, Z., Mercado, F. J., Yu, S., Jiang, F., Wheeler, C., Wetzel, A., Anglés-Alcázar, D., Boylan-Kolchin, M., Quataert, E., Faucher-Giguère, C.-A., and Kereš, D. (2022). Galaxies lacking dark matter produced by close encounters in a cosmological simulation. *Nature Astronomy*, 6:496–502.

Moster, B. P., Naab, T., and White, S. D. M. (2013). Galactic star formation and accretion histories from matching galaxies to dark matter haloes. *MNRAS*, 428(4):3121–3138.

Muzahid, S., Schaye, J., Cantalupo, S., Marino, R. A., Bouché, N. F., Johnson, S., Maseda, M., Wendt, M., Wisotzki, L., and Zabl, J. (2021). MUSEQuBES: characterizing the circumgalactic medium of redshift ≈3.3 Ly α emitters. *MNRAS*, 508(4):5612–5637.

Naab, T. and Ostriker, J. P. (2017). Theoretical Challenges in Galaxy Formation. *ARA&A*, 55(1):59–109.

Naoz, S., Barkana, R., and Mesinger, A. (2009). Gas in simulations of high-redshift galaxies and minihaloes. *MNRAS*, 399(1):369–376.

Navarro, J. F., Frenk, C. S., and White, S. D. M. (1996). The Structure of Cold Dark Matter Halos. *ApJ*, 462:563.

Navarro, J. F., Frenk, C. S., and White, S. D. M. (1997). A Universal Density Profile from Hierarchical Clustering. *ApJ*, 490(2):493–508.

Nelson, D., Pillepich, A., Springel, V., Pakmor, R., Weinberger, R., Genel, S., Torrey, P., Vogelsberger, M., Marinacci, F., and Hernquist, L. (2019). First results from the TNG50 simulation: galactic outflows driven by supernovae and black hole feedback. *MNRAS*, 490(3):3234–3261.

Nelson, D., Sharma, P., Pillepich, A., Springel, V., Pakmor, R., Weinberger, R., Vogelsberger, M., Marinacci, F., and Hernquist, L. (2020). Resolving small-scale cold circumgalactic gas in TNG50. *MNRAS*, 498(2):2391–2414.

Nielsen, N. M., Kacprzak, G. G., Pointon, S. K., Churchill, C. W., and Murphy, M. T. (2018). MAGIICAT VI. The Mg II Intragroup Medium Is Kinematically Complex. *ApJ*, 869(2):153.

Okamoto, T., Gao, L., and Theuns, T. (2008). Mass loss of galaxies due to an ultraviolet background. *MNRAS*, 390(3):920–928.

Oppenheimer, B. D., Schaye, J., Crain, R. A., Werk, J. K., and Richings, A. J. (2018). The multiphase circumgalactic medium traced by low metal ions in EAGLE zoom simulations. *MNRAS*, 481(1):835–859.

Peacock, J. A. (1997). The evolution of galaxy clustering. *MNRAS*, 284:885–898.

Peebles, P. J. E. (1983). The sequence of cosmogony and the nature of primeval departures from homogeneity. *ApJ*, 274:1–6.

Peeples, M. S., Corlies, L., Tumlinson, J., O'Shea, B. W., Lehner, N., O'Meara, J. M., Howk, J. C., Earl, N., Smith, B. D., Wise, J. H., and Hummels, C. B. (2019). Figuring Out Gas & Galaxies in Enzo (FOGGIE). I. Resolving Simulated Circumgalactic Absorption at $2 \leq z \leq 2.5$. *ApJ*, 873(2):129.

Pereira Wilson, M., Navarro, J., Santos Santos, I., and Benitez Llambay, A. (2022). The beginning and the end of star formation in faint field dwarf galaxies. *arXiv e-prints*, page arXiv:2206.05338.

Péroux, C. and Howk, J. C. (2020). The Cosmic Baryon and Metal Cycles. *ARA&A*, 58:363–406.

Pillepich, A., Nelson, D., Springel, V., Pakmor, R., Torrey, P., Weinberger, R., Vogelsberger, M., Marinacci, F., Genel, S., van der Wel, A., and Hernquist, L. (2019). First results from the TNG50 simulation: the evolution of stellar and gaseous discs across cosmic time. *MNRAS*, 490(3):3196–3233.

Planck Collaboration, Adam, R., Ade, P. A. R., Aghanim, N., Akrami, Y., Alves, M. I. R., Argüeso, F., Arnaud, M., Arroja, F., Ashdown, M., Aumont, J., Baccigalupi, C., Ballardini, M., Banday, A. J., Barreiro, R. B., Bartlett, J. G., Bartolo, N., Basak, S., Battaglia, P., Battaner, E., Battye, R., Benabed, K., Benoît, A., Benoit-Lévy, A., Bernard, J. P., Bersanelli, M., Bertincourt, B., Bielewicz, P., Bikmaev, I., Bock, J. J., Böhringer, H., Bonaldi, A., Bonavera, L., Bond, J. R., Borrill, J., Bouchet, F. R., Boulanger, F., Bucher, M., Burenin, R., Burigana, C., Butler, R. C., Calabrese, E., Cardoso, J. F., Carvalho, P., Casaponsa, B., Castex, G., Catalano, A., Challinor, A., Chamballu, A., Chary, R. R., Chiang, H. C., Chluba, J., Chon, G., Christensen, P. R., Church, S., Clemens, M., Clements, D. L., Colombi, S., Colombo, L. P. L., Combet, C., Comis, B., Contreras, D., Couchot, F., Coulais, A., Crill, B. P., Cruz, M., Curto, A., Cuttaia, F., Danese, L., Davies, R. D., Davis, R. J., de Bernardis, P., de Rosa, A., de Zotti, G., Delabrouille, J., Delouis, J. M., Désert, F. X., Di Valentino, E., Dickinson, C., Diego, J. M., Dolag, K., Dole, H., Donzelli, S., Doré, O., Douspis, M., Ducout, A., Dunkley, J., Dupac, X., Efstathiou, G., Eisenhardt, P. R. M., Elsner, F., Enßlin, T. A., Eriksen, H. K., Falgarone, E., Fantaye, Y., Farhang, M., Feeney, S., Fergusson, J., Fernandez-Cobos, R., Feroz, F., Finelli, F., Florido, E., Forni, O., Frailis, M., Fraisse, A. A., Franceschet, C., Franceschi, E., Frejsel, A., Frolov, A., Galeotta, S., Galli, S., Ganga, K., Gauthier, C., Génova-Santos, R. T., Gerbino, M., Ghosh, T., Giard, M., Giraud-Héraud, Y., Giusarma, E., Gjerløw, E., González-Nuevo, J., Górski, K. M., Grainge, K. J. B., Gratton, S., Gregorio, A., Gruppuso, A., Gudmundsson, J. E., Hamann, J., Handley, W., Hansen, F. K., Hanson, D., Harrison, D. L., Heavens, A., Helou, G., Henrot-Versillé, S., Hernández-Monteagudo, C., Herranz, D., Hildebrandt, S. R., Hivon, E., Hobson, M., Holmes, W. A., Hornstrup, A., Hovest, W., Huang, Z., Huffenberger, K. M., Hurier, G., Ilić, S., Jaffe, A. H., Jaffe, T. R., Jin, T., Jones, W. C., Juvela, M., Karakci, A., Keihänen, E., Keskitalo, R., Khamitov, I., Kiiveri, K., Kim, J., Kisner, T. S., Kneissl, R., Knoche, J., Knox, L., Krachmalnicoff, N., Kunz, M., Kurki-Suonio, H., Lacasa, F., Lagache, G., Lähteenmäki, A., Lamarre, J. M., Langer, M., Lasenby, A., Lattanzi, M., Lawrence, C. R., Le Jeune, M., Leahy, J. P., Lellouch, E., Leonardi, R., León-Tavares, J., Lesgourgues, J., Levrier, F., Lewis, A., Liguori, M., Lilje, P. B., Lilley, M., Linden-Vørnle, M., Lindholm, V., Liu, H., López-Caniego, M., Lubin, P. M., Ma, Y. Z., Macías-Pérez, J. F., Maggio, G., Maino, D., Mak, D. S. Y., Mandolesi, N., Mangilli, A., Marchini, A., Marcos-Caballero, A., Marinucci, D., Maris, M., Marshall, D. J., Martin, P. G., Martinelli, M., Martínez-González, E., Masi, S., Matarrese, S., Mazzotta, P., McEwen, J. D., McGehee, P., Mei, S., Meinhold, P. R., Melchiorri, A., Melin, J. B., Mendes, L., Mennella, A., Migliaccio, M., Mikkelsen, K., Millea, M., Mitra, S., Miville-Deschênes, M. A., Molinari, D., Moneti, A., Montier, L., Moreno, R., Morgante, G., Mortlock, D., Moss, A., Mottet, S., Münchmeyer, M., Munshi, D., Murphy, J. A., Narimani, A., Naselsky, P., Nastasi, A., Nati, F., Natoli, P., Negrello, M., Netterfield, C. B., Nørgaard-Nielsen, H. U., Noviello, F., Novikov, D., Novikov, I., Olamaie, M., Oppermann, N., Orlando, E., Oxborrow, C. A., Paci, F., Pagano, L., Pajot, F., Paladini, R., Pandolfi, S., Paoletti, D., Partridge, B., Pasian, F., Patanchon, G., Pearson, T. J., Peel, M., Peiris, H. V., Pelkonen, V. M., Perdereau, O., Perotto, L., Perrott, Y. C., Perrotta, F., Pettorino, V., Piacentini, F., Piat, M., Pierpaoli, E., Pietrobon, D., Plaszczynski, S., Pogosyan, D., Pointecouteau, E., Polenta, G., Popa, L., Pratt, G. W., Prézeau, G., Prunet, S., Puget, J. L., Rachen, J. P., Racine, B., Reach, W. T., Rebolo, R., Reinecke, M., Remazeilles, M., Renault, C., Renzi, A., Ristorcelli, I., Rocha, G., Roman, M., Romelli, E., Rosset, C., Rossetti, M., Rotti, A., Roudier, G., Rouillé d'Orfeuil, B., Rowan-Robinson, M., Rubiño-Martín, J. A., Ruiz-Granados, B., Rumsey, C., Rusholme, B., Said, N., Salvatelli, V., Salvati, L., Sandri, M., Sanghera, H. S., Santos, D., Saunders, R. D. E., Sauvé, A., Savelainen, M., Savini, G., Schaefer, B. M., Schammel, M. P., Scott, D., Seiffert, M. D., Serra, P., Shellard, E. P. S., Shimwell,

T. W., Shiraishi, M., Smith, K., Souradeep, T., Spencer, L. D., Spinelli, M., Stanford, S. A., Stern, D., Stolyarov, V., Stompor, R., Strong, A. W., Sudiwala, R., Sunyaev, R., Sutter, P., Sutton, D., Suur-Uski, A. S., Sygnet, J. F., Tauber, J. A., Tavagnacco, D., Terenzi, L., Texier, D., Toffolatti, L., Tomasi, M., Tornikoski, M., Tramonte, D., Tristram, M., Troja, A., Trombetti, T., Tucci, M., Tuovinen, J., Türler, M., Umana, G., Valenziano, L., Valiviita, J., Van Tent, F., Vassallo, T., Vibert, L., Vidal, M., Viel, M., Vielva, P., Villa, F., Wade, L. A., Walter, B., Wandelt, B. D., Watson, R., Wehus, I. K., Welikala, N., Weller, J., White, M., White, S. D. M., Wilkinson, A., Yvon, D., Zacchei, A., Zibin, J. P., and Zonca, A. (2016). Planck 2015 results. I. Overview of products and scientific results. *A&A*, 594:A1.

Planck Collaboration, Ade, P. A. R., Aghanim, N., Alves, M. I. R., Armitage-Caplan, C., Arnaud, M., Ashdown, M., Atrio-Barandela, F., Aumont, J., Aussel, H., Baccigalupi, C., Banday, A. J., Barreiro, R. B., Barrena, R., Bartelmann, M., Bartlett, J. G., Bartolo, N., Basak, S., Battaner, E., Battye, R., Benabed, K., Benoît, A., Benoit-Lévy, A., Bernard, J.-P., Bersanelli, M., Bertincourt, B., Bethermin, M., Bielewicz, P., Bikmaev, I., Blanchard, A., Bobin, J., Bock, J. J., Böhringer, H., Bonaldi, A., Bonavera, L., Bond, J. R., Borrill, J., Bouchet, F. R., Boulanger, F., Bourdin, H., Bowyer, J. W., Bridges, M., Brown, M. L., Bucher, M., Burenin, R., Burigana, C., Butler, R. C., Calabrese, E., Cappellini, B., Cardoso, J.-F., Carr, R., Carvalho, P., Casale, M., Castex, G., Catalano, A., Challinor, A., Chamballu, A., Chary, R.-R., Chen, X., Chiang, H. C., Chiang, L.-Y, Chon, G., Christensen, P. R., Churazov, E., Church, S., Clemens, M., Clements, D. L., Colombi, S., Colombo, L. P. L., Combet, C., Comis, B., Couchot, F., Coulais, A., Crill, B. P., Cruz, M., Curto, A., Cuttaia, F., Da Silva, A., Dahle, H., Danese, L., Davies, R. D., Davis, R. J., de Bernardis, P., de Rosa, A., de Zotti, G., Déchelette, T., Delabrouille, J., Delouis, J.-M., Démoclès, J., Désert, F.-X., Dick, J., Dickinson, C., Diego, J. M., Dolag, K., Dole, H., Donzelli, S., Doré, O., Douspis, M., Ducout, A., Dunkley, J., Dupac, X., Efstathiou, G., Elsner, F., Enßlin, T. A., Eriksen, H. K., Fabre, O., Falgarone, E., Falvella, M. C., Fantaye, Y., Fergusson, J., Filliard, C., Finelli, F., Flores-Cacho, I., Foley, S., Forni, O., Fosalba, P., Frailis, M., Fraisse, A. A., Franceschi, E., Freschi, M., Fromenteau, S., Frommert, M., Gaier, T. C., Galeotta, S., Gallegos, J., Galli, S., Gandolfo, B., Ganga, K., Gauthier, C., Génova-Santos, R. T., Ghosh, T., Giard, M., Giardino, G., Gilfanov, M., Girard, D., Giraud-Héraud, Y., Gjerløw, E., González-Nuevo, J., Górski, K. M., Gratton, S., Gregorio, A., Gruppuso, A., Gudmundsson, J. E., Haissinski, J., Hamann, J., Hansen, F. K., Hansen, M., Hanson, D., Harrison, D. L., Heavens, A., Helou, G., Hempel, A., Henrot-Versillé, S., Hernández-Monteagudo, C., Herranz, D., Hildebrandt, S. R., Hivon, E., Ho, S., Hobson, M., Holmes, W. A., Hornstrup, A., Hou, Z., Hovest, W., Huey, G., Huffenberger, K. M., Hurier, G., Ili´c, S., Jaffe, A. H., Jaffe, T. R., Jasche, J., Jewell, J., Jones, W. C., Juvela, M., Kalberla, P., Kangaslahti, P., Keihänen, E., Kerp, J., Keskitalo, R., Khamitov, I., Kiiveri, K., Kim, J., Kisner, T. S., Kneissl, R., Knoche, J., Knox, L., Kunz, M., Kurki-Suonio, H., Lacasa, F., Lagache, G., Lähteenmäki, A., Lamarre, J.-M., Langer, M., Lasenby, A., Lattanzi, M., Laureijs, R. J., Lavabre, A., Lawrence, C. R., Le Jeune, M., Leach, S., Leahy, J. P., Leonardi, R., León-Tavares, J., Leroy, C., Lesgourgues, J., Lewis, A., Li, C., Liddle, A., Liguori, M., Lilje, P. B., Linden-Vørnle, M., Lindholm, V., López-Caniego, M., Lowe, S., Lubin, P. M., Macías-Pérez, J. F., MacTavish, C. J., Maffei, B., Maggio, G., Maino, D., Mandolesi, N., Mangilli, A., Marcos-Caballero, A., Marinucci, D., Maris, M., Marleau, F., Marshall, D. J., Martin, P. G., Martínez-González, E., Masi, S., Massardi, M., Matarrese, S., Matsumura, T., Matthai, F., Maurin, L., Mazzotta, P., McDonald, A., McEwen, J. D., McGehee, P., Mei, S., Meinhold, P. R., Melchiorri, A., Melin, J.-B., Mendes, L., Menegoni, E., Mennella, A., Migliaccio, M., Mikkelsen, K., Millea, M., Miniscalco, R., Mitra, S., Miville-Deschênes, M.-A., Molinari, D., Moneti, A., Montier, L., Morgante, G., Morisset, N., Mortlock, D., Moss, A., Munshi, D., Murphy, J. A., Naselsky, P., Nati, F., Natoli, P., Negrello, M., Nesvadba, N. P. H., Netterfield, C. B., Nørgaard-Nielsen, H. U., North, C., Noviello, F., Novikov, D., Novikov, I., O´Dwyer, I. J., Orieux, F., Osborne, S., O´Sullivan, C., Oxborrow, C. A., Paci, F., Pagano, L., Pajot, F., Paladini, R., Pandolfi, S., Paoletti, D., Partridge, B., Pasian, F., Patanchon, G., Paykari, P., Pearson, D., Pearson, T. J., Peel, M., Peiris, H. V., Perdereau, O., Perotto, L., Perrotta, F., Pettorino, V., Piacentini, F., Piat, M., Pierpaoli, E., Pietrobon, D., Plaszczynski, S., Platania, P., Pogosyan, D., Pointecouteau, E., Polenta, G., Ponthieu, N., Popa, L., Poutanen, T., Pratt, G. W., Prézeau, G., Prunet, S., Puget, J.-L., Pullen, A. R., Rachen, J. P., Racine, B., Rahlin, A., Räth, C., Reach, W. T., Rebolo, R., Reinecke, M., Remazeilles, M., Renault, C., Renzi, A., Riazuelo, A., Ricciardi, S., Riller, T., Ringeval, C., Ristorcelli, I., Robbers, G., Rocha, G., Roman, M., Rosset, C., Rossetti, M., Roudier, G., Rowan-Robinson, M., Rubiño-Martín, J. A., Ruiz-Granados, B., Rusholme, B., Salerno, E., Sandri, M., Sanselme, L., Santos, D., Savelainen, M., Savini, G., Schaefer, B. M., Schiavon, F., Scott, D., Seiffert, M. D., Serra, P., Shellard, E. P. S., Smith, K., Smoot, G. F., Souradeep, T., Spencer, L. D., Starck, J.-L., Stolyarov, V., Stompor, R., Sudiwala, R., Sunyaev, R., Sureau, F., Sutter, P., Sutton, D., Suur-Uski, A.-S., Sygnet, J.-F., Tauber, J. A., Tavagnacco, D., Taylor, D., Terenzi, L., Texier, D., Toffolatti, L., Tomasi, M., Torre, J.-P., Tristram, M., Tucci, M., Tuovinen, J., Türler, M., Tuttlebee, M., Umana, G., Valenziano, L., Valiviita, J., Van Tent, B., Varis, J., Vibert, L., Viel, M., Vielva, P., Villa, F., Vittorio, N., Wade, L. A., Wandelt, B. D., Watson, C., Watson, R., Wehus, I. K., Welikala, N., Weller, J., White, M., White, S. D. M., Wilkinson, A., Winkel, B., Xia, J.-Q., Yvon, D., Zacchei, A., Zibin, J. P., and Zonca, A. (2014). Planck 2013 results. i. overview of products and scientific results. *A&A*, 571:A1.

Planck Collaboration, Aghanim, N., Akrami, Y., Ashdown, M., Aumont, J., Baccigalupi, C., Ballardini, M., Banday, A. J., Barreiro, R. B., Bartolo, N., Basak, S., Battye, R., Benabed, K., Bernard, J.-P., Bersanelli, M., Bielewicz, P., Bock, J. J., Bond, J. R., Borrill, J., Bouchet, F. R., Boulanger, F., Bucher, M., Burigana, C., Butler, R. C., Calabrese, E., Cardoso, J.-F., Carron, J., Challinor, A., Chiang, H. C., Chluba, J., Colombo, L. P. L., Combet, C., Contreras, D., Crill, B. P., Cuttaia, F., de Bernardis, P., de Zotti, G., Delabrouille, J., Delouis, J.-M., Di Valentino, E., Diego, J. M., Doré, O., Douspis, M., Ducout, A., Dupac, X., Dusini, S., Efstathiou, G., Elsner, F., Enßlin,

T. A., Eriksen, H. K., Fantaye, Y., Farhang, M., Fergusson, J., Fernandez-Cobos, R., Finelli, F., Forastieri, F., Frailis, M., Fraisse, A. A., Franceschi, E., Frolov, A., Galeotta, S., Galli, S., Ganga, K., Génova-Santos, R. T., Gerbino, M., Ghosh, T., González-Nuevo, J., Górski, K. M., Gratton, S., Gruppuso, A., Gudmundsson, J. E., Hamann, J., Handley, W., Hansen, F. K., Herranz, D., Hildebrandt, S. R., Hivon, E., Huang, Z., Jaffe, A. H., Jones, W. C., Karakci, A., Keihänen, E., Keskitalo, R., Kiiveri, K., Kim, J., Kisner, T. S., Knox, L., Krachmalnicoff, N., Kunz, M., Kurki-Suonio, H., Lagache, G., Lamarre, J.-M., Lasenby, A., Lattanzi, M., Lawrence, C. R., Le Jeune, M., Lemos, P., Lesgourgues, J., Levrier, F., Lewis, A., Liguori, M., Lilje, P. B., Lilley, M., Lindholm, V., López-Caniego, M., Lubin, P. M., Ma, Y.-Z., Macías-Pérez, J. F., Maggio, G., Maino, D., Mandolesi, N., Mangilli, A., Marcos-Caballero, A., Maris, M., Martin, P. G., Martinelli, M., Martínez-González, E., Matarrese, S., Mauri, N., McEwen, J. D., Meinhold, P. R., Melchiorri, A., Mennella, A., Migliaccio, M., Millea, M., Mitra, S., Miville-Deschênes, M.-A., Molinari, D., Montier, L., Morgante, G., Moss, A., Natoli, P., Nørgaard-Nielsen, H. U., Pagano, L., Paoletti, D., Partridge, B., Patanchon, G., Peiris, H. V., Perrotta, F., Pettorino, V., Piacentini, F., Polastri, L., Polenta, G., Puget, J.-L., Rachen, J. P., Reinecke, M., Remazeilles, M., Renzi, A., Rocha, G., Rosset, C., Roudier, G., Rubiño-Martín, J. A., Ruiz-Granados, B., Salvati, L., Sandri, M., Savelainen, M., Scott, D., Shellard, E. P. S., Sirignano, C., Sirri, G., Spencer, L. D., Sunyaev, R., Suur-Uski, A.-S., Tauber, J. A., Tavagnacco, D., Tenti, M., Toffolatti, L., Tomasi, M., Trombetti, T., Valenziano, L., Valiviita, J., Van Tent, B., Vibert, L., Vielva, P., Villa, F., Vittorio, N., Wandelt, B. D., Wehus, I. K., White, M., White, S. D. M., Zacchei, A., and Zonca, A. (2020a). Planck 2018 results - vi. cosmological parameters. *A&A*, 641:A6.

Planck Collaboration, Akrami, Y., Arroja, F., Ashdown, M., Aumont, J., Baccigalupi, C., Ballardini, M., Banday, A. J., Barreiro, R. B., Bartolo, N., Basak, S., Benabed, K., Bernard, J. P., Bersanelli, M., Bielewicz, P., Bock, J. J., Bond, J. R., Borrill, J., Bouchet, F. R., Boulanger, F., Bucher, M., Burigana, C., Butler, R. C., Calabrese, E., Cardoso, J. F., Carron, J., Challinor, A., Chiang, H. C., Colombo, L. P. L., Combet, C., Contreras, D., Crill, B. P., Cuttaia, F., de Bernardis, P., de Zotti, G., Delabrouille, J., Delouis, J. M., Di Valentino, E., Diego, J. M., Donzelli, S., Doré, O., Douspis, M., Ducout, A., Dupac, X., Dusini, S., Efstathiou, G., Elsner, F., Enßlin, T. A., Eriksen, H. K., Fantaye, Y., Fergusson, J., Fernandez-Cobos, R., Finelli, F., Forastieri, F., Frailis, M., Franceschi, E., Frolov, A., Galeotta, S., Galli, S., Ganga, K., Gauthier, C., Génova-Santos, R. T., Gerbino, M., Ghosh, T., González-Nuevo, J., Górski, K. M., Gratton, S., Gruppuso, A., Gudmundsson, J. E., Hamann, J., Handley, W., Hansen, F. K., Herranz, D., Hivon, E., Hooper, D. C., Huang, Z., Jaffe, A. H., Jones, W. C., Keihänen, E., Keskitalo, R., Kiiveri, K., Kim, J., Kisner, T. S., Krachmalnicoff, N., Kunz, M., Kurki-Suonio, H., Lagache, G., Lamarre, J. M., Lasenby, A., Lattanzi, M., Lawrence, C. R., Le Jeune, M., Lesgourgues, J., Levrier, F., Lewis, A., Liguori, M., Lilje, P. B., Lindholm, V., López-Caniego, M., Lubin, P. M., Ma, Y. Z., Macías-Pérez, J. F., Maggio, G., Maino, D., Mandolesi, N., Mangilli, A., Marcos-Caballero, A., Maris, M., Martin, P. G., Martínez-González, E., Matarrese, S., Mauri, N., McEwen, J. D., Meerburg, P. D., Meinhold,

P. R., Melchiorri, A., Mennella, A., Migliaccio, M., Mitra, S., Miville-Deschênes, M. A., Molinari, D., Moneti, A., Montier, L., Morgante, G., Moss, A., Münchmeyer, M., Natoli, P., Nørgaard-Nielsen, H. U., Pagano, L., Paoletti, D., Partridge, B., Patanchon, G., Peiris, H. V., Perrotta, F., Pettorino, V., Piacentini, F., Polastri, L., Polenta, G., Puget, J. L., Rachen, J. P., Reinecke, M., Remazeilles, M., Renzi, A., Rocha, G., Rosset, C., Roudier, G., Rubiño-Martín, J. A., Ruiz-Granados, B., Salvati, L., Sandri, M., Savelainen, M., Scott, D., Shellard, E. P. S., Shiraishi, M., Sirignano, C., Sirri, G., Spencer, L. D., Sunyaev, R., Suur-Uski, A. S., Tauber, J. A., Tavagnacco, D., Tenti, M., Toffolatti, L., Tomasi, M., Trombetti, T., Valiviita, J., Van Tent, B., Vielva, P., Villa, F., Vittorio, N., Wandelt, B. D., Wehus, I. K., White, S. D. M., Zacchei, A., Zibin, J. P., and Zonca, A. (2020b). Planck 2018 results. X. Constraints on inflation. *A&A*, 641:A10.

Planelles, S., Schleicher, D. R. G., and Bykov, A. M. (2015). Large-Scale Structure Formation: From the First Non-linear Objects to Massive Galaxy Clusters. *Space Sci. Rev.*, 188(1-4):93–139.

Pointon, S. K., Nielsen, N. M., Kacprzak, G. G., Muzahid, S., Churchill, C. W., and Charlton, J. C. (2017). The Impact of the Group Environment on the O VI Circumgalactic Medium. *ApJ*, 844(1):23.

Portinari, L., Chiosi, C., and Bressan, A. (1998). Galactic chemical enrichment with new metallicity dependent stellar yields. *A&A*, 334:505–539.

Potter, D., Stadel, J., and Teyssier, R. (2017). PKDGRAV3: beyond trillion particle cosmological simulations for the next era of galaxy surveys. *Computational Astrophysics and Cosmology*, 4(1):2.

Power, C., Navarro, J. F., Jenkins, A., Frenk, C. S., White, S. D. M., Springel, V., Stadel, J., and Quinn, T. (2003). The inner structure of ΛCDM haloes - I. A numerical convergence study. *MNRAS*, 338(1):14–34.

Putman, M. E., Zheng, Y., Price-Whelan, A. M., Grcevich, J., Johnson, A. C., Tollerud, E., and Peek, J. E. G. (2021). The Gas Content and Stripping of Local Group Dwarf Galaxies. *ApJ*, 913(1):53.

Quinn, P. J., Salmon, J. K., and Zurek, W. H. (1986). Primordial density fluctuations and the structure of galactic haloes. *Nature*, 322(6077):329–335.

Quinn, T., Katz, N., and Efstathiou, G. (1996). Photoionization and the formation of dwarf galaxies. *MNRAS*, 278(4):L49–L54.

Ramesh, R. and Nelson, D. (2023). Zooming in on the circumgalactic medium: resolving small-scale gas structure with the GIBLE cosmological simulations. *arXiv e-prints*, page arXiv:2307.11143.

Rasmussen, J., Ponman, T. J., and Mulchaey, J. S. (2006). Gas stripping in galaxy groups - the case of the starburst spiral NGC 2276. *MNRAS*, 370(1):453–467.

Read, J. I., Iorio, G., Agertz, O., and Fraternali, F. (2017). The stellar mass-halo mass relation of isolated field dwarfs: a critical test of ΛCDM at the edge of galaxy formation. *MNRAS*, 467(2):2019–2038.

Rees, M. J. (1986). Lyman absorption lines in quasar spectra - Evidence for gravitationally-confined gas in dark minihaloes. *MNRAS*, 218:25P–30P.

Rey, M. P., Pontzen, A., Agertz, O., Orkney, M. D. A., Read, J. I., Saintonge, A., Kim, S. Y., and Das, P. (2022). EDGE: What shapes the relationship between H I and stellar observables in faint dwarf galaxies? *MNRAS*, 511(4):5672–5681.

Riess, A. G., Filippenko, A. V., Challis, P., Clocchiatti, A., Diercks, A., Garnavich, P. M., Gilliland, R. L., Hogan, C. J., Jha, S., Kirshner, R. P., Leibundgut, B., Phillips, M. M., Reiss, D., Schmidt, B. P., Schommer, R. A., Smith, R. C., Spyromilio, J., Stubbs, C., Suntzeff, N. B., and Tonry, J. (1998). Observational Evidence from Supernovae for an Accelerating Universe and a Cosmological Constant. *AJ*, 116(3):1009–1038.

Roberts, I. D., van Weeren, R. J., McGee, S. L., Botteon, A., Ignesti, A., and Rottgering, H. J. A. (2021). Lotss jellyfish galaxies - ii. ram pressure stripping in groups versus clusters. *A&A*, 652:A153.

Robertson, H. P. (1935). Kinematics and World-Structure. *ApJ*, 82:284.

Robertson, H. P. (1936a). Kinematics and World-Structure II. *ApJ*, 83:187.

Robertson, H. P. (1936b). Kinematics and World-Structure III. *ApJ*, 83:257.

Roy, M., Su, K.-Y., Tonnesen, S., Fielding, D. B., and Faucher-Giguère, C.-A. (2023). Seeding the CGM: How Satellites Populate the Cold Phase of Milky Way Halos. *arXiv e-prints*, page arXiv:2310.04404.

Rubin, V. C., Ford, W. K., J., and Thonnard, N. (1980). Rotational properties of 21 SC galaxies with a large range of luminosities and radii, from NGC 4605 (R=4kpc) to UGC 2885 (R=122kpc). *ApJ*, 238:471–487.

Sales, L. V., Navarro, J. F., Abadi, M. G., and Steinmetz, M. (2007). Cosmic ménage à trois: the origin of satellite galaxies on extreme orbits. *MNRAS*, 379(4):1475–1483.

Santos-Santos, I. M. E., Navarro, J. F., and McConnachie, A. (2023). The Tucana dwarf spheroidal: a distant backsplash galaxy of M31? *MNRAS*, 520(1):55–62.

Sato, K. (1981). First-order phase transition of a vacuum and the expansion of the Universe. *MNRAS*, 195:467–479.

Schaller, M., Dalla Vecchia, C., Schaye, J., Bower, R. G., Theuns, T., Crain, R. A., Furlong, M., and McCarthy, I. G. (2015). The EAGLE simulations of galaxy formation: the importance of the hydrodynamics scheme. *MNRAS*, 454(3):2277–2291.

Schaye, J., Crain, R. A., Bower, R. G., Furlong, M., Schaller, M., Theuns, T., Dalla Vecchia, C., Frenk, C. S., McCarthy, I. G., Helly, J. C., Jenkins, A., Rosas-Guevara, Y. M., White, S. D. M., Baes, M., Booth, C. M., Camps, P., Navarro, J. F., Qu, Y., Rahmati, A., Sawala, T., Thomas, P. A., and Trayford, J. (2015). The EAGLE project: simulating the evolution and assembly of galaxies and their environments. *MNRAS*, 446(1):521–554.

Schaye, J. and Dalla Vecchia, C. (2008). On the relation between the Schmidt and Kennicutt-Schmidt star formation laws and its implications for numerical simulations. *MNRAS*, 383(3):1210–1222.

Schneider, P. (2015). *Extragalactic Astronomy and Cosmology*, volume 2. Springer.

Seljak, U. and Zaldarriaga, M. (1996). A Line-of-Sight Integration Approach to Cosmic Microwave Background Anisotropies. *ApJ*, 469:437.

Shen, Z., van Dokkum, P., and Danieli, S. (2023). Confirmation of an Anomalously Low Dark Matter Content for the Galaxy NGC 1052-DF4 from Deep, High-resolution Continuum Spectroscopy. *ApJ*, 957(1):6.

Shin, E.-j., Jung, M., Kwon, G., Kim, J.-h., Lee, J., Jo, Y., and Oh, B. K. (2020). Dark Matter Deficient Galaxies Produced via High-velocity Galaxy Collisions in High-resolution Numerical Simulations. *ApJ*, 899(1):25.

Silk, J. (2019). Ultra-diffuse galaxies without dark matter. *MNRAS*, 488(1):L24–L28.

Somerville, R. S. and Davé, R. (2015). Physical Models of Galaxy Formation in a Cosmological Framework. *ARA&A*, 53:51–113.

Sousbie, T. (2011). The persistent cosmic web and its filamentary structure - I. Theory and implementation. *MNRAS*, 414(1):350–383.

Sousbie, T., Pichon, C., and Kawahara, H. (2011). The persistent cosmic web and its filamentary structure - II. Illustrations. *MNRAS*, 414(1):384–403.

Springel, V. (2005). The cosmological simulation code GADGET-2. *MNRAS*, 364(4):1105–1134.

Springel, V., Di Matteo, T., and Hernquist, L. (2005). Modelling feedback from stars and black holes in galaxy mergers. *MNRAS*, 361(3):776–794.

Springel, V. and Hernquist, L. (2002). Cosmological smoothed particle hydrodynamics simulations: the entropy equation. *MNRAS*, 333(3):649–664.

Springel, V., White, S. D. M., Tormen, G., and Kauffmann, G. (2001). Populating a cluster of galaxies - I. Results at z=0. *MNRAS*, 328(3):726–750.

Starobinsky, A. A. (1980). A new type of isotropic cosmological models without singularity. *Physics Letters B*, 91(1):99–102.

Suresh, J., Bird, S., Vogelsberger, M., Genel, S., Torrey, P., Sijacki, D., Springel, V., and Hernquist, L. (2015). The impact of galactic feedback on the circumgalactic medium. *MNRAS*, 448(1):895–909.

Ta-Pei, C. (2010). *Relativity, Gravitation and Cosmology : A Basic Introduction.* Number Vol. 11 in Oxford Master Series in Physics. OUP Oxford.

Thoul, A. A. and Weinberg, D. H. (1996). Hydrodynamic Simulations of Galaxy Formation. II. Photoionization and the Formation of Low-Mass Galaxies. *ApJ*, 465:608.

Trujillo, I., Beasley, M. A., Borlaff, A., Carrasco, E. R., Di Cintio, A., Filho, M., Monelli, M., Montes, M., Román, J., Ruiz-Lara, T., Sánchez Almeida, J., Valls-Gabaud, D., and Vazdekis, A. (2019). A distance of 13 Mpc resolves the claimed anomalies of the galaxy lacking dark matter. *MNRAS*, 486(1):1192–1219.

Tumlinson, J., Peeples, M. S., and Werk, J. K. (2017). The Circumgalactic Medium. *ARA&A*, 55(1):389–432.

Turner, M. L., Schaye, J., Crain, R. A., Rudie, G., Steidel, C. C., Strom, A., and Theuns, T. (2017). A comparison of observed and simulated absorption from H I, C IV, and Si IV around z $\approx$ 2 star-forming galaxies suggests redshift-space distortions are due to inflows. *MNRAS*, 471(1):690–705.

van de Voort, F., Bieri, R., Pakmor, R., Gómez, F. A., Grand, R. J. J., and Marinacci, F. (2021). The effect of magnetic fields on properties of the circumgalactic medium. *MNRAS*, 501(4):4888–4902.

van de Voort, F., Springel, V., Mandelker, N., van den Bosch, F. C., and Pakmor, R. (2019). Cosmological simulations of the circumgalactic medium with 1 kpc resolution: enhanced H I column densities. *MNRAS*, 482(1):L85–L89.

van den Bergh, S. (1994). The Evolutionary History of Low-Luminosity Local Group Dwarf Galaxies. *ApJ*, 428:617.

van Dokkum, P., Cohen, Y., Danieli, S., Kruijssen, J. M. D., Romanowsky, A. J., Merritt, A., Abraham, R., Brodie, J., Conroy, C., Lokhorst, D., Mowla, L., O'Sullivan, E., and Zhang, J. (2018a). An Enigmatic Population of Luminous Globular Clusters in a Galaxy Lacking Dark Matter. *ApJ*, 856(2):L30.

van Dokkum, P., Danieli, S., Abraham, R., Conroy, C., and Romanowsky, A. J. (2019a). A Second Galaxy Missing Dark Matter in the NGC 1052 Group. *ApJ*, 874(1):L5.

van Dokkum, P., Danieli, S., Cohen, Y., Merritt, A., Romanowsky, A. J., Abraham, R., Brodie, J., Conroy, C., Lokhorst, D., Mowla, L., O'Sullivan, E., and Zhang, J. (2018b). A galaxy lacking dark matter. *Nature*, 555(7698):629–632.

van Dokkum, P., Danieli, S., Romanowsky, A., Abraham, R., and Conroy, C. (2019b). The Distance to NGC 1042 in the Context of its Proposed Association with the Dark Matter-deficient Galaxies NGC 1052-DF2 and NGC 1052-DF4. *Research Notes of the American Astronomical Society*, 3(2):29.

van Dokkum, P., Shen, Z., Keim, M. A., Trujillo-Gomez, S., Danieli, S., Dutta Chowdhury, D., Abraham, R., Conroy, C., Kruijssen, J. M. D., Nagai, D., and Romanowsky, A. (2022). A trail of dark-matter-free galaxies from a bullet-dwarf collision. *Nature*, 605(7910):435–439.

Vazquez, J. A., Padilla, L. E., and Matos, T. (2018). Inflationary Cosmology: From Theory to Observations. *arXiv e-prints*, page arXiv:1810.09934.

Vogelsberger, M., Marinacci, F., Torrey, P., and Puchwein, E. (2020). Cosmological simulations of galaxy formation. *Nature Reviews Physics*, 2(1):42–66.

Vulcani, B., Poggianti, B. M., Jaffé, Y. L., Moretti, A., Fritz, J., Gullieuszik, M., Bettoni, D., Fasano, G., Tonnesen, S., and McGee, S. (2018). GASP - XII. The variety of physical processes occurring in a single galaxy group in formation. *MNRAS*, 480(3):3152–3169.

Walker, A. G. (1937). On Milne's Theory of World-Structure. *Proceedings of the London Mathematical Society*, 42:90–127.

Weinberg, D. H., Hernquist, L., and Katz, N. (1997). Photoionization, Numerical Resolution, and Galaxy Formation. *ApJ*, 477(1):8–20.

White, S. D. M. and Rees, M. J. (1978). Core condensation in heavy halos: a two-stage theory for galaxy formation and clustering. *MNRAS*, 183:341–358.

Wiersma, R. P. C., Schaye, J., and Smith, B. D. (2009a). The effect of photoionization on the cooling rates of enriched, astrophysical plasmas. *MNRAS*, 393(1):99–107.

Wiersma, R. P. C., Schaye, J., Theuns, T., Dalla Vecchia, C., and Tornatore, L. (2009b). Chemical enrichment in cosmological, smoothed particle hydrodynamics simulations. *MNRAS*, 399(2):574–600.

Wilde, M. C., Tchernyshyov, K., Werk, J. K., Tripp, T. M., Burchett, J. N., Prochaska, J. X., Tejos, N., Lehner, N., Bordoloi, R., O'Meara, J. M., Tumlinson, J., and Howk, J. C. (2023). CGM^2 + CASBaH: The Mass Dependence of H I Lyα-Galaxy Clustering and the Extent of the CGM. *ApJ*, 948(2):114.

Workman, R. L. and Others (2022). Review of Particle Physics. *PTEP*, 2022:083C01.

Wright, A. C., Brooks, A. M., Weisz, D. R., and Christensen, C. R. (2019). Reignition of star formation in dwarf galaxies. *MNRAS*, 482(1):1176–1189.

Wright, R. J., Lagos, C. d. P., Power, C., and Mitchell, P. D. (2020). The impact of stellar and AGN feedback on halo-scale baryonic and dark matter accretion in the EAGLE simulations. *MNRAS*, 498(2):1668–1692.

Yoon, J. H. and Putman, M. E. (2013). The Influence of Environment on the Circumgalactic Medium. *ApJ*, 772(2):L29.

Ringraziamenti - Danksagung

Ich möchte mich bei meinen Eltern für die jahrelange Unterstützung bedanken, ohne die es mir niemals möglich gewesen wäre, bis hier her zu kommen. Weiters möchte ich mich bei meinem Bruder Martin bedanken fürs gemeinsame Skaten und Xbox spielen sowie die Diskussionen während des ersten Jahres meines Doktorats, als ich in Passail war und hoffe, dass auch er irgendwann seinen Weg gehen wird. Ich möchte mich auch bei meinem Bruder Lukas, seiner Frau Saskia sowie Sophia und dem neuen Mitglied der Familie bedanken, nicht nur für die finanzielle Unterstützung, als mir die Uni einige tausend Euro geschuldet hat, sondern auch für die Gastfreundschaft, wenn ich sie in Irland besucht habe.

Furthermore, I want to thank Michele for the help and guidance through this process even if it was not always easy. I want to thank Alejandro for teaching me all the basics about simulations, for the long and fruitful discussions in his office which sometimes turned into discussions of politics or just life in general, as well as for the patience in explaining some things several times if I did not understand them straight away or simply forgot. I want to thank Alessia, Emma, Louise, and Rajeshwari for being such a great group of colleagues and friends inside and outside of the university, as well as for exploring Italy together on our trips to Venezia, Trieste, Catania, and Cagliari. I also want to thank Giulia for being such a good addition to our group in the few months she was with us.

I want to thank Luca for the coffee breaks and friendship and David and the others of the Caravaggio office for having their door always open and for their help. I want to thank Fabiola, Ludovica, Marta, and all the other PhD students for being in this adventure together and for the mutual support. I want to thank Yrupe for coffee, beer, and going out as well as the positive energy she brought to the department. Voglio anche ringraziare la Alice per le pause di caffè e pranzo, per portarmi in Spagna e essere la mia maestra di surf. Voglio anché ringraziarla per la sua pazienza quando ho di nuovo sbagliato la forma del congiuntivo e condizionale o quando ho di nuovo inventato una nuova parola in italiano.

I want to thank Ulrich for the continuous friendship and for hosting me in Vienna whenever I was visiting. I also want to thank him for making me see an Italian police station from the inside. I want to thank Megan for supporting me through a very difficult time. And I want to thank Silvester for showing me Torino and bringing me to the ESC public viewing.

I want to thank everyone from Cafezal for keeping me caffeinated while writing up my thesis or relaxing during the weekend. I want to thank the people from Namascé for the great concerts and Robin and everyone else at Art Rock Cafe who made me drunk and kept me company when I needed it. Furthermore, I want to thank all the people at the above places who gave me free coffee, cookies, or a discount on beer when their bosses did not look.

Grazie anché ai miei coinquilini, e grazie a tutti del mio gruppo di Capoeira che è diventato una seconda famiglia.

Finally, I also want to thank Stefano Ragazzi for looking after our health by making us walk up to his office several times whenever we wanted to have a mission approved. I want to thank Bicocca for taking several months to reimburse us so that sometimes I did not know how to pay my bills. I want to thank the managers of the student residence U22 for only giving us a few day's notice whether we are homeless or not for the next academic year. Without this existential angst of homelessness and poverty, my PhD experience would not have been the same. Furthermore, I want to thank the Italian bureaucracy for making me understand how the protagonists in Kafka's novels must have felt.

To end on a good note, I want to thank Giulia Liguori who was the one who kept everything running at the Astrophysics department in Bicocca. It was a shame that you had to go.